GHENT UNIVERSITY

Ghent University
Faculty of Sciences
Department of Physics and Astronomy

Consolidation and longevity of the CMS Resistive Plate Chamber system in view of the High-Luminosity LHC Upgrade

Alexis Fagot

Thesis to obtain the degree of
Doctor of Philosophy in Physics
Academic year 2018-2019

Ghent University
Faculty of Sciences
Department of Physics and Astronomy

Promotors: Dr. Michael Tytgat
Prof. Dr. Dirk Ryckbosch

Ghent University
Faculty of Sciences

Department of Physics and Astronomy
Proeftuinstraat 86, B-9000 Ghent, Belgium

Tel.: +32 9 264.65.28
Fax.: +32 9 264.66.97

Alexis Fagot

Thesis to obtain the degree of
Doctor of Philosophy in Physics
Academic year 2018-2019

Acknowledgements

XX/XX/2018
Alexis Fagot

Table of Contents

Acknowledgements **i**

Nederlandse samenvatting **vii**

English summary **ix**

1 Introduction **1-1**

2 Investigating the TeV scale **2-1**
- 2.1 The Standard Model of Particle Physics . . . 2-1
  - 2.1.1 A history of particle physics . . . 2-2
  - 2.1.2 Construction and validation of the Standard Model . . . 2-14
  - 2.1.3 Investigating the TeV scale . . . 2-15
- 2.2 The Large Hadron Collider & the Compact Muon Solenoid . . . 2-20
  - 2.2.1 LHC, the most powerful particle accelerator . . . 2-20
  - 2.2.2 Timeline of operation . . . 2-23
  - 2.2.3 High Luminosity LHC . . . 2-25
  - 2.2.4 The Compact Muon Solenoid experiment . . . 2-25
    - 2.2.4.1 The silicon tracker . . . 2-27
    - 2.2.4.2 The calorimeters . . . 2-27
    - 2.2.4.3 The muon system . . . 2-28

3 Muon Phase-2 Upgrade **3-1**
- 3.1 Motivations for HL-LHC and the upgrade of CMS . . . 3-1
- 3.2 Desciption of the muon system . . . 3-5
  - 3.2.1 The Drift Tubes . . . 3-5
  - 3.2.2 The Cathode Strip Chambers . . . 3-6
  - 3.2.3 The Resistive Plate Chambers . . . 3-7
- 3.3 Necessity for improved electronics . . . 3-8
- 3.4 New detectors and increased acceptance . . . 3-10
  - 3.4.1 Gas electron multipliers . . . 3-12
  - 3.4.2 Improved forward resistive plate chambers . . . 3-15
- 3.5 Impact on Level-1 Trigger and physics performance . . . 3-17
- 3.6 Ecofriendly gas studies . . . 3-20

4 Physics of Resistive plate chambers **4-1**
- 4.1 Principle . . . 4-1
- 4.2 Rate capability and time resolution of Resistive Plate Chambers . . . 4-3
  - 4.2.1 Operation modes . . . 4-3
  - 4.2.2 Standard gas mixture for RPCs operated in collider experiments . . . 4-5
  - 4.2.3 Detector designs and performance . . . 4-9

4.2.3.1 Double-gap RPC 4-12
4.2.3.2 Multigap RPC (MRPC) 4-13
4.2.3.3 Charge distribution and performance limitations 4-17
4.3 Signal formation 4-19
4.3.1 Energy loss at intermediate energies 4-20
4.3.2 Primary ionization 4-24
4.3.3 Development and propagation of avalanches 4-28
4.3.4 Drift and diffusion of the electron cloud 4-32
4.3.5 Space charge effect & streamers 4-34
4.4 Effect of atmospherical conditions on the detector's performance 4-38

5 Longevity studies and Consolidation of the present CMS RPC subsystem 5-1
5.1 Testing detectors under extreme conditions 5-2
5.1.1 GIF 5-4
5.1.2 GIF++ 5-5
5.2 Preliminary studies at GIF 5-7
5.2.1 RPC test setup 5-7
5.2.2 Geometrical acceptance of the setup layout to cosmic muons 5-9
5.2.2.1 Description of the simulation layout 5-10
5.2.2.2 Simulation procedure 5-11
5.2.2.3 Results and limitations 5-12
5.2.3 Photon flux at GIF 5-14
5.2.4 Results and discussions 5-17
5.3 Longevity tests at GIF++ 5-20
5.3.1 Selection and characterization of CMS RPCs for longevity at GIF++ 5-20
5.3.2 RPC test setup 5-22
5.3.3 GIF++ data flow 5-24
5.3.4 Measurements performed during beam periods 5-26
5.3.4.1 Efficiency scans 5-26
5.3.4.2 Rate scans 5-26
5.3.4.3 Offline analysis and Data Quality Monitoring 5-27
5.3.5 Measurements performed during irradiation periods 5-28
5.3.5.1 Longevity scans 5-29
5.3.5.2 Daily rate monitoring scans 5-30
5.3.5.3 Weekly noise monitoring scans 5-31
5.3.5.4 Weekly source scans 5-31
5.3.5.5 Weekly current scans 5-32
5.3.5.6 Resistivity measurements 5-32
5.3.6 Results and discussions 5-32

6 Improved RPC investigation and preliminary electronics studies 6-1
6.1 FEE candidates for the production of iRPCs 6-1
6.1.1 CMS RPCROC: the RPC upgrade baseline 6-2
6.1.2 INFN Front-End Board: a robust back-up solution 6-4
6.2 Preliminary electronics tests at CERN 6-5
6.2.1 INFN preamplifiers as upgrade candidates 6-5
6.2.2 INFN preamplifiers mounted onto CMS Front-End Board 6-9
6.2.3 HARDROC 2 based RPC read-out 6-20
6.3 Certification of the CMS RPCROC prototype 6-25
6.4 Certification of the INFN FEB prototype 6-25

7 Conclusions and outlooks **7-1**
7.1 Conclusions . . . 7-1
7.2 Outlooks . . . 7-1

A A data acquisition software for CAEN VME TDCs **A-1**
A.1 GIF++ DAQ file tree . . . A-1
A.2 Usage of the DAQ . . . A-2
A.3 Description of the readout setup . . . A-3
A.4 Data read-out . . . A-3
A.4.1 V1190A TDCs . . . A-4
A.4.2 DataReader . . . A-7
A.4.3 Data quality flag . . . A-10
A.5 Communications . . . A-12
A.5.1 V1718 USB Bridge . . . A-13
A.5.2 Configuration file . . . A-14
A.5.3 WebDCS/DAQ intercommunication . . . A-17
A.5.4 Example of inter-process communication cycle . . . A-17
A.6 Software export . . . A-18

B Details on the offline analysis package **B-1**
B.1 GIF++ Offline Analysis file tree . . . B-1
B.2 Usage of the Offline Analysis . . . B-2
B.2.1 Output of the offline tool . . . B-3
B.2.1.1 ROOT file . . . B-3
B.2.1.2 CSV files . . . B-5
B.3 Analysis inputs and information handling . . . B-6
B.3.1 Dimensions file and IniFile parser . . . B-7
B.3.2 TDC to RPC link file and Mapping . . . B-8
B.4 Description of GIF++ setup within the Offline Analysis tool . . . B-9
B.4.1 RPC objects . . . B-9
B.4.2 Trolley objects . . . B-10
B.4.3 Infrastructure object . . . B-10
B.5 Handeling of data . . . B-12
B.5.1 RPC hits . . . B-13
B.5.2 Clusters of hits . . . B-14
B.6 DAQ data Analysis . . . B-15
B.6.1 Determination of the run type . . . B-16
B.6.2 Beam time window calculation for efficiency runs . . . B-17
B.6.3 Data loop and histogram filling . . . B-18
B.6.4 Results calculation . . . B-21
B.6.4.1 Rate normalisation . . . B-21
B.6.4.2 Rate and activity . . . B-23
B.6.4.3 Correction of muon performance parameters . . . B-25
B.6.4.4 Strip masking tool . . . B-27
B.6.4.5 Output CSV files filling . . . B-29
B.7 Current information extraction . . . B-31

Nederlandse samenvatting –Dutch Summary–

English summary

List of Figures

2.1 Solar spectrum with spectral lines as it visually appeared to Fraunhofer. 2-2

2.2 Through the gold foil experiment, Rutherford could show that most of the mass of atoms was contained in a positively charged nucleus and could then propose a more accurate atomic model than that of Thomson. 2-3

2.3 Figure 2.3a: The orbits in which the electron may travel according to the Borh model of the hydrogen atom. An electron jumps between orbits and is accompanied by an emitted or absorbed amount of electromagnetic energy ($h\nu$).The orbits radius increases as n^2. Figure 2.3b: Elliptical orbits with the same energy and quantized angular momentum $l = 0, 1, ..., n - 1$ in the case $n = 5$. Figure 2.3c: Illustration of quantum mechanical orbital angular momentum. The cones and plane represent possible orientations of the angular momentum vector for $l = 2$ and $m = -2, -1, 0, 1, 2$. 2-5

2.4 Figure 2.4a: The spectral lines of mercury vapor lamp anomalous Zeeman effect without magnetic field (A) and with magnetic field (B - transverse Zeeman effect & C - longitudinal Zeeman effect). Figure 2.4b: Stern–Gerlach experiment: Silver atoms traveling through an inhomogeneous magnetic field and being deflected up or down depending on their spin. 2-6

2.5 Figure 2.5a: decay of a μ-meson in an emulsion. Figure 2.5b: track of a π-meson in an emulsion signed by Lattes, Powell, and Occhialini. 2-8

2.6 Figure 2.6a: Meson octet. Figure 2.6b: Baryon octet. Figure 2.6c: Baryon decuplet. . 2-9

2.7 Discovery of the J/Ψ by both SPEAR (SLAC [74]) in Figure 2.7a and AGS (BNL [75]) in Figure 2.7b. In Figure 2.7a, the cross section versus energy is showed for (a) multi hadron final states, (b) e^+e^- final states, and (c) $\mu^+\mu^-$, $\pi^+\pi^-$ and K^+K^- final states.2-10

2.8 Figure 2.8a: the color field of QCD only allows for "white" *baryons*, particles composed of quarks, to exist. Examples are given for mesons, composed of a quark and its anti-quark, and hadrons, composed of three differently colored quarks or anti-quarks. Other exotic baryons have been predicted and observed, such as tetraquarks and pentaquarks. Figure 2.8b: a crossed analysis performed thanks to the data collected by various experiments at different energies have showed that the coupling constant evolves as predicted by the mechanism of asymptotic freedom [87]. 2-11

2.9 Energy spectrum of beta particles emitted by a source of ^{210}Bi. 2-12

2.10 As explained through Figure 2.10a, the Wu experiment consisted in measuring the preferred direction of emission of beta rays of a Colbalt source placed in a stable magnetic field aligned, in one case, and anti-aligned, in the other case, with the nuclear spin. The result of Figure 2.10b showed a violation of parity. 2-13

2.11 The elementary particles of the Standard Model are shown along with their properties. Their interactions with the strong, weak and electromagnetic forces have been made explicit using color squares. In the left column, the scalar Higgs boson is depicted. The center is focused on the matter particles, the fermions, and the right column on the force carriers, the gauge bosons. The role of the Higgs boson in electroweak symmetry breaking is highlighted, and the corresponding way properties of the various particles differ in the (high-energy) symmetric phase (top) and the (low-energy) broken-symmetry phase (bottom) are shown. 2-15

2.12 Figure 2.12a: Total proton-proton cross-section as a function of the collisions center-of-mass energy $\sqrt{s}$ [116] with cosmic-ray data from Akeno Observatory and Fly's Eye Collaboration. Figure 2.12b: Total proton-(anti)proton and interaction channel cross-sections in the TeV scale. 2-16

2.13 Rotation curve (points) of the galaxy M33 compared with best fitting model (line). The short-dashed line represents the rotation profile that would be expected from the observation of the stellar disc alone [128]. 2-17

2.14 Cosmic Microwave Background as measured by the space observatory Planck which mean temperature is $T_\gamma = (2.7255 \pm 0.0006)\mathrm{K}$ with anisotropies of the order of a few μK. 2-18

2.15 CERN accelerator complex. 2-20

2.16 Pictures of the different accelerators. From top to bottom: first the LINAC 2 and the Pb source of LINAC 3. Then the Booster and the LEIR. Finally, the PS, the SPS and the LHC. 2-21

2.17 Figure 2.17a: schematics of the LHC cryodipoles. 1: Superconducting Coils, 2: Beam pipe, 3: Heat exchanger Pipe, 4: Helium-II Vessel, 5: Superconducting Bus-bar, 6: Iron Yoke, 7: Non-Magnetic Collars, 8: Vacuum Vessel, 9: Radiation Screen, 10: Thermal Shield, 11: Auxiliary Bus-bar Tube, 12: Instrumentation Feed Throughs, 13: Protection Diode, 14: Quadrupole Bus-bars, 15: Spool Piece Bus-bars. Figure 2.17b: magnetic field and resulting motion force applied on the beam particles. 2-22

2.18 The LHC quadrupoles (Figure 2.18a) showed together with the magnetic fields and resulting focussing force applied on the beam by two consecutive quadrupoles (Figure 2.18b). 2-23

2.19 Distribution of the four-lepton invariant mass for the $ZZ \to 4l$ analysis as presented by both ATLAS [112] and CMS [113] in 2012. 2-23

2.20 Detailed timeline projection of LHC and HL-LHC operation until 2039 showing the evolution of the instantaneous and integrated luminosity as designed (Figure 2.20a) and in the ultimate case where the instantaneous luminosity is increased to $7.5 \times 10^{34}\mathrm{cm}^{-2}\,\mathrm{s}^{-1}$thanks to a new increase of instantaneous luminosity during Run 5 (Figure 2.20b) [175–177]. 2-24

2.21 Picture of the CMS barrel. The red outer layer is the muon system hosted into the red iron return yokes. The calorimeters are the blue cylinder inside in magnet solenoid and the tracker is the inner yellow cylinder built around the beam pipe. 2-26

2.22 View of the CMS apparatus and of its different components. 2-26

2.23 Slice showing CMS sub-detectors and how particles interact with them. 2-27

2.24 The CMS tracker. 2-27

2.25 Figure 2.25a: The electromagnetic calorimeter. Figure 2.25b: The lead tungstate crystals composing the ECAL. 2-28

2.26 The CMS hadron calorimeter barrel. 2-28

2.27 A quadrant of the muon system, showing DTs (yellow), RPCs (blue), and CSCs (green). 2-29

3.1 The measured transit time of an HSCP in CMS is compared to the transit time of a particle traveling at near the speed of light [177]. 3-2

3.2 Slice of the CMS detector showing examples of passage of SM particles and R-hadrons. On the one hand, lepton-like HSCPs will appear to behave like slow and heavy muons. On the other hand, R-hadrons are likely to convert into other kind of charged or neutral R-hadrons due to interactions inside the detector volume. 3-2

3.3 Distribution of the energy-loss dE/dx as described by Bethe-Bloch formula through the estimator I_h with increasing particle momentum for tracks in the $13\,\mathrm{TeV}$ data. The estimator depends on the charge deposition of the particles per unit length in the silicon detectors of CMS which is related to their energy loss as explained in a publication by the CMS Collaboration [181]. The simulated HSCPs are singly or multiply charged particles with masses of 400 and $1000\,\mathrm{GeV}$. 3-3

3.4 Distribution of the average number of interactions per crossing (pileup) for pp-collisions in 2011 (red), 2012 (blue), 2015 (purple), 2016 (orange), 2017 (light blue), and 2018 (navy blue). The overall mean values and the minimum bias cross sections are also shown [189]. 3-4

3.5 Absorbed dose in the CMS Cavern after an integrated luminosity of $3000\,\mathrm{fb}^{-1}$. Using the interaction point as reference, R is the transverse distance from the beamline and Z is the distance along the beamline [177]. 3-4

3.6 Figure 3.6a: Barrel wheel with its detector rings and return yokes. Figure 3.6b: CSC endcap disk with the two CSC stations. The outer station is made of $10\,\mathrm{deg}$ detectors while the inner station is made of $20\,\mathrm{deg}$ detectors. Figure 3.6c: RPC endcap disk. The inner station is not equipped, leaving the inner CSC station visible. 3-5

3.7 Figure 3.7a: Cross section of a DT module showing the two superlayers measuring the ϕ coordinate, perpendicular to the cross section plane, and the superlayer measuring the η coordinate, placed in between the two others with a honeycomb plate and parallel to the cross section plane. The DT detector is sandwiched in between 2 RPCs whose readout strips are perpendicular to the cross section plane, measuring the ϕ coordinate. Figure 3.7b: A DT cell is shown together with its electric field. The path of a muon through a superlayer is shown. 3-6

3.8 Figure 3.8a: Cathode strips and anode wire layout of a CSC panel. Figure 3.8b: Avalanche development and charge collection by anode wires and induction on cathode strips inside of a CSC panel. 3-7

3.9 Muon track reconstruction through the six panels of a CMS CSC using the information of anode wire groups and cathode strip charge distribution combined with comparator bits to decide on which half strip the muon is more likely to have passed. 3-7

3.10 Double-gap layout of CMS RPCs. Muons passing through the gas volumes will create electron-ions pairs by ionising the gas. This ionisation will immediately translate into a developing avalanche. 3-8

3.11 Extrapolated fraction of failing channels of the present DT MiC1 electronics as a function of the integrated luminosity for different scenarios until LS4 [177]. 3-8

3.12 The event loss fractions as a function of the instantaneous luminosity is compared for CFEBs (Phase-1) and DCFEBs (Phase-2) at different CSC locations. HL-LHC luminosity is marked with the dashed brown line [177]. 3-9

3.13 Comparison of the simulated time residuals in between reconstructed and true muon times without (blue) and with (red) the upgraded RPC link system [177]. 3-9

3.14 Figure 3.14a: Time delay with respect to a particle traveling at the speed of light measured at consecutive RPC stations for particles originating at different bunch crossings and traveling at different velocities [177]. Figure 3.14b: In blue is showed the standard Level-1 muon trigger efficiency as a function of β and in blue is showed the RPC-HSCP trigger efficiency after upgrade of the RPC Link System [177]. . . . 3-10

3.15 A quadrant of the muon system, showing DTs (yellow), RPCs (blue), and CSCs (green). The locations of new forward muon detectors for Phase-2 are contained within the dashed box and indicated in red for GEM stations (ME0, GE1/1, and GE2/1) and dark blue for improved RPC (iRPC) stations (RE3/1 and RE4/1). 3-11

3.16 RMS of the multiple scattering displacement as a function of muon p_T for the proposed forward muon stations. All of the electromagnetic processes such as bremsstrahlung and magnetic field effect are included in the simulation. 3-11

3.17 Schematics of a GEM. On top is the cathode and on the bottom, the anode on which a 2D read-out is installed. Finally, the GEM foil separates the gas volume into the drift region, in between the cathode and the foil, and the induction region, in between the foil and the anode. A negative voltage is applied on the cathode. The anode is connected to the ground. 3-12

3.18 Top: Picture of a CMS GEM foil provided by a scanning electron microscope. Bottom: Representation of the electric field in a GEM hole and of the amplification electrons and ions undergo due to the very intense electric field. 3-12

3.19 Schematic representation of CMS triple-GEMs. The gas volume is divided into four areas. The drift area is the region where the primary electrons are created before being amplified a first time while passing through the first GEM foil. Then the process of drift and amplification is repeated twice in following two transfer areas and GEM foils. Finally, the charges have been amplified enough to induce current in the read-out strips while in the last drift area. The typical dimensions, potentials and electric fields are provided. 3-13

3.20 Simulated efficiency and rate of the standalone Level-1 muon trigger using tracks reconstructed in CSCs and all GEM stations compared with Phase-1 values in the case where only CSCs are used or CSCs+GE1/1. The zones of inefficiency of the CSC subsystem are compensated by the addition of GEMs during Phase-2 and the trigger rates is kept from increasing due to the high luminosity [177]. 3-14

3.21 Figure 3.21a: Simulated resolution of the muon direction measurement $\Delta\phi$ with Phase-2 conditions. In the second endcap station, the resolution is compared in the case of CSCs (ME2/1) alone and CSCs+GEMs (GE2/1+ME2/1) while a similar resolution measurement is given in the case of the first station (GE1/1+ME1/1) [177]. Figure 3.21b: The addition of GEM detectors on stations 1 and 2 (ME0 is considered to contribute to station 1) as redundant system to CSCs allows improving the muon momentum improvement through a more accurate measurement of the local bending angles ϕ_1 and ϕ_2 [177]. 3-14

3.22 Simulation of the impact of RPC hit inclusion onto the local trigger primitive efficiency in station 3 (Figure 3.22a) and station 4 (Figure 3.22b) [177]. The contribution of iRPC starts above $|\eta| = 1.8$. 3-15

3.23 Expected hit rate due to neutrons, photons, electrons and positrons at HL-HLC instantaneous luminosity of $5 \times 10^{34}\ \mathrm{cm}^{-2}\mathrm{s}^{-1}$ in RE3/1 and RE4/1 chambers [196, 197]. The sensitivities of iRPCs used in the simulation for each particle are reported and differ from one endcap disk to another as the energies of the considered particles varies with the increasing distance from the interaction point. 3-16

3.24 Measured average charge per avalanche as a function of the effective electric field for different gas gap thickness in double-gap RPCs using HPL electrodes [177]. . . . 3-17

3.25 Level-1 Trigger data flow during Phase-2 operations [177]. 3-17

3.26 Efficiency of the L1 trigger in the endcap region after Phase-2 upgrade in the case CSC/GEM/RPC hits are requested in at least two stations out of four (3.26a) and in all four stations (3.26b) [177]. 3-18

3.27 Comparison of L1 trigger performances for prompt muons with and without the addition of GEMs in the region $2.1 < |\eta| < 2.4$ at Phase-2 conditions [177]. GEMs would allow a reduction of the trigger accept rate by an order of magnitude (Figure 3.27a) while increasing the trigger efficiency (Figure 3.27b). 3-19

3.28 The angular resolution on reconstructed muon tracks in the GEM overlap region $2.0 < |\eta| < 2.15$ is compared for Phase-2 conditions in the case CSC are alone (Figure 3.28a) and in the case the GEMs' data, including ME0, is combined to which of CSCs (Figure 3.28b) [177]. 3-19

3.29 Resolution of the LCT ambiguous events thanks to the combination of CSC and iRPC readout data. Using CSCs only, two pairs of hits are possible [177]. 3-20

3.30 Efficiency (Figure 3.30a [202]) and cluster size (Figure 3.30b) of a standard double-gap RPC operated with CO_2 mixtures for different ratios of SF_6. 3-21

3.31 Efficiency of a CMS double-gap RPC operated with 30% of HFO, 4.5% of iC_4H_{10}, 1% of SF_6 and 64.5% of CO_2 [202]. 3-21

3.32 The efficiency (solid lines) and streamer probability (dashed lines) of HFO/CO_2 (Figure 3.32a) and CF_3I/CO_2 (Figure 3.32b) based gas mixtures as a function of the effective high-voltage are compared with the present CMS RPC gas mixture represented in black [177, 202]. The detector used for the study is a single-gap RPC with similar properties than CMS RPCs. The streamer probability is defined as the proportion of events with a deposited charge greater than 20 pC. 3-22

3.33 Efficiency (open symbols) and cluster size (full symbols) of an iRPC as a function of the effective voltage for the standard CMS gas mixture and an environmental-friendly gas mixture [177]. 3-22

4.1 Different phases of the avalanche development in the RPC gas volume subjected to a constant electric field E_0. a) An avalanche is initiated by the primary ionisation caused by the passage of a charged particle through the gas volume. b) Due to its growing size, the avalanche starts to locally influence the electric field. c) The electrons, lighter than the cations reach the anode first. d) The ions reach the cathode. While the charges have not recombined, the electric field in the small region around the avalanche stays affected and locally blinds the detector. 4-2

4.2 Movement of the charge carriers in an RPC. Figure 4.2a: Voltage across an RPC whose electrodes have a relative permittivity of 5 at the moment the tension is applied. Figure 4.2b: After the charge carriers moved, the electrodes are charged and there is no voltage drop over the electrodes anymore. The full potential is applied on the gas gap only. Figure 4.2c: The streamer discharge initiated by a charged particle transports electrons and cations towards the anode and cathode respectively. 4-4

4.3 Typical oscilloscope pulses in streamer mode (Figure 4.3a) and avalanche mode(Figure 4.3b). In the case of streamer mode, the very small avalanche signal is visible. 4-4

4.4 Rate capability comparison for the streamer and avalanche mode of operation. An order of magnitude in rate capability for a maximal efficiency drop of 10% is gained by using the avalanche mode over the streamer mode. 4-5

4.5 Comparison of the charge distribution of signals induced by cosmic muons in an RPC operated with a gas mixture of argon, butane and bromotrifluoromethane (CF_3Br). The Ar/C_4H_10 is kept constant at 60/40 in volume while the total amount of CF_3Br in the mixture is varied: 0% (Figure 4.5a), 4% (Figure 4.5b) and 8% (Figure 4.5c) [209]. 4-6

4.6 Comparison of the efficiency and streamer probability, defined as the fraction of events with an induced charge 10 times larger than that of the average avalanche, with and without irradiation by a $24\,\mathrm{GBq}$ ^{137}Cs source of an RPC successively operated with a 90/10 mixture $C_2H_2F_4$/i-C_4H_{10} (Figure 4.6a) and a 70/5/10/15 mixture of Ar/i-C_4H_{10}/CO_2/$C_2H_2F_4$ (Figure 4.6b) [210]. 4-6

4.7 Comparison of the fast charge ratio with and without irradiation by a $24\,\mathrm{GBq}$ ^{137}Cs source of an RPC successively operated with a 90/10 mixture $C_2H_2F_4$/i-C_4H_{10} (Figure 4.7a) and a 70/5/10/15 mixture of Ar/i-C_4H_{10}/CO_2/$C_2H_2F_4$ (Figure 4.7b). The results are provided for both single-gap and double-gap operation [210]. 4-7

4.8 Effeciency (circles and stars with $30\,\mathrm{mV}$ and $100\,\mathrm{mV}$ thresholds respectively) and streamer probability (opened circles) as function of the operating voltatge of a $2\,\mathrm{mm}$ single-gap HPL RPC flushed with a gas mixture containing (a) 5%, (b) 2%, (c) 1% and (d) no SF_6 [212]. 4-8

4.9 Evolution of the efficiency, working voltage, and voltage at 50% of maximum efficiency for CMS Barrel (Figure 4.9a) and Endcap (Figure 4.9b) RPCs obtained through yearly voltage scans since 2011. The working voltage of each RPC is updated after each voltage scan to ensure optimal operation [227]. 4-9

4.10 Comparison of the rate capability of $8\,\mathrm{mm}$ and $2\,\mathrm{mm}$ wide RPCs. The lines are linear fits on the data [229]. 4-10

4.11 Distributions of the induced charge of fast signals on $2\,\mathrm{mm}$ (Figure 4.11a) and $8\,\mathrm{mm}$ (Figure 4.11b) RPCs exposed to a radiation rate of $100\,\mathrm{Hz/cm^2}$. Average induced charge of fast signals as a function of the high voltage applied on $2\,\mathrm{mm}$ and $8\,\mathrm{mm}$ RPCs (Figure 4.11c). In the case of the $2\,\mathrm{mm}$ RPC, a saturation of the pre-amplifier was observed. The average of the distribution is underestimated, and the median is showed together with the average to account for this bias [229]. 4-11

4.12 Time distributions of the leading, trailing, and average of both leading and traling edges for $2\,\mathrm{mm}$ (top row) and $8\,\mathrm{mm}$ (bottom row) RPCs exposed to a $100\,\mathrm{Hz/cm^2}$ radiation rate. The data was collected with RPCs operated at the voltage corresponding to the knee of the efficiency distribution, defined as the point where 95% of the maximum efficiency is obtained [229]. 4-12

4.13 Possible double-gap RPC layouts: a) "standard" 1D double-gap RPC, as used in CMS experiment, where the anodes are facing each other and a 1D read-out plane is sandwiched in between them, b) double read-out double-gap RPC as used in ATLAS experiment, where the cathodes are facing each other and 2 read-out planes are used on the outer surfaces. This last layout can offer the possibility to use a 2D reconstruction by using orthogonal read-out planes. 4-13

4.14 Comparison of performance of CMS double and single-gap RPCs using cosmic muons [225]. Figure 4.14a: Comparison of efficiency sigmoids. Figure 4.14b: Voltage distribution at 95% of maximum efficiency. Figure 4.14c: $\Delta^{90\%}_{10\%}$ distribution. . . 4-13

4.15 Representation of different RPC layouts (wide gap on Figure (a), double-gap on Figure (b) and multigap on Figure (c)), of the corresponding sensitive volume in gray, and of the associated avalanche size [215]. 4-14

4.16 Time distributions of the leading, trailing, and average of both leading and trailing edges for multigap RPCs consisting in two $4\,\mathrm{mm}$ (Figure 4.16a) and four $2\,\mathrm{mm}$ (Figure 4.16b) exposed to a $100\,\mathrm{Hz/cm^2}$ radiation rate. The data was collected with RPCs operated at the voltage corresponding to the knee of the efficiency distribution, defined as the point where 95% of the maximum efficiency is obtained [215]. 4-15

4.17 Presentation of a study of a possible ALICE MRPC cell using $250\,\mu\mathrm{m}$ gas gaps, $620\,\mu\mathrm{m}$ outer glass electrodes, and $550\,\mu\mathrm{m}$ inner floating electrodes (Figure 4.17a), and of its time resolution performance as a function of the applied high voltage for different radiation levels referred through different filter settings of the $740\,\mathrm{GBq}$ ^{137}Cs source the former CERN GIF facility [230]. 4-15

4.18 Particle identification applied to electrons in the STAR experiment. The identification is performed combining ToF and dE/dx measurements [235]. 4-16

4.19 Comparison of the detector performance of ALICE ToF MRPC [236] at fixed applied voltage (in blue) and at fixed effective voltage (in red). The effective voltage is kept fixed by increasing the applied voltage accordingly to the current drawn by the detector.4-17

4.20 Ratio between total induced and drifting charge have been simulated for single-gap, double-gap and multigap layouts [237]. The total induced charge for a double-gap RPC is a factor 2 higher than for a multigap. 4-18

4.21 Charge spectra have been simulated for single-gap, double-gap and multigap layouts [237]. It appears that when single-gap shows a decreasing spectrum, double and multigap layouts exhibit a spectrum whose peak is detached from the origin. The detachment gets stronger as the number of gaps increases. 4-18

4.22 The maximal theoretical efficiency is simulated for single-gap, double-gap and multigap layouts [237] at a constant gap thickness of $2\,\mathrm{mm}$ and using an effective Townsend coefficient of $9\,\mathrm{mm}^{-1}$. 4-19

4.23 Mass stopping power as a function of $\beta\gamma = p/Mc$ for positive muons in copper [115]. The total stopping power is indicated with a solid line and local components with dashed lines. The vertical bands are used to indicate boundaries between different approximations used at different energy range. 4-19

4.24 Mean mass stopping power for liquid hydrogen, as used in bubble chambers, gaseous helium, carbon, aluminum, iron, tin, and lead without the inclusion of radiative effect at higher $\beta\gamma$ necessary for pions and muons in denser materials [115]. 4-21

4.25 Mean excitation energies normalized to the atomic number as adopted by the ICRU [115, 241, 242]. 4-22

4.26 Mean mass stopping power at minimum ionization as a function of the atomic number [115]. 4-22

4.27 Example of straggling function $f(\Delta)$ of particles passing through $1.2\,\mathrm{cm}$ of Argon gas with a $\beta\gamma$ of 3.6 and represented with a solid line. The original Landau distribution is showed with a dashed line [243]. 4-23

4.28 Evolution of straggling functions $f(\Delta)$ of particles passing through a volume of Argon gas with a $\beta\gamma$ of 3.6 with increasing thickness x [243]. 4-23

4.29 Photoabsorption cross section as computed by `HEED` for nobles gases with different electric shell numbers [239]. 4-25

4.30 Photoabsorption cross section as computed by `HEED` for typical RPC gas mixtures [239]. The RPC mixture with CO_2 corresponds to the mixture used by CALICE SDHCAL [247] while the other one was forseen for the experiment ATLAS [248] but has been changed since then. 4-26

4.31 Distributions of number of electrons (left) and energy loss (right) for a $5\,\mathrm{GeV/c}$ muon passing through $1.2\,\mathrm{mm}$ of Helium (Figure 4.31a), Argon (Figure 4.31b) or a typical RPC gas mixture (Figure 4.31c) [239]. 4-27

4.32 Figure 4.32a: Mean cluster density for muons through different gas volumes [239]. Figure 4.32b: Distribution of the number of electrons per cluster for a $5\,\mathrm{GeV/c}$ muon traveling through a mixture of 96.7% $C_2H_2F_4$, 3% i-C_4H_{10} and 0.3% SF_6 [239, 248]. 4-28

4.33 Townsend and attachment coefficient for a typical 96.7/3/0.3 mixture of $C_2H_2F_4$/i-C_4H_{10}/SF_6, at a temperature T =$296.15\,\mathrm{K}$ and a pressure P =$1013\,\mathrm{hPa}$ [239, 248]. 4-29

4.34 Comparison of the distribution law of Furry and the Poisson law for $\bar{n} = 5$ [251]. . . 4-29

4.35 Single-electron avalanche size distribution in a proportional counter filled with methylal at different E/p values. (a) 70, (b) 76.5, (c) 105, (d) 186.5, (e) $426\mathrm{V/cm\,torr}$ [252].4-30

4.36 Figure 4.36a: Comparison of avalanche size distributions for different values of Townsend and attachment coefficients. The effective Townsend coefficient is the same for both distributions. Figure 4.36b: Fluctuation in avalanches size for avalanche started by a single electron with α = $13\,\mathrm{mm}^{-1}$ and η = $3.5\,\mathrm{mm}^{-1}$ [248]. 4-32

4.37 Figure 4.37a: Electrons mean drift velocity v_D in pure $C_2H_2F_4$ and typical RPC gas mixtures. Figure 4.37b: Transverse diffusion coefficient in pure $C_2H_2F_4$ and a typical RPC gas mixture. Figure 4.37c: Longitudinal diffusion coefficient in pure $C_2H_2F_4$ and a typical RPC gas mixture. All results are given with a pressure $P = 760\,\mathrm{Torr}$ and a temperature $T = 296.15\,\mathrm{K}$ [239]. 4-33

4.38 Comparison of the free charge carriers in the gas after a time $t = 7.90\,\mathrm{ns}$ in the case where no diffusion is taken into account to simulate the avalanche (Figure 4.38a) and in the case where the diffusion is implemented (Figure 4.38b) [239]. 4-33

4.39 Schematic representation of an avalanche and of the electric field deformation it causes due to the local concentration of charge carriers [221]. 4-35

4.40 Evolution of the charge induced by an avalanche started by a single electron in a $1.2\,\mathrm{mm}$ thick RPC with an applied electric field of $54\,\mathrm{kV/cm}$ in the case space charge is not taken into account (Figure 4.40a) and in the case it is implemented into the simulation (Figure 4.40b). The total induced charge is correlated to the size of the avalanche [239]. 4-36

4.41 Distributions of charge carriers within the gas volume of a $1.2\,\mathrm{mm}$ thick RPC and the corresponding deformation of the electric field at different time steps with an applied electric field of $55.5\,\mathrm{kV/cm}$ [239]. 4-37

4.42 Representation of the weighting field in the volume of an RPC and the resulting induced current in the strip placed at $1\,\mathrm{V}$ and its neighbour connected to the ground. The induced current corresponds, as can be understood from Formula 4.22 [221]. . . 4-38

4.43 Schematics of CMS RPC FEE logic. 4-39

4.44 Equivalence in between the charge of the induced signal in input of the CMS FEE and the signal strength on the output of the pre-amplifier. 4-39

4.45 Description of the principle of a CFD. A comparison of threshold triggering (left) and constant fraction triggering (right) is shown in Figure 4.45a. Constant fraction triggering is obtained thanks to zero-crossing technique as explained in Figure 4.45b. The signal arriving at the input of the CFD is split into three components. A first one is delayed and connected to the inverting input of a first comparator. A second component is connected to the noninverting input of this first comparator. A third component is connected to the noninverting input of another comparator along with a threshold value connected to the inverting input. Finally, the output of both comparators is fed through an AND gate. 4-40

4.46 Typical efficiency sigmoid of a CMS RPC detector. The black dots correspond to the data, the blue line to the sigmoid fit and the opened cross to the knee and working extracted from the fit line. 4-41

4.47 Effect of the temperature variation on the rate (Figure 4.47a) and the efficiency (Figure 4.47b) of an RPC [253]. 4-42

4.48 Effect of the pressure variation on the rate (Figure 4.48a) and the efficiency (Figure 4.48b) of an RPC [254]. 4-43

5.1 Mean RPC Barrel (left column) and Endcap (right column) rate (top row) and current (bottom row) as a function of the instantaneous luminosity as measured in 2017 p-p collision data. 5-2

5.2 Figure 5.2a: The hit rate per region (Barrel, Endcap) is linearly extrapolated to HL-LHC highest instantaneous luminosity ($5 \times 10^{34}\ \mathrm{cm}^{-2}\,\mathrm{s}^{-1}$) using the rate as a function of instantaneous luminosity recorded by RPCs in 2017 showing a linear dependence. Figure 5.2b: The integrated charge per region (Barrel, Endcap) is extrapolated to HL-LHC integrated luminosity ($3000\,\mathrm{fb}^{-1}$) using the data accumulated in 2016 in every HV channel. 5-3

5.3 CMS RPC mean integrated charge in the Barrel region (Figure 5.3a) and the Endcap region (Figure 5.3b). The integrated charge per year is shown in blue. The red curve shows the evolution of the accumulated integrated charge through time. The blank period in 2013 and 2014 corresponds to LS1. The total integrated charge for the entire operation period (Oct.2009 - Dec.2017) is estimated to be about $1.66\,\mathrm{mC/cm^2}$ in the Barrel and $4.58\,\mathrm{mC/cm^2}$ in the Endcap. 5-3

5.4 Layout of the test beam zone called X5c GIF at CERN. Photons from the radioactive source produce a sustained high rate of random hits over the whole area. The zone is surrounded by $8\,\mathrm{m}$ high and $80\,\mathrm{cm}$ thick concrete walls. Access is possible through three entry points. Two access doors for personnel and one large gate for material. A crane allows installation of heavy equipment in the area. 5-4

5.5 ^{137}Cs decays by β^- emission to the ground state of ^{137}Ba (BR = 5.64%) and via the $662\,\mathrm{keV}$ isomeric level of ^{137}Ba (BR = 94.36%) whose half-life is 2.55min. 5-5

5.6 Floor plan of the GIF++ facility. When the facility downstream of the GIF++ takes electron beam, a beam pipe is installed along the beam line (z-axis). The irradiator can be displaced laterally (its center moves from $x = 0.65\,\mathrm{m}$ to $2.15\,\mathrm{m}$), to increase the distance to the beam pipe. 5-6

5.7 Simulated unattenuated current of photons in the xz plane (Figure 5.7a) and yz plane (Figure 5.7b) through the source at $x = 0.65\,\mathrm{m}$ and $y = 0\,\mathrm{m}$ [263]. With angular correction filters, the current of $662\,\mathrm{keV}$ photons is made uniform in xy planes. . . . 5-6

5.8 Description of the RPC setup. Dimensions are given in mm. A tent containing RPCs is placed at $1720\,\mathrm{mm}$ from the source container. The source is situated in the center of the container. RE-4-2-BARC-161 chamber is $160\,\mathrm{mm}$ inside the tent. This way, the distance between the source and the chambers plan is $2060\,\mathrm{mm}$. Figure 5.8a provides a side view of the setup in the xz plane while Figure 5.8b shows a top view in the yz plane. 5-7

5.9 `RE-4-2-BARC-161` chamber is inside the tent as described in Figure 5.8. In the top right, the two scintillators used as trigger can be seen. This trigger system has an inclination of $10°$ relative to horizontal and is placed above half-partition B2 of the RPCs. PMT electronics are shielded thanks to lead blocks placed in order to protect them without stopping photons from going through the scintillators and the chamber. 5-8

5.10 Hit distributions over all three partitions of `RE-4-2-BARC-161` chamber is showed. Top, middle and bottom figures respectively correspond to partitions A, B, and C. The profiles show that some events still occur in other half-partitions than B2, which corresponds to strips 49 to 64, in front of which the trigger is placed, contributing to the inefficiency of detection of cosmic muons. In the case of partitions A and C, the very low amount of data can be interpreted as noise. On the other hand, it is clear that a little portion of muons reach the half-partition B1, corresponding to strips 33 to 48. 5-8

5.11 Signals from the RPC strips are shaped by the FEE described on Figure 5.11a. Output LVDS signals are then read-out by a TDC module connected to a computer or converted into NIM and sent to scalers. Figure 5.11b describes how these converted signals are put in coincidence with the trigger. 5-9

5.12 Results are derived from data taken on half-partition B2 only. On the 18^{th} of June 2014, data has been taken on chamber `RE-4-2-BARC-161` at CERN building 904 (Prevessin Site) with cosmic muons providing us a reference efficiency plateau of $(97.54{\pm}0.15)\%$ represented by a black curve. A similar measurement has been done at GIF on the 21^{st} of July with the same chamber giving a plateau of $(78.52{\pm}0.94)\%$ represented by a red curve. 5-10

5.13 Representation of the layout used for the simulations of the test setup. The RPC read-out plane is represented as a yellow trapezoid while the two scintillators as blue cuboids looking at the sky. The green plane corresponds to the muon generation plane within the simulation. Figure 5.8a shows a global view of the simulated setup. Figure 5.8b shows a zoomed view that allows to see the two scintillators as well as the full RPC plane. 5-11

5.14 Geometrical acceptance distribution as provided by the Monte Carlo simulation. . . . 5-12

5.15 Correction of the efficiency without source. The efficiency after correction gets much closer to the Reference measurement performed before the study in GIF by reaching a plateau of $(93.52 \pm 2.64)\%$. 5-13

5.16 Hit distributions over read-out partition B of `RE-4-2-BARC-161` chamber together with skew distribution fits corresponding to forward and backward coming muons. 5-14

5.17 Figure 5.17a shows the linear approximation fit performed on data extracted from table 5.2. Figure 5.17b shows a comparison of Formula 5.5 with the simulated flux using a and b given in figure 5.17a in formulae 5.3 and the reference value $D_0 = 50\,\mathrm{cm}$ and the associated flux for each absorption factor F_0^{ABS} from table 5.1. 5-16

5.18 Efficiency (Figure 5.18a) and cluster size (Figure 5.18b) of chamber RE-4-2-BARC-161 measured at GIF with Source OFF (red) and Source ON using different absorber settings: ABS 5 (green), ABS 2 (blue) and ABS 1 (yellow). The results are compared to the Reference values obtained with cosmics. 5-17

5.19 Rates in chamber RE-4-2-BARC-161 measured at GIF with Source OFF (red) and Source ON using different absorber settings: ABS 5 (green), ABS 2 (blue) and ABS 1 (yellow). On Figure 5.19b, the rates of Figure 5.19a were normalized to the measured efficiency, and constant fits are performed on Source ON data showing the gamma rate in the chamber. 5-18

5.20 Evolution of the voltages at half maximum and at 95% of the maximum efficiency (Figure 5.20a), and of the maximum efficiency (Figure 5.20b) as a function of the rate in chamber RE-4-2-BARC-161. The data is extracted from the fits in Figures 5.18a and 5.19b. 5-18

5.21 Presentation of a double-gap endcap RPC with its three RPC gaps. Due to the partitioniing of the read-out strips into three rolls, the TOP layer of gap is divided into two gaps: TOP NARROW (TN) and TOP WIDE (TW). The BOTTOM (B) only consists in one gap. 5-19

5.22 Current density and charge deposition per gamma avalanche, defined as the current density normalized to the measured rate taken from Figure 5.19a as a function of the effective high voltage in chamber RE-4-2-BARC-161 measured at GIF with Source ON using different absorber settings: ABS 5 (green), ABS 2 (blue) and ABS 1 (yellow). 5-20

5.23 Characterization of CMS RPC detectors foreseen to be used at GIF++ for longevity studies of the present system. Using cosmic muons, efficiency (Figure 5.23a) and cluster size (Figure 5.23b) were measured as well as noise rate (Figure 5.23c) and current density (Figure 5.23d). For each detector, the working voltage, defined as in Formula 4.25, was extracted from sigmoid fits performed in Figure 5.23a and the values of efficiency, cluster size, noise rate and current density at this voltage are reported using open crosses. 5-21

5.24 CMS RPC setup inside of GIF++ bunker during test beam (Figure 5.24a) and ageing periods (Figure 5.24b). The space in between the RPCs and the source is usually used by other detectors while the space in between T1 and the upstream wall is not filled. Due to the presence of the beam pipe, the trolley is moved away from the beam line during irradiation periods and placed farther away from the source for less intense irradiation. The position of the trolley can vary due to the use of the space by other setups and is then not exact. In the contrary, the position of the chambers in the trolley is fixed and given in Figure 5.24c. 5-23

5.25 Visualisation of the main data flows in GIF++. The yellow flow lines correspond to the DIP flow used for source, environmental and gas information. The red flow lines are for the CAEN flow through which the WebDCS communicates the voltages to be applied on the detectors using pressure and temperature information and retrieves the monitored voltages and currents. Finally, the blue flow lines correspond to the DAQ flow through which the RPC data is collected from the TDCs by the computer. . 5-24

5.26 DIP monitoring history accessed through GIF++ WebDCS interface. 5-25

5.27 Example of DQM page available on CMS RPC WebDCS in GIF++. The rate measured in one of the tracking chambers, namely GT1_20_20-BKL_JUL16_4, is presented here. The DQM page allows clicking on each histogram to extend its view and to navigate through the histograms thanks to the left and right arrows. 5-27

5.28 Example of DQM ROOT Browser page available on CMS RPC WebDCS in GIF++. The strip activity profile, defined as the rate profile normalized to the mean rate, in one of the tracking chambers, namely GT1_20_20-BKL_JUL16_4, is presented here. Available ROOT files and histograms can be browsed thanks to the left panel showing the directory and files structures. 5-28

5.29 Longevity statistics of chamber RE2-2-NPD-BARC-9 in GIF++. For each month since July 2017, the integrated charge (in blue) as well as the time efficiency of irradiation (in gray) is reported. 5-28

5.30 Example of current monitoring (Figure 5.30a) and of corresponding integrated charge (Figure 5.30b) of chamber RE2-2-NPD-BARC-09. The decrease of current is related to a decrease of the voltage due to the daily rate scan procedure or to periods during which the source was turned OFF. 5-29

5.31 Example of rate (Figure 5.31a) and current (Figure 5.31b) monitoring of chamber RE2-2-NPD-BARC-09 with increasing integrated charge. The variations of the rate and current are correlated and corresponds to change of source irradiation, gas flow, gas humidity, or environmental conditions. 5-30

5.32 Example of strip activity of chamber RE2-2-NPD-BARC-09 monitoring through time. The activity of a strip is defined as the rate of the individual channel normalized to the mean rate measured in the corresponding read-out partition. 5-31

5.33 Total integrated charge in the irradiated RPCs, RE2-2-NPD-BARC-9 and RE4-2-CERN-165, before starting August 2018 test beam period. The irradiation of the RE2 chamber started in June 2016 while the RE4 chamber couldn't be irradiated before November 2016. 5-33

6.1 PETIROC 2A block diagram. 6-2

6.2 View of the RPCROC Front-End Electronics in which the PETIROC 2A ASIC is visible as well as the FPGA on which the TDC is hosted. 6-3

6.3 The PETIROC time jitter as a function of the input signal amplitude, measured with and without internal clocks. 6-3

6.4 View of the coaxial design (Figure 6.4a) and of the return design (Figure 6.4b) of read-out panels used in the iRPC prototypes. Only half PCBs with 48 strips are showed. 6-4

6.5 Experimental setup used to test the INFN preamplifier with respect to the CMS FEEs. 6-5

6.6 The four channels of INFN preamplifiers are mounted directly on a CMS RPC and connected to the four outermost read-out strips of the detector. 6-6

6.7 Experimental setup used to test the INFN preamplifier with respect to the CMS FEEs. 6-7

6.8 The block diagrams corresponding to the signal treatment for both INFN preamplifier (Figure 6.8a) and CMS FEEs (Figure 6.8b) are shown. The digitized signals are then counted in coïncidence with the trigger signals provided by PMTs (Figure 6.8c). 6-8

6.9 Efficiency (Figure 6.9a) and noise rate per unit area (Figure 6.9b) of the CMS RE2-2 detector tested with the standard CMS FEBs (black) and with the INFN preamplifier at different thresholds (red and blue). An extra HV scan was performed with better conditions to measure the noise with a threshold of 3 fC on the INFN preamplifiers. . 6-9

6.10 Figure reffig:Setup-INFN-904:A: Shielded Front-End Board on which the INFN preamplifiers are to be mounted. Figure reffig:Setup-INFN-904:B: Three INFN preamplifiers connected onto the test FEB. Figure reffig:Setup-INFN-904:C: Experimental setup used to test the INFN preamplifier single mounted on a FEB similar to the CMS FEB. 6-10

6.11 Similarly to Figure 6.8c, the signals are counted in coïncidence with the trigger signals provided by PMTs. To estimate the cluster size, the channels are counted by groups of three, two but also alone. 6-11
6.12 Efficiency (Figure 6.12a), cluster size (Figure 6.12b) and noise rate per unit area (Figure 6.12c) of the CMS RE2-2 detector tested with the standard CMS FEBs (black and red) and with the INFN preamplifier mounted onto the CMS FEB at different thresholds (blue, pink, green and purple). 6-12
6.13 The glass RPC developped by Ghent uses a double-gap design (Figure 6.13a). The electrodes are made of four pieces of float glass glued into a single plate (Figure 6.13b). Indeed a gluing technique has been investigated as most new low resistivity materials foreseen for RPCs of the new generation are not available in large areas. 6-13
6.14 Figure 6.14a: A gap used to concieve the gRPC tested at CERN. Figure 6.14b: Both gaps with their read-out panel are placed into a faraday made out of copper. Figure 6.14c: The faraday cage containing the double-gap gRPC is finally placed into its aluminium case. 6-14
6.15 Experimental setup used to test the INFN preamplifier mounted on the CMS like FEB with the glass RPC build by Ghent. 6-15
6.16 Efficiency (Figure 6.16a), cluster size (Figure 6.16b) and noise rate per unit area (Figure 6.16c) of the Ghent gRPC detector tested with the standard CMS FEBs (red) and with the INFN preamplifier mounted onto the CMS FEB at different thresholds (blue, pink, green and purple). 6-16
6.17 Figure 6.17a: Time difference between the first and last hit composing a cluster in the gRPC. The maximum time difference is set to 300 ns. Figure 6.17b: Variation of the reconstructed average cluster size as a function of the time constraint used in the algorithm. 6-17
6.18 Evolution of the cluster size distribution with increasing voltage for the gRPC tested with the INFN preamplifiers using a threshold of 5 fC. 6-18
6.19 Map of the cluster size distribution as a function of the cluster position with increasing voltage for the gRPC tested with the INFN preamplifiers using a threshold of 5 fC. 6-18
6.20 Noise profile measured in the glass RPC built by Ghent tested with the standard CMS FEB (Figure 6.20a) and the INFN preamplifiers mounted on a CMS-like FEB (Figure 6.20b). 6-19
6.21 The arrival time of the hits recorded in the gRPC tested with the CMS FEB (Figure 6.21a) and with the INFN preamplifiers (Figure 6.21b), and recorded in the CMS RE2 RPC tested with the INFN preamplifiers (Figure 6.21c). 6-20
6.22 Experimental setups used to test the HARDROC2 electronics with a CMS RE4-3 gap (Figure 6.22a) and a gRPC gap built in Ghent (Figure 6.22b). 6-21
6.23 HARDROC2 control chip with its ”Mezzanine” used to collect the data from the different HARDROC ASICs and communicate with the computer. On top of the picture, the trigger is brought by a coaxial cable. The connection with the computer is assured by both the USB cables. 6-21
6.24 Efficiency (Figure 6.24a), cluster size (Figure 6.24b) and noise rate per unit area (Figure 6.24c) of the CMS RE4-3 detector tested in single gap mode with the standard CMS FEBs (black) and with the HARDROC 2 readout panel at different thresholds (red, blue and pink). 6-22

6.25 Measured muon (Figure 6.25a) and noise (Figure 6.25a) profiles in the read-out pads of the HARDROC 2 over a CMS RE4-3 gap. The inner structure of the gap and the presence of the spacers in the volume is visible. 6-23

6.26 Efficiency (Figure 6.24a), cluster size (Figure 6.24b) and noise rate per unit area (Figure 6.24c) of the UGent gRPC tested in double-gap mode with the standard CMS FEBs (black) and in single-gap with the HARDROC 2 readout panel at a threshold of 143 fC (red). 6-24

6.27 Measured muon (Figure 6.27a) and noise (Figure 6.27a) profiles in the read-out pads of the HARDROC 2 over a gRPC gap built by Ghent. 6-25

A.1 (A.1a) View of the front panel of a V1190A TDC module [264]. (A.1b) View of the front panel of a V1718 Bridge module [265]. (A.1c) View of the front panel of a 6U 6021 VME crate [282]. A-3

A.2 Module V1190A *Trigger Matching Mode* timing diagram [264]. A-4

A.3 Structure of the ROOT output file generated by the DAQ. The 5 branches (`EventNumber`, `number_of_hits`, `Quality_flag`, `TDC_channel` and `TDC_TimeStamp`) are visible on the left panel of the ROOT browser. On the right panel is visible the histogram corresponding to the variable `nHits`. In this specific example, there were approximately 50k events recorded to measure the gamma irradiation rate on the detectors. Each event is stored as a single entry in the `TTree`. A-10

A.4 The effect of the quality flag is explained by presenting the content of `TBranch` `number_of_hits` of a data file without `Quality_flag` in Figure A.4a and the content of the same `TBranch` for data corresponding to a `Quality_flag` where all TDCs were labelled as `GOOD` in Figure A.4b taken with similar conditions. It can be noted that the number of entries in Figure A.4b is slightly lower than in Figure A.4a due to the excluded events. A-12

A.5 Using the same data as previously showed in Figure A.4, the effect of the quality flag is explained by presenting the reconstructed hit multiplicity of a data file without `Quality_flag` in Figure A.5a and the reconstructed content of the same RPC partition for data corresponding to a `Quality_flag` where all TDCs were labelled as `GOOD` in Figure A.5b taken with similar conditions. The artificial high content of bin 0 is completely suppressed. A-12

A.6 WebDCS DAQ scan page. On this page, shifters need to choose the type of scan (Rate, Efficiency or Noise Reference scan), the gamma source configuration at the moment of data taking, the beam configuration, and the trigger mode. These information will be stored in the DAQ ROOT output. Are also given the minimal measurement time and waiting time after ramping up of the detectors is over before starting the data acquisition. Then, the list of HV points to scan and the number of triggers for each run of the scan are given in the table underneath. A-14

B.1 Example of expected hit time distributions in the cases of efficiency (Figure B.1a) and noise/gamma rate per unit area (Figure B.1b) measurements as extracted from the raw ROOT files. The unit along the x-axis corresponds to ns. The fact that ”the” muon peak is not well defined in Figure B.1a is due to the contribution of all the RPCs being tested at the same time that don’t necessarily have the same signal arrival time. Each individual peak can have an offset with the ones of other detectors. The inconsistancy in the first 100 ns of both time distributions is an artefact of the TDCs and are systematically rejected during the analysis. B-16

B.2 The effect of the quality flag is explained by presenting the reconstructed hit multiplicity of a data file without Quality_flag. The artificial high content of bin 0 is the effect of corrupted data. B-21

B.3 Display of the maskting tool page on the webDCS. The window on the left allows the shifter to edit ChannelsMapping.csv. To mask a channel, it only is needed to set the 3rd field corresponding to the strip to mask to 0. It is not necessary for older mapping file formats to add a 1 for each strip that is not masked as the code is versatile and the default behaviour is to consider missing mask fields as active strips. The effect of the mask is directly visible for noisy channels as the corresponding bin turns red. The global effect of masking strips will be an update of the rate value showed on the histogram that will take into consideration the rejected channels. B-28

List of Tables

3.1 Details of the greenhouse fluorinated gases used in CMS and of their GWP [177]. . . 3-20

4.1 Properties of the most used electrode materials for RPCs. 4-3

5.1 Total photon flux ($E\gamma \leq 662\,\mathrm{keV}$) with statistical error predicted considering a ^{137}Cs activity of $740\,\mathrm{GBq}$ at different values of the distance D to the source along the x-axis of irradiation field [261]. 5-14

5.2 Correction factor c is computed thanks to Formula 5.4 taking as reference $D_0 = 50\,\mathrm{cm}$ and the associated flux F_0^{ABS} for each absorption factor available in table 5.1. 5-15

5.3 The data at D_0 in 1997 is taken from [261]. Using Formula 5.5, the flux at D, including an error of $1\,\mathrm{cm}$, can be estimated in 1997. Then, taking into account the attenuation of the source activity, the flux at D can be estimated at the time of the tests in GIF in 2014. Assuming a sensitivity of the RPC to γ $s = 2 \times 10^{-3}$, an estimation of the hit rate per unit area is obtained. 5-16

5.4 Summary of the characterization measurement performed in Ghent on CMS RPC detectors foreseen to be used at GIF++ for longevity studies of the present system. For each detector, the working voltage, defined as in Formula 4.25, was extracted from sigmoid fits performed in Figure 5.23a and the values of efficiency, cluster size, noise rate and current density at this voltage are reported. 5-22

6.1 Results of the sigmoid fit (Formula 4.24) performed on the data presented in Figure 6.9a. The working point and its corresponding efficiency are computed using Formulas 4.24 and 4.25. 6-9

6.2 Results of the sigmoid fit (Formula 4.24) performed on the data presented in Figure 6.12a. The working point and its corresponding efficiency are computed using Formulas 4.24 and 4.25. 6-12

6.3 Results of the sigmoid fit (Formula 4.24) performed on the data presented in Figure 6.16a. The working point and its corresponding efficiency are computed using Formulas 4.24 and 4.25. 6-16

6.4 Results of the sigmoid fit (Formula 4.24) performed on the data presented in Figure 6.24a. The working point and its corresponding efficiency are computed using Formulas 4.24 and 4.25. 6-22

6.5 Results of the sigmoid fit (Formula 4.24) performed on the data presented in Figure 6.26a. The working point and its corresponding efficiency are computed using Formulas 4.24 and 4.25. 6-24

A.1 Inter-process communication cycles in between the webDCS and the DAQ through file string signals. A-18

List of Acronyms

List of Acronyms

AFL	Almost Full Level
ALCTs	Anode local charged track boards
BARC	Bhabha Atomic Research Centre
BCS	Bardeen–Cooper–Schrieffer
BJT	Bipolar Junction Transistor
BLT	Block Transfer
BMTF	Barrel Muon Track Finder
BNL	Brookhaven National Laboratory
BSM	Physics beyond the Standard Model
BR	Branching Ratio
CAEN	Costruzioni Apparecchiature Elettroniche Nucleari S.p.A.
CERN	European Organization for Nuclear Research
CFD	Constant Fraction Discriminator
CFEBs	cathode front-end boards
CKM	Cabibbo–Kobayashi–Maskawa
CMB	Cosmic Microwave Background
CMS	Compact Muon Solenoid
CSC	Cathode Strip Chamber
CuOF	copper-to-optical-fiber translators
DAQ	Data Acquisition
DCS	Detector Control Software
DMBs	Data acquisition mother boards
DQM	Data Quality Monitoring
DT	Drift Tube
EDM	electric dipole moment
ECAL	electromagnetic calorimeter
EMTF	Endcap Muon Track Finder
FCC	Future Circular Collider
FEB	Front-End Board
FEE	Front-End Electronics
FWHM	full-width-at-half-maximum
GEANT	GEometry ANd Tracking - a series of software toolkit platforms developed by CERN
GEB	GEM Electronics board
GEM	Gas Electron Multiplier
GIF	Gamma Irradiation Facility
GIF++	new Gamma Irradiation Facility
gRPCs	glass RPCs

GWP	Global Warming Potential
HARDROC	HAdronic RPC Digital Read-Out Chip
HCAL	hadron calorimeter
HEP	High-Energy Physics
HJT	Hetero Junction bipolar Transistor
HL-LHC	High Luminosity LHC
HPL	High-pressure laminate
HSCPs	Heavy Stable Charged Particles
HV	High Voltage
ICRU	International Commission on Radiation Units & Measurements
ILC	International Linear Collider
IPNL	Institut de Physique Nucléaire de Lyon
iRPC	improved RPC
IRQ	Interrupt Request
ISR	Intersecting Storage Rings
LEIR	Low Energy Ion Ring
LEP	Large Electron-Positron
LHC	Large Hadron Collider
LS1	First Long Shutdown
LS2	Second Long Shutdown
LS3	Third Long Shutdown
LSP	lightest supersymmetric particle
LV	Low Voltage
LVDS	Low-Voltage Differential Signaling
MC	Monte Carlo
MCNP	Monte Carlo N-Particle
MiC	Minicrate electronics
MiC1	first version of Minicrate electronics
mip's	minimum ionizing particles
MRPC	Multigap RPC
MSSM	Minimal Supersymmetric Standard Model
mSUGRA	minimal SUper GRAvity
NIM	Nuclear Instrumentation Module logic signals
OH	Optohybrid Board
OMTF	Overlap Muon Track Finder
OTMBs	Optical TMBs
PAI	Photo-Absorption Ionisation
PAIR	Photo-Absorption Ionisation with Relaxation
PMT	PhotoMultiplier Tube
PS	Proton Synchrotron
PU	pile-up
QCD	Quantum Chromodynamics
QED	Quantum Electrodynamics
RADMON	Radiation Monitoring
RMS	Root Mean Square
ROOT	a framework for data processing born at CERN
RPC	Resistive Plate Chamber
SC	Synchrocyclotron
SDHCAL	Semi-Digital HCAL

SiPM	Silicon Photomultiplier
SLAC	Stanford Linear Accelerator Center
SM	Standard Model
SPS	Super Proton Synchrotron
SUSY	supersymmetry
TDC	Time-to-Digital Converter
TDR	Technical Design Report
TMBs	Trigger mother boards
ToF	Time-of-flight
ToT	Time-over-Threshold
TPG	trigger primitives
webDCS	Web Detector Control System
WIMPs	Weakly Interacting Massive Particles
YETS	Year End Technical Stop

1

Introduction

Grasping an understanding of the world in which they are leaving in has always been part of human life. Beyond the metaphysical questioning of our origins and purpose, curiosity has brought mankind to question its surroundings. Following the philosophy of the ancient Greeks and Indians came the development of the sciences as the systematic experimentation aimed at testing hypothesis and reproducing results obtained by fellow natural philosophers. With the industrial revolution and the organisation of science, it became possible to go always further in the understanding of the universe and of the matter in particular. Investigation on the constituent of matter proved to require more and more powerful machines in order to break apart the bricks of the world into ever smaller pieces, study their behaviour and extract new knowledge to help the development of humanity. So far, the largest and most powerful machine that was built to study the particles composing matter and test the models thought by physicists to explain their behaviour is the Large Hadron Collider (LHC), a circular particle accelerator used to collide protons and heavy ions. After only a few years of investigations conducted thanks to the LHC, several discoveries, predicted by the existing models, have been made. In the future, in order to boost the discovery potential on the LHC and be able to test hypotheses lying beyond the already acknowledged models, the instantaneous luminosity, i.e. the rate of particle interactions, will be slightly increased into a so-called High Luminosity phase to boost its discovery potential.

As the Large Hadron Collider will see its instantaneous luminosity be increased, the detectors on the different experimental sites will have to suffer an increased background irradiation due to the byproducts of the interaction of the beams with the infrastructure. This will cause for the detectors a stress which implications need to be understood throughout the High Luminosity LHC (HL-LHC) phase of operations. In the case of the Compact Muon Solenoid (CMS) experiment, it is important to understand if the detectors that will be subjected to the higher levels of radiation will be able to sustain higher detection rates while displaying the same performance they have so far been operated at and if this level of performance of the detectors will stay stable for a period longer than ten years. More specifically, the detectors placed very close to the beam line will be the most subjected to the change of luminosity. In CMS, the endcap detectors will then be particularly affected by the stronger background radiation. The endcap detectors compose a part of the muon system of CMS and among them, the Resistive Plate Chamber (RPC) plays a key role in providing the experiment a reliable trigger on potentially interesting data. This PhD work takes place into this very specific context of muon detector consolidation and certification for the HL-LHC period in order to provide the CMS experiment with robust new detectors and confirm that the present system will survive through the next 20 years.

CMS experiment main focus revolves around testing the Standard Model (SM) of particle physics using a multipurpose detector design to detect the interaction products of the protons and ions colliding along the LHC. Looking at the successive evolution of the theoretical models that gave birth to the SM, the need for very intense particle beams in high energy physics experiment becomes clear in that the higher the center-of-mass energy for each interaction, the greater the probe on very small cross-section processes predicted by the theory, justifying the successive increase in beam energy and intensity at LHC.

The implications for LHC experiments and in particular for the CMS detector explain the need for longevity and rate capability studies conducted on the Resistive Plate Chambers which are an important part of its Muon System as it is needed to certify the quality of operation of the trigger detectors throughout the lifetime of HL-LHC.

RPCs are gaseous detectors which physics principles are non trivial and are still being investigated. Nevertheless, key processes driving the electron multiplication in the gas volume, rate capability and ageing have been successfully identified and will define the parameters that will have to be taken into consideration while producing the detectors extending the pseudo-rapidity coverage of RPCs toward the beam line as well as the ones to be monitored during the on-going longevity and rate capability certification campaign.

On the one hand, the present RPC sub-system consists in two different RPC productions. Indeed, most of the RPC detectors were produced in view of the start of LHC activities in 2010. These detectors were build in between 2007 and 2008 to equip the barrel and the three disks of each endcaps of the CMS apparatus. But during the First Long Shutdown (LS1) of LHC in between end of 2012 and 2015, a fourth disk of endcap was added in order to reinforce the redundancy of the endcap trigger. Hence, new RPC detectors using the same technology were built in between 2012 and 2013. These two sets of detector productions only differ in the properties of the High-pressure laminate (HPL) used for their electrodes that could lead to a different ageing rate. This is why spare detectors of both production periods have been tested over the past years to certify their good operation through HL-LHC.

On the other hand, producing detectors to equip a highly irradiated region such as the extension of CMS RPC endcaps requires to substantially improve the ageing properties of the chosen technology by reducing the charge deposition per ionizing particle. This can be achieved both by modifying the design of the detector volume or by improving the signal to noise ratio of the Front-End Electronics (FEE) used to process the charge collected by the read-out strips making them more sensitive to weaker signals. Two improved RPC (iRPC) designs were selected and tested in order to extend of CMS endcap coverage.

Thanks to the study presented in this document, preliminary conclusions will be brought on the production of iRPCs and on the longevity of the present RPC system, providing with a better understand of the future performance of the RPC sub-system within the CMS experiment.

2

Investigating the TeV scale

Throughout history, physics experiment became more and more powerful in order to investigate finer details of nature to help understanding the building blocks of matter and the fundamental interactions that bind them in the microscopic world. Nowadays, the Standard Model of particle physics is the most accurate theory designed to explain the behaviour of particles and is able to make very precise predictions that are constantly verified. Nevertheless, some hints of new physics are visible as bricks are still missing to obtain a global description of the Universe.

To highlight the limits of the SM and test the different alternative theories, evermore powerful machines are needed. It is in this context that the Large Hadron Collider has been thought and built to accelerate and collide particles at energies exceeding anything that had been done before. Higher collision energies and high pile-up imply the use of enormous detectors to measure the properties of the interaction products. The Compact Muon Solenoid is a multipurpose experiment that have been designed to study the proton-proton collisions of the LHC and give answers on various high-energy physics scenarios such as different supersymmetry (SUSY) extensions to the Standard Model or Extra Dimensions models.

This Chapter will be the occasion to go through the history of the Standard Model of Particle Physics to understand the research conducted today in High-Energy Physics (HEP) facilities. From the discovery of the atom and of its inner structure to the development of the theories governing the fundamental interactions, all the elements leading to the construction SM will be discussed. Furthermore, highlights on the Physics beyond the Standard Model (BSM) will be given to replace the document in the context of today's research. Finally, a full description of the LHC and of the CMS detector will be provided.

2.1 The Standard Model of Particle Physics

In the early 21^{st} century it is now widely accepted that matter is made of elementary blocks referred to as *elementary particles*. The physics theory that classifies and describes the best the behaviour and interaction of such elementary particles is the so-called Standard Model. The SM formalizes three of the four fundamental interactions (electromagnetic, weak and strong interactions). Its development happened since the 1960s thanks to a strong collaboration between theoretical and experimental physicists.

2.1.1 A history of particle physics

The idea that nature is composed of elementary bricks, called *atomism*, is not contemporary as it was already discussed by Indian or Greek philosophers during antiquity. In Greece, atomism has been rejected by *Aristotelianism* as the existence of *atoms* would imply the existence of a void that would violate the physical principles of Aristotle philosophy. Aristotelianism has been considered as a reference in the european area until the 15^{th} century. With the *Rinascimento*, antic text and history started to be more deeply studied. The re-discovery of Platon's philosophy allowed opening the door to alternative theories and give a new approach to natural sciences where experimentation would become central. A new era of knowledge was starting. By the beginning of the 17^{th} century, atomism was re-discovered by philosophers. The very first attempt at estimating the number of *particles* in a volume was provided by Magnenus in 1646 by calculating that the number of *particles* in a stick of incense [1]. He found a value of the order of 10^{18} simply by considering the time necessary to smell it everywhere in a large church after the stick was lit on. It is now known that this number only falls short only by 1 order of magnitude.

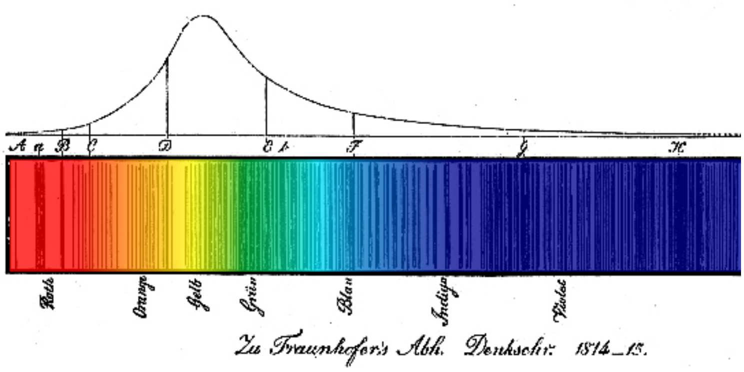

Figure 2.1: Solar spectrum with spectral lines as it visually appeared to Fraunhofer.

An alternative philosophy to atomism popularized by Descartes was *corpuscularianism*. Built on ever divisible corpuscles, contrary to atoms, its principles were mainly used by alchemists like Newton who would later develop a corpuscular theory of light. Boyle combined together ideas of both atomism or corpuscularianism leading to mechanical philosophy. The 18^{th} century has seen the development of engineering providing philosophical thought experiments with repeatable demonstration and a new point of view to explain the composition of matter. Lavoisier greatly contributed to chemistry and atomism by publishing in 1789 a list of 33 chemical elements corresponding to what are now called *atoms* [2]. In the early 19^{th} century Dalton summarized the knowledge on composition of matter [3]. In his atomic model, the atoms are ball-like constituents of the chemical elements. All atoms of a given element are identical, in size, mass, and other properties while the atoms of different elements differ. He also considered that atoms cannot be divided into smaller particles, created nor destroyed and that they combine into chemical compounds. The essence of chemical reaction was then the combination, separation or rearrangement of atoms. Soon after, Fraunhofer invented the spectrometer and discovered the spectral lines in the sunlight spectrum, as showed in Figure 2.1 [4]. These were later linked to the absorption by chemical elements present in the solar atmosphere by Kirchhoff and Bunsen. The rise of atomic physics, chemistry and mathematical formalism unraveled the different atomic elements and ultimately, the 20^{th} century saw the very first sub-atomic particles.

Discovery of the inner structure of the atom

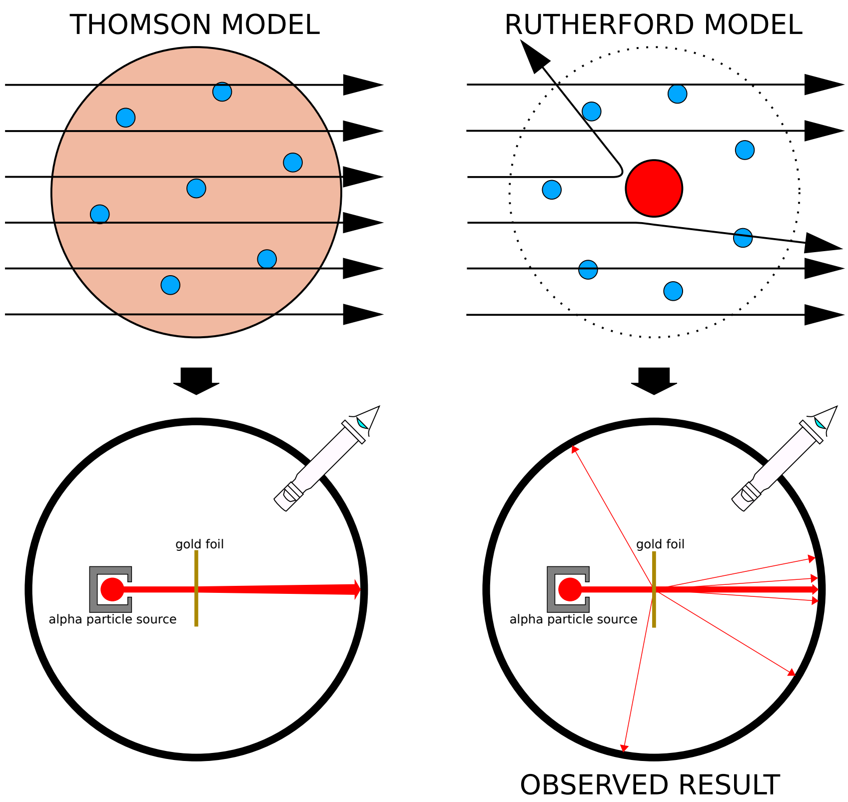

Figure 2.2: Through the gold foil experiment, Rutherford could show that most of the mass of atoms was contained in a positively charged nucleus and could then propose a more accurate atomic model than that of Thomson.

The negatively charged *electron* was the first to be discovered in 1897 by Thomson after three decades of research on cathode rays [5]. He proved that the electrification observed in an electroscope, as reported by Perrin [6], was due to the rays themselves. Hence, they had to be composed of electrically charged particles. In 1900, Becquerel showed the *beta rays* emitted by radium had the same charge over mass ratio as was measured by Thomson for cathode rays, pointing to electrons as a constituent of atoms [7]. This discovery leads to Thomson's plum pudding atomic model in which electrons are embed into a uniform positively charged atom [8]. In 1907, Rutherford and Royds showed that *alpha* particles were helium ions [9]. Indeed, once captured in a tube and subjected to an electric spark causing an electron avalanche, they could combine with two electrons to form a ^{4}He.

This discovery was directly followed by the constraint of the atom structure in between 1908 and 1913 through the Geiger–Marsden gold foil experiments in which the deflection angle of alpha particles fired at a very thin gold foil was measured [10–13]. It highlighted that atoms were mainly empty with nearly all their mass contained into a tiny positively charged *nucleus*. With these two observations, Rutherford could formulate the Rutherford planetary model of the atom in 1911 [14], shown together with the Thomson plum pudding model in Figure 2.2. The link between atomic number and number of positive and negative charges contained into the atoms would fast be understood. Hence, the different kinds of element transmutations appeared to be purely nuclear processes making clear that the electromagnetic nature of chemical transformations could not possibly change nuclei. A new branch in physics appeared to exclusively study nuclei: *nuclear physics*. By studying alpha emission and the product of their interaction with nitrogen gas, Rutherford reported in 1919 the very first nuclear reaction [15]. It leads to the discovery that the hydrogen nucleus was composed of a single positively charged particle that was later baptised *proton* [16]. This idea came from 1815 Prout's hypothesis proposing that all atoms are composed of *"protyles"* (i.e. hydrogen atoms) [17, 18]. By using scintillation detectors, Rutherford could highlight typical hydrogen nuclei signature and understand that the impact of alpha particles with nitrogen would knock out a hydrogen nucleus and produce an oxygen 17, as showed in Formula 2.1 and would then postulate that protons are building bricks of all elements.

$$^{14}N + \alpha \rightarrow ^{17}O + p \tag{2.1}$$

With this assumption and the discovery of *isotopes* together with Aston, elements with identical atomic number but different masses, Rutherford proposed that all elements' nuclei but hydrogen are composed of both charged particles, protons, and of chargeless particles, which he called *neutrons* [16, 19]. These neutral particles helped maintaining nuclei as one, as charged protons were likely to electrostatically repulse each other. He then introduced the idea of a new force, a *nuclear* force. The first idea concerning neutrons was a bond state of protons and electrons as it was known that the beta decay, emitting electrons, was taking place in the nucleus. However, it was then shown that electrons being confined into the nucleus would hardly be possible due to Heisenberg's uncertainty principle. Finally, in 1932, following the discovery of a new neutral radiation, Chadwick could discover the neutron as an uncharged particle with a mass similar to that of the proton which would solve the nucleus puzzle [20–24].

Development of the Quantum Electrodynamics

Historically, the development of the quantum theory revolved around the question of emission and absorption of discrete amount of energy through light. Einstein used the initial intuition of Planck about the black-body radiation to develop in 1905 a model to explain the photoelectric effect in which light was described by discrete *quanta* now called *photons* [25, 26]. For this model, Einstein introduced the concept of wave-particle duality as classical theory was not able to describe the phenomenon. With the new understanding of atoms and of their structure, classical theories also proved unable to explain atoms' stability. Indeed, using classical mechanics, electrons orbiting around a nucleus should radiate an energy proportional to their angular momentum and hence, loose energy through time and the spectrum of energy emission should then be continuous. However, it was known since the 19^{th} century and the discovery of spectral lines that the emission spectrum of material was discrete [4].

In 1913, quantum physics was introduced into the atomic model by Bohr to overcome the electron's energy loss due to orbiting radiation emission [27]. Using the correspondence principle stating that for large enough numbers the quantum calculations should give the same results than the classical theory, he proposed the very first quantum model of the hydrogen atom explaining the line spectrum by introducing the *principal quantum number* n describing the electron *shell*. The same year, Moseley confirmed Borh's model through the Moseley's law [28]. Debye and then Sommerfeld extended it by introducing the quantization of the angular momentum [29]. The quantization the z-component of the angular momentum led to the *second* and *third quantum numbers*, or *azimuthal* and *magnetic quantum number*, l and m. The second defines the orbital angular momentum of the electrons on their shells and hence, the shape of the orbital, while the third the available orbital on the subshell for each electron as shown in Figure 2.3.

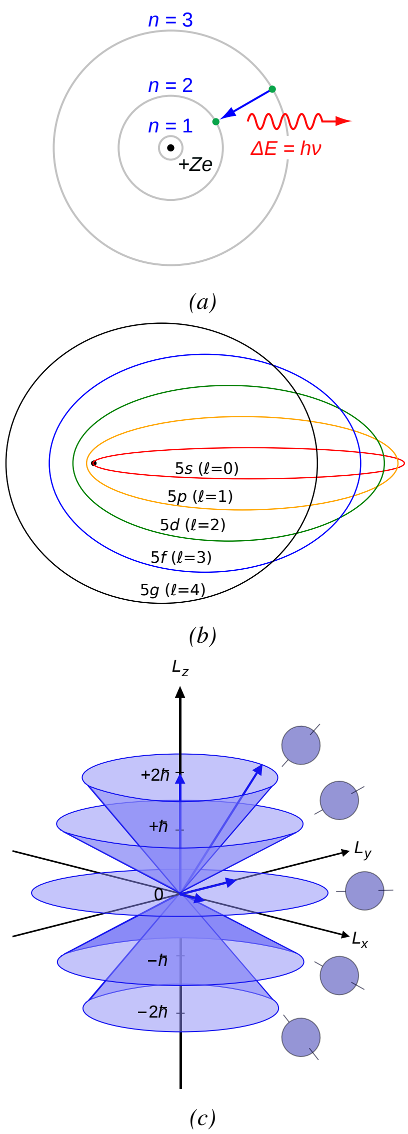

Figure 2.3: Figure 2.3a: The orbits in which the electron may travel according to the Borh model of the hydrogen atom. An electron jumps between orbits and is accompanied by an emitted or absorbed amount of electromagnetic energy ($h\nu$).The orbits radius increases as n^2. Figure 2.3b: Elliptical orbits with the same energy and quantized angular momentum $l = 0, 1, ..., n-1$ in the case $n = 5$. Figure 2.3c: Illustration of quantum mechanical orbital angular momentum. The cones and plane represent possible orientations of the angular momentum vector for $l = 2$ and $m = -2, -1, 0, 1, 2$.

Nevertheless, although the model was not only limited to spherical orbitals anymore, making the atom more realistic, the Zeeman effect couldn't be completely explained by just using n, l and m [30–33] nor could the result of the Stern-Gerlach experiment [34]. Both experiments are shown in Figure 2.4. A solution was brought after Pauli in 1925 proposed together with his exclusion principle the idea of a new quantum degree of freedom in order to resolve the apparent problem [35, 36]. This degree of freedom was interpreted as an intrinsic angular momentum vector associated to the particle itself, not to the orbital [37], and associated to a new quantum number s, the *spin* projection quantum number explaining the lift of degeneracy to an even number of energy levels [38]. The new quantum number helped in theorizing the neutron as a neutral particle rather than a bond state of a proton and an electron confined in the nucleus itself.

The introduction of the *spin* happened one year after another attempt of improvement of the theory was made by De Broglie in his Ph.D. thesis [39]. The original formulation of the quantum theory only considered photons as energy quanta behaving as both *waves* and *particles*. De Broglie proposed that *all* matter are described by waves and that their momentum is proportional to the oscillation of quantized electromagnetic field oscillators. This interpretation was able to reproduce the previous version of the quantum energy levels by showing that the quantum condition involves an integer multiple of 2π, as shown by Formula 2.2.

$$p = \hbar k \Leftrightarrow \int p dx = \hbar \int k dx = 2\pi\hbar n \tag{2.2}$$

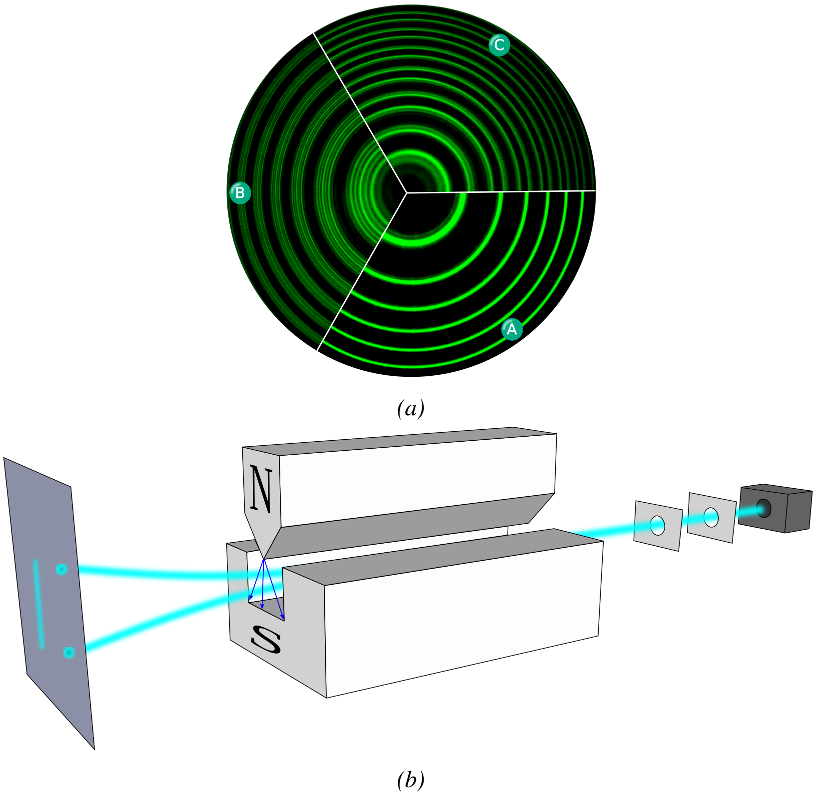

Figure 2.4: Figure 2.4a: The spectral lines of mercury vapor lamp anomalous Zeeman effect without magnetic field (A) and with magnetic field (B - transverse Zeeman effect & C - longitudinal Zeeman effect). Figure 2.4b: Stern–Gerlach experiment: Silver atoms traveling through an inhomogeneous magnetic field and being deflected up or down depending on their spin.

Although the intuition of De Broglie about the wave-particle duality of all matter was a step in the right direction, his interpretation was semiclassical and it is in 1926 that the first full quantum wave equation would be introduced by Schrödinger to describe electron-like particles, reproducing the previous semiclassical formulation without inconsistencies [40]. This complex equation describes the evolution of the wave function Ψ of the quantum system, defined by its position vector $\mathbf{r}$ and time t as an energy conservation law, in which the hamiltonian of the system $\hat{H}$ is explicit, by solving the Equation 2.3.

$$i\hbar\frac{\partial}{\partial t}|\Psi(\mathbf{r},t)\rangle = \hat{H}|\Psi(\mathbf{r},t)\rangle \tag{2.3}$$

The spin was then included into Schrödinger equation by Pauli to take into account the interaction with an external magnetic field, as shown in Equation 2.4 in which the Hamiltonian operator is a 2×2 matrix operator due to the Pauli matrices [38]. $\mathbf{A}$ is the vector potential and ϕ is the scalar electric potential.

$$i\hbar\frac{\partial}{\partial t}|\Psi\rangle = \left[\frac{1}{2m}(\sigma\cdot(\mathbf{p}-q\mathbf{A})^2+q\phi)\right]|\Psi\rangle \tag{2.4}$$

Later in 1927, Dirac went further in his paper about emission and absorption of radiation by proposing a second quantization not only of the physical process at play but also of the electromagnetic field [41]. His equation provided the ingredients to the first formulation of *Quantum Electrodynamics (QED)* and the description of photon emission by electrons dropping into a lower energy state in which the final number of particles is different than the initial one. Nevertheless, in order to properly treat electromagnetism, the incorporation of the special relativity developed by Einstein was necessary. Derived in 1928, the Dirac equation, shown as Equation 2.5, similarly to Schrödinger equation, is a single-particle equation but it incorporates special relativity in addition to quantum mechanics rules [42].

$$i\hbar\gamma^\mu\partial_\mu\psi - mc\psi = 0 \tag{2.5}$$

It features the 4×4 gamma matrices γ^μ built using 2×2 Pauli matrices and the unitary matrix, the 4-gradient ∂_μ, the rest mass m of any half integer spin massive particle described by the wave function $\psi(x,t)$, also called a Dirac spinor and the speed of light c. In addition to perfectly reproduce the results obtained with quantum mechanics so far, it also provided *negative-energy solutions* that would later be interpreted as a new form of matter, *antimatter* [43, 44]. In the non-relativistic limit, the Dirac equation gives a theoretical justification to the Pauli equation that was phenomenologically constructed to account for the spin.

The successes of the QED were soon followed with theoretical problems as computations of any physical process involving photons and charged particles were shown to be only reliable at the first order of the *perturbation theory* [45]. At higher order of the theory, divergent contributions were appearing giving nonsensical results. Only two effects were contributing to these infinities.

- The self-energy of the electron (or positron), the energy that the particle has due to its own interaction with its environment.
- The vacuum polarization, virtual electron–positron pairs produced by a background electromagnetic field in the vacuum which is not an ”empty” space. These virtual pairs affect the charge and current distributions generated by the original electromagnetic field.

Solving this apparent problem was done by carefully defining the concepts of each observable, for example mass or charge, as these quantities are understood within the context of a non-interacting field equation. From the experimental point of view, they are abstractions as what is measured is ”renormalized observables” shifted from their ”bare” value by the interaction taking place in the measuring process. The infinities needed to be connected to corrections of mass and charge as those are fixed to finite values by experiment. This was the intuition of Bethe in 1947 who successfully computed the effect of such *renormalization* in the non-relativistic case [46]. Full covariant formulations of QED including renormalization were achieved by 1949 by Tomonaga, Schwinger, Feynman, and Dyson [47]. With the resolution of infinities, QED had mostly reached its final form, being still today the most accurate physical theory, and would serve as a model to build all other quantum field theories.

Development of the quark model and Quantum Chromodynamics

To explain the nuclear force that holds *nucleons* (protons and neutrons) together, Yukawa proposed in 1934 the existence of a force carrier called *meson* due to its predicted mass in the range in between the electron and nucleon masses [48]. Discovered in 1936 by Anderson and Neddermeyer [49, 50], and confirmed using bubble chambers in 1937 by Street and Stevenson [51], a first meson candidate was observed in the decay products of cosmic rays. Assuming it had the same electric charge as electrons and protons, this particle was observed to have a curvature due to magnetic field that was sharper than protons but smoother than electrons resulting in a mass in between the two. But its properties were not compatible with Yukawa's theory, which was emphasized by the discovery of a new candidate in 1947, again in cosmic ray products using photographic emulsions [52–54]. The detections of the mu-meson and of the pi-meson in emulsions are showed in Figure 2.5.

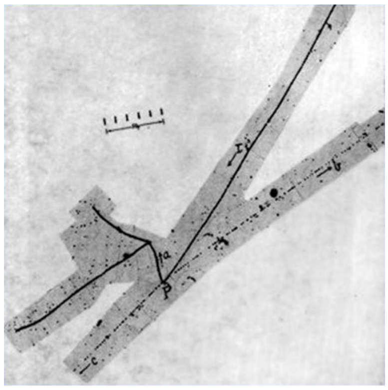

(a)

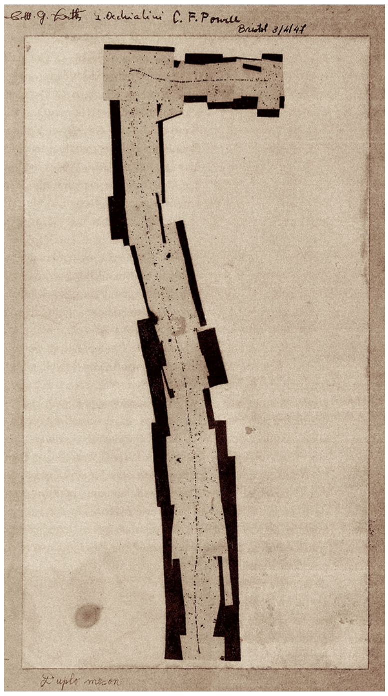

(b)

Figure 2.5: Figure 2.5a: decay of a μ-meson in an emulsion. Figure 2.5b: track of a π-meson in an emulsion signed by Lattes, Powell, and Occhialini.

This new candidate, although it had a similar mass than the already believed *meson*, would rather decay into it. For distinction, the first candidate would then be renamed "*mu meson*" when the second would be the "*pi meson*". The *mu meson* was behaving like a heavy electron and didn't participate in the strong interaction whereas the pion was believed to be the carrier of the nuclear interaction. This led to classify the *mu* in a new category of particles that shared similar properties called *leptons* under the name of *muon* together with the electron. The *pi meson* was finally found to be a triplet of particles: a positively charged, a negatively charged, and a neutral particle. The neutral *pi meson* has been more difficult to identify as it wouldn't leave tracks on emulsions nor on bubble chambers and needed to be studied via its decay products. It was ultimately identified in University of California's cyclotron in 1950 through the observation of its decay into 2 photons [55].

Also discovered in 1947 but in cloud chamber photographs, the *K meson* has also been an important step towards the establishment of the Standard Model [56]. A triplet of particles, two charged and a neutral, with a mass roughly half that of a proton, were reported. These particles were baptised *K meson* in contrast to the "light" *pi* and *mu* "L-mesons". The particularity of the *K* is their very slow decays with a typical lifetime of the order of 10^{-10}s much longer than the 10^{-23}s of *pi*-proton reactions. The concept of *strangeness*, a new quantum number was then introduced thanks to an idea of Pais as an attempt to explain this phenomenon as *strange* particles appeared as the pair production of a strange and anti-strange particle [57].

With the development of synchrotrons, the particle *zoo* grew to several dozens during the 1950s as higher energies were reachable through acceleration. In 1961, a first classification system, called *Eightfold Way*, was proposed by Gell-Mann [58]. It found its roots in the Gell-Mann–Nishijima formula, which relates the electric charge Q, the third component of the isospin I_3, the *baryon* number B and the strangeness S, as showed in Formula 2.6 [59–61].

$$Q = I_3 + \frac{1}{2}(B + S) \tag{2.6}$$

The isospin is a quantum number introduced in 1932 to explain symmetries of the newly discovered neutron using representation theory of SU(2) [62]. The baryon number, was introduced by Nishijima as a quantum number for baryons, i.e. particles of the same family as nucleons [59]. The mesons were classified in an octet and baryons of spin $\pm\frac{1}{2}$ and $\pm\frac{3}{2}$ were respectively classified into an octet and a decuplet, as shown in Figure 2.6. To complete the baryon decuplet, Gell-Mann predicted the existence of baryon Ω^- which would later be discovered in 1964 [63].

Gell-Mann, and independently Zweig, then proposed a full theoretical model in which *hadrons* (strongly interacting particles, i.e. mesons and baryons) were not elementary particles anymore [64–66]. They were rather composed of three flavors of particles called *quarks* and their anti-particles. The three flavors were called *up*, *down* and *strange*. *Up* and *down* were used to explain the nucleons and non-strange mesons, while *strange* came into the composition of hadrons showing strangeness. *Up* and *down* flavors were discovered in 1968 thanks to the deep inelastic scattering experiments conducted at the Stanford Linear Accelerator Center (SLAC) [67, 68], and *strange* could only be indirectly validated even though it provided a robust explanation to *kaon* (K) and *pion* (π).

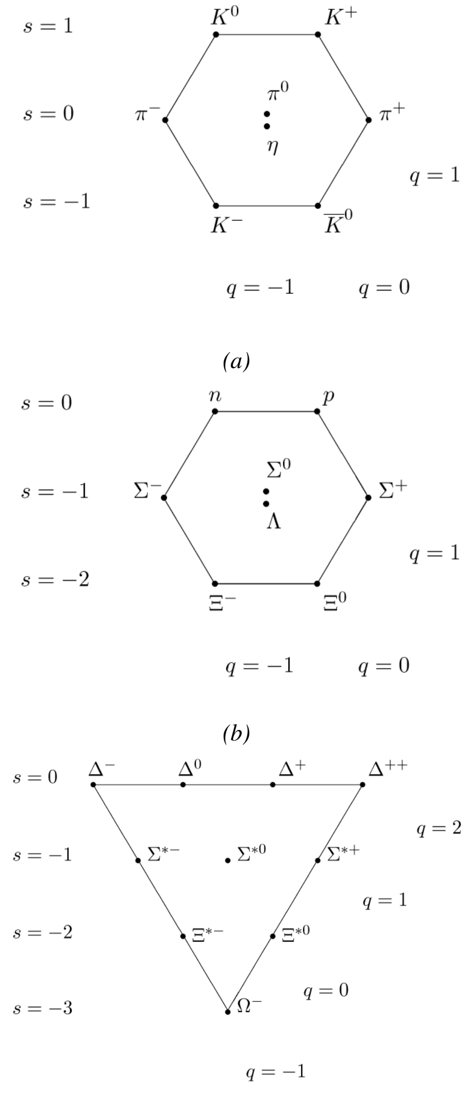

Figure 2.6: Figure 2.6a: Meson octet. Figure 2.6b: Baryon octet. Figure 2.6c: Baryon decuplet.

However, in the decade following the Gell-Mann-Zweig quark model proposition, several improvement to the model were brought. First by Glashow and Bjorken the same year that predicted the existence of a fourth quark flavor, the *charm*, that would equalize the then known number of quarks and leptons [69, 70]. Finally in 1973 by Kobayashi and Maskawa that increased the number of quarks to six to explain the experimental observation of CP violation [71, 72]. These two quarks were referred to as *top* and *bottom* for the first time in 1975 [73]. It's only after these additions to the quark model that finally the *charm* was discovered in 1974 at both SLAC and Brookhaven National Laboratory (BNL) [74, 75]. A meson in which the *charm* is bonded with an *anti-charm*, called J/ψ and presented in Figure 2.7, helped convince the physics community of the validity of the model. The *bottom* was discovered soon after in 1977 in Fermilab [76] and indicated the existence of the *top* that resisted to discovery until Fermilab's experiments CDF and D∅ in 1995 due its very large mass and the energy needed to produce it [77, 78].

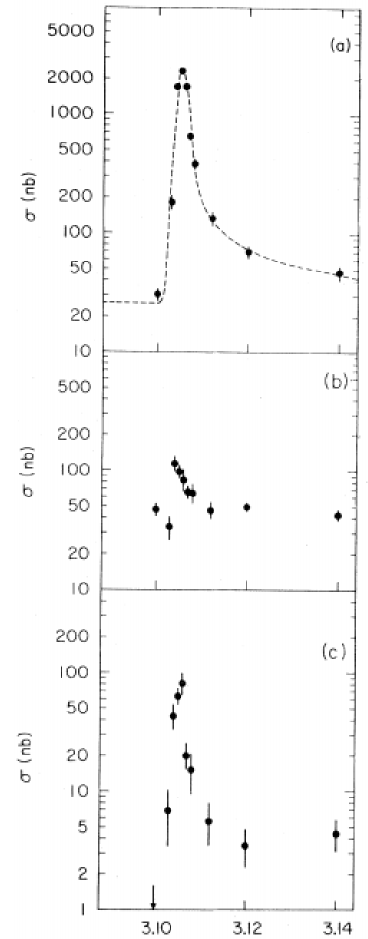

(a)

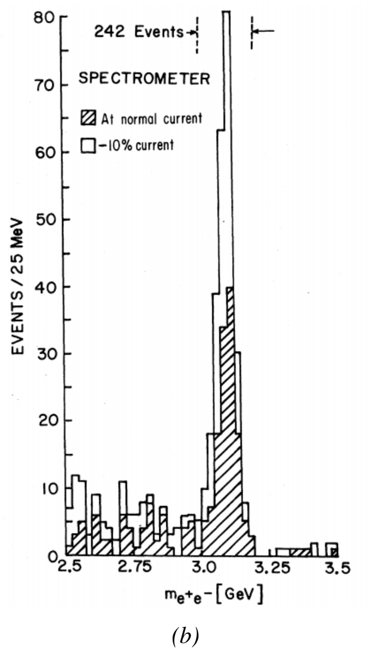

(b)

Figure 2.7: Discovery of the J/Ψ by both SPEAR (SLAC [74]) in Figure 2.7a and AGS (BNL [75]) in Figure 2.7b. In Figure 2.7a, the cross section versus energy is showed for (a) multi hadron final states, (b) e^+e^- final states, and (c) $\mu^+\mu^-$, $\pi^+\pi^-$ and K^+K^- final states.

As remarked by Struminsky, due to mesons such as Ω^- or Δ^{++}, the first SU(3) model already should have possessed an additional quantum number [79]. Indeed, these mesons are composed of three identical quarks, respectively three *strange* and *up* quarks, with parallel spins, which should be forbidden by the exclusion principle. Independently, Greenberg, and Han and Nambu proposed an additional SU(3) degree of freedom for the quarks [80, 81]. It was later referred to as *color charge gauge*, that could interact through *gluons*, the gauge boson octet corresponding to this degree of freedom. The color field is presented in Figure 2.8a. Nevertheless, as observing free quarks to prove their existence proved to be impossible, two visions of the quarks were argued. On one side, Gell-Mann proposed to see quarks as mathematical construct instead of real particles, as they are always confined, implying that quantum field theory would not describe entirely the strong interaction. He promoted the S-matrix approach to treat the strong interaction. Opposed to this vision, Feynman on the contrary argued that quarks are real particles, that he would call *partons*, that should be described as all other particles by a distribution of position and momentum [82]. The implications of quarks as point-like particles were verified at SLAC and helped abandon the S-matrix to the benefit of QFT [83]. The concept of *color* was then added to the quark model in 1973 by Fritzsch and Leutwyler together with Gell-Mann to propose a description of the strong interaction through the theory of Quantum Chromodynamics (QCD) [84]. The discovery the same year of asymptotic freedom within the QCD by Gross, Politzer, and Wilczek, allowed for very precise predictions thanks to perturbation theory [85, 86]. The evolution of the gauge constant of QCD with respect to the energy as described by asymptotic freedom is showed in Figure 2.8b.

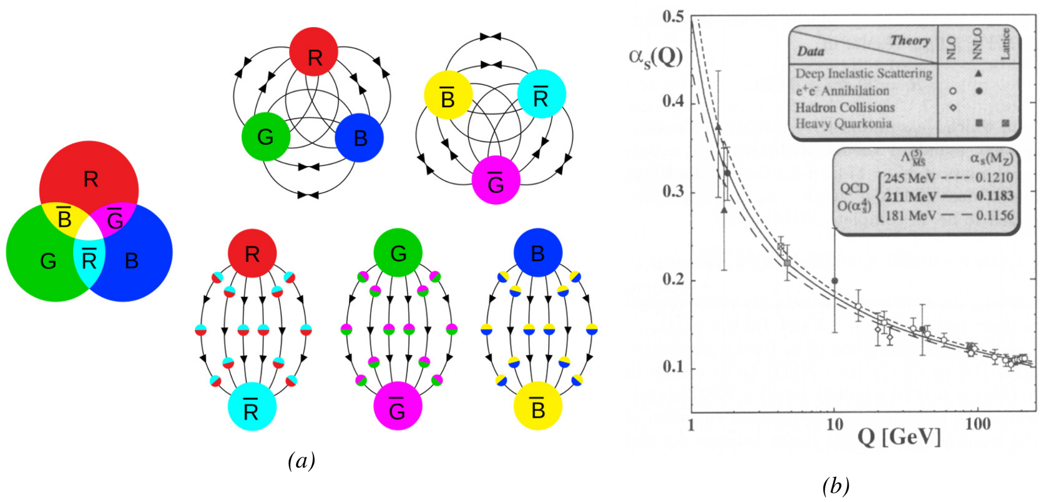

Figure 2.8: Figure 2.8a: the color field of QCD only allows for "white" baryons, particles composed of quarks, to exist. Examples are given for mesons, composed of a quark and its anti-quark, and hadrons, composed of three differently colored quarks or anti-quarks. Other exotic baryons have been predicted and observed, such as tetraquarks and pentaquarks. Figure 2.8b: a crossed analysis performed thanks to the data collected by various experiments at different energies have showed that the coupling constant evolves as predicted by the mechanism of asymptotic freedom [87].

The Weak interaction, spontaneous symmetry breaking, the Higgs mechanism and the Electroweak unification

The weak interaction is the process that causes radioactive decays. Thanks to the neutron discovery [23], Fermi could explain in 1934 beta radiations through the beta decay process in which the neutron decays into a proton by emitting an electron [88]. Though the missing energy observed during this process triggered a huge debate about the apparent non-conservation of energy, momentum and spin of the process, Fermi, as Pauli before him [89], proposed that the missing energy was due to a neutral not yet discovered particle that was then baptised *neutrino*. The impossibility to detect such a particle left some members of the scientific community sceptical, but hints of energy conservation and of the existence of the neutrino were provided by measuring the energy spectrum of electrons emitted through beta decay, as there was a strict limit on their energy, as showed in Figure 2.9.

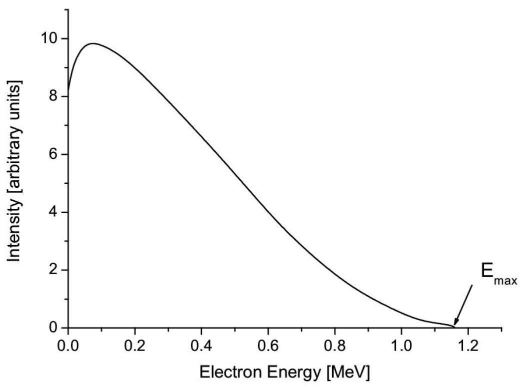

Figure 2.9: Energy spectrum of beta particles emitted by a source of ^{210}Bi.

It's only 30 years later in 1953 that it was discovered by the team of Cowan and Reines using the principle of inverse beta decay described through Formula 2.7 [90].

$$\overline{\nu} + p \rightarrow n + e^{+} \tag{2.7}$$

The experiment consisted in placing water tanks sandwiched in between liquid scintillators near a nuclear reactor with an estimated neutrino flux of $5 \times 10^{13}\mathrm{cm}^{-2}\,\mathrm{s}^{-1}$. However, in order to explain the absence of some reactions in the experiment of Cowan and Reines and constraint the beta decay theory of Fermi and extend it to the case of the muon, Konopinski and Mahmoud proposed in 1953 that the muon decay would eject a particle similar to the neutrino [91]. They predicted the existence of a muon neutrino that would be different to the one involved in the beta decay, related to the electron. With this, the idea of *lepton number* arised. The *muon neutrino* was successfully detected in 1962 by Lederman, Schwartz, and Steinberger [92].

The theory could not be valid though as the probability of interaction, called *cross-section*, would have been increasing without limitation with the square of the energy. Fermi had proposed a two vector current coupling but Lee and Yang noted that an axial current could appear and would violate parity [93]. Gamov and Teller had already tried to account for such parity violation by describing Fermi's interaction through allowed (parity-violating) and superallowed (parity-conserving) decays [94]. The Wu experiment in 1956 confirmed the parity violation [95], as showed by Figure 2.10. But the success of QED as a quantum field theory sparked the development of similar theory to describe the weak interaction.

As previously discussed, the great success of QED was built on an underlying symmetry, interpreted as a gauge invariance so that the effect of the force is the same in all space-time coordinates, and of the possibility to renormalize it in order to resolve infinities. In 1967, Weinberg found a way to unite both the electromagnetic and weak interaction into a gauge theory involving four gauge bosons, three of which are massive and carry out the weak interaction and the last is a massless boson carrying the electromagnetic interaction [96]. Among the three massive bosons, two are charged and one is neutral, similarly to the previously theorized *pi meson* vector of the Yukawa model [48] and all have a mass much greater than nucleons and thus a very short life time implying a finite very short range, contrary to the contact interaction originally proposed by Fermi.

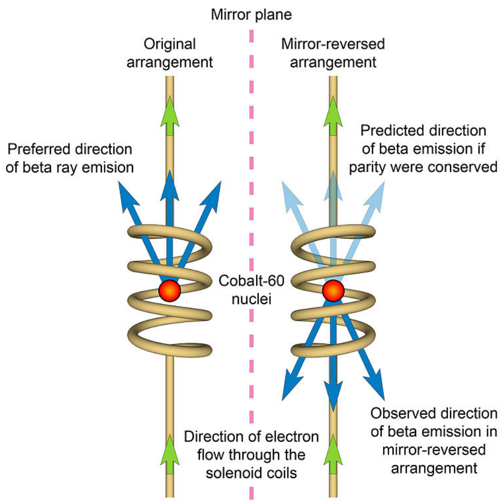

(a)

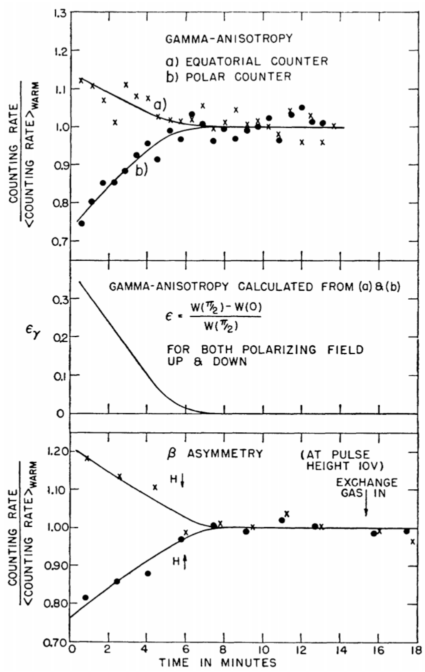

(b)

Figure 2.10: As explained through Figure 2.10a, the Wu experiment consisted in measuring the preferred direction of emission of beta rays of a Colbalt source placed in a stable magnetic field aligned, in one case, and anti-aligned, in the other case, with the nuclear spin. The result of Figure 2.10b showed a violation of parity.

Breakthroughs in other fields of physics contributed in giving theoretical support and interpretation to the unified electroweak theory. The stepping stone was the use of spontaneous symmetry breaking that was inspired to Nambu at the beginning of the 1960s [97, 98] following the development of the Bardeen–Cooper–Schrieffer (BCS) superconductivity mechanism in 1957 [99]. Cooper had shown that BCS pairs, pairs of electrons bound together at low temperature, can have lower energy than the Fermi Energy and are responsible for superconductivity. This led to the discovery of Goldstone-Nambu bosons [100, 101] as a result of the spontaneous breaking of the chiral symmetry in a theory describing nucleons and mesons developed by Nambu and Jona-Lasinio in 1961, and now understood as a low-energy approximation of QCD. Similarly to the mechanism of energy gap appearance in superconductivity, the nucleon mass is suggested to be the result of a self-energy of a fermion field and is studied through a four-fermion interaction in which, as a consequence of the symmetry, bound states of nucleon-antinucleon pairs appear and can be regarded as virtual pions. Though the symmetry is maintained in the equations, the ground state is not preserved. Goldstone showed that the bound states correspond to spinless bosons with zero mass [101].

Although the model in itself didn't revolutionize particle physics, spontaneous symmetry breaking was generalized to quantum field theories. As all fundamental interactions are described using gauge theories based on underlying symmetries, processes such as the chiral symmetry breaking were introduced soon after the publication of Nambu and Jona-Lasinio. In 1962, Anderson, discussed the implications of spontaneous symmetry breaking in particles physics [102]. He did so by following the idea of Schwinger who suggested that zero-mass vector bosons were not necessarily required to describe the conservation of baryons, contrary to the bosons emerging from chiral symmetry breaking [103]. A model was finally independently built in 1964 by Brout and Englert [104], Higgs [105], and Guralnik, Hagen, and Kibble [106], who discovered that combining an additional field into a gauge theory in order to break the symmetry, the resulting gauge bosons acquire a nonzero mass. Moreover, Higgs stated that this implied the existence of at least one new massive, i.e. self-interacting, scalar boson corresponding to this additional field, that is now known as *Higgs boson*. The Higgs mechanism today specifically refers to the process through which the gauge bosons of the weak interaction acquire mass. In 1967, Weinberg could point to the Higgs mechanism to integrate a Higgs field into a new version of the electroweak theory in which the spontaneous symmetry breaking mechanism of the Higgs field would explicitly explain the masses of the weak interaction gauge bosons and the zero-mass of photons [96].

2.1.2 Construction and validation of the Standard Model

The Standard Model of particle physics was built in the middle of the 1970s after the experimental confirmation of the existence of quarks [107]. It is based on the assembly of the models previously introduced and describing the fundamental interactions and their gauge bosons, except for gravitation, as well as the way elementary "matter" particles interact with the fields associated with these force carriers. In this sense, the development of QED and the unification of the electroweak interaction, of the Yukawa interaction and of QCD, and of the Higg mechanism made it possible to explain most of the contemporary physics.

In the SM, "matter" particles, are described by twelve fermion fields of spin $\frac{1}{2}$ obeying the Fermi-Dirac statistics, i.e. subjected to the Pauli exclusion principle. To each fermion is associated its corresponding anti-particle. The fermions are classified according to the way they interact and thus according to the charges they carry. Six of them are classified as quarks (u, d, c, s, t, and b) and are subjected to all interactions and the six others as leptons (e^-, μ^-, τ^-, ν_e, ν_μ, and ν_τ). Leptons are not subjected to the strong interaction and among them, the three neutrinos only interact weakly as they are neutral particles, which explains why they are so difficult to detect. The gauge boson fields are the gluons g for the strong interaction, the photon γ for the electromagnetic interaction and the weak bosons W^+, W^-, and Z^0 for the weak interaction. Finally, the Higgs field H^0 is responsible, through the spontaneous symmetry breaking, of the mixing of the massless electroweak boson fields W_1, W_2, W_3, and B leading to the observable states γ, W^+, W^-, and Z^0 that can gain mass while interacting with the Higgs field. This picture of the SM is summarized through Figure 2.11 where the antifermions are not shown.

When the model was first finalized, the existence of the weak gauge bosons, of the charm, of the third quark generation composed of top and bottom quarks to explain the observed CP violation was not proven but the predictions were measured with good precision in the years following [74–78]. The weak bosons W and Z were discovered during the next decade in 1983 [108–111]. The very last predicted elementary particle of the model that was not observed yet proved to be very difficult to observe. The Higgs boson needed the start of the LHC to finally be observed in 2012 [112, 113]. A few years more of tests were necessary to measure its properties to confirm the observation of a scalar boson compatible with the predicted Higgs boson H^0 [114].

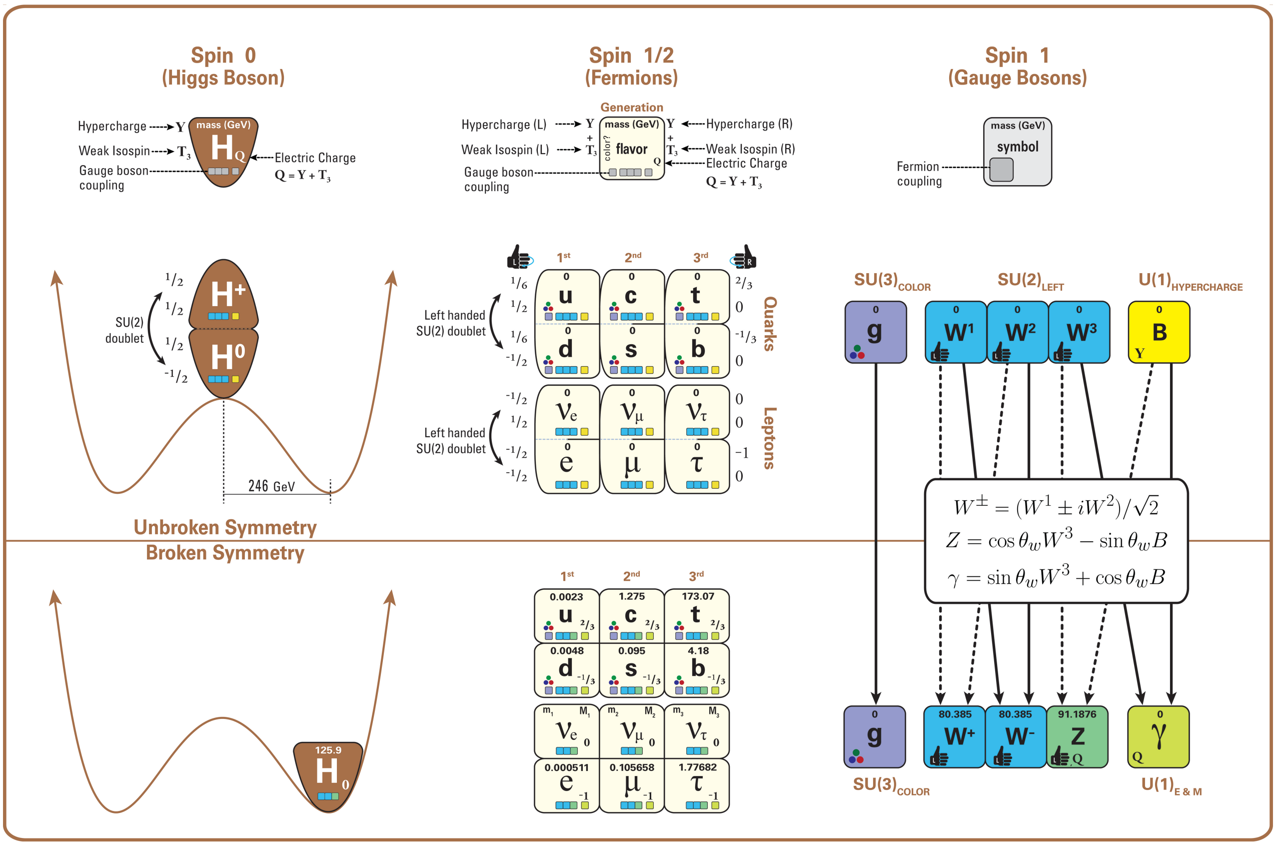

Figure 2.11: The elementary particles of the Standard Model are shown along with their properties. Their interactions with the strong, weak and electromagnetic forces have been made explicit using color squares. In the left column, the scalar Higgs boson is depicted. The center is focused on the matter particles, the fermions, and the right column on the force carriers, the gauge bosons. The role of the Higgs boson in electroweak symmetry breaking is highlighted, and the corresponding way properties of the various particles differ in the (high-energy) symmetric phase (top) and the (low-energy) broken-symmetry phase (bottom) are shown.

2.1.3 Investigating the TeV scale

In High-Energy Physics, the number of experimental events depends on the total interaction cross-section of the colliding particles and of the *instantaneous luminosity* [115]. The luminosity is a quantity providing an information on the interaction rate normalised to the interaction cross-section. The relationship between number of events N, cross-section and instantaneous luminosity $\mathcal{L}$ is given in Formula 2.8.

$$\mathcal{L} = \frac{1}{\sigma}\frac{\mathrm{d}N}{\mathrm{d}t} \Leftrightarrow N = \sigma \int \mathcal{L}\,\mathrm{d}t = \sigma\mathcal{L}_{int} \tag{2.8}$$

The integral of the luminosity over time is referred to as the *integrated luminosity* $\mathcal{L}_{int}$. In fact, the instantaneous luminosity can be deduced from the beam parameters. New colliders now use bunched beams. The instantaneous luminosity then depends on the bunch crossing frequency f_{BX}, on the number of particles contained in each bunch n, and on the RMS transverse beam sizes in the horizontal, σ_x^*, and vertical directions, σ_y^*, at the level of the interaction point. The beam sizes can be assumed to be identical, leading to the relation of Formula 2.9.

$$\mathcal{L} = f_{BX} \frac{n^2}{\sigma^*} \tag{2.9}$$

This expression doesn't depend on time anymore and leads to a simple estimation of the integrated luminosity and hence, knowing the cross-section of each available physics channel, to the expected number of events in each channel. The total interaction cross section is the sum of all the different output channels allowed by the interaction process. In the case of highly relativistic protons, the proton-proton (pp) total cross-section increases with the center-of-mass energy of interactions, as can be seen from Figure 2.12.

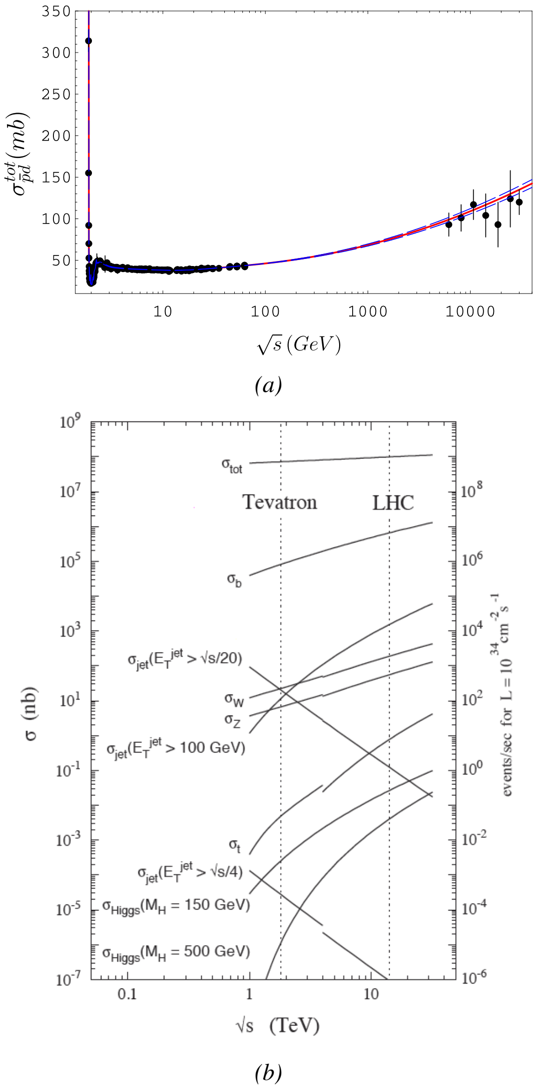

Figure 2.12: Figure 2.12a: Total proton-proton cross-section as a function of the collisions center-of-mass energy $\sqrt{s}$ [116] with cosmic-ray data from Akeno Observatory and Fly's Eye Collaboration. Figure 2.12b: Total proton-(anti)proton and interaction channel cross-sections in the TeV *scale.*

Enhancing rare processes that allow to finely test the Standard Model is then achieved through an increase in both energy and luminosity. At the energy range that were scanned thanks to high-energy colliders, the SM has so far been a well tested theory. Nevertheless, several hints of physics going beyond its scope have been observed.

Dark matter and gravity: The discrepancy of velocity dispersion of stars in galaxies with respect to the visible mass they contain is known since the end of the 19^{th} century where Kelvin proposed that this problem could be solved if a great majority of the stars would be dark bodies, idea strongly criticized by Pointcaré [117]. Throughout the 20^{th} century, physicists like Kapteyn [118] or Zwicky [119, 120], showed the first hints of a *dark matter* by studying star velocities and galactic clusters, followed by robust measurements of galaxy rotation curves by Babcock which suggested that the mass-to-luminosity ratio was different from what would be expected from watching the visible light [121]. Later in the 1970s, Rubin and Ford from direct light observations [122] and Rogstad and Shostak from radio measurements [123] showed that the radial velocity of visible objects in galaxies was increasing with increasing distance to the center of the galaxy. An example of galaxy rotation curve is provided in Figure 2.13. Finally observation of lensing effect by galaxy clusters, temperature distribution of hot gas in galaxies and clusters, and the anisotropies in the Cosmic Microwave Background (CMB), showed in Figure 2.14, kept on pointing to a *dark matter* [124]. From all the data accumulated, the visible matter would only account to no more than 5% of the total content on the visible universe [125]. Alternative theories have tried to investigate modified versions of the General Relativity as this theory is only well tested at the scale of the solar system but is not sufficiently tested on wider ranges or even theories in which gravitation is not a fundamental force but rather an emergent one [126, 127]. But so far, such theories have difficulties to reproduce all the experimental observations as easily as through dark matter.

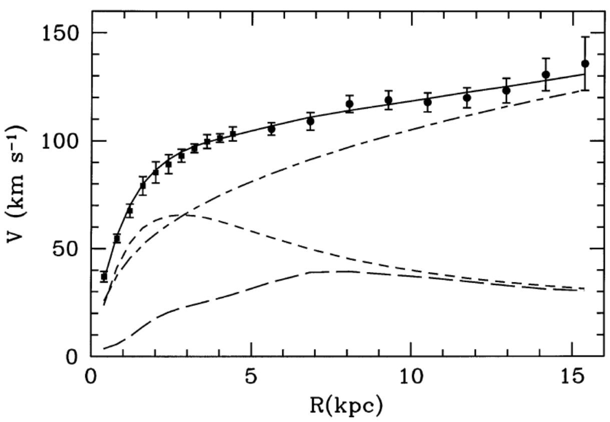

Figure 2.13: Rotation curve (points) of the galaxy M33 compared with best fitting model (line). The short-dashed line represents the rotation profile that would be expected from the observation of the stellar disc alone [128].

A possible theory to offer dark matter candidates would be *supersymmetry* (SUSY) which proposes a relationship in between bosons and fermions in the frame of the Minimal Supersymmetric Standard Model (MSSM). In this model, each elementary particle, through a spontaneous space-time symmetry breaking mechanism would have a *super partner* from the other family of particles, pairing bosons and fermions together. The model was first introduced as a way to solve the *Hierarchy Problem* [129]. The discrepancy between the strength of the weak force and gravity translates into a light Higgs boson compared to the *Planck Mass*. In the SM, the Higgs mass is left to be a measured parameter rather than a calculated one even though the model requires a mass in between 100 and 1000 $\mathrm{GeV/c^2}$ to stay unitary. Nevertheless, quantum corrections to the Higgs mass coming from its interactions with virtual particles should make the scalar boson much heavier than what measured [130]. Through the MSSM, the stability of fermion masses would provide stability to the Higgs boson mass via the introduction of a fermionic super partner.

On top of providing a solution to the Hierarchy Problem, the model comes with heavy dark matter candidates in the TeV scale [131]. Indeed, in the case *R-parity* is not violated, the lightest supersymmetric particle (LSP) cannot decay and could then explain the dark matter. The LSP in the model is neutral and can only interact through the weak and gravitational interactions. Typical candidates are the *neutralino*, the *sneutrino* or the *gravitino*.

Finally, gravity is not explained through the SM, and huge difficulties are encountered when trying to include it. The strength of gravitational interaction is expected to be negligible at the scale of elementary particles, nevertheless, adding gravitation in the perspective of developing a *"theory of everything"* leads to divergent integrals that could not be fixed through renormalization. Extensions to the MSSM, and in particular minimal SUper GRAvity (mSUGRA), include general relativity as mediator of the symmetry breaking. mSUGRA gives access to the hidden sector in which the MSSM only interacts gravitationally and suppresses the infinities arising from attempts to include gravity into the SM thanks to possible renormalization [132].

Signatures for the MSSM would come from the super partners of quarks and gluons that can decay into an LSP that could then be identified as missing energy as it escapes the detectors undetected. But even in the case MSSM predictions are not to be seen, the other models treating dark matter also propose Weakly Interacting Massive Particles (WIMPs) that could be observed in similar ways than LSPs [133]. Moreover alternative models exist to provide solutions to the Hierarchy Problem. The most investigated models are extra dimensions such as Arkani-Hamed Dimopoulos Dvali [134, 135], Kaluza–Klein [136, 137] or Randall-Sundrum models [138, 139] that usually also include gravitation. Finally, alternative models also exist for the production of dark matter candidates. Models with a hidden valley that would unravel the existence of a new group of light particles through the extension of the SM with a new confining gauge group [140].

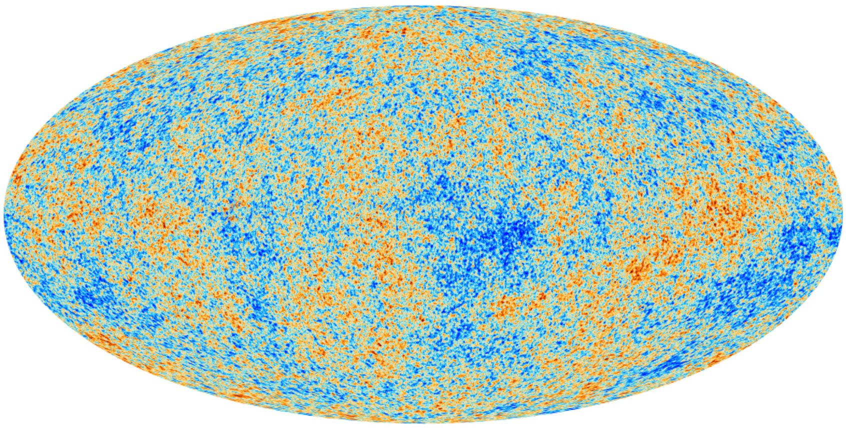

Figure 2.14: Cosmic Microwave Background as measured by the space observatory Planck which mean temperature is $T_\gamma = (2.7255 \pm 0.0006)$K *with anisotropies of the order of a few* μK.

Baryon asymmetry: Another intriguing fact is that the universe is dominated by matter. However, the SM predicted that matter and antimatter should have been created in equal amounts. For an interaction to produce matter and antimatter at different rates within the SM, three necessary conditions were highlighted by Sakharov[141]. First of all, there must be a violation of the baryon number B. Then, there must be a C-symmetry and CP-symmetry violation. The C-symmetry violation must happen to make sure that the processes creating more baryons than antibaryons are not compensated by processes creating more anti-baryons and similarly, the CP-symmetry violation makes sure that there are not equal numbers of left-handed baryons and right-handed anti-baryons produced. Finally, the interactions must happen out of thermal equilibrium to make sure that CPT-symmetry does not balance the processes increasing the baryon number with processes doing otherwise [142]. An out-of-equilibrium interaction implies a new instable heavy particle.

The favoured model to explain this imbalance is the *baryogenesis* that requires electroweak symmetry breaking to be first order phase transition to fall within the scope of SM [143, 144]. This means that the symmetry breaking process must involve the absorption or release of a fixed latent heat. Through the baryogenesis, the phase transition breaks P-symmetry spontaneously and allows for CP-symmetry violation. In turn, the CP violation makes the amplitude of interactions involving quarks different than the ones involving anti-quarks leading to the greater creation rate of baryons with respect to anti-baryons. The key to this baryon net creation would be found into the *sphaleron*. A sphaleron is a particle-like saddle point of the energy functional that appears at the top of the transition barrier and that could be created if a sufficiently large amount of energy is brought as the tunneling effect through the barrier is largely suppressed for electroweak interactions. The existence of the sphaleron would allow violation of the conservation of B but also of the leptonic number L while conserving $B - L$. The detection at $p-p$-colliders of such a transition is foreseen to be made through processes with high-multiplicity final states such as $u+u \rightarrow e^+\mu^+\tau^+\bar{t}\bar{t}\bar{b}\bar{c}\bar{c}\bar{s}\bar{d}+X$[145]. To be probed, the sphaleron transition requires an energy $E_{sph} \approx 9\,\mathrm{TeV}$. Nevertheless, if such transition cannot be observed, other BSM models such as the WIMP baryogenesis could be then observed thanks to the detection of displaced vertices, featuring the decay of a WIMP leading to violation of B [146].

Another possibility to explain the apparent asymmetry would be the existence of an electric dipole moment (EDM) in any fundamental particle that would permit matter and antimatter particles to decay at different rates [147]. Indeed, the presence of an EDM violates in itself both P and T symmetries. Experiments are able to probe for the EDM of various fundamental particles sich as the electron [147], the charm and strange quarks [148] or even a heavy neutrino EDM [149].

Neutrino mass and sterile neutrino scenario: The SM considers neutrinos to be massless. But it was showed in the late 1960s by the Homestake experiment that the flux of solar neutrinos (i.e. ν_e) measured didn't match the predicted values [150]. The mechanism of neutrino oscillations as a solution to the discrepancy was proposed by Pontecorvo [151] and confirmed in the early 2000s by the Sudbury Neutrino Observatory [152]. This oscillation implies that neutrinos that can be observed are a superposition of massive neutrino states. The research on neutrino oscillation is already quite advanced with experiments looking at atmospheric, reactor or beam neutrinos in order to determine the elements of the mixing matrix (Pontecorvo–Maki–Nakagawa–Sakata matrix [153]) similar to the Cabibbo–Kobayashi–Maskawa (CKM) matrix describing the mixing of quarks [72]. Nevertheless, no answer to the origin of neutrino mass is yet provided.

Explaining the light non-zero mass of the neutrinos ν_l ($l = e, \mu, tau$) of the order of the eV can be done through the Seesaw mechanism [154, 155]. This model features heavy Majorana counterparts N_l ($l = e, \mu, tau$) to the ν_l. The masses of the light and heavy neutrinos are linked through a 2×2 mass matrix A with eigenvalues $\lambda_\pm$ expressed as in Equation 2.10.

$$\begin{aligned} A &= \begin{pmatrix} 0 & M \\ M & B \end{pmatrix} \\ \lambda_\pm &= \frac{B \pm \sqrt{B^2+4M^2}}{2} \end{aligned} \tag{2.10}$$

The Majorana mass term B is assumed to be comparable to the Grand Unified Theory scale (10^{16} GeV) while the Dirac mass term M is of the order of electroweak scale (246 GeV). In these conditions, the eigenvalue λ_+ is almost B while λ_- is close to the ratio $-M^2/B$ compatible with very light neutrinos with masses of the order of 1 eV. Studying the left-right symmetric model seeking for the parity violation in weak interactions leads to the incorporation of three additional gauge bosons W_R and Z' as a result of the spontaneous symmetry breaking. The processes that are predicted by the model and can be probed at colliders are processes such as $pp \rightarrow W_R \rightarrow l + N_l + X$ and $pp \rightarrow Z' \rightarrow N_l + N_l + X$ where the heavy neutrinos decay as $N_l \rightarrow l + j_1 + j_2$, j_i being jets [156]. Other version of seesaw mechanisms exist to account for the neutrino mass that can also be explained thanks to supersymmetric models [157].

2.2 The Large Hadron Collider & the Compact Muon Solenoid

Throughout its history, CERN has played a leading role in high-energy physics. Large regional facilities such as CERN were planned after the second world war in an attempt to increase international scientific collaboration and to allow scientists to share the forever increasing costs of experimental facilities. Indeed, it is necessary to use always more powerful tools to improve the fine understanding of our Universe. The construction of the first CERN accelerators at the end of the 50s, the Synchrocyclotron (SC) and the Proton Synchrotron (PS), was directly followed by the first observation of antinuclei in 1965 [158]. The very first proton-proton collider showing hints of protons not being elementary particles was the Intersecting Storage Rings (ISR). From this experience, the Super Proton Synchrotron (SPS) was built in the 70s to investigate the structure of protons, the preference for matter over antimatter, the state of matter in the early universe or exotic particles, and led to the discovery in 1983 of the W and Z bosons [108–111]. These newly discovered particles and the electroweak interaction were then studied in detail by the Large Electron-Positron (LEP) collider that proved that there only are three generations of elementary particles in 1989 [159]. The LEP was then dismantled in 2000 to allow for the LHC to be constructed in the existing tunnel.

2.2.1 LHC, the most powerful particle accelerator

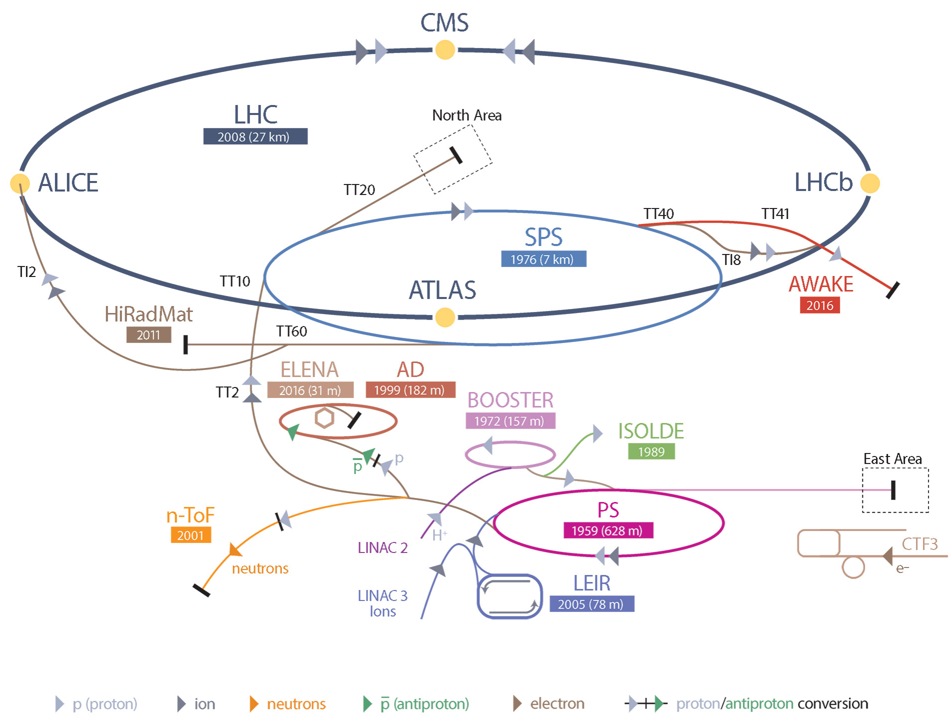

Figure 2.15: CERN accelerator complex.

The different aspects of physics beyond the Standard Model of particle physics and the Standard Model itself can be tested through the use of very energetic and intense hadron and ion colliders. Powerful hadron colliders are suited for searching for strongly interacting particles. The LHC at

CERN is a perfect tool to seek answers to these open questions and the experiments build along its beam lines already started investigating further into the SM and BSM physics.

The LHC has always been considered as an option for the future of CERN. At the moment of the construction of the LEP beneath the border between France and Switzerland, the tunnel was built in order to accommodate what would be a Large Hadron Collider with a dipole field of $10\,\mathrm{T}$ and a beam energy in between 8 and $9\,\mathrm{TeV}$ [160]. In 1985, the creation of a 'Working Group on the Scientific and Technological Future of CERN' took place to investigate such a collider [161]. The decision was finally taken almost ten years later, in 1994, to construct the LHC in the LEP tunnel [162] and the approval of the 4 main experiments that would take place at the four interaction points came in 1997 [163] and 1998 [164]:

- ALICE [165] has been designed for the purpose of studying the confinement of quarks through exploration of the quark-gluon plasma that is believed to have been a state of matter that existed in the very first moment of the universe.
- ATLAS [166] and CMS [167] are general purpose experiments that have been designed with the goal of continuing the exploration of the Standard Model and the investigation of new physics.
- LHCb [168] has been designed to investigate the preference of matter over antimatter in the universe through CP violation.

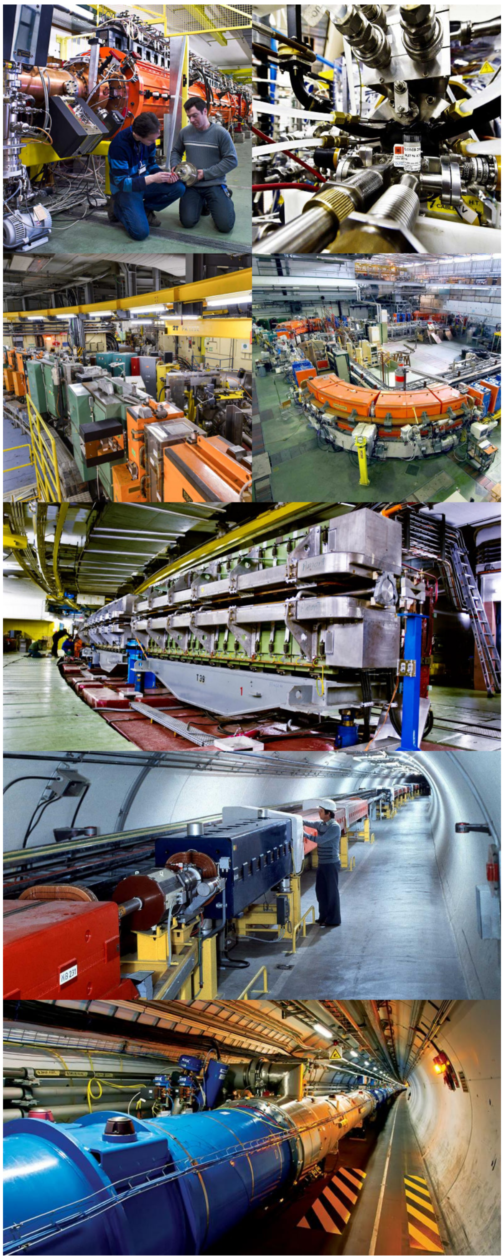

Figure 2.16: Pictures of the different accelerators. From top to bottom: first the LINAC 2 and the Pb source of LINAC 3. Then the Booster and the LEIR. Finally, the PS, the SPS and the LHC.

These large-scale experiments, as well as the full CERN accelerator complex, are displayed in Figure 2.15. The LHC is a $27\,\mathrm{km}$ long hadron collider and the most powerful accelerator used for particle physics since 2008 [169]. The LHC is designed to collide protons at a center-of-mass energy of $14\,\mathrm{TeV}$ and luminosity of 10^{34} $\mathrm{cm}^{-2}\mathrm{s}^{-1}$, as well as Pb ions at a center-of-mass energy of $2.8\,\mathrm{TeV/A}$ with a peak luminosity of 10^{27} $\mathrm{cm}^{-2}\mathrm{s}^{-1}$. The collider is the last of a long series of accelerating devices. Indeed, before being accelerated by the LHC, the particles need to pass through different acceleration stages. All these acceleration stages are visible on Figure 2.15 and pictures of the accelerators are shown in Figure 2.16.

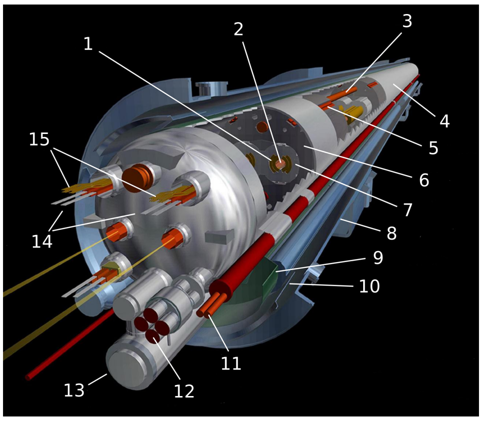

(a)

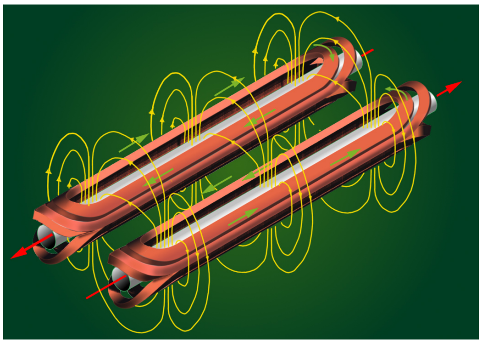

(b)

Figure 2.17: Figure 2.17a: schematics of the LHC cryodipoles. 1: Superconducting Coils, 2: Beam pipe, 3: Heat exchanger Pipe, 4: Helium-II Vessel, 5: Superconducting Bus-bar, 6: Iron Yoke, 7: Non-Magnetic Collars, 8: Vacuum Vessel, 9: Radiation Screen, 10: Thermal Shield, 11: Auxiliary Bus-bar Tube, 12: Instrumentation Feed Throughs, 13: Protection Diode, 14: Quadrupole Bus-bars, 15: Spool Piece Bus-bars. Figure 2.17b: magnetic field and resulting motion force applied on the beam particles.

The story of accelerated protons at CERN starts with a bottle of hydrogen gas injected into the source chamber of the linear particle accelerator *LINAC 2* in which a strong electric field strips the electron off the hydrogen molecules only to keep their nuclei, the protons. The cylindrical conductors then accelerate the protons to an energy of $50\,\mathrm{MeV}$. When exiting the LINAC 2, the protons are divided into four bunches and injected into the four superimposed synchrotron rings of the *Booster* where they are then accelerated to reach an energy of $1.4\,\mathrm{GeV}$ before being injected into the *PS*. The four proton bunches are hence sent as one to the PS where their energy eventually reaches $26\,\mathrm{GeV}$. The PS not only accelerates protons. It also accelerates heavy ions from the *Low Energy Ion Ring (LEIR)*. Lead is first injected into the dedicated linear collider *LINAC 3*, that accelerates the ions. Electrons are striped off the lead ions all along the acceleration process and eventually, only bare nuclei are injected in the LEIR whose goal is to transform the long ion pulses received into short dense bunches for LHC. Ions injected and stored in the PS were accelerated by the LEIR from $4.2\,\mathrm{MeV}$ to $72\,\mathrm{MeV}$. Directly following the PS, is finally the last acceleration stage before the LHC, the $7\,\mathrm{km}$ long *SPS*. The SPS accelerates the protons to $450\,\mathrm{GeV}$ and inject them in both LHC accelerator rings that will increase their energy up to $7\,\mathrm{TeV}$. When the LHC runs with heavy lead ions for ALICE and LHCb, ions are injected and accelerated to reach the energy of $2.8\,\mathrm{TeV/A}$.

The LHC beams are not continuous but are rather organised in bunches of particles. When in pp-collision mode, the beams are composed of 2808 bunches of 1.15×10^{11} protons separated by $25\,\mathrm{ns}$. When in Pb-collision mode, the 592 Pb bunches are on the contrary composed of 2.2×10^{8} ions separated by $100\,\mathrm{ns}$. The two parallel proton beams of the LHC are contained in a single twin-bore magnet due to the space restriction in the LEP tunnel. Indeed, building two completely separate accelerator rings next to each other was impossible. The dipoles of the 1232 twin-bore magnets are shown in Figure 2.17 alongside the magnetic field generated along the dipole section to accelerate the particles. The dipoles generate a nominal field of $8.33\,\mathrm{T}$, needed to give protons and lead nucleons their nominal energy. Some 392 quadrupoles, presented in Figure 2.18, are also used to focus to the beams, as well as other multipoles to correct smaller imperfections.

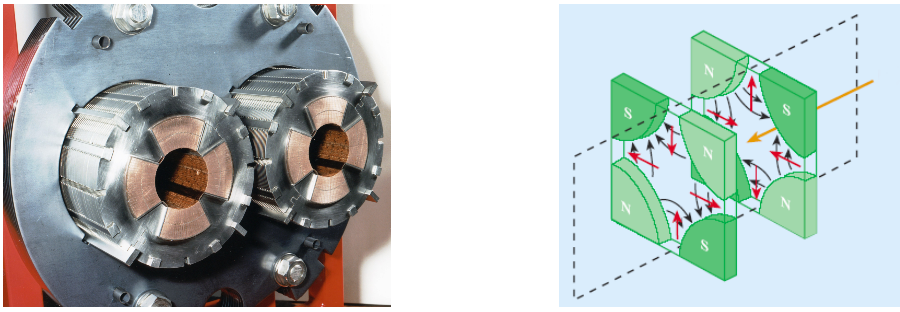

(a) *(b)*

Figure 2.18: The LHC quadrupoles (Figure 2.18a) showed together with the magnetic fields and resulting focussing force applied on the beam by two consecutive quadrupoles (Figure 2.18b).

2.2.2 Timeline of operation

LHC accelerated its first proton in September 2008 but the first collisions only started one year later in November 2009. At this moment the LHC machine officially became the world's most powerful particle accelerator and entered its Physics Run 1 that lasted until February 2013. During Run 1 of the LHC program, the center-of-mass energy was only half of the nominal LHC energy. Nevertheless, the energy and luminosity displayed during Run 1 were enough for both CMS and ATLAS to discover the Higgs boson [112, 113] as showed in Figure 2.19 and for LHCb to discover pentaquarks [170] and confirm the existence of tetraquarks [171]. During this period, ALICE also reported a successful observation of the quark-gluon plasma aimed at studying the early universe [172], ATLAS reported the observation of a new particle before the discovery of the Higgs [173] and a first test of super-symmetric models was performed [174].

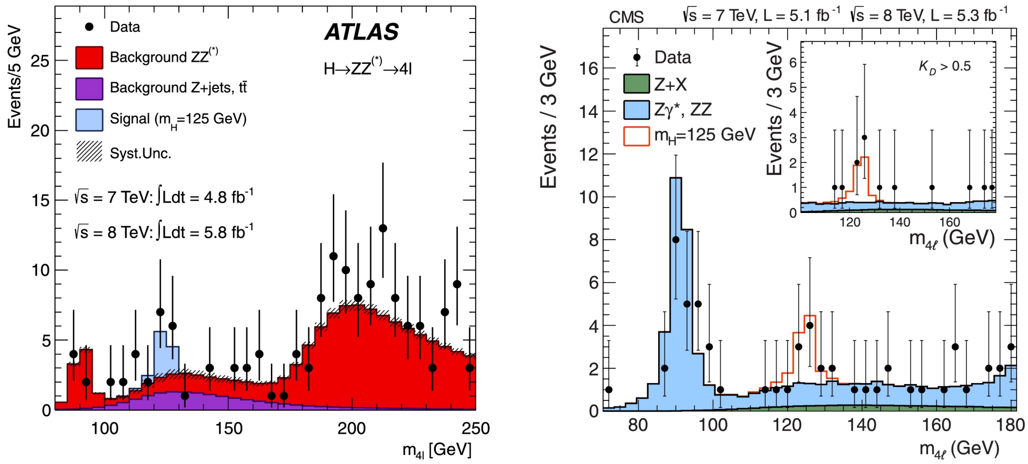

(a) *(b)*

Figure 2.19: Distribution of the four-lepton invariant mass for the $ZZ \to 4l$ analysis as presented by both ATLAS [112] and CMS [113] in 2012.

Run 1 was brought to an end with the start of the First Long Shutdown, an almost two years technical stop aimed at increasing the energy of the center-of-mass collisions to $\sqrt{s} = 13\,\text{TeV}$

as well as the instantaneous luminosity. This maintenance stop was also effectively used by the experiments which upgraded part of their detection systems. Run 2 then started in 2015 and lasted until end of 2018 where the activities ended with a last heavy ion run. During the operation, the instantaneous was successfully brought to a value of $1.7 \times 10^{34} \mathrm{cm}^{-2}\,\mathrm{s}^{-1}$exceeding the design value. Run 2 has been the occasion to acquire more data to study the properties of the Higgs boson with more precision. The boson discovered in the first physics run seems to be consistent with the SM Higgs boson [114].

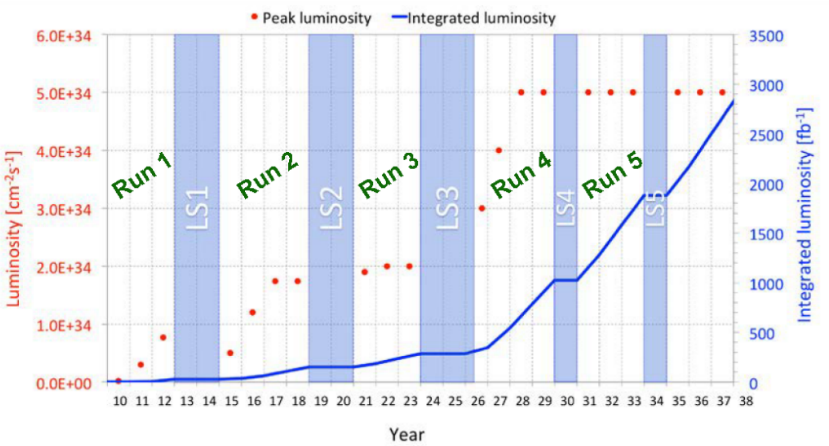

(a)

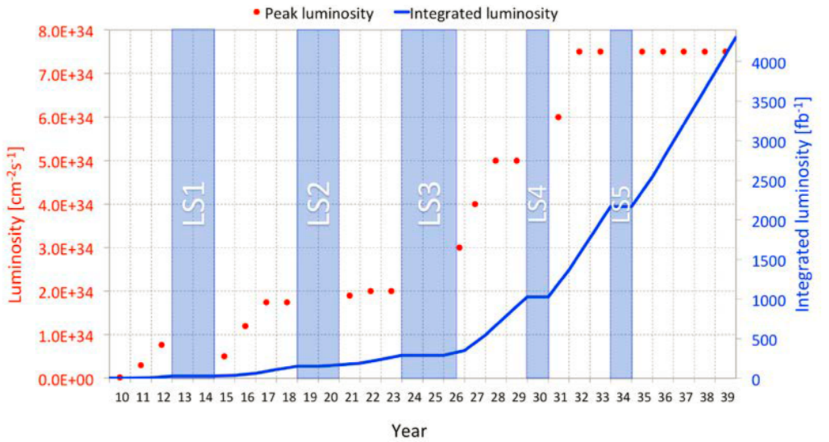

(b)

Figure 2.20: Detailed timeline projection of LHC and HL-LHC operation until 2039 showing the evolution of the instantaneous and integrated luminosity as designed (Figure 2.20a) and in the ultimate case where the instantaneous luminosity is increased to $7.5 \times 10^{34} \mathrm{cm}^{-2}\,\mathrm{s}^{-1}$thanks to a new increase of instantaneous luminosity during Run 5 (Figure 2.20b) [175–177].

From the end of 2018 to early 2021 the Second Long Shutdown will take place. This second maintenance stop will be the occasion to boost once again the beam energy to finally reach the design energy of LHC, $14\,\mathrm{TeV}$. On the side of the maintenance work, preliminary work for the High Luminosity LHC will be performed. The preparations will consist of detector, on the side of the experiments, and beam machine upgrades, on the side of LHC. In 2021, the physics program will be resumed with an instantaneous liminosity fixed at $2 \times 10^{34}\mathrm{cm}^{-2}\,\mathrm{s}^{-1}$. During these 3 years of run, the LHC will deliver as much integrated luminosity as what what brought during the almost 7 years of both Run 1 and 2 of data taking. Phase-1 will end with an overall $300\,\mathrm{fb}^{-1}$ delivered. The timeline so far described is summarized through the evolution of the instantaneous luminosity and of the corresponding integrated luminosity provided in Figure 2.20.

After the Third Long Shutdown (2024-2026) that will close the activities of Run 3, the accelerator will enter the HL-LHC configuration [175], increasing the instantaneous luminosity to an unprecedented level of $5 \times 10^{34}\mathrm{cm}^{-2}\,\mathrm{s}^{-1}$for pp-collisions ($4.5 \times 10^{27}\mathrm{cm}^{-2}\,\mathrm{s}^{-1}$for Pb-collisions), boosting the discovery potential of the LHC. The HL-LHC phase should last at least another 10 years depending on the breakthrough this machine would lead to. Already a new accelerating device, the FCC, as been proposed and is being investigated to prepare the future of high-energy physics after the LHC.

2.2.3 High Luminosity LHC

After approximately fifteen years of operation, the LHC will undergo a new series of upgrades during the LS3 in order to boost its discovery potential as previously discussed. The period after LS3 is what is referred to HL-LHC or Phase-2. The goal is to aim for a luminosity 5 to 7 times stronger than the nominal one trying to reach even 10 times this value if possible [175, 176]. Increasing the luminosity means that the beam size at the collision points needs to be reduced to boost the number of collisions per bunch crossing. For this purpose, new focusing and bending magnets and collimators will be installed at the collision points as well as newly developed *"crab cavities"* that will tilt the particle bunches just prior to the collisions by giving them transverse momentum and thus increasing their meeting area. In addition, the full proton injection line will be upgraded.

On the experiments side, the pile-up (PU) will be increased up to 150 to 200 interactions per bunch crossing in ATLAS and CMS, making necessary a strong upgrade of the trigger system and of the inner trackers and of the calorimeters. Both ATLAS and CMS will also need to upgrade the muon trigger at the level of their endcaps mainly focusing on the coverage near the beam line in order to increase the detection acceptance and event selection. Moreover, the increased luminosity will also lead to an increased background rate and a faster ageing of the detectors.

The end of 2018 marked the beginning of LS2 and the start of Phase-2 upgrade activities. From the HL-LHC period onwards, i.e. past LS3, the performance degradation due to integrated radiation as well as the average number of inelastic collisions per bunch crossing will rise substantially. This has become a major challenge for all of the LHC experiments, like CMS, that were forced to address an upgrade program for Phase-2 [177]. Dealing with the data from the muon detectors will force to upgrade the detectors and electronics towards the most recent technologies.

2.2.4 The Compact Muon Solenoid experiment

Among the four main LHC experiments is the Compact Muon Solenoid used as a multipurpose tool to investigate the SM and the physics beyond its scope. The CMS apparatus in itself is the heaviest detector ever built starring a $15\,\mathrm{m}$ diameter and a $29\,\mathrm{m}$ length for a total weight of $14\,\mathrm{kT}$. A thick $4\,\mathrm{T}$ solenoid magnet located at the beam interaction point hosts trackers and calorimeters. Extending in all directions around the magnet, heavy iron return yokes are installed to extend the magnetic field and support a muon system. The apparatus consists of a barrel, referring to the magnet and the detectors contained in it and the part of the muon system built directly in the cylinder around the magnet, and of two endcaps in the forward and backward region of the detector that closes the apparatus and complete the detection coverage along the beam line. A front view on the barrel is provided in Figure 2.21 while a detailed view of the apparatus is given in Figure 2.22.

In order to efficiently detect all long living particles and measure their properties with good precision, the CMS detector uses an onion like layout around of the interaction point in order to maximize the covered solid angle. As detailed in Figure 2.23, in the innermost region of the detector, closest to the interaction point, the silicon tracker records the trajectory of charged particles. Around it, the electromagnetic calorimeter (ECAL) stops and measures the energy deposition of electrons and photons. In the next layer, the hadron calorimeter (HCAL), hadrons are stopped are their energy measured. These layers are contained inside of the magnet of CMS, the superconducting solenoid. Outside of the magnet are the muon chambers embedded into iron return yokes used to control the magnetic field and gives muons, the only particles traveling completely through the whole detector, a double bending helping in reconstructing their energy and trajectory. Note that photons and neutral hadrons are differentiated from electrons and charged hadrons in the calorimeters by the fact that they don't interact with the silicon tracker and are not influenced by the magnetic field, as can be seen ni Figure 2.23.

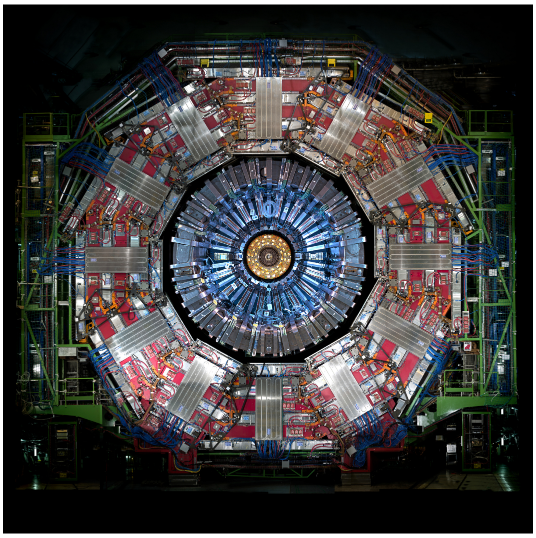

Figure 2.21: Picture of the CMS barrel. The red outer layer is the muon system hosted into the red iron return yokes. The calorimeters are the blue cylinder inside in magnet solenoid and the tracker is the inner yellow cylinder built around the beam pipe.

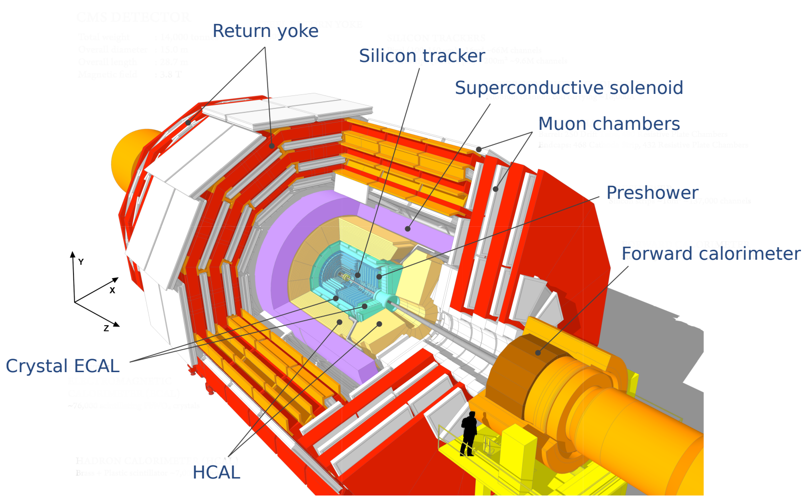

Figure 2.22: View of the CMS apparatus and of its different components.

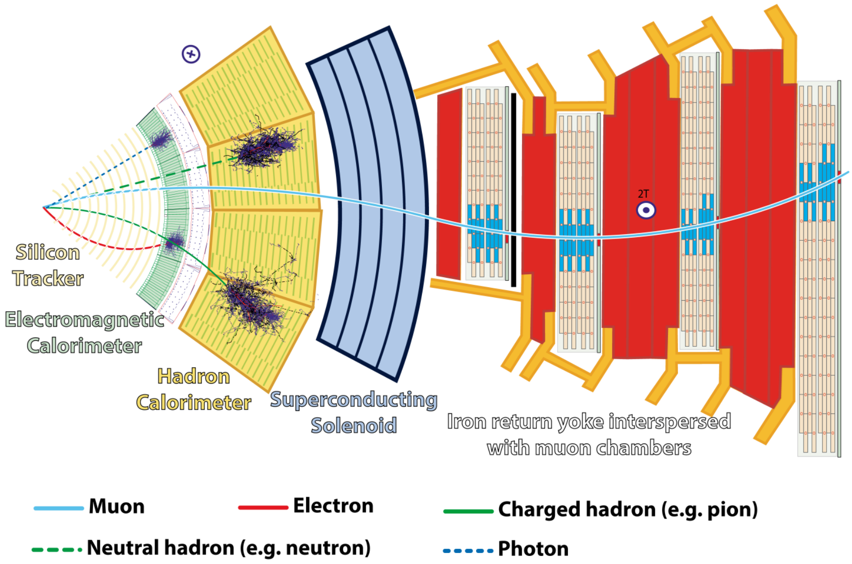

Figure 2.23: Slice showing CMS sub-detectors and how particles interact with them.

2.2.4.1 The silicon tracker

The silicon tracker visible in Figure 2.24 is divided into two different sub-systems: the *pixel detector* at the very core and the *microstrip detector* around it. This system is composed of 75 million individual read-out channels with up to 6000 channels per squared centimeter for the pixels making it the world's biggest silicon detector. This density allows for measurements of the particle tracks with a precision of the order of $10\,\mu\mathrm{m}$. This is necessary to reconstruct all the different interaction vertices with precision and have a precise measure of the curvature of the charged particles traveling through the magnetic field to estimate their charge and momentum.

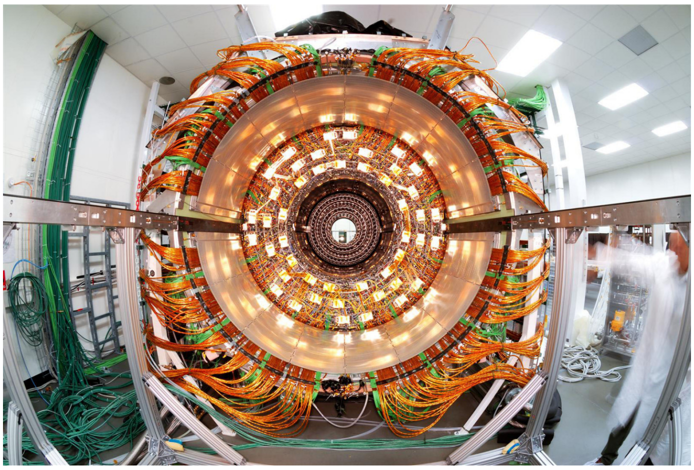

Figure 2.24: The CMS tracker.

2.2.4.2 The calorimeters

The ECAL directly surrounding the tracker is composed of crystals of lead tungstate, $PbWO_4$, a very dense but optically transparent material used to stop high-energy electrons and photons. These crystal blocks basically are extremely dense scintillators which scintillate in fast, short light bursts proportionally to the energy deposition. The light is contained at 80% in the corresponding $25\,\mathrm{ns}$

lasting bunch crossing. Each crystal is isolated from the other by the carbon fiber matrix they are embedded in.

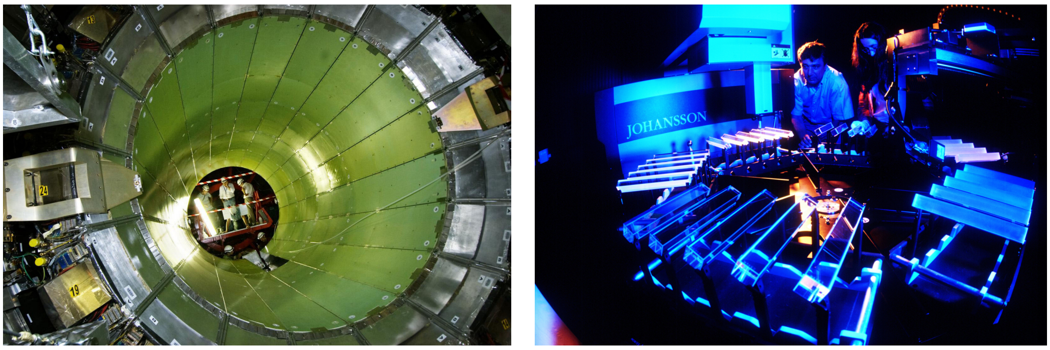

(a) *(b)*

Figure 2.25: Figure 2.25a: The electromagnetic calorimeter. Figure 2.25b: The lead tungstate crystals composing the ECAL.

The ECAL is composed of a barrel containing more than 60,000 crystals and of closing endcaps containing another 15,000 crystals. In front of the ECAL endcap is installed a preshower detector made out of two layers of lead and silicon strip detectors to increase the spatial resolution close to the beam line for pion-photon and single-double photon discrimination purposes. Figure 2.25 shows the calorimeter inside of the magnet and the crystals.

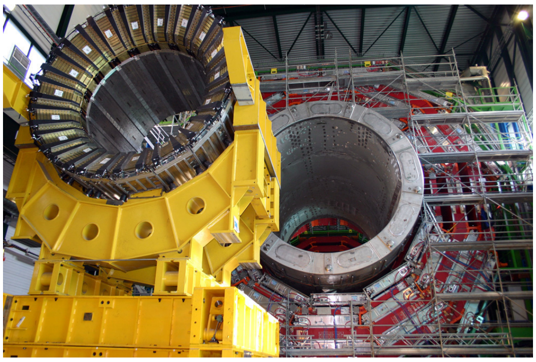

Figure 2.26: The CMS hadron calorimeter barrel.

The next layer is the HCAL. The role of these forward calorimeters, made using steel and quartz fibers, is to precisely measure the momentum very energetic hadrons. Several layers of brass or steel are interleaved with plastic scintillators readout by photodiodes using wavelength-shifting fibers. The HCAL is also composed of a barrel, shown in Figure 2.26 and of endcaps. It also features forward calorimeters on both sides of CMS in the region very close to the beam line at high pseudorapidity ($3.0 < |\eta| < 5.0$).

2.2.4.3 The muon system

Finally, in the outer region of the apparatus, a muon system is used to trigger on potentially interesting event by identifying muons. Three different subsystems compose the muon system as shown in Figure 2.27 in which a quadrant of the CMS detector focuses on muon system. Drift Tubes (DTs) are found in the barrel region covering the low pseudorapidity region where particles transverse momentum is lower and Cathode Strip Chambers (CSCs) are found in the endcap region covering higher pseudorapidity region closer to beam line where particles have a stronger momentum. The redundancy of the system is insured by Resistive Plate Chambers (RPCs) in both the barrel and endcap. Nevertheless, the region closest to the beam line ($|\eta| > 1.8$) was not equipped with RPCs. This lack of redundancy in the high pseudo rapidity region will be solved during LS2, the following Year End Technical Stop (YETS) in 2021 and 2022, and LS3 where the necessary services, detectors and Link System, that collects the data and synchronizes them, will be installed.

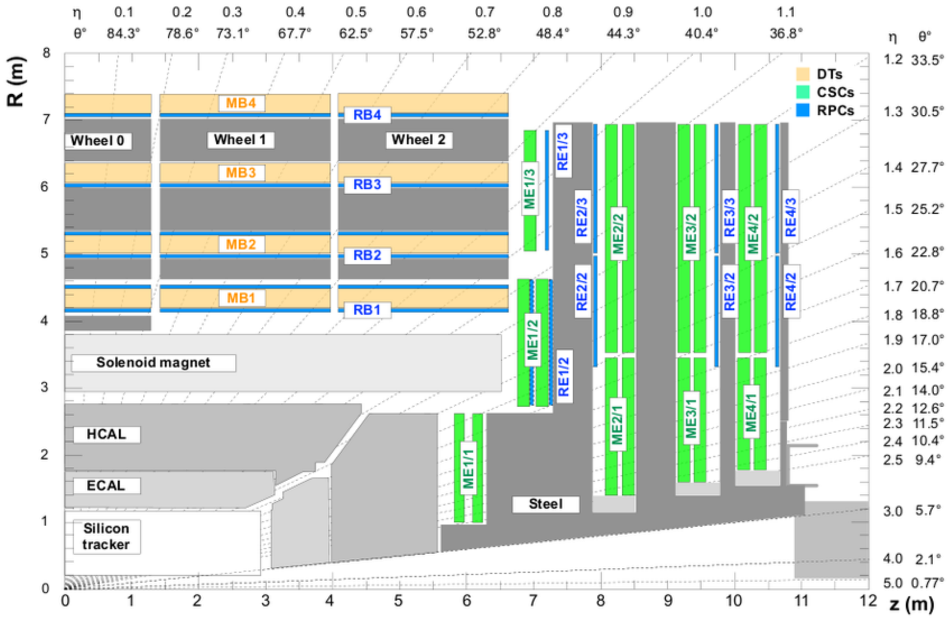

Figure 2.27: A quadrant of the muon system, showing DTs (yellow), RPCs (blue), and CSCs (green).

3

Muon Phase-2 Upgrade

In the previous chapter, the timeline of the LHC has been described and the upcoming High Luminosity LHC was introduced. LS3 has now started and the first HL-LHC related upgrade of CMS will take place. In order to understand the context in which the work of this thesis was performed as well as its motivations, it is necessary to give more insight into the reasons behind the increased instantaneous luminosity of LHC. In a first section of the chapter, these motivations will be discussed.

The muon system of CMS will then be presented in greater details than what was done in the previous chapter in order to have a better understanding of the need for upgrades of its different subsystems in the perspective of HL-LHC. Most of the detectors will require new electronics to adapt to the new data flow and be integrated into a more robust trigger. Moreover, the redundancy of the muon system in the endcaps will need to be improved. This will be achieved by the addition of new detectors.

Finally, some insight will be given on ecofriendly gas studies for the specific case of Resistive Plate Chambers. These studies don't fall into the scope of the HL-LHC upgrades but the necessity of operating the detectors with gas mixtures that are more respectful of the environment is real. The European union is starting to press the scientific community for solutions and the research institutes are investing time into finding replacements to the gases used while maintaining similar working performances.

3.1 Motivations for HL-LHC and the upgrade of CMS

As detailed in Section 2.2.2, the first data taking period, during which the LHC was only operated at a center-of-mass energy of $7\,\mathrm{TeV}$, took place until the start of LS1. It has been sufficient to claim the discovery of a new $125\,\mathrm{GeV/c^2}$ particle compatible with the Higgs boson by both CMS and ATLAS in July 2012 and hence achieve a major milestone in the history of science towards the understanding of the fundamental nature of the universe. Nevertheless, the LHC machine holds the potential to go further and help unravel the remaining mysteries the High-Energy Physics (HEP) community is facing.

Over its full lifetime, the HL-LHC is expected to deliver an outstanding integrated luminosity of $3000\,\mathrm{fb}^{-1}$, nearly an order of magnitude higher than what will be delivered by LHC until LS3 starts, as shown in Figure 2.20. In the case of Higgs studies, this will lead to measuring the couplings of the boson to a precision of 2 to 5%. Thanks to the estimated 15 millions of Higgs bosons created every year, a more precise measurement of potential deviations from the theoretical predictions is expected. The properties of the boson will hence be tested and compared to the SM Higgs neutral boson. SUSY and heavy gauge boson studies would also see their mass range limits pushed away by at least $1\,\mathrm{TeV}$ and could lead to a new breakthrough. Many of the Standard Model extensions discussed in Section 2.1.3 yield Heavy Stable Charged Particles (HSCPs), i.e. heavy long-lived particles. These particles would be produced at the LHC with a high momentum but a velocity significantly lower than the speed of light ($\beta < 0.9$) [178–182] and/or a charge that differs from the elementary charge ($|Q| = e$, $|Q| < e$ or $|Q| > e$) [181–186]. Depending on the model considered, HSCPs could be lepton-like heavy particles or on the contrary R-hadron, i.e. particles composed of a supersymmetric particle and at least one quark [181].

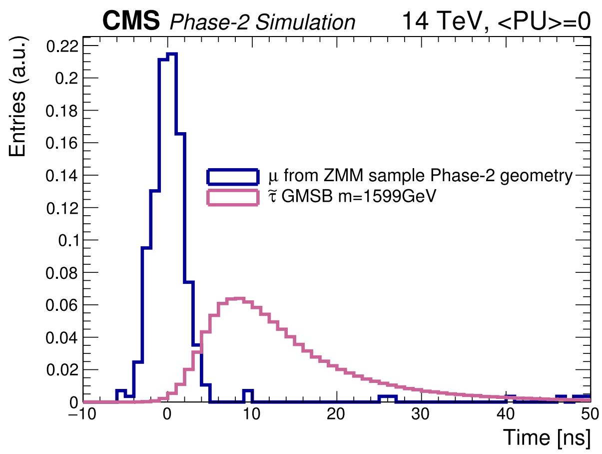

Figure 3.1: The measured transit time of an HSCP in CMS is compared to the transit time of a particle traveling at near the speed of light [177].

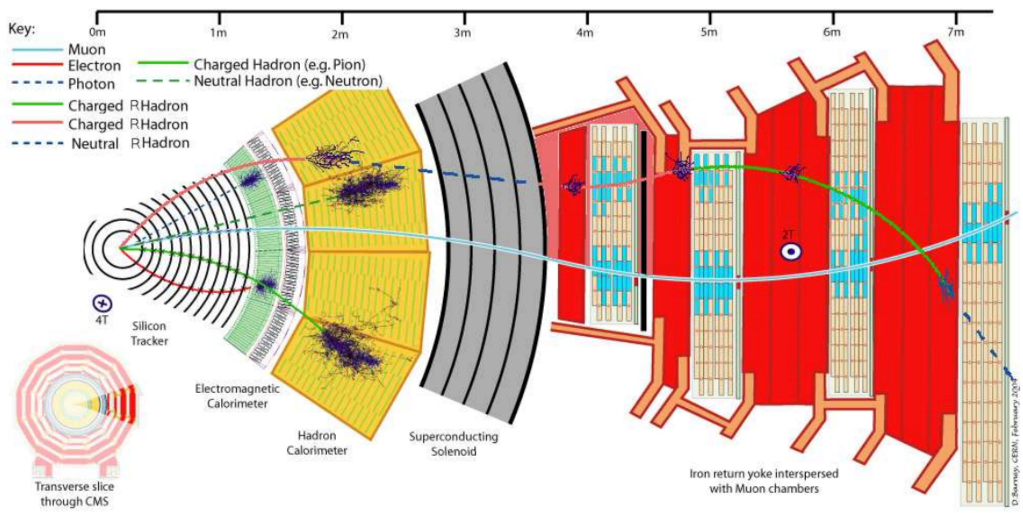

Figure 3.2: Slice of the CMS detector showing examples of passage of SM particles and R-hadrons. On the one hand, lepton-like HSCPs will appear to behave like slow and heavy muons. On the other hand, R-hadrons are likely to convert into other kind of charged or neutral R-hadrons due to interactions inside the detector volume.

Due to lifetimes of the order of a few ns, HSCPs would travel for long enough distances to cross through entire typical collider detectors while appearing almost stable. Because of their low velocity, they can be reconstructed and assigned to bunch crossings different to the ones they effectively have been produced, as shown in Figure 3.1, if reconstructed at all. Indeed, the trigger algorithms in use at CMS were not designed for such slow particles, and they assume most particles of interest will have a velocity close to the speed of light [182, 187].

As HSCPs are long-lived particles, their identification would be possible thanks to the muon system. The main background will consist of wrongly measured muons which should have a lower transverse momentum, a near to speed-of-light velocity and a low ionisation energy loss. An example of passage of HSCPs through a slice of the CMS detector is showed in Figure 3.2. The tracks associated to the HSCPs would then have to be reconstructed in both the silicon detectors, for precise dE/dx measurement, and the muon system detectors. In this case, the muon system will be used to perform Time-of-flight (ToF) measurements to discriminate between near spead-of-light particles and slower ones. The full reconstruction will then look for useful signatures such as the large transverse momentum of the candidates, or their large ionisation energy loss alongside the low velocity accurately measured thanks to the muon system as depicted in Figure 3.3. The ToF measurement to identify beyond the Standard Model particles will mostly rely on the time information provided by the Drift Tubes, in the barrel region of the detector, and Cathode Strip Chambers, in the endcaps. From CMS point of view, it will then become necessary to increase the acceptance and redundancy of the endcaps toward higher pseudo-rapiditiy as the pseudo-rapidity region $1.6 < |\eta| < 2.5$ is only covered by CSCs.

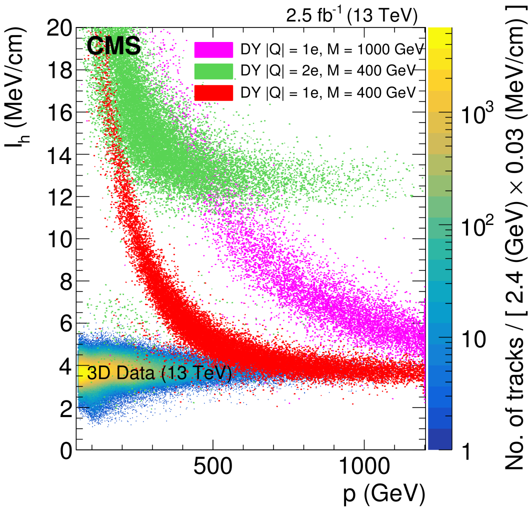

Figure 3.3: Distribution of the energy-loss dE/dx as described by Bethe-Bloch formula through the estimator I_h with increasing particle momentum for tracks in the $13\,\mathrm{TeV}$ *data. The estimator depends on the charge deposition of the particles per unit length in the silicon detectors of CMS which is related to their energy loss as explained in a publication by the CMS Collaboration [181]. The simulated HSCPs are singly or multiply charged particles with masses of 400 and* $1000\,\mathrm{GeV}$.

A natural consequence of the higher instantaneous luminosity will be the increase of collisions per bunch crossing. It is estimated that the pile-up will rise from the approximate average of 40 collisions per bunch crossing in 2017 and 2018, presented in Figure 3.4, to 140 to 200 depending on the scenario considered [188]. The trigger rate will then be affected in the same way putting a lot of stress on the trigger algorithms. Upgrading the electronics of some of the detectors and working on the data flow within the experiment would help going through HL-LHC with keeping similar performance than during Phase-1. On the other hand, the impact of the increased background will become problematic in many ways and will force for upgrades or many sub-systems of CMS. The main effects will be a large increase of the irradiation of the detectors, mainly close to the beam line. Both the detectors already installed and the new detectors that will extend the coverage of the muon system toward higher pseudo-rapidity need to be certified for the irradiation levels they will be subjected to until the end of HL-LHC. Simulations of the expected distribution of absorbed dose in the CMS detector under HL-LHC conditions show, in Figure 3.5, that detectors placed close to the beam line will have to withstand high irradiation, the radiation dose being of the order of a few tens of Gy.

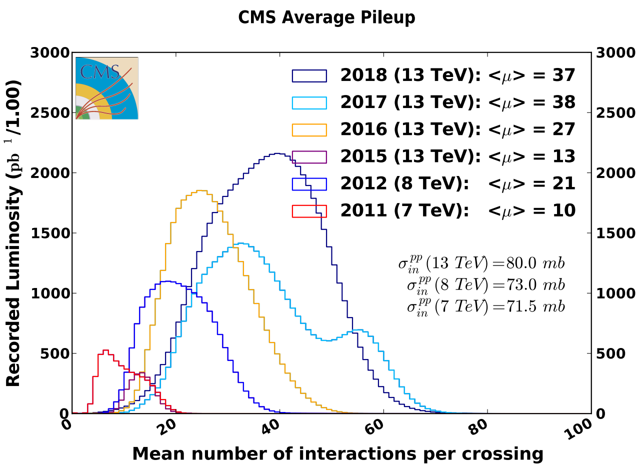

Figure 3.4: Distribution of the average number of interactions per crossing (pileup) for pp-collisions in 2011 (red), 2012 (blue), 2015 (purple), 2016 (orange), 2017 (light blue), and 2018 (navy blue). The overall mean values and the minimum bias cross sections are also shown [189].

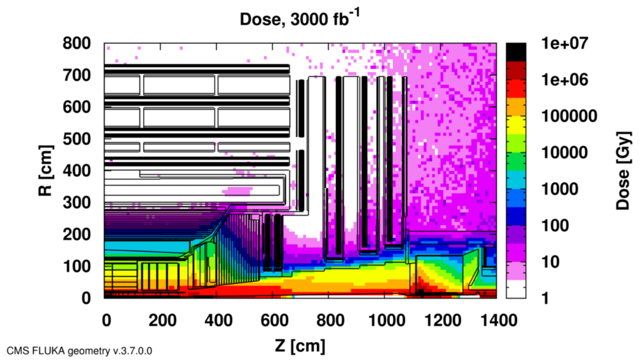

Figure 3.5: Absorbed dose in the CMS Cavern after an integrated luminosity of $3000\,\mathrm{fb}^{-1}$*. Using the interaction point as reference, R is the transverse distance from the beamline and Z is the distance along the beamline [177].*

Improving this situation will come with the increase of hit numbers recorded along the particle track to reduce the ambiguity on muon versus background detection. Moreover, the measurement of small production cross-section and/or decay branching ratio processes, such as the Higgs boson coupling to charge leptons, and in particular to muons, or the $B_s \to \mu^+\mu^-$ decay, is of major interest. Such considerations give more weight to the upgrade of the forward regions to maximize the physics acceptance to the largest possible solid angle.

To ensure proper trigger performance within the present coverage, the muon system will be completed with new chambers, and the electronics of the present system will need to be upgraded. A first step into this direction will be taken by installing new gaseous detectors in each endcap layer and extend the coverage up to $|\eta| = 2.8$. Nevertheless, the region beyond $|\eta| > 2.8$ and extending to $|\eta| = 5.0$ only is covered by the forward HCAL detectors and lack redundant muon detector coverage. Extensions of the tracker in the context of HL-LHC will increase its coverage up to $|\eta| = 4.0$ but the identification of muons and measurement of their energy with reasonable precision only using the tracker is nearly impossible. Thus, this increased tracker coverage range needs to be put in parallel with a matching muon detector and will open doors to multi-lepton final states in which leptons are likely to have a low transverse momentum and to be found near the beam line.

Finally, as the muon system is composed only of gaseous detectors, strong environmental concerns have risen over the last years as the European directives will restrict the use of fluorine based gas mixtures. Both the CSC and RPC subsystems, using CF_4, $C_2H_2F_4$, or SF_6, will need to adapt their working gas in order to strongly reduce the greenhouse potential of the mixtures released into the atmosphere due to gas leaks.

3.2 Desciption of the muon system

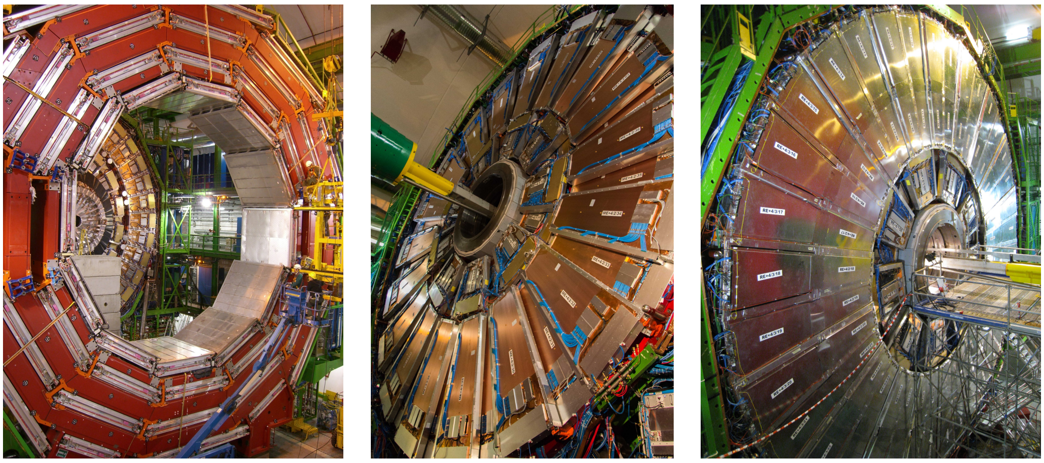

(a) *(b)* *(c)*

Figure 3.6: Figure 3.6a: Barrel wheel with its detector rings and return yokes. Figure 3.6b: CSC endcap disk with the two CSC stations. The outer station is made of $10\,\mathrm{deg}$ *detectors while the inner station is made of* $20\,\mathrm{deg}$ *detectors. Figure 3.6c: RPC endcap disk. The inner station is not equipped, leaving the inner CSC station visible.*

The barrel region is divided into five *wheels* made out of four *rings* of detectors with iron return yokes in between them whereas the endcaps are made out of four disks, each divided into pseudorapidity stations, two for CSCs (except for the first disk where three stations are equipped) and three for RPCs, although only two RPCs stations are equipped at present. The wheels and disks are shown in Figure 3.6. So far, each subsystem was dedicated to a particular task. DTs, in the barrel, and CSCs, in the endcaps, are used mainly for their spatial resolution. Indeed, DTs' resolution is of the order of $100\,\mu\mathrm{m}$ along both the $(r-\phi)$ and $(r-z)$ components while the resolution of CSCs is similar but varies in a range from $50\,\mu\mathrm{m}$ to $140\,\mu\mathrm{m}$ depending on the distance to the beamline. On the other hand, RPCs are used as redundant detection system in the whole muon system. They display a very good intrinsic time resolution of $1.5\,\mathrm{ns}$ although the electronics only provide bunch crossing information with a time resolution of $25\,\mathrm{ns}$.

3.2.1 The Drift Tubes

The 250 CMS DTs, found in the barrel covering the pseudorapidity region $0 < |\eta| < 1.2$ and whose structure is shown in Figure 3.7, are composed of three *superlayers* of DT cells. Two of these superlayers are dedicated to measuring the ϕ coordinate of the muons and while the last one measures the η (or z) coordinate. Each superlayer consists on four layers of 60 to 70 DT cells arranged in quincunx to allow for a precise reconstruction of the muon path through the DT layers.

Each DT cell is a rectangular aluminium gas volume with a central anode wire. Cathode strips are placed on the narrow surface of the cells and electrode strips are placed on the wide surface to help shaping the electric field to ensure a consistent drift velocity of electrons in the drift volume. These detectors are operated using a 85/15 mixture of Ar and CO_2. Outside the gas volume of each DT chamber is attached a Minicrate electronics (MiC) that hosts both read-out and trigger electronics.

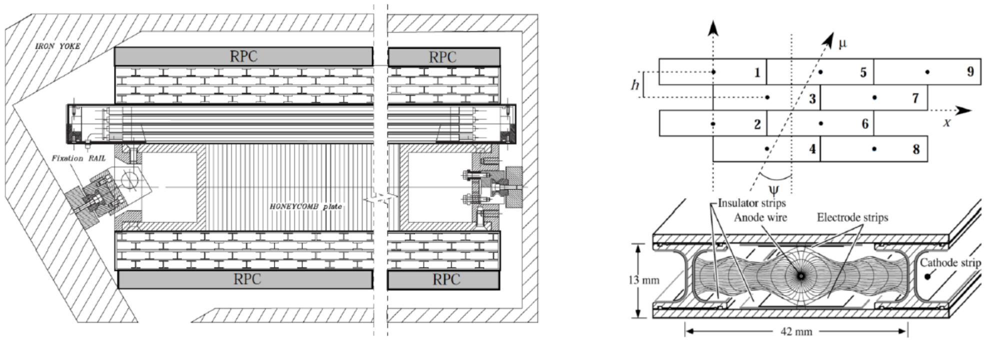

(a) *(b)*

Figure 3.7: Figure 3.7a: Cross section of a DT module showing the two superlayers measuring the ϕ coordinate, perpendicular to the cross section plane, and the superlayer measuring the η coordinate, placed in between the two others with a honeycomb plate and parallel to the cross section plane. The DT detector is sandwiched in between 2 RPCs whose readout strips are perpendicular to the cross section plane, measuring the ϕ coordinate. Figure 3.7b: A DT cell is shown together with its electric field. The path of a muon through a superlayer is shown.

3.2.2 The Cathode Strip Chambers

The 540 CMS CSCs are found in the endcaps covering the pseudorapidity region $0.9 < |\eta| < 2.5$ and described through Figures 3.8 and 3.9. Each module is composed of six panels of CSC, each panel consisting in a wide gas volume of $9.5\,\mathrm{mm}$ ($7\,\mathrm{mm}$ in the case of ME1/1 station) containing anode wires and whose surfaces are cathodes. The top cathode is a wide copper plane of the size of the gas volume. The bottom cathode is divided into thin trapezoidal copper strips radially arranged to measure the azimuthal coordinate ϕ with a pitch ranging from 8 to $16\,\mathrm{mm}$. The $0.50\,\mathrm{\mu m}$ anode wires are placed perpendicularly to the strips to measure radial coordinate r and are grouped by ten to fifteen with a wire to wire space of $3.2\,\mathrm{mm}$. In he specific case of ME1/1 placed against the HCAL endcap, the $0.30\,\mathrm{\mu m}$ anode wires have a wire to wire distance of $2.5\,\mathrm{mm}$ and are not disposed perpendicularly to the strips but slightly tilted by an angle of $29\,\mathrm{deg}$ to compensate for the lorentz force due to the very strong local magnetic field of $4\,\mathrm{T}$. These detectors are operated with a 40/50/10 mixture of Ar, CO_2 and CF_4. Combining the information of the multiple CSC panels, the detectors achieve a very precise measurement of the muon track. The read-out of the cathode strip signals is performed by cathode front-end boards (CFEBs) mounted on the detectors. The boards are used to collect and digitize the charge of the signals and transfer it to off-chamber electronics called Data acquisition mother boards (DMBs). In parallel, the data from the CFEBs together with the data from the anode wires, after treatment by on-chamber electronics called Anode local charged track boards (ALCTs), is used to build a fast trigger information which is sent other off-chamber electronics called Trigger mother boards (TMBs).

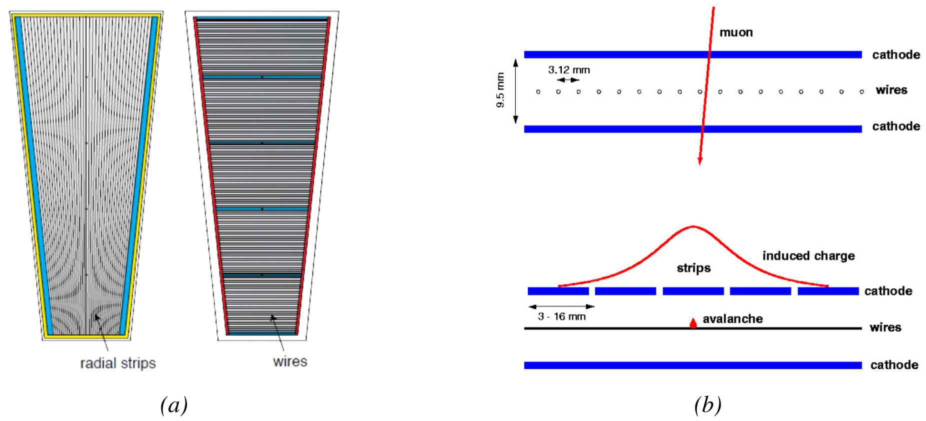

Figure 3.8: Figure 3.8a: Cathode strips and anode wire layout of a CSC panel. Figure 3.8b: Avalanche development and charge collection by anode wires and induction on cathode strips inside of a CSC panel.

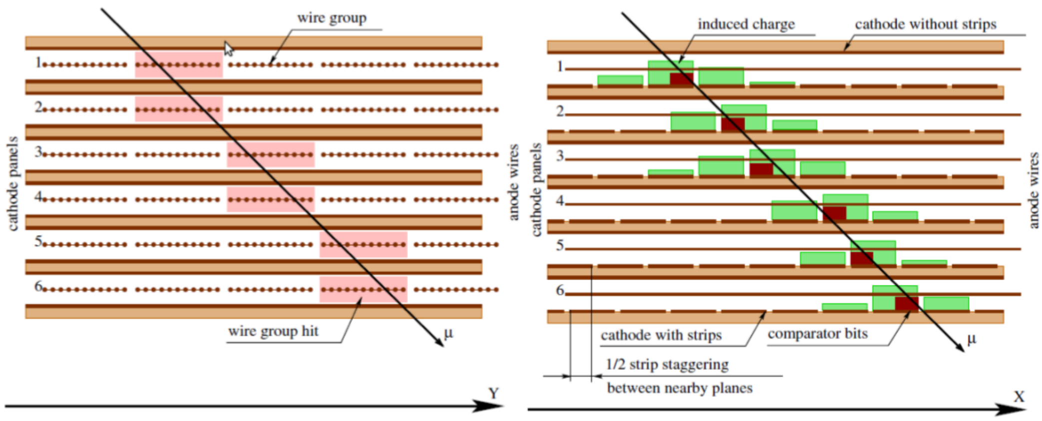

Figure 3.9: Muon track reconstruction through the six panels of a CMS CSC using the information of anode wire groups and cathode strip charge distribution combined with comparator bits to decide on which half strip the muon is more likely to have passed.

3.2.3 The Resistive Plate Chambers

Despite their excellent spatial resolution, the wire chambers (DTs and CSCs) are limited in terms of time resolution by the fact that the charge needs to drift towards the anode wire and be collected before having the confirmation that a particle was detected as the drift volume is not used to develop avalanches. Indeed, the stronger electric field close to the anode wire triggers the avalanche and the gain of the detector. Due to the drift, the time resolution is thus limited at best to approximately 2 to 3 ns. In addition, even though the intrinsic time resolution of the tracking chambers is rather good compared to the 25 ns in between successive collisions, the processing time of the trigger system doesn't allow for very fast triggering as it provides a time precision of only 12.5 ns. Thus, detectors fully dedicated to timing measurement have been installed as a redundant system. These detectors are RPCs, also gaseous detectors but that use current induction instead of charge collection allowing for a time resolution of the order of 1 ns only. Theoretically, depending on the design used, RPCs could reach a time resolution of the order of 10 ps but in the context of LHC where bunch crossing happen every 25 ns, a time resolution of 1 ns is sufficient to accurately assign the right bunch crossing to each detected muon.

The 1056 RPCs equip the CMS muon system both in the barrel and endcap regions and cover the pseudorapidity region $0 < |\eta| < 1.6$. They are composed of two layers of RPC *gaps* as described in Figure 3.10. Each gap consists in two resistive electrodes made out of 2 mm thick Bakelite enclosing a 2 mm thick gas volume containing a 95.2/4.5/0.3 mixture of $C_2H_2F_4$, $i - C_4H10$ and SF_6. Due to this geometry, the electric field inside of a gap is homogeneous and linear at every point in the gas translating into a uniform development of avalanches in the gas volume as soon as a passing muon ionises the gas. The two gaps sandwich a readout copper strip plane. A negative voltage is applied on the outer electrodes, used as cathodes, and the inner electrodes, the anodes, are simply connected to the ground as well as the readout panel that picks up the current induced by the accumulated charge of the growing avalanches in one or both of the gas gaps. This OR system allows for a lower gain (i.e. a lower electric field) on both gaps to reach the maximal efficiency of such a detector.

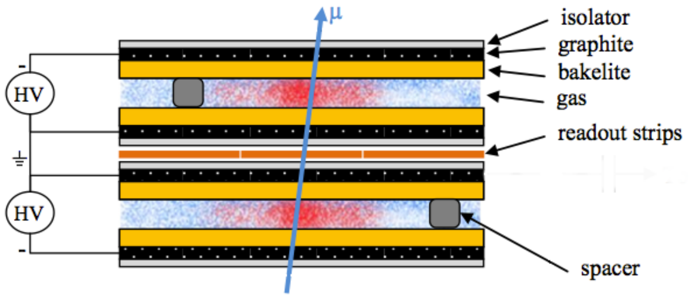

Figure 3.10: Double-gap layout of CMS RPCs. Muons passing through the gas volumes will create electron-ions pairs by ionising the gas. This ionisation will immediately translate into a developing avalanche.

3.3 Necessity for improved electronics

Drift Tubes and Cathode Strip Chambers are important components used to identify and measure muons, especially thanks to their spatial resolution of the order of 100 µm. Nevertheless, the luminosity and irradiation during HL-LHC will cause serious event loss and ageing on the electronics of these subsystems that will comprise the triggering and data transferring needs of CMS. Thus, electronics upgrade is foreseen to address these expected problems. While only the RPCs' electronic system is able to operate under Phase-2 requirements [190], DTs and CSCs will need to improve their trigger acceptance rate and latency to ensure that the Level-1 trigger thresh-

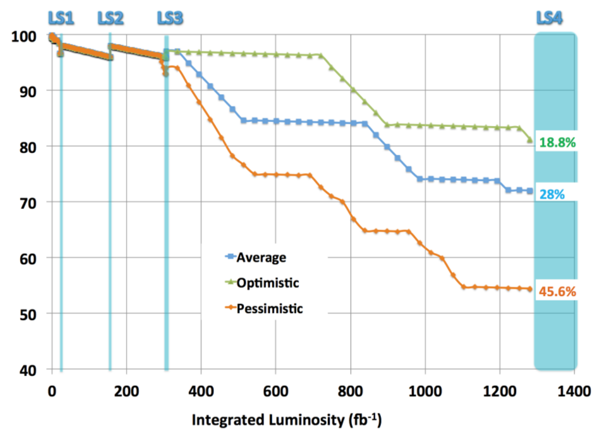

Figure 3.11: Extrapolated fraction of failing channels of the present DT MiC1 electronics as a function of the integrated luminosity for different scenarios until LS4 [177].

old can stay at the same level [191]. The Level-1 trigger consists of custom hardware processors receiving data from the calorimeters and the muon system. In return, they generate a trigger signal within $3\,\mu s$, with a maximum rate of $100\,\mathrm{kHz}$. In the perspective of HL-LHC, each subsystem needs to achieve a minimum rate of $500\,\mathrm{kHz}$ with a latency not greater than $12.5\,\mu\mathrm{s}$. DTs and CSCs will also need to improve their Data Acquisition (DAQ) transfer rate to reach a minimum near $1\,\mathrm{Tbit/s}$. The foreseen upgrades are expected to exceed the requirements.

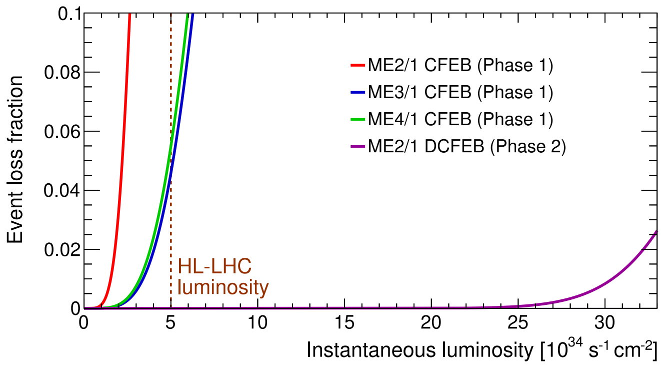

Figure 3.12: The event loss fractions as a function of the instantaneous luminosity is compared for CFEBs (Phase-1) and DCFEBs (Phase-2) at different CSC locations. HL-LHC luminosity is marked with the dashed brown line [177].

The first version of Minicrate electronics (MiC1) used by DTs don't allow for high enough trigger rate. In addition to this problem, it was shown that these electronics contain components that are not radiation hard enough to sustain HL-LHC conditions and hence, a too large number of channels may fail due to radiations as showed in Figure 3.11. The MiC1 will be replaced on each detector by an improved version referred to as MiC2 while Front-End Electronics (FEE) and High Voltage (HV) modules will not need any replacement. On the other hand, CSCs showed that their electronics would be able to live through the 10 years of Phase-2, but the limited buffer depth might cause memory overflows and read-out inefficiencies with a fraction of event loss ranging from 5 to more than 10% at an instantaneous luminosity similar to which of HL-LHC depending on the expected background. The replacement of CSCs' CFEBs by digital ones, DCFEBs, with a deeper buffer would permit to make event loss negligible and satisfy HL-LHC requirements as can be seen in Figure 3.12. All these new DT and CSC electronics will be connected to the trigger electronics via optical links to ensure a faster communication [177].

The upgrade on the side of Resistive Plate Chambers will not be done at the level of the electronics but rather that of the Link System located in the service cavern of CMS. RPC Link System connects the front-end electronics data of RPCs into CMS trigger processors. The main motivation for such and upgrade is that the electronic board composing the link system are built using ob-

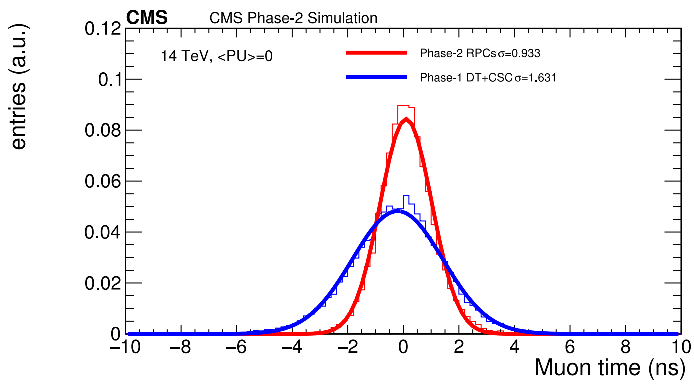

Figure 3.13: Comparison of the simulated time residuals in between reconstructed and true muon times without (blue) and with (red) the upgraded RPC link system [177].

solete and/or weak components that can easily suffer from the electromagnetic noise. These components may become the source of failing channels throughout Phase-2. Moreover, these link boards were originally designed only to match RPC digitized signals with the corresponding bunch crossing. Due to this feature, the time resolution of the full RPC chain is hence limited to 25 ns and does not make use of the full time resolution of the detectors. The time resolution foreseen after the upgrade can be seen through Figure 3.13 and is of the order of 1 ns. The exploitation of the full time resolution would make the synchronization of the RPC system easier and allow to have a finer offline out-of-time background removal within the 25 ns between consecutive bunch crossings. Moreover, this would greatly improve the trigger and reconstruction on HSCPs. Using the TOF information in between consecutive RPC stations, the minimal particle velocity than could be probed will drop from approximately 0.6 to 0.25 times the speed of light as showed in Figure 3.14.

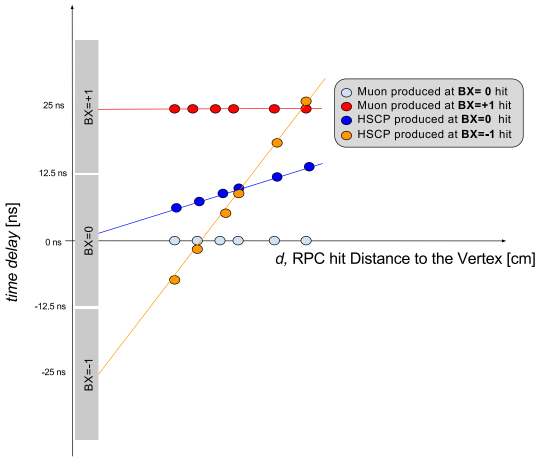

(a)

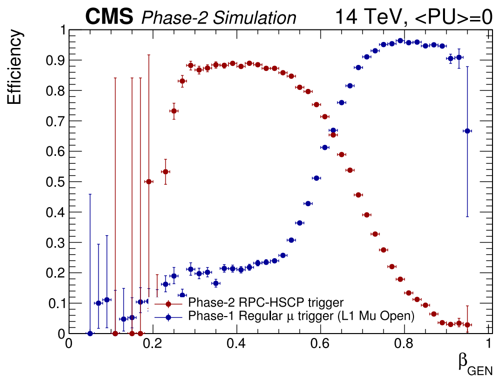

(b)

Figure 3.14: Figure 3.14a: Time delay with respect to a particle traveling at the speed of light measured at consecutive RPC stations for particles originating at different bunch crossings and traveling at different velocities [177]. Figure 3.14b: In blue is showed the standard Level-1 muon trigger efficiency as a function of β and in blue is showed the RPC-HSCP trigger efficiency after upgrade of the RPC Link System [177].

Upgrading RPC link system will require the installation of 1376 new link boards and 216 control boards. The new boards will make use of the recent progress made with fast FPGAs and will be a great improvement to the ASICs formerly used as they will be able to process signals from several detectors in parallel.

3.4 New detectors and increased acceptance

In the present muon system, the redundancy is assured by RPCs used for their robust bunch crossing assignments. The extension of the muon system towards higher pseudo-rapidity in an effort to complete the redundancy and to contribute to the precision of muon momentum measurements will require muon chambers with a spatial resolution less or comparable to the multiple scattering muons are subjected to while traveling through the detector volume [192].

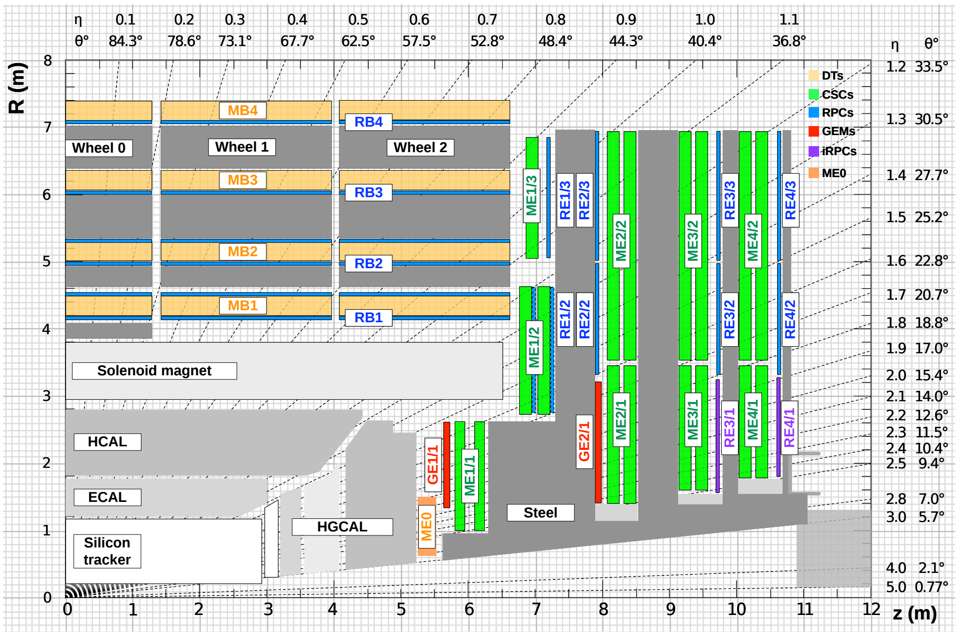

Figure 3.15: A quadrant of the muon system, showing DTs (yellow), RPCs (blue), and CSCs (green). The locations of new forward muon detectors for Phase-2 are contained within the dashed box and indicated in red for GEM stations (ME0, GE1/1, and GE2/1) and dark blue for improved RPC (iRPC) stations (RE3/1 and RE4/1).

Figure 3.15 shows a similar quadrant of CMS than the one presented in Figure 2.27 with the addition of Gas Electron Multiplier (GEM) (ME0, GE1/1 and GE2/1) and improved RPC (iRPC) (RE3/1 and RE4/1) in the pseudo-rapidity region $1.6 < |\eta| < 2.4$. The completion of the redundancy was already scheduled in the original CMS Technical Proposal [193] but never addressed. The coming Phase-2I is then the occasion to equip the region with the newest GEM and RPC technology. In order to match CMS requirements, a spatial resolution of $\mathcal{O}(\text{few mm})$ will be necessary for the proposed new RPC stations while the GEMs will need a resolution better than $1\,\text{mm}$, as showed by the simulation in Figure 3.16. Indeed, most of the plausible physics will be covered only considering muons with p_T<$100\,\text{GeV}$.

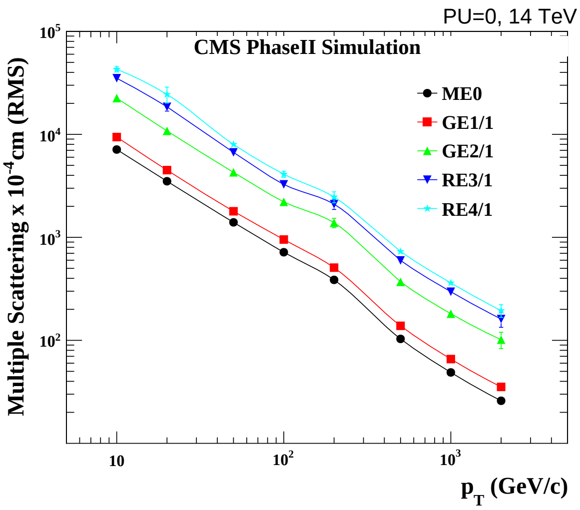

Figure 3.16: RMS of the multiple scattering displacement as a function of muon p_T for the proposed forward muon stations. All of the electromagnetic processes such as bremsstrahlung and magnetic field effect are included in the simulation.

3.4.1 Gas electron multipliers

In the region closer to the interaction point where the spatial resolution is requested for the new detectors to be better than 1 mm (at least for ME0 and GE1/1 according to Figure 3.16) and where the background rate will be the highest for muon detectors, the choice has been made to use triple GEMs, micro pattern gaseous detectors, instead of the originally planed RPCs. The GE1/1 project has been the first to be approved and demonstrators have been installed in CMS already during LS1. The rest of the detectors will be installed during LS2 while the GE2/1 and ME0 projects are still under development. ME0, GE1/1 and GE2/1 will be installed respectively close to the HCAL endcap, on the first and on the second muon endcap disks as can be seen from Figure 3.15.

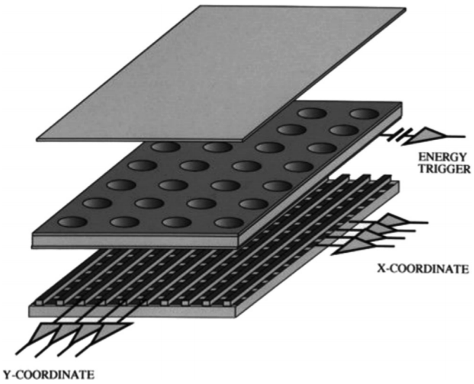

Figure 3.17: Schematics of a GEM. On top is the cathode and on the bottom, the anode on which a 2D read-out is installed. Finally, the GEM foil separates the gas volume into the drift region, in between the cathode and the foil, and the induction region, in between the foil and the anode. A negative voltage is applied on the cathode. The anode is connected to the ground.

Gas Electron Multipliers are gaseous detectors [194] whose gas volume is confined between two planar electrodes, the anode serving as read-out panel. The gas volume is divided in two or more regions by a single or multiple *GEM foils* as showed in Figure 3.17. These foils are very thin, of the order of a few tens of μm, and are pierced with holes as can be seen in Figure 3.18. Both surfaces of the GEM foils are clad with copper in order to apply a strong electric field in between each side that will generate very strong potentials in the holes. The gas region contained in between the cathode and the GEM foil is called the drift region as the electric field is not strong enough to cause avalanches and thus start an amplification. The primary electrons drift toward the foil and are accelerated and amplified by the very high potential within the holes, as showed in Figure 3.18. Then the electrons reach the second drift region where they will induce a signal on the read-out located on the anode. By restraining the amplification process at the level of the holes, the electrons can stay confined in a very little space and thus induce a very localized current, providing the GEMs

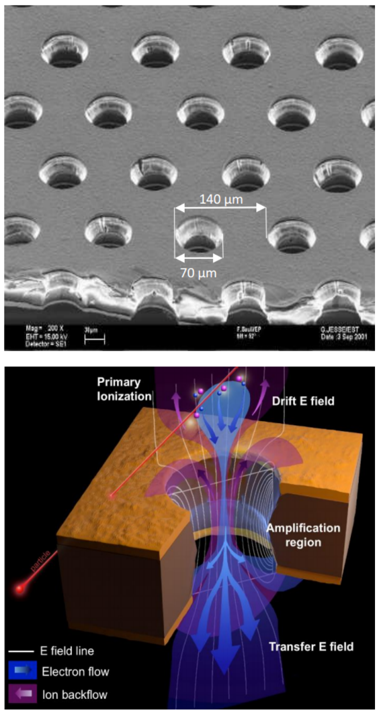

Figure 3.18: Top: Picture of a CMS GEM foil provided by a scanning electron microscope. Bottom: Representation of the electric field in a GEM hole and of the amplification electrons and ions undergo due to the very intense electric field.

with a very good spatial resolution. The process can be repeated several times in a row, in order to achieve a stronger amplification. The GEMs that will be used in CMS are triple-GEM detectors operated with a 70/30 gas mixture of Ar/CO_2. They contain three GEM foils and hence three electron amplifications, as can be seen in Figure 3.19. The GEM foils used in CMS are $50\,\mu\mathrm{m}$ foils clad with $5\,\mu\mathrm{m}$ of copper on each side. The foils are pierced with double-canonical holes which inner and outer diameters are respectively 50 and $70\,\mu\mathrm{m}$ which are placed $140\,\mu\mathrm{m}$ from each other in a hexagonal pattern, as showed in Figure 3.18. These detectors have a time resolution better than $10\,\mathrm{ns}$ and reach very good spatial resolutions of less than $200\,\mu\mathrm{rad}$ as indeed the position of the hits is not measured along the strips but following the azimuthal angle granularity of the radially organized trapezoidal strips.

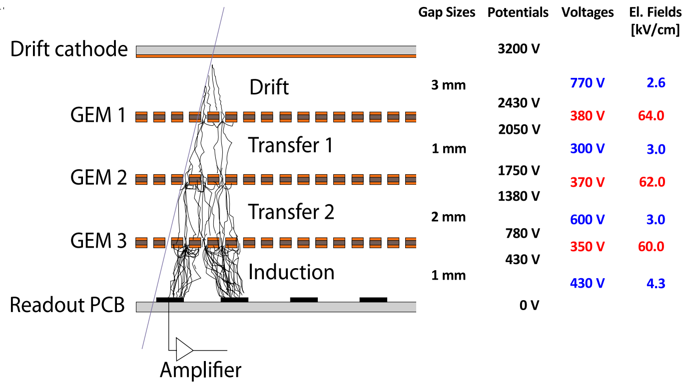

Figure 3.19: Schematic representation of CMS triple-GEMs. The gas volume is divided into four areas. The drift area is the region where the primary electrons are created before being amplified a first time while passing through the first GEM foil. Then the process of drift and amplification is repeated twice in following two transfer areas and GEM foils. Finally, the charges have been amplified enough to induce current in the read-out strips while in the last drift area. The typical dimensions, potentials and electric fields are provided.

The GEM Upgrade project started with GE1/1 [195]. GE1/1 detectors will already be installed during LS2. GE2/1 and ME0, on the other hand, will profit of the R&D knowledge and skills developed for GE1/1 while the requirements for each subsystem are different as they are not placed at the same distance from the interaction point. In this very forward region, a different position with respect to the center of the detector can dramatically change the conditions in which the detectors will have to be operated. In terms of rate capability, GE2/1, which is the furthest, is required to withstand $2.1\,\mathrm{kHz/cm^2}$ while GE1/1 needs to be better than $10\,\mathrm{kHz/cm^2}$ and ME0, better than $150\,\mathrm{kHz/cm^2}$. In terms of ageing with respect to charge deposition, ME0 needs to be certified to $840\,\mathrm{mC/cm^2}$, GE1/1 to $200\,\mathrm{mC/cm^2}$ and GE2/1 only to $9\,\mathrm{mC/cm^2}$. All 3 detectors need to have a time resolution better than $10\,\mathrm{ns}$ and an angular resolution better than $500\,\mu\mathrm{rad}$.

On each GE1/1 ring, 36 super chambers, consisting of two single GEM layers and spanning $10°$, will be installed covering the pseudo-rapidity region $1.6 < |\eta| < 2.2$ together with ME1/1 CSCs. The reach of the muon system will be improved thanks to the GE2/1 that will overlap with the GE1/1 and cover a region from $|\eta| > 1.6$ to $|\eta| < 2.4$ and complete the redundancy of ME2/1. The super chambers, built with two triple-GEM layers each consisting of four single GEM modules due to the rather large surface of the GE2/1 chambers, that will be installed on the first ring of the second endcap will span $20°$ each. Hence, a total of 72 chambers will be assembled to equip the muon system. Finally, the ME0 installed near the HCAL endcap will cover the region $2.0 < |\eta| < 2.8$. This subsystem will consist in super modules of six layers of triple-GEM detectors covering an azimuthal angle of $20°$ leading to the construction of 216 single detectors.

Adding the GEMs into the forward region of the muon system will allow to strongly enhance the Level-1 Trigger performance as shown in Figure 3.20. In the region $1.6 < |\eta| < 2.4$, the trigger efficiency of the current system would lie between 80 and 90% under HL-LHC conditions. The installation of GEMs would bring the efficiency to a consistent 92 to 94% on the entire region. At the same time, the trigger rate is expected to fluctuate from 3 to 10 kHz with the current system alone. The addition of detectors to complete the redundancy would allow keeping the rate mostly under 2 kHz. Moreover, benefiting from the good spatial and angular resolution of the GEMs, the precision into the muon measurement will also be improved by an order of magnitude thanks to the addition of GEMs as can be seen from the simulation presented in Figure 3.21.

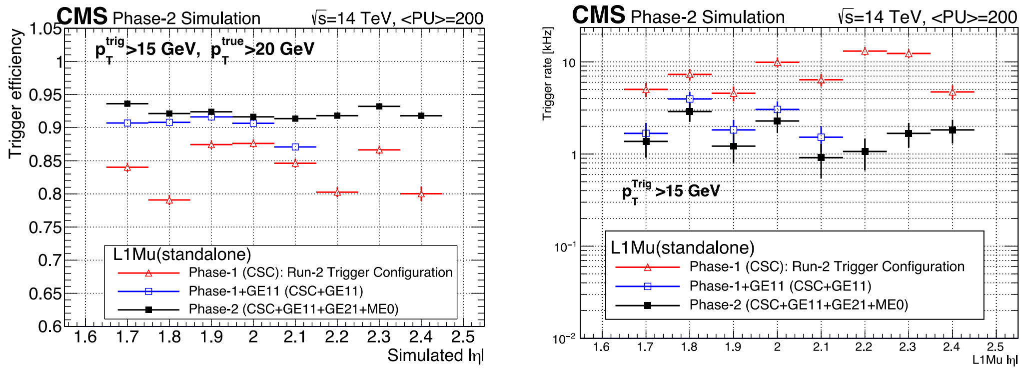

(a) *(b)*

Figure 3.20: Simulated efficiency and rate of the standalone Level-1 muon trigger using tracks reconstructed in CSCs and all GEM stations compared with Phase-1 values in the case where only CSCs are used or CSCs+GE1/1. The zones of inefficiency of the CSC subsystem are compensated by the addition of GEMs during Phase-2 and the trigger rates is kept from increasing due to the high luminosity [177].

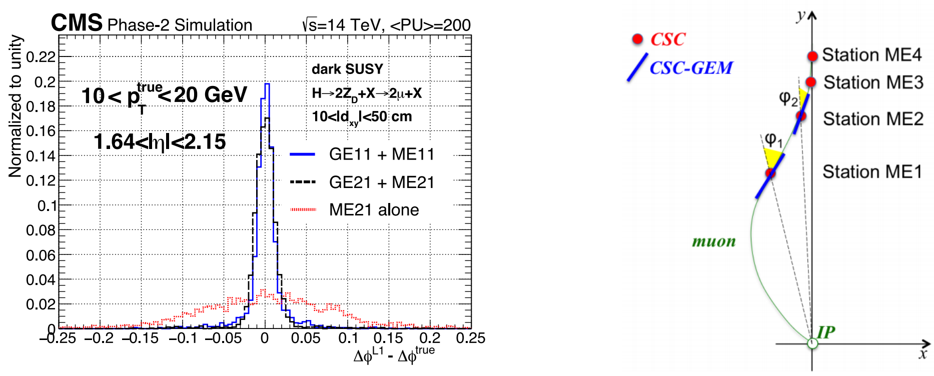

(a) *(b)*

Figure 3.21: Figure 3.21a: Simulated resolution of the muon direction measurement $\Delta\phi$ with Phase-2 conditions. In the second endcap station, the resolution is compared in the case of CSCs (ME2/1) alone and CSCs+GEMs (GE2/1+ME2/1) while a similar resolution measurement is given in the case of the first station (GE1/1+ME1/1) [177]. Figure 3.21b: The addition of GEM detectors on stations 1 and 2 (ME0 is considered to contribute to station 1) as redundant system to CSCs allows improving the muon momentum improvement through a more accurate measurement of the local bending angles ϕ_1 and ϕ_2 [177].

3.4.2 Improved forward resistive plate chambers

Figure 3.15 shows that the iRPCs that will equip the third and fourth endcap disks in position RE3/1 and RE4/1 will finally be the partners of the CSCs in position ME3/1 and ME4/1. They will complete Phase-1 plans by bringing the needed upgrades in the perspective of Phase-2 as the older chambers are not suitable to equip the forward region of CMS due to HL-LHC rates and charge deposition. By completing the redundancy, more hits along the muon track will be available and the lever arm will be improved. The benefits from extending the redundancy of the muon system with iRPCs to the forward most region is shown in Figure 3.22 in which the trigger efficiency is presented with and without RPCs. It is possible to see that the efficiency of the CMS muon trigger with the complete redundancy is consistently improved to a level above 95% in the region $|\eta| > 1.8$ as the iRPCs help filling the holes in the CSC system.

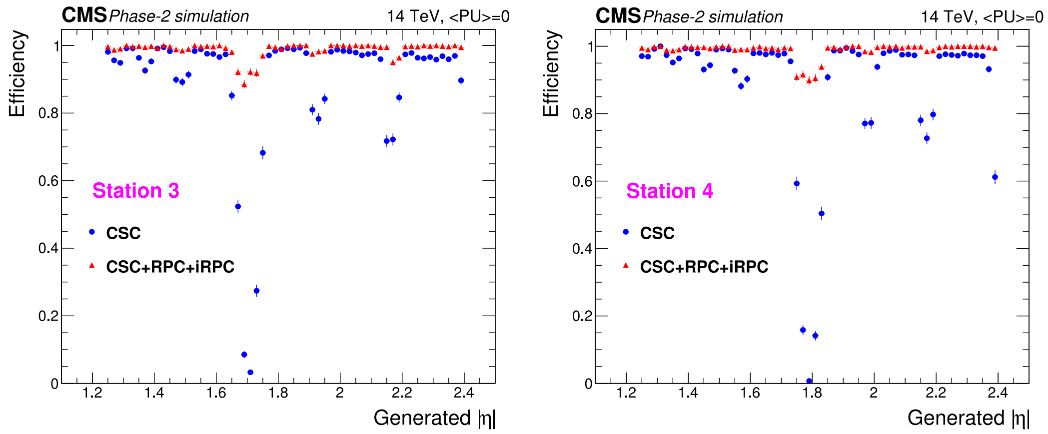

(a) *(b)*

Figure 3.22: Simulation of the impact of RPC hit inclusion onto the local trigger primitive efficiency in station 3 (Figure 3.22a) and station 4 (Figure 3.22b) [177]. The contribution of iRPC starts above $|\eta| = 1.8$.

The detectors that will be installed in the coming years will have similarities with the already existing RPC system. 18 of the new chambers, each spanning $20°$ in φ around the beam axis with 96 radially oriented trapezoidal read-out strips, will cover each muon endcap disk leading to the production of 72 iRPCs. The main difference with the old RPC detectors will be found at the level of the read-out panels. Indeed, the new chambers will not feature read-out strips segmented in η but rather will favor a read-out on both strip ends to determine the position of the hits along the chamber. By using fast front-end electronics a radial spatial resolution of the order of $2\,\mathrm{cm}$ could be achieved to contribute to the better reconstruction of muons in the forward region where the bending due to the magnetic field is low. This technical choice is motivated by the fact that, in the case a η segmentation were to be used, at least five pseudo-rapidity partitions would have been necessary to reach the minimal radial spatial resolution ($\approx 20\,\mathrm{cm}$). Having only one strip along the chamber read-out from both ends reduces by 60% the total number of channels and the necessary cabling, and allows for a better spatial resolution. The strip pitch will range from $6.0\,\mathrm{mm}$ ($5.9\,\mathrm{mm}$) on the high pseudo-rapidity end to $12.3\,\mathrm{mm}$ ($10.9\,\mathrm{mm}$) on the low one on position RE3/1 (RE4/1). The spatial resolution in the direction perpendicular to the strips should reach approximately $3\,\mathrm{mm}$, better than the minimal needed resolution (Figure 3.16). Finally, the overall time resolution of the new installation will be equally $1\,\mathrm{ns}$, as for the present due to the same link system being used even though the detector itself can achieve a time resolution of less than $100\,\mathrm{ps}$, necessary for a spatial reconstruction of the hits with a resolution of $2\,\mathrm{cm}$ or less along the strip length.

Having only a single strip instead of pseudo-rapidity segmentation will increase the probability of double hits in the same channel. The probability was estimated to be low enough as it shouldn't exceed 0.7%. This estimation was made assuming an average hit rate per unit area of $600\,\mathrm{Hz/cm^2}$ in the iRPCs (see Figure 3.23), a cluster size (average number of strips fired per muon) of 2, a strip active area of $158.4 \times 0.87\,\mathrm{cm}^2$ and a safety factor 3. The corresponding rate per strip is estimated to be $380\,\mathrm{kHz}$ leading to an average time interval in between two consecutive hits of $2600\,\mathrm{ns}$. This is compared to the minimal time interval of $16\,\mathrm{ns}$ necessary to avoid ambiguities. Indeed, a maximum of $10\,\mathrm{ns}$ is spent by the signal traveling through the strip to reach the electronics to which can be added $1\,\mathrm{ns}$ of dead time and 2 Time-to-Digital Converter (TDC) clock cycles of $2.5\,\mathrm{ns}$ to convert the signal arrival time into a digital value in the FEEs. The probability of having ambiguous double hits in a strip is then the ratio between the minimal time interval in between two consecutive hits and the average time interval estimated from the rate the detectors would be subjected to.

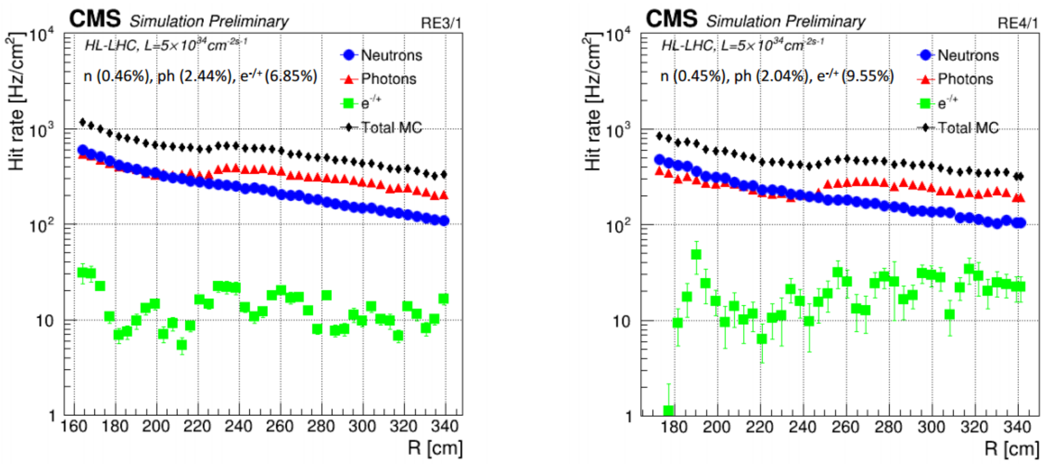

Figure 3.23: Expected hit rate due to neutrons, photons, electrons and positrons at HL-HLC instantaneous luminosity of $5 \times 10^{34}\ \mathrm{cm^{-2}s^{-1}}$ *in RE3/1 and RE4/1 chambers [196, 197]. The sensitivities of iRPCs used in the simulation for each particle are reported and differ from one endcap disk to another as the energies of the considered particles varies with the increasing distance from the interaction point.*

The instantaneous luminosity at HL-LHC being very high, the rates at the position of the new chambers needed to be simulated in order to understand the necessary requirements for these detectors. The simulated results for different background components (neutrons, photons, electrons and positrons) are shown in Figure 3.23 assuming known sensitivities to these particles. It is shown that on average over the iRPC areas the rates would be of the order of $600\,\mathrm{Hz/cm^2}$ ($600\,\mathrm{Hz/cm^2}$ seen in RE3/1 and $480\,\mathrm{Hz/cm^2}$ in RE4/1) [196, 197]. Thus, taking into account a safety factor of about 3, it was decided that improved RPCs should at least be certified for rates reaching $2\,\mathrm{Hz/cm^2}$ which will be achieved thanks to several improvements on the design and on the electronics. The detectors design will be based on the existing RPCs as they will also feature double RPC gaps. Similarly to the existing RPC system, the electrode material will be HPL although the thickness of the electrodes and of the gas gap will be reduced to $1.4\,\mathrm{mm}$ as a thinner gas gap leads to a decrease of deposited charge per avalanche as showed in Figure 3.24. The charge deposition in the case of $1.4\,\mathrm{mm}$ thick electrodes is reduced by a factor greater than 5 when compared to $2\,\mathrm{mm}$ electrodes at a similar electric field. The smaller the gas gap, the more the detector becomes sensitive to gap non-uniformities across the electrode planes, making a gap of $1.4\,\mathrm{mm}$ a good compromise in between these two competing factors.

A lower charge deposition inside of the detector volume means a slower ageing and a longer lifetime for detectors subjected to high irradiation. But, in order to take advantage of the lower detector gain, more sensitive electronics are required such that part of the gain that was formerly achieved in the gas volume can be moved to the electronics. Achieving this with the technology developed more than ten years ago for the present system is not possible as the signal over noise ratio of such electronics doesn't allow to detect charges as low as $10\,\mathrm{fC}$. Moreover, the new front-end electronics will need to be radiation hard to survive more than ten years of HL-LHC conditions. The new technology that has been chosen is based on the PETIROC ASIC manufactured by OMEGA and is a 64-channel ASIC called CMS RPCROC[177, 198, 199]. The properties of these electronics will be discussed in Chapter 6.

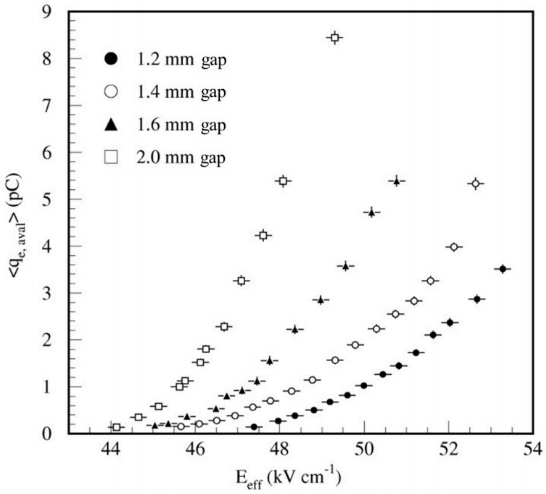

Figure 3.24: Measured average charge per avalanche as a function of the effective electric field for different gas gap thickness in double-gap RPCs using HPL electrodes [177].

3.5 Impact on Level-1 Trigger and physics performance

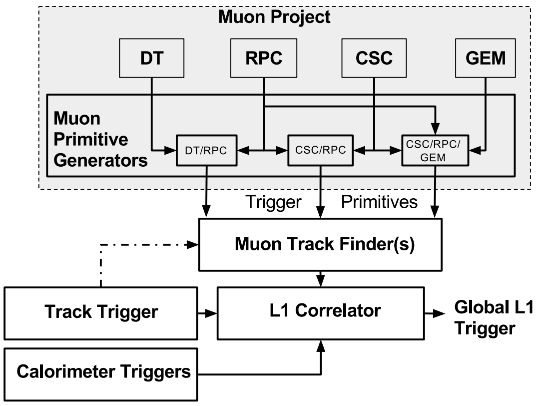

Figure 3.25: Level-1 Trigger data flow during Phase-2 operations [177].

The upgrades of the different subsystems will have a subsequent impact on the Level-1 Trigger. Indeed, although its main scheme will not be affected, the efficiency of the trigger in identifying muons and provide the DAQ with good and fast trigger that can cope with HL-LHC instantaneous luminosity is a major improvement. In addition to the upgrade of the muon system in terms of trigger accept rate and latency, the Level-1 Trigger will get extra information by including the Tracker Trigger into its Muon Track Finder logic and combine the L1 Muon Trigger with Tracker and Calorimeter Triggers to generate a Global L1 Trigger, as shown in Figure 3.25. Using the track candidates of both the muon system and the tracker in spatial coincidence will allow for a much better momentum resolution thanks to better identified muons and, hence, better measured transverse impulsion as described in reference [177].

In terms of muon trigger, three regions are considered due to their different track finding logic: the Barrel Muon Track Finder (BMTF), the Endcap Muon Track Finder (EMTF) for both the barrel and endcap regions, and finally the Overlap Muon Track Finder (OMTF) which concerns the pseudo-rapidity region in which there is a common coverage by both the barrel and endcap muon systems. This region can be seen in Figure 3.15 for $0.9 < |\eta| < 1.2$ and requires a specific more complex logic to provide an efficient reconstruction of muons due to the different orientation of the detectors and of the more complex magnetic field of this region. The development of a track finder specific to the overlap region was achieved during the Phase-1 upgrade of the L1-Trigger [200].

The upgraded RPC link system, allowing to take profit of the full $1\,\mathrm{ns}$ resolution of the detectors, will help reducing the neutron induced background, slightly improve the bunch crossing assignment, and help increasing the trigger efficiency in every sector. The upgrade of DT electronics is also to take into account as the trigger primitive generator will be renewed through the use of TDCs that will send the digitized signals directly to common DT/RPC back-end electronics instead of having an on-detector trigger logic as it will be the case until the end of Phase-1. The combination of RPC hits together with DT primitives will bring extra improvement in the bunch crossing assignment in the barrel and overlap regions and improve the efficiency of the trigger between the wheels were the quality of DT primitives is the poorest.

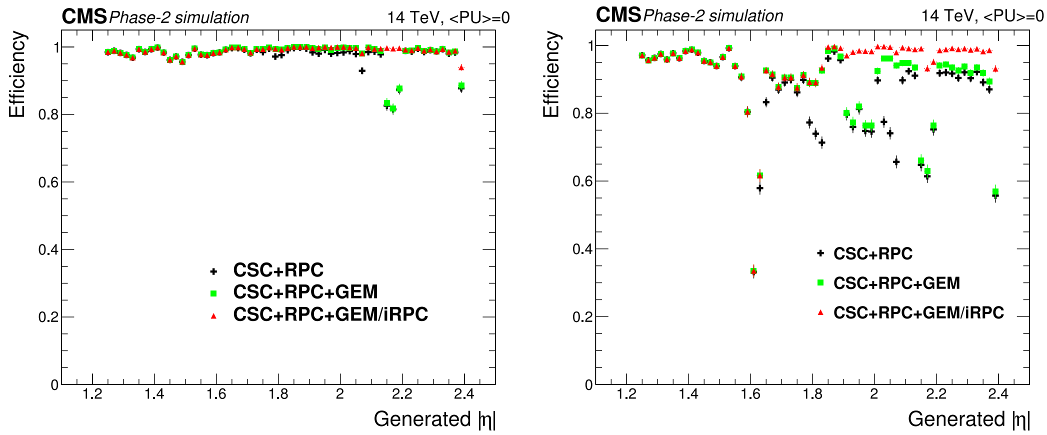

(a) *(b)*

Figure 3.26: Efficiency of the L1 trigger in the endcap region after Phase-2 upgrade in the case CSC/GEM/RPC hits are requested in at least two stations out of four (3.26a) and in all four stations (3.26b) [177].

The current EMTF already uses more sophisticated algorithms by combining together RPC hits and CSC primitives. The GEMs, in stations 1 and 2, and the iRPCs, in stations 3 and 4, will be added into the EMTF algorithm. Both these contributions will help increase the efficiency of the L1 trigger in the endcap region in one hand, as showed by Figure 3.26, and help lowering the L1 trigger rate in the other hand, especially in the most forward region. Similarly to the RPC/CSC algorithms, data from both CSCs and GEMs are combined into the Optical TMBs (OTMBs) to build on each station, GEM/CSC primitives matching space and time information from both subsystems. The efficiency improvement and rate reduction close to the beam line will be naturally enhanced by the addition of more hits along the muon tracks, as can be seen from Figure 3.27 that focuses especially in the most challenging pseudo-rapidity region. Indeed, the contribution from the GEMs to the lever arm of each track thanks to their high angular resolution will be a great asset in achieving such results, as can be seen in Figure 3.28. The rate will be partly reduced in the forward region thanks to the better spatial resolution of iRPCs, with respect to the current RPC system. The ambiguity brought by multiple local charged tracks in CSCs will be reduced, as explained through Figure 3.29. Indeed, as the rates will increase, the probability to record more than a single local charged track will greatly increase. This is due to the fact that the trigger algorithm uses information from three consecutive bunch crossings to find muon tracks. It is estimated that with iRPCs operated at 95% efficiency the resolution of ambiguous events would be of the order of 99.7%.

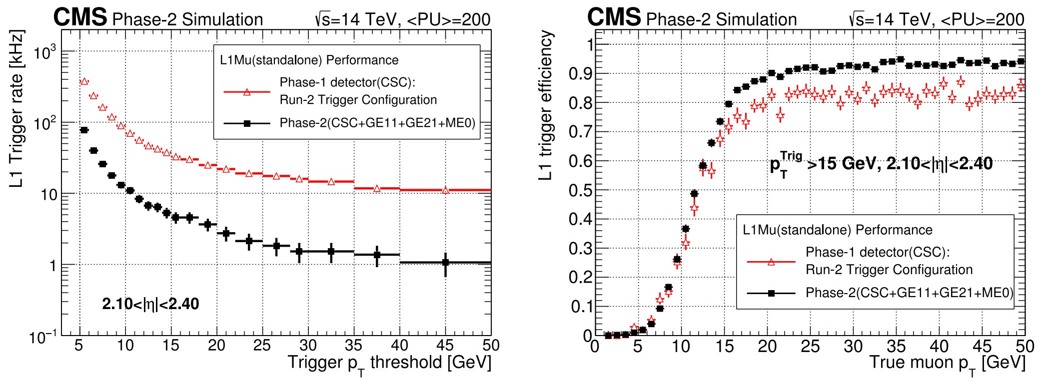

(a) *(b)*

Figure 3.27: Comparison of L1 trigger performances for prompt muons with and without the addition of GEMs in the region $2.1 < |\eta| < 2.4$ at Phase-2 conditions [177]. GEMs would allow a reduction of the trigger accept rate by an order of magnitude (Figure 3.27a) while increasing the trigger efficiency (Figure 3.27b).

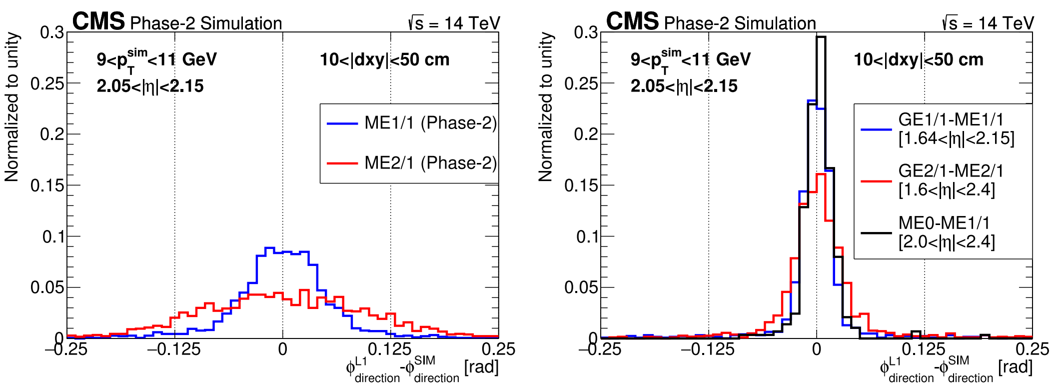

(a) *(b)*

Figure 3.28: The angular resolution on reconstructed muon tracks in the GEM overlap region $2.0 < |\eta| < 2.15$ is compared for Phase-2 conditions in the case CSC are alone (Figure 3.28a) and in the case the GEMs' data, including ME0, is combined to which of CSCs (Figure 3.28b) [177].

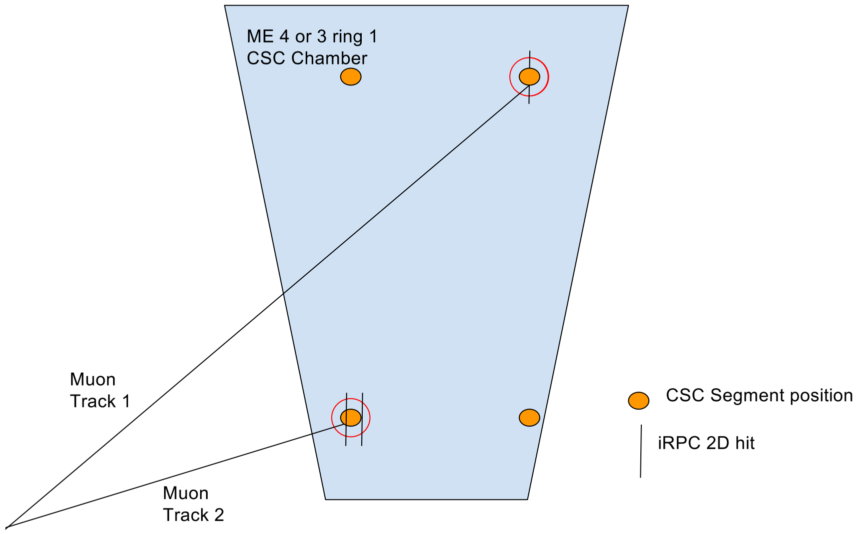

Figure 3.29: Resolution of the LCT ambiguous events thanks to the combination of CSC and iRPC readout data. Using CSCs only, two pairs of hits are possible [177].

3.6 Ecofriendly gas studies

The European Commission adopted a new ”F-gas regulation” in 2014 [201] with the goal to strongly control and reduce the use of fluorinated gases with high Global Warming Potential (GWP). Using CF_4, $C_2H_2F_4$ and SF_6, both CSC and RPC subsystems will need to address this problem by finding new gas mixture for the operation of their detectors. Finding a replacement for these gas components that were used for very specific reasons is a great challenge. Indeed, CSCs use CF_4 in order to enhance the longevity of the detectors, increase the drift velocity of electrons and quench photons with a non-flammable gas mixture. RPCs use a mixture mainly composed of $C_2H_2F_4$, or *R134a*, that features a high effective Townsend coefficient and the great average fast charge allowing for operations with a high threshold. The mixture also contains a small fraction of SF_6 that is used for its electronegative properties that prevents the development of delta-rays in the gas volume that might trigger multiple ionization and avalanches.

	CSC	RPC
Greenhouse gases used	CF_4	$C_2H_2F_4$ and SF_6
Greenhouse gases fraction in the gas mixture	10%	95.2% and 0.3%
Global Warming Potential (relative to CO_2)	6500	1300 and 23900
Gas mixture re-circulation	Yes, 90%	Yes, 85%
Gas mixture replenishing rate (l/hr)	700	1100
F-gas recuperation	Yes, ≈40%	No
F-gas venting rate (l/hr)	42	1047 and 3.3
CO_2-equivalent rate (m^3/h)	273	1440
Relative impact (entire muon system = 100%)	16%	84%

Table 3.1: Details of the greenhouse fluorinated gases used in CMS and of their GWP [177].

Nevertheless, all these gases have a very high GWP, as reported in Table 3.1, and only few options are left. The subsystems need to work on strongly decreasing the loss of these gases due to leaks in the gas system or need to completely change their gas mixture for more ecofriendly ones. Reducing the amount of F-gas released in the atmosphere due to leaks on the current gas system will require installation of a F-gas recuperation system on RPCs side and an upgrade of CSCs existing one in addition to the repair of existing leaks. With such measures, it is expected that the total rate of greenhouses gas vented in the atmosphere would represent only 1.6% of the current levels [177]. In the most critical case the F-gas were to be banned, it would be necessary to have replacement mixtures to operate CMS. CSC is presently investigating replacement for CF_4 such as CF_3I, C_4F_6, IC_3F_6, C_3F_8 or CHF_3. RPCs, in collaboration with the ATLAS RPC group which uses the same gas mixture, have identified CF_3I (GWP ≤ 1) and $C_3H_2F_4$ (GWP ~ 6), referred to as *HFO-1234ze*, as potential candidates with mixtures containing CO_2. CO_2 is already widely used by various RPC experiments in mixtures with argon. More R&D needs to be conducted for both subsystems before concluding on the best alternative. Finding no good alternative to the present mixtures will require very efficient abatement system in CMS to burn and convert the greenhouse gases into less harmful ones. This way, the air pollution would be strongly reduced.

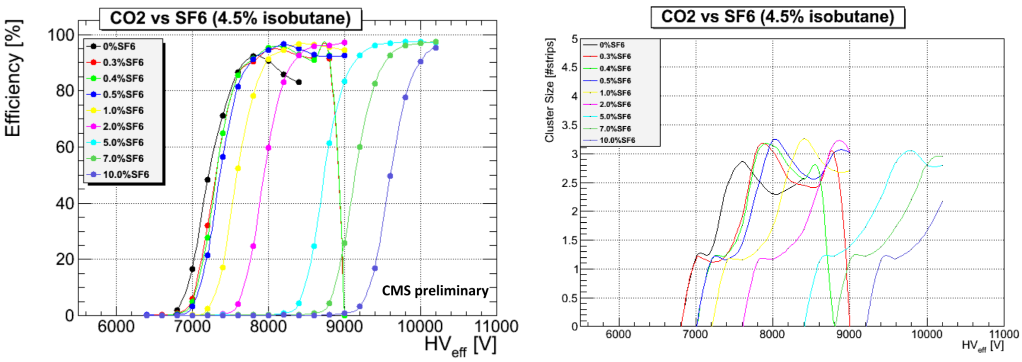

(a) *(b)*

Figure 3.30: Efficiency (Figure 3.30a [202]) and cluster size (Figure 3.30b) of a standard double-gap RPC operated with CO_2 mixtures for different ratios of SF_6.

Preliminary studies conducted in Ghent confirmed that CO_2 alone would require more than 1% of SF_6 to reach full efficiency, as presented in Figure 3.30. Even though the results obtained in Ghent don't show the streamer probability (the probability to have very large avalanches whose induced charge is greater than 20 pC), the variation of the cluster size indicates that the streamers become predominant before the efficiency plateau is reached. Then, a very first test with an HFO/CO_2 was performed. Only one ratio was tested as can be seen from Figure 3.31 that displays a good efficiency with a plateau located at a similar high voltage than with $R134a$ based mixtures

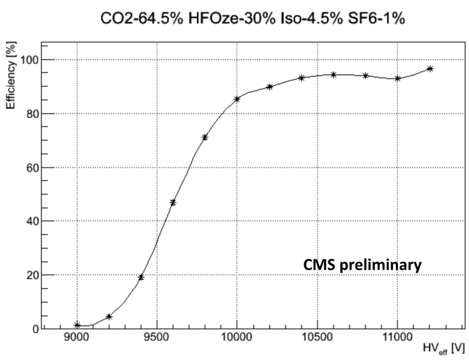

Figure 3.31: Efficiency of a CMS double-gap RPC operated with 30% of HFO, 4.5% of iC_4H_{10}, 1% of SF_6 and 64.5% of CO_2 [202].

(Figure 3.32). The status of RPC studies is presented in Figure 3.32 in which the performance (efficiency and streamer probability) of a CMS double-gap RPC operated with alternative gas mixtures is compared to the present CMS RPC mixture. Although the efficiency of detectors operated with mixtures containing CO_2/CF_3I or CO_2/HFO as a replacement for $C_2H_2F_4$ seems to reach similar levels than which of the detectors operated with the present mixture, the new gas mixtures feature a streamer probability that far exceeds which of the present fluorinated mixture. The SF_6 doesn't seem to prevent the formation of streamers as efficiently even when used at levels more than three times higher than with the standard CMS RPC mixture. Nevertheless, it is important to note that these results were obtained with a single-gap RPC while the use of a double-gap RPC reduces the operation voltage by 200 to 300 V, lowering the induced charge. A compromise in between good efficiency and acceptable level of streamer probability, and the fine-tuned composition of potential replacement gas mixtures will be keep on being studied using a standard double-gap CMS RPC.

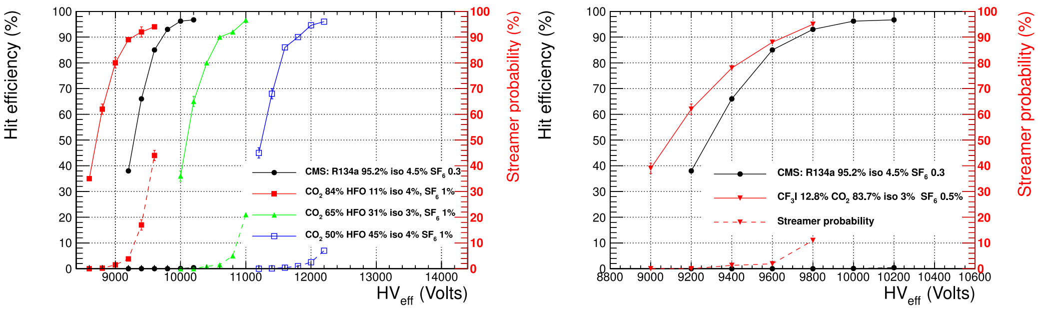

(a) *(b)*

Figure 3.32: The efficiency (solid lines) and streamer probability (dashed lines) of HFO/CO_2 (Figure 3.32a) and CF_3I/CO_2 (Figure 3.32b) based gas mixtures as a function of the effective high-voltage are compared with the present CMS RPC gas mixture represented in black [177, 202]. The detector used for the study is a single-gap RPC with similar properties than CMS RPCs. The streamer probability is defined as the proportion of events with a deposited charge greater than 20 pC.

Although the technology certification was conducted with the standard CMS gas mixture which is a known reference, the iRPCs will need to be operated with new environmental-friendly gas mixtures. Studies have then been conducted with iRPCs, assuming that the HFO/CO_2 mixture containing an almost equal level of both components was the most likely candidate to replace the standard mixture. In this purpose, an iRPC prototype has been built to be tested with an HFO/CO_2 gas mixture. The mixture, referred to as *"eco-gas"* in Figure 3.33, contained 50% of HFO, 4.5% of iC_4H_{10}, 0.3% of SF_6 and 45.2% of CO_2. In Figure 3.33 is presented a result consistent with the blue curve obtained with 45% of HFO, 4% of iC_4H_{10}, 1% of SF_6 and 50%

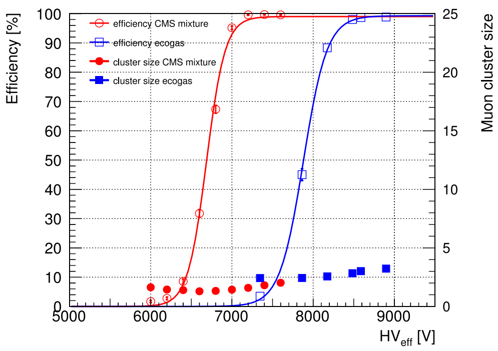

Figure 3.33: Efficiency (open symbols) and cluster size (full symbols) of an iRPC as a function of the effective voltage for the standard CMS gas mixture and an environmental-friendly gas mixture [177].

of CO_2 flushed into a standard double-gap RPC. Instead of the streamer probability, the cluster size is shown. The average number of hits generated by a muon passing through the chamber seem to have increased by 1 at the level of the knee of the sigmoid plateau using the ecogas.

4

Physics of Resistive plate chambers

A Resistive Plate Chamber (RPC) is a gaseous detector used in high-energy physics experiments as described in Chapter 3. It has been developed in 1981 by Santonico and Cardarelli [203], under the name of *Resistive Plate Counter*, as an alternative to the local-discharge spark counters proposed in 1978 by Pestov and Fedotovich [204, 205]. Working with spark chambers implied using high-pressure gas and high mechanical precision which the RPC simplified by formerly using a gas mixture of argon and butane flowed at atmospheric pressure and a constant and uniform electric field propagated in between two parallel electrode plates. Moreover, a significant increase in rate capability was introduced by the use of electrode plate material with high bulk resistivity, preventing the discharge from growing throughout the whole gas gap. Indeed, the effect of using resistive electrodes is that the constant electric field is locally canceled out by the development of the discharge, limiting its growth.

Through its development history, different operating modes [206–208], gas mixtures [203, 208–213] and new detector designs [214–216] have been discovered, leading to further improvement of the rate capability of such a detector. The low developing costs and easily achievable large detection areas offered by RPCs, as well as the wide range of possible designs, made them a natural choice to as muon chambers and/or trigger detectors in multipurpose experiments such as CMS [192] or ATLAS [217], time-of-flight detectors in ALICE [218], calorimeter with CALICE [219] or even detectors for volcanic muography with ToMuVol [220].

4.1 Principle

RPCs are ionisation detectors composed of two parallel resistive plate electrodes in between which a constant electric field is set. The space in between the electrodes, referred to as *gap*, is filled with a dense gas that is used to generate primary ionization into the gas volume. The free charge carriers (electrons and cations) created by the ionization of the gas molecules are then accelerated towards the electrodes by the electric field, as shown in Figure 4.1 [221]. RPCs being passive detectors, a current on pick-up copper read-out placed outside of the gas volume is induced by the charge accumulation during the growth of the avalanche resulting from the acceleration of the charge carriers. As a consequence, the time resolution of the detector is substantially increased as the output signal is generated while the electrons are still in movement. The advantage of a constant electric field, over multi-wire proportional chambers, is that the electrons are being fully accelerated from the moment charge carriers are freed and feel the full strength of the electric field that doesn't depend on the distance to the readout and that the output signal doesn't need for the electrons to be physically collected.

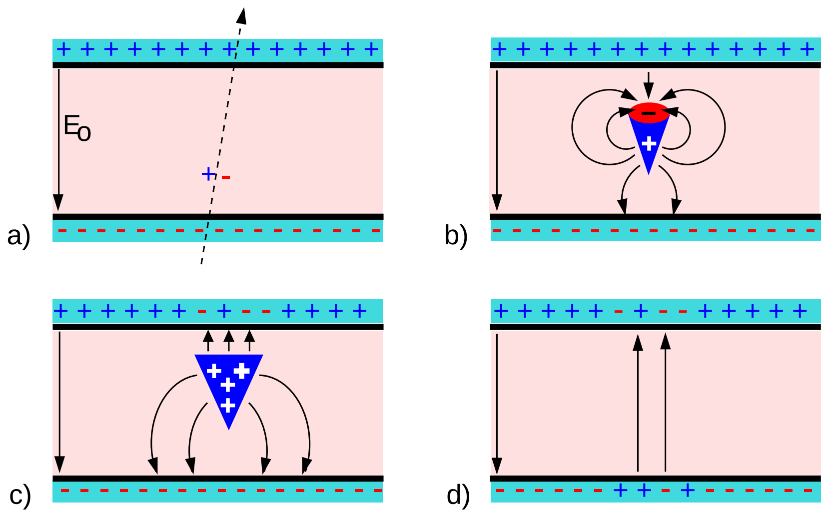

Figure 4.1: Different phases of the avalanche development in the RPC gas volume subjected to a constant electric field E_0. a) An avalanche is initiated by the primary ionisation caused by the passage of a charged particle through the gas volume. b) Due to its growing size, the avalanche starts to locally influence the electric field. c) The electrons, lighter than the cations reach the anode first. d) The ions reach the cathode. While the charges have not recombined, the electric field in the small region around the avalanche stays affected and locally blinds the detector.

After an avalanche developed in the gas, a time long compared to the development of a discharge is needed to recombine the charge carriers in the electrode material due to their resistivity. This property has the advantage of affecting the local electric field and avoiding sparks in the detector but, on the other hand, the rate capability is intrinsically limited by the time constant τ_{RPC} of the detector. Using a quasi-static approximation of Maxwell's equations for weakly conducting media, it can be shown that the time constant τ_{RPC} necessary to the charge recombination at the interface in between the electrode and the gas volume is given by the Formula 4.1 [222].

$$\tau_{RPC} = \frac{\epsilon_{electrode} + \epsilon_{gas}}{\sigma_{electrode} + \sigma_{gas}} \tag{4.1}$$

A gas can be assimilated to vacuum, leading to $\epsilon_{gas} = \epsilon_0$ and $\sigma_{gas} = 0$, and the electrodes permittivity and conductivity can be written as $\epsilon_{electrode} = \epsilon_r\epsilon_0$ and $\sigma_{electrode} = 1/\rho_{electrode}$, showing the strong dependence of the time constant to the electrodes resistivity in Formula 4.2.

$$\tau_{RPC} = (\epsilon_r + 1)\epsilon_0 \times \rho_{electrode} \tag{4.2}$$

Very few materials with a low enough resistivity exist in nature. The resistivity targeted to build RPCs ranges from 10^9 to $10^{12}\ \Omega \cdot \mathrm{cm}$. The most common RPC electrode materials are displayed in Table 4.1. When the doped glass and ceramics can offer short time constants of the order of $1\,\mathrm{ms}$, the developing cost of such materials is quite high due to the very low demand. Thus, High-pressure laminate (HPL) is often the choice for high-rate experiments using very large RPC detection areas. Other experiments working at cosmic muon fluxes can safely operate with ordinary float glass.

Material	$\rho_{electrode}$ ($\Omega \cdot \mathrm{cm}$)	ϵ_r	τ_{RPC} (ms)
Float glass	10^{12}	$\sim$7	$\sim$700
High-pressure laminate	10^{10} to 10^{12}	$\sim$6	$\sim$6 to 600
Doped glass (LR S)	10^9 to 10^{11}	$\sim$10	$\sim$1 to 100
Doped ceramics (SiN/SiC)	10^9	$\sim$8.5	$\sim$1
Doped ceramics (Ferrite)	10^8 to 10^{12}	$\sim$20	$\sim$0.2 to 2000

Table 4.1: Properties of the most used electrode materials for RPCs.

4.2 Rate capability and time resolution of Resistive Plate Chambers

The electrode material plays a key role in the maximum intrinsic rate capability of RPCs. R&D is continuously being done to develop at always cheaper costs material with lower resistivity. Nevertheless, the amount of charge released, i.e. the size of the discharge, if reduced leads to a smaller blind area in the detector, increasing the rate capability of the detector. On the other hand, the drift velocity of electrons in the gas volume being quite stable with the applied electric field, the design of a detector and the associated read-out and pulse-processing electronics will be a major component of the time resolution of RPCs. Moreover, the sensitivity of the electronics will also help increasing the rate capability by lowering the gain the gas volume needs to be operated at, increasingly lowering the gas volume in which the signals will develop.

4.2.1 Operation modes

Being a gaseous detector using an accelerating electric field to amplify the signal of primary charge carriers, the RPC can be operated into different modes as the electric field intensity varies. Each mode offers different performances for such a detector, and it will be showed that the operating mode corresponding to the lowest electric field possible is best suited for high-rate detectors working in collider experiments.

RPCs where developed early 1980s. At that time it was using an operating mode now referred to as *streamer mode*. Streamers are large discharges that develop in between the two electrodes enough to locally discharge the electrodes. If the electric field inside of the gas volume is strong enough, with electrons being fast compared to ions, a large and dense cloud of positive ions will develop nearby the anode and extend toward the cathode while the electrons are being collected, eventually leading to a streamer discharge due to the increase of the field seen at the cathode. The field is then strong enough so that electrons are pulled out of the cathode. Electrodes, though they are a unique volume of resistive material, can be assimilated to capacitors. At the moment an electric field is applied in between their outer surfaces, the charge carriers inside of the volume will start moving leading to a situation where there is no voltage across the electrodes and a higher density of negative charges, i.e. electrons, on the inner surface of the cathode. Finally, when a streamer discharge occurs, these electrons are partially released in the gas volume contributing to increase the discharge strength until the formation of a conductive plasma, the streamer. This can be understood through Figure 4.2 [206]. Streamer signals are very convenient in terms of read-out as no further amplification is required with output pulses amplitudes of the order of a few tens to few hundreds of mV as can be seen on Figure 4.3.

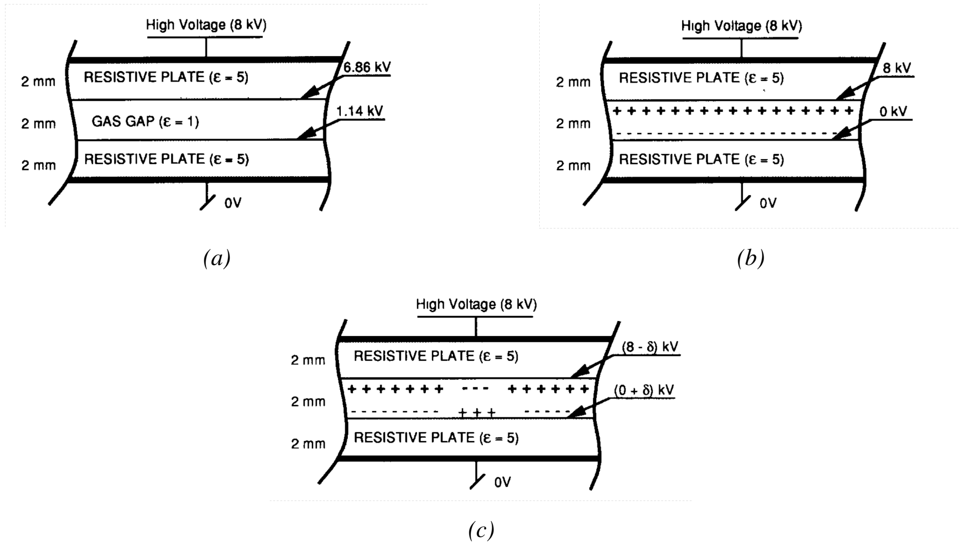

Figure 4.2: Movement of the charge carriers in an RPC. Figure 4.2a: Voltage across an RPC whose electrodes have a relative permittivity of 5 at the moment the tension is applied. Figure 4.2b: After the charge carriers moved, the electrodes are charged and there is no voltage drop over the electrodes anymore. The full potential is applied on the gas gap only. Figure 4.2c: The streamer discharge initiated by a charged particle transports electrons and cations towards the anode and cathode respectively.

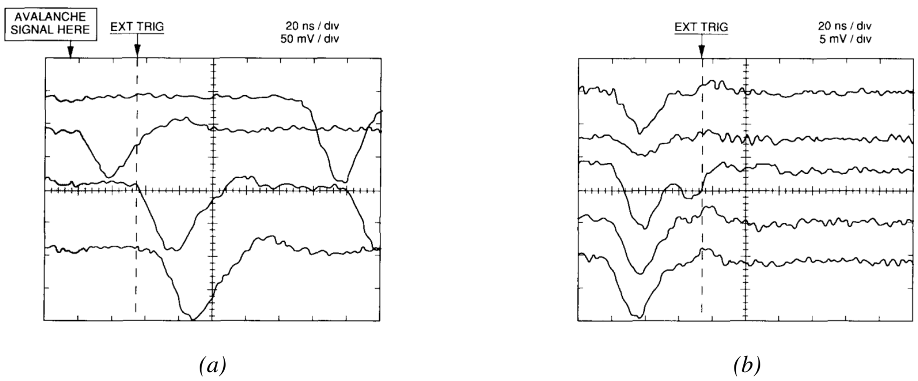

Figure 4.3: Typical oscilloscope pulses in streamer mode (Figure 4.3a) and avalanche mode(Figure 4.3b). In the case of streamer mode, the very small avalanche signal is visible.

Though, when the electric field is reduced, the electronic gain is small until the electrons get close enough to the anode and the positive ion cloud is much smaller. The electric field cannot rise to the point a field emission of electrons on the cathode is possible. The resulting signal is weak, of the order of a few mv as shown on Figure 4.3, and requires amplification. This is the *avalanche mode* of RPC operation. This mode offers a higher rate capability by providing smaller discharges that don't affect the electrodes charge and are more locally contained in the gas volume as was demonstrated by Crotty with Figure 4.4 [206]. The detector only stays locally blind the time the charge carriers are recombined and there is no need for electrode recharge which is a long process affecting a large portion of the detector. Another advantage of avalanche signals over streamer is the great time consistency. Figure 4.3 shows very clearly that avalanche signals have a very small time jitter. Thus, using such a mode is a natural choice for experiments in which the detectors are required to have a high detection rate.

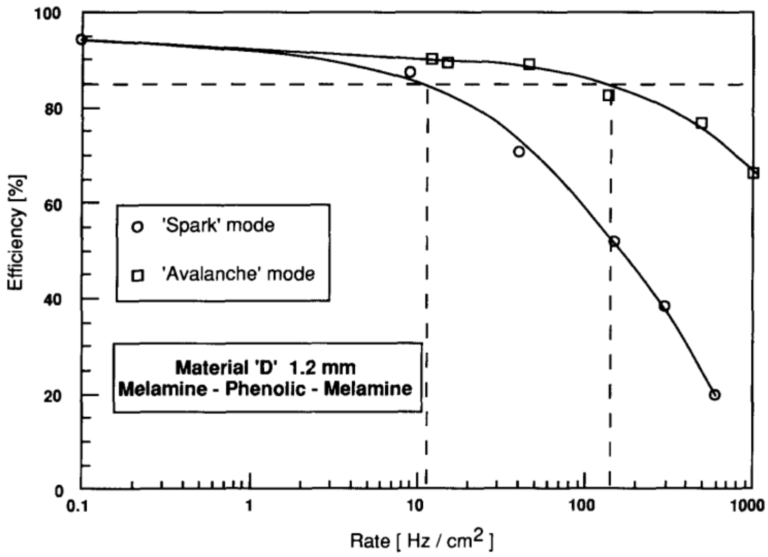

Figure 4.4: Rate capability comparison for the streamer and avalanche mode of operation. An order of magnitude in rate capability for a maximal efficiency drop of 10% is gained by using the avalanche mode over the streamer mode.

4.2.2 Standard gas mixture for RPCs operated in collider experiments

The first RPC working in streamer mode was operated with a 50/50 mixture of argon and butane [203], a standard mixture used at that time in multi-wire proportional chambers, taking profit of the good effective Townsend coefficient of argon to maximize the number of primary charge carriers freed in the gas by ionizing particles and of the quenching properties of butane. Before the discovery of the avalanche mode of RPC operation and concerned about the rate capability of RPCs operated in streamer mode, the performance improvement of the detectors through the increase of fast charge ratio in the signal development, decreasing the charge induced per avalanche as can be seen through Figure 4.5, was studied by adding Freon based gases, such as CF_3Br, into the typical Ar/C_4H_{10} gas mixture was studied and showed that a lower induced charge could lead to an improvement the rate capability [209]. This consideration led to the discovery of the avalanche mode which confirmed that the smaller the induced charge, the better the rate capability of the RPCs [206]. This discovery could be made thanks to the increased number of lower induced charge events allowed by adding a fraction of strong quencher in the gas mixture.

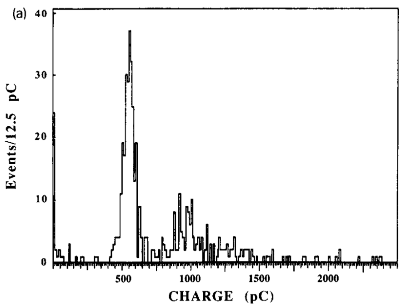

(a)

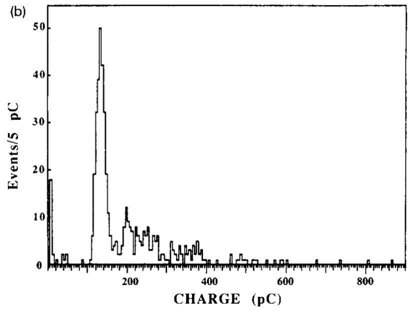

(b)

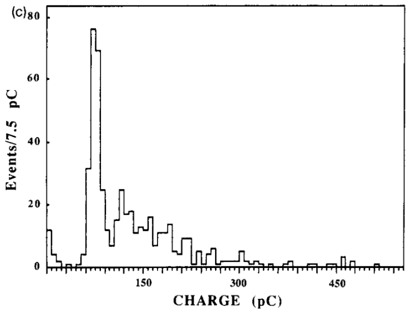

(c)

Figure 4.5: Comparison of the charge distribution of signals induced by cosmic muons in an RPC operated with a gas mixture of argon, butane and bromotrifluoromethane (CF_3Br). The Ar/C_4H_10 is kept constant at 60/40 in volume while the total amount of CF_3Br in the mixture is varied: 0% (Figure 4.5a), 4% (Figure 4.5b) and 8% (Figure 4.5c) [209].

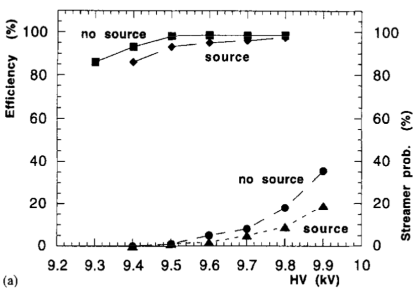

(a)

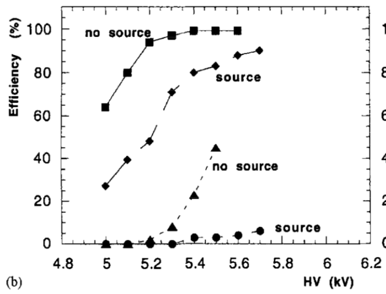

(b)

Figure 4.6: Comparison of the efficiency and streamer probability, defined as the fraction of events with an induced charge 10 times larger than that of the average avalanche, with and without irradiation by a 24 GBq *^{137}Cs source of an RPC successively operated with a 90/10 mixture $C_2H_2F_4$/i-C_4H_{10} (Figure 4.6a) and a 70/5/10/15 mixture of Ar/i-C_4H_{10}/CO_2/$C_2H_2F_4$ (Figure 4.6b) [210].*

From this moment onward, more and more studies were conducted in order to find a gas mixture that would allow for the best suppression of streamers for the benefit of low charge avalanches. Most

R&D groups working with narrow gaps started using freon-based gas mixtures while users of wide gap RPCs kept using Ar/CO_2 based mixtures. The differences in between narrow and wide gaps will be later discussed in Section 4.2.3. The CF_3Br having a high GWP, tetrafluoroethane was preferred to it as more suitable ecofriendly gas in the middle of the 90s. An advantage of this new freon component is that it featured a high primary ionization and a low operating voltage, as reported by Cardarelli [208]. Thus, the new gas mixtures used were mainly composed of tetrafluoroethane alone with lower content of isobutane in order to reduce the flammability of the mixtures in the case it were to be used in accelerator experiments for safety reasons. Performance and models about such mixtures were discussed in papers of Abbrescia [210, 211] and showed a better suitability of such a gas mixture, with respect to argon based ones, for operations with high radiation backgrounds leading to a need for high-rate capability of the detectors, as can be seen from Figures 4.6 and 4.7. Indeed, although the operating voltage of a tetrafluoroethane based mixture is higher than which of an argon based mixture but the efficiency under irradiation is more stable, the voltage range with negligible streamer probability is much wider, and the fast charge ratio available is much greater, providing with more stable operation of the detector.

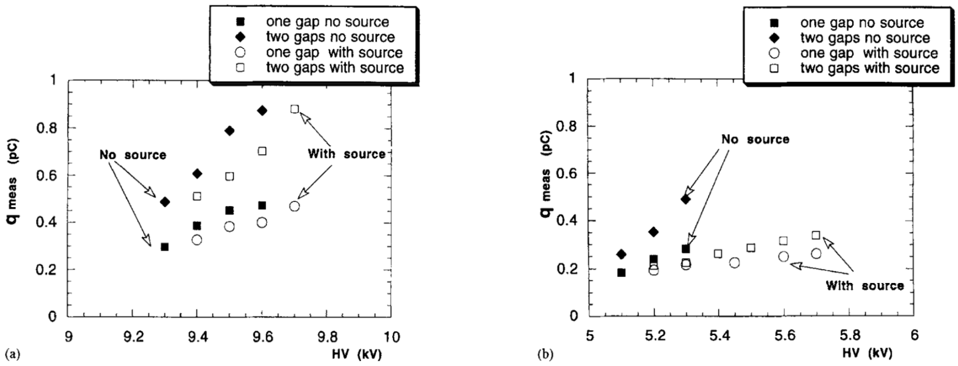

(a) *(b)*

Figure 4.7: Comparison of the fast charge ratio with and without irradiation by a $24\,\mathrm{GBq}$ ^{137}Cs *source of an RPC successively operated with a 90/10 mixture* $C_2H_2F_4$*/i-*C_4H_{10} *(Figure 4.7a) and a 70/5/10/15 mixture of Ar/i-*C_4H_{10}*/*CO_2*/*$C_2H_2F_4$ *(Figure 4.7b). The results are provided for both single-gap and double-gap operation [210].*

Aside of the improvement of the rate capability through linseed oil surface treatment of HPL electrodes, which allowed for a lower intrinsic noise rate and dark current of the detectors by improving the smoothness of the electrodes surface [223], it was later found that the streamers could be further suppressed by adding an electronegative compound into the gas mixture. The benefits of adding SF_6 in order to push the transitions from avalanche to streamers towards high voltages has been discussed in 1998 [212, 213] and eventually the high-rate RPC destined to be used in accelerator physics would unanimously start using this compound into RPC gas mixtures. Being able to control the creation of streamers allows for slower ageing of the detector and lower power consumption as the currents driven by the electrodes consecutively to the induced charges would be smaller. In summary, the typical gas mixture RPCs are operated with is generally composed of the following 3 gas compounds, although as mentioned in Chapter 3.6, research is being conducted into new more ecofriendly gas mixture using gases with a much lower Global Warming Potential:

- Tetrafluoroethane ($C_2F_4H_2$), also referred to as *Freon* or *R134a*, is the principal compound of the RPC gas mixtures, with a typical fraction above 90%. It is used for it's high effective Townsend coefficient and the great average fast charge that allows to operate the detector with a high threshold with respect to argon, for example, that has similar effective Townsend coefficient but suffers from a lower fast charge. To operate with similar conditions, argon would require a higher electric field leading to a higher fraction of streamers, thus limiting the rate capability of the detector [210, 211].

- Isobutane (i-C_4H_{10}), only present in a few percent in the gas mixtures, is used for its UV quenching properties [224] helping to prevent streamers due to UV photon emission during the avalanche growth.
- Sulfur hexafluoride, (SF_6), simply referred to as *SF6*, is used in very little quantities for its high electronegativity. Any excess of electrons is absorbed by the compound and streamers are suppressed [212, 213]. Nevertheless, a fraction of SF_6 higher than 1% will not bring any extra benefice in terms of streamer cancelation power but will lead to higher operating voltage [212], as can be understood through Figure 4.8.

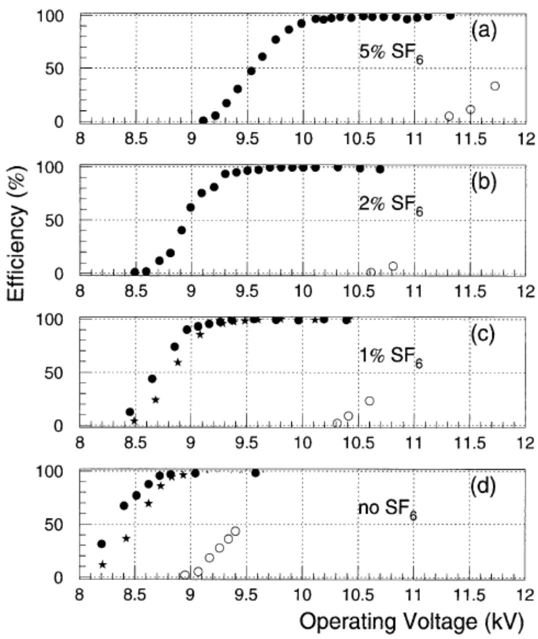

Figure 4.8: Effeciency (circles and stars with $30\,\mathrm{mV}$ *and* $100\,\mathrm{mV}$ *thresholds respectively) and streamer probability (opened circles) as function of the operating voltatge of a* $2\,\mathrm{mm}$ *single-gap HPL RPC flushed with a gas mixture containing (a) 5%, (b) 2%, (c) 1% and (d) no* SF_6 *[212].*

In the last steps of R&D, the gas mixture of CMS RPCs was forseen to be a 96.2/3.5/0.3 composition of $C_2H_2F_4$/i-C_4H_{10}/SF_6 [225] but finally it was slightly changed into a 95.2/4.5/0.3 mixture of the same gases [226]. A summary of the operation performance of the RPCs since the start of LHC and of CMS data taking is given in Figure 4.9 [227]. The performance of the detectors is regularly monitored and the operating voltages updated in order to obtain a very stable performance through time. Nevertheless, the detectors will face new challenges during Phase-II during which they will exposed to more extreme radiation conditions. Description of the longevity tests with extreme irradiation and the conclusions regarding the operation of the present RPC system will be given in Chapter 5.

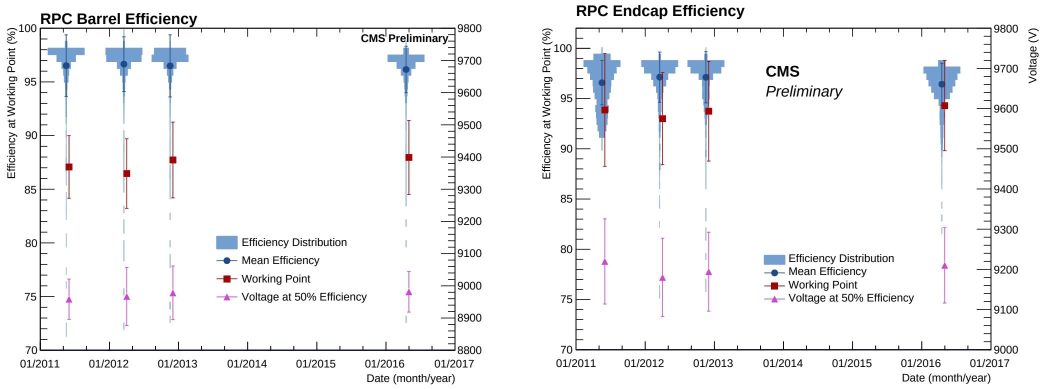

(a) *(b)*

Figure 4.9: Evolution of the efficiency, working voltage, and voltage at 50% of maximum efficiency for CMS Barrel (Figure 4.9a) and Endcap (Figure 4.9b) RPCs obtained through yearly voltage scans since 2011. The working voltage of each RPC is updated after each voltage scan to ensure optimal operation [227].

It was already discussed that in the future, it is likely that the use of freon gases could be banned. As potential replacement for tetrafluoroethane was proposed the trifluoroiodomethane (CF_3I), a molecule with similar properties than CF_3Br which was replaced by the tetrafluoroethane, and the 1,3,3,3-tetrafluoropropene ($C_3H_2F_4$ or HFO-1234re), a molecule with similar properties than the actual tetrafluoroethane and proposed as a replacement in refrigerating and air conditioning systems [228]. These two gases have stronger quenching properties than $C_2H_2F_4$ which means a much stronger electric field needs to be applied on the parallel electrodes of the RPCs in order to reach full efficiency. But the power supply system of CMS RPC is limited to $15\,\mathrm{kV}$ and so is ATLAS power supply system which is participating in a joined R&D. As can be seen from Figure 3.32, reducing the working voltage was achieved by mixing the potential replacements together with CO_2. Introducing carbon dioxide into the mixture while keeping similar levels of isobutane and SF_6 increases the streamer probability and the best candidate identified for a compromise in between low enough working voltage and acceptable levels of streamers corresponds to a mixture containing 50% of HFO, 4.5% of iC_4H_{10}, 0.3% of SF_6 and 45.2% of CO_2 but is not yet considered satisfactory. On the other hand, no good replacement for SF_6 has yet been identified. With its very high Global Warming Potential (23900), even small fraction of this gas in the mixture (it only represents 0.3% of CMS standard mixture but more than 5% of its overall GWP) substantially increase the danger for the environment. Although finding a replacement for this gas is less critical than for the tetrafluoroethane composing more than 90% of usual RPC standard mixtures, the problem will need to be addressed.

4.2.3 Detector designs and performance

Different RPC designs have been used, and each of them presents its own advantages. Historically, the first type of RPC to have been developed is what is now referred to as *narrow gap* RPC [203, 2694 229].

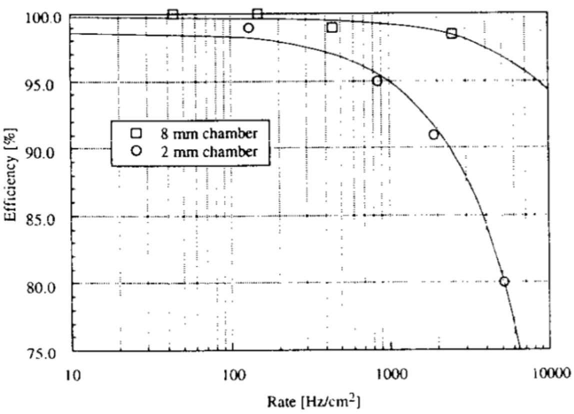

Figure 4.10: Comparison of the rate capability of 8 mm *and* 2 mm *wide RPCs. The lines are linear fits on the data [229].*

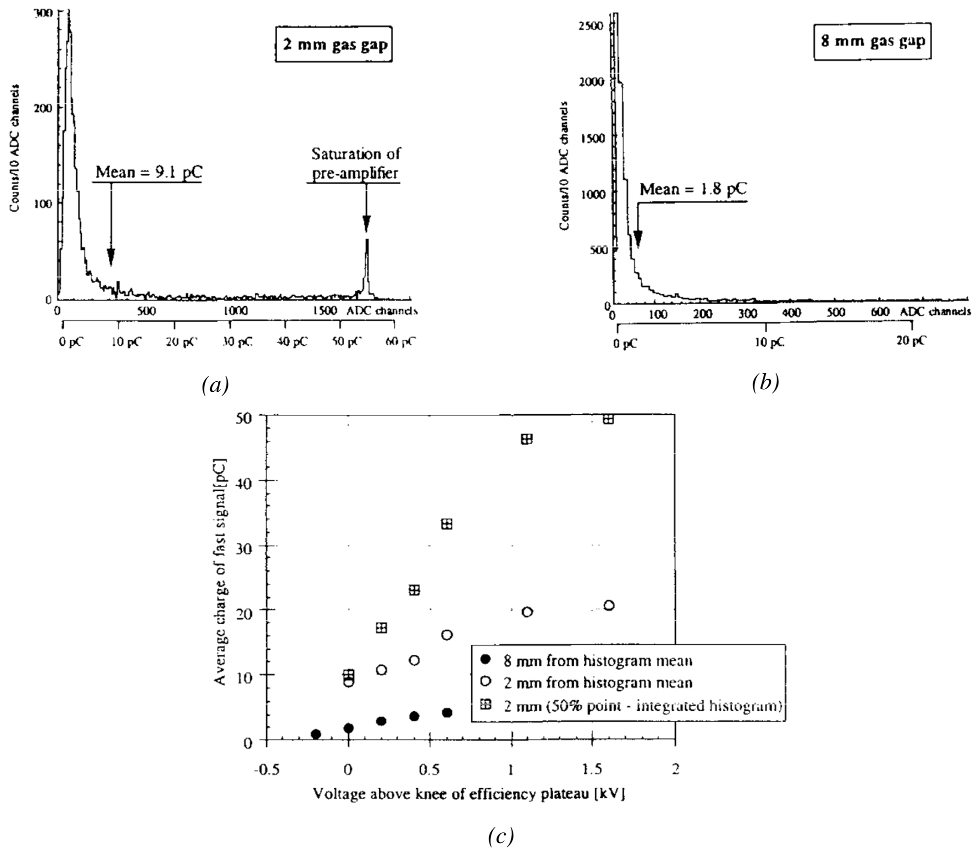

Figure 4.11: Distributions of the induced charge of fast signals on $2\,\mathrm{mm}$ *(Figure 4.11a) and* $8\,\mathrm{mm}$ *(Figure 4.11b) RPCs exposed to a radiation rate of* $100\,\mathrm{Hz/cm^2}$*. Average induced charge of fast signals as a function of the high voltage applied on* $2\,\mathrm{mm}$ *and* $8\,\mathrm{mm}$ *RPCs (Figure 4.11c). In the case of the* $2\,\mathrm{mm}$ *RPC, a saturation of the pre-amplifier was observed. The average of the distribution is underestimated, and the median is showed together with the average to account for this bias [229].*

After the avalanche mode has been discovered [206], it has been showed that increasing the width of the gas gap lead to higher rate capability, due to lower charge deposition per avalanche, and lower power dissipation [229], as is showed in Figures 4.10 and 4.11. The distance in between the electrode being greater, a weaker electric field can be applied and a lower gain used as a longer gas volume will contribute to the signal induction on the read-out circuit. Nevertheless, by increasing the gas gap width, the time resolution of the detector decreases. This is a natural result if the increase of active gas volume in the detector is taken into account. Indeed, for a given detection threshold on the induced charge per signal, only the small fraction of gas closest to the cathode will provide enough gain to have a detectable signal. In the case of a wider gas volume, the active region is then larger and a larger time jitter is introduced with the variation of starting position of the avalanche, as discussed in [214] and showed in Figure 4.12.

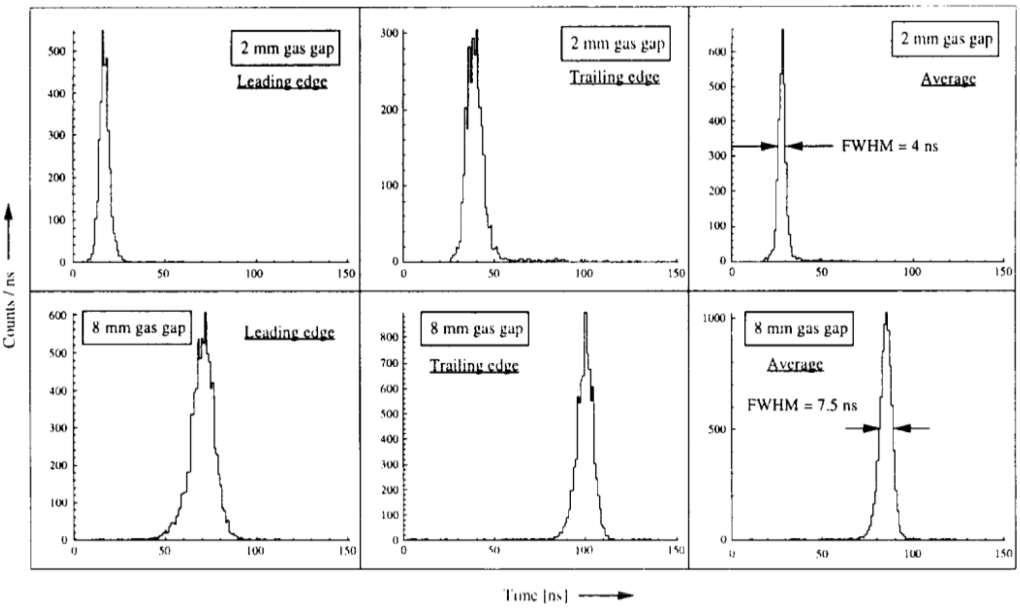

Figure 4.12: Time distributions of the leading, trailing, and average of both leading and traling edges for $2\,\mathrm{mm}$ *(top row) and* $8\,\mathrm{mm}$ *(bottom row) RPCs exposed to a* $100\,\mathrm{Hz/cm^2}$ *radiation rate. The data was collected with RPCs operated at the voltage corresponding to the knee of the efficiency distribution, defined as the point where 95% of the maximum efficiency is obtained [229].*

To improve both the time resolution and the rate capability, different methods were used trying to take advantage of both narrow and wide gap RPCs into a single design. Thus, double-gap RPCs, combining two narrow gaps into a single detector to increase the effective sensitive volume, and multigap RPCs, which divided the large volume of a wide gap RPC into thinner sub-gaps by adding intermediate electrodes in between the cathode and anode to improve the time resolution by mimicking narrow gap RPCs, were developed starting from the middle of the 90s.

4.2.3.1 Double-gap RPC

Made out of two narrow RPC detectors stacked on top of each other as shown in Figure 4.13, this detector layout, popularized by the two multipurpose experiments CMS [192] and ATLAS [217] at LHC, can be used as an OR system in which each individual chamber participates in the ouput signal and increases the overall sensitive volume of the detector apparatus. Keeping the copper strip read-out system at the ground, CMS and ATLAS, due to different goals, have chosen different designs as CMS RPCs possess a 1D read-out while ATLAS RPCs offer a 2D read-out. The difference comes from placing the read-out in between the gaps, the anodes facing each other, or to have both RPC gaps in between two layers of read-out panels, one along the X-axis and one along the Y-axis, the cathodes facing each other.

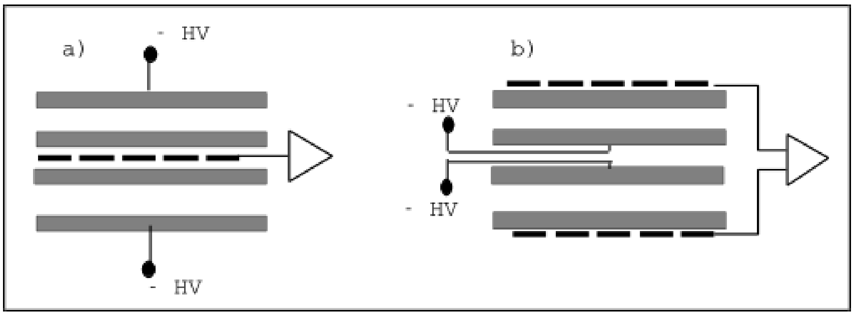

Figure 4.13: Possible double-gap RPC layouts: a) "standard" 1D double-gap RPC, as used in CMS experiment, where the anodes are facing each other and a 1D read-out plane is sandwiched in between them, b) double read-out double-gap RPC as used in ATLAS experiment, where the cathodes are facing each other and 2 read-out planes are used on the outer surfaces. This last layout can offer the possibility to use a 2D reconstruction by using orthogonal read-out planes.

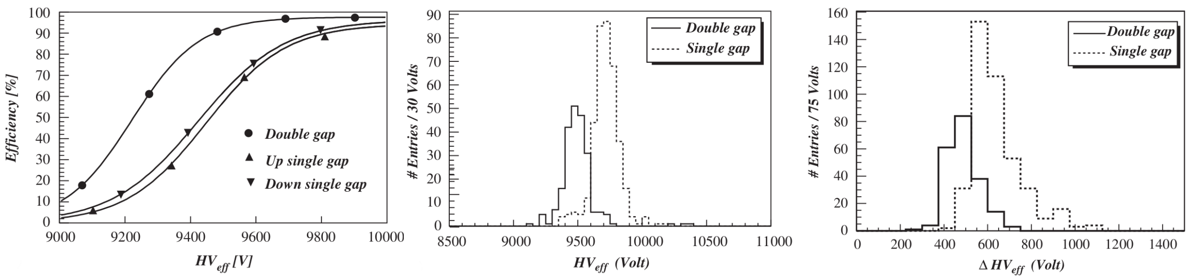

(a) (b) (c)

Figure 4.14: Comparison of performance of CMS double and single-gap RPCs using cosmic muons [225]. Figure 4.14a: Comparison of efficiency sigmoids. Figure 4.14b: Voltage distribution at 95% of maximum efficiency. Figure 4.14c: $\Delta^{90\%}_{10\%}$ distribution.

The gain of such a detector is reduced by a factor 2 with respect to single-gap RPCs with an efficiency plateau reached at lower voltage, as visible on Figure 4.14, due to the two gas gaps contributing to the signal formation and offering a dynamic range closer to witch of a wide gap RPC. A double-gap is then fully efficient while the individual RPC gaps composing it are only 70 to 80% efficient. Naturally, by operating the double-gap at a lower voltage, the rate capability in found to be increased as the induced charge per gap is then lower than in the can than a single-gap detector also leading to a reduction of the streamer probability and a better extraction of the fast charge of the total signal as could be seen through previously presented Figure 4.7.

4.2.3.2 Multigap RPC (MRPC)

MRPCs are layouts in which floating sub electrode plates are placed into a wide gap RPC to divide the gas volume and create a sum of narrow gaps [214, 215]. Similarly to the double-gap RPC for which the gain could be reduced by increasing the dynamic range, the multigap reduces the gain while keeping a total dynamic range similar to which of a wide gap RPC by reducing the size of each individual sub-gap composing the detector. The dynamic range, associated to the sensitive volume, and the comparison of each detector layout to the wide gap RPC is showed in Figure 4.15.

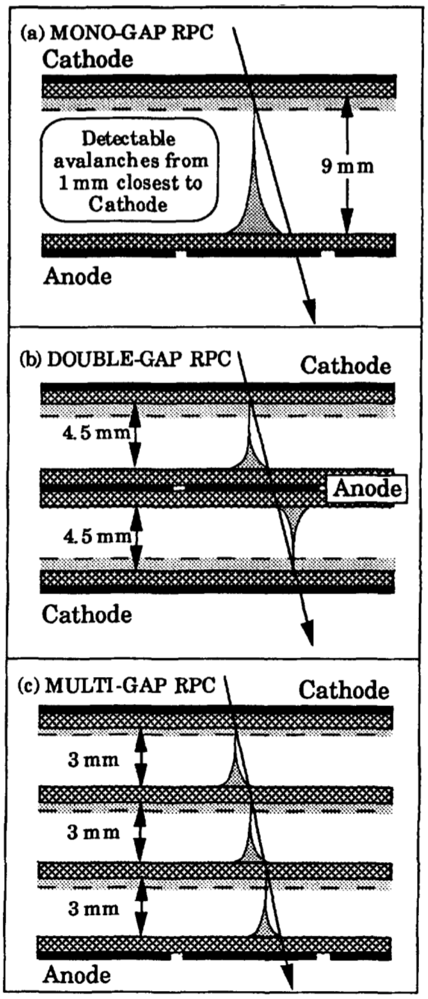

Figure 4.15: Representation of different RPC layouts (wide gap on Figure (a), double-gap on Figure (b) and multigap on Figure (c)), of the corresponding sensitive volume in gray, and of the associated avalanche size [215].

By operating the detector with thinner gaps, the time resolution is improved. Comparatively to the time resolution presented in Figure 4.12 for the wide gap RPC of $8\,\mathrm{mm}$, a complementary study was conducted on multigaps using two $4\,\mathrm{mm}$ and four $2\,\mathrm{mm}$ subgaps and showed, via Figure 4.16, an improvement of the time resolution with the reduction of the gap width and of the number of gaps while the same sensitive volume was kept [215].

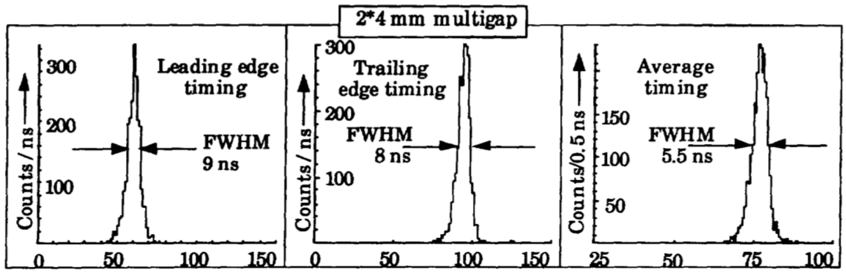

(a)

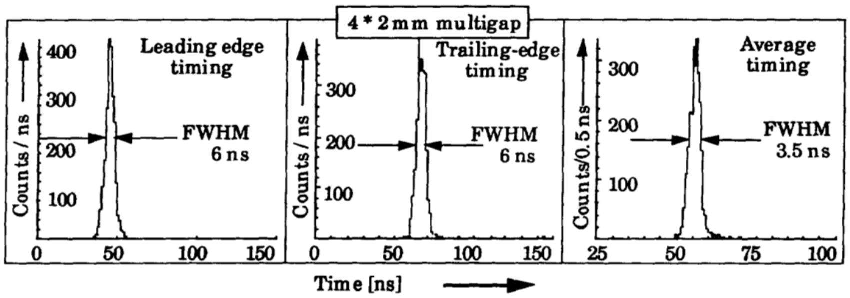

(b)

Figure 4.16: Time distributions of the leading, trailing, and average of both leading and trailing edges for multigap RPCs consisting in two $4\,\mathrm{mm}$ *(Figure 4.16a) and four* $2\,\mathrm{mm}$ *(Figure 4.16b) exposed to a* $100\,\mathrm{Hz/cm^2}$ *radiation rate. The data was collected with RPCs operated at the voltage corresponding to the knee of the efficiency distribution, defined as the point where 95% of the maximum efficiency is obtained [215].*

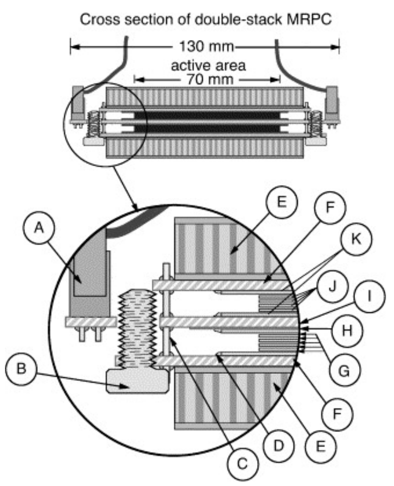

(a)

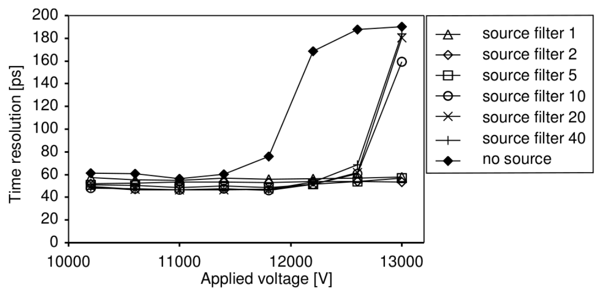

(b)

Figure 4.17: Presentation of a study of a possible ALICE MRPC cell using $250\,\mu\mathrm{m}$ *gas gaps,* $620\,\mu\mathrm{m}$ *outer glass electrodes, and* $550\,\mu\mathrm{m}$ *inner floating electrodes (Figure 4.17a), and of its time resolution performance as a function of the applied high voltage for different radiation levels referred through different filter settings of the* $740\,\mathrm{GBq}$ ^{137}Cs *source the former CERN GIF facility [230].*

After the problem of streamers was solved by adding SF_6 into the gas mixture, the size of the

MRPCs decreased as the research groups started applying the concept of dividing the gas volume into subvolumes to the narrow gap RPCs leading to the, now, widely used micro gap MRPCs. The time resolution of such a detector can reach of few tens of ps, with gas gaps of the order of a few hundred $\mu\mathrm{m}$ as showed in Figure 4.17 representing a single cell of ALICE Time-of-flight (ToF) system consisting of double MRPCs, as it was studied in the early 2000s [230].

Sometimes used as a double multigap RPC, taking advantage of the OR of double-gap RPCs to both be able to operate a higher number of gaps while keeping a reasonable high voltage applied in between the cathode and anode and to further reduce the gain, the MRPC is mainly used as ToF detector [230–234] due to its excellent timing properties that allow to perform particle identification as explained by Williams in [235]. The principle of particle identification using ToF is simply the measurement of the velocity of a particle. Indeed, particles are defined by their mass (for the parameter of interest here, their electric charge being measured using the bending angle of the particles traveling through a magnetic field) and this mass can be calculated by measuring the velocity β and momentum of the particle:

$$\beta = \frac{p}{\sqrt{p^2 + m^2}} \tag{4.3}$$

Intuitively, it is trivial to understand that 2 different particles having the same momentum will have a different velocity due to the mass difference and thus a different flight time T_1 and T_2 through the detector and this is used to separate and identify particles. The better the time resolution of the ToF system used, the stronger will the separation be:

$$T = \frac{L}{v} = \frac{L}{c \cdot \beta}, \quad \Delta T = T_1 - T_2 = \frac{L}{c}\left(\sqrt{1 + m_1^2/p^2} - \sqrt{1 + m_2^2/p^2}\right) \cong (m_1^2 - m_2^2)\frac{L}{2cp^2} \tag{4.4}$$

An example of particle identification is given for the case of STAR experiment in Figure 4.18.

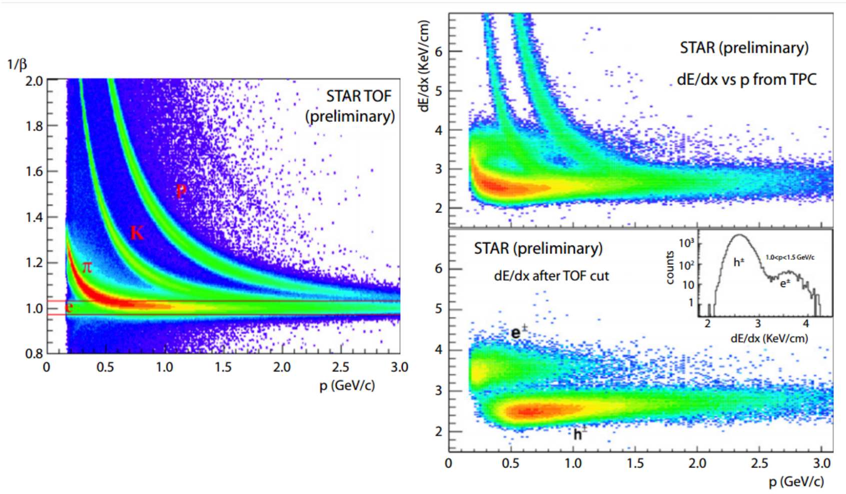

Figure 4.18: Particle identification applied to electrons in the STAR experiment. The identification is performed combining ToF and dE/dx measurements [235].

Taking into account the distortion effect on the electric field inside of an MRPC built using micro gaps due to the exposition to irradiation, distortion that can be understood by monitoring the current drawn by the detector which should stay constant at constant electric field, another benefice of using such small gas gaps is the strong reduction of the average avalanche volume and thus of the blind spot on MRPCs leading to an improved rate capability. Multigaps can sustain backgrounds of several $\mathrm{kHz/cm^2}$ as demonstrated in Figure 4.19.

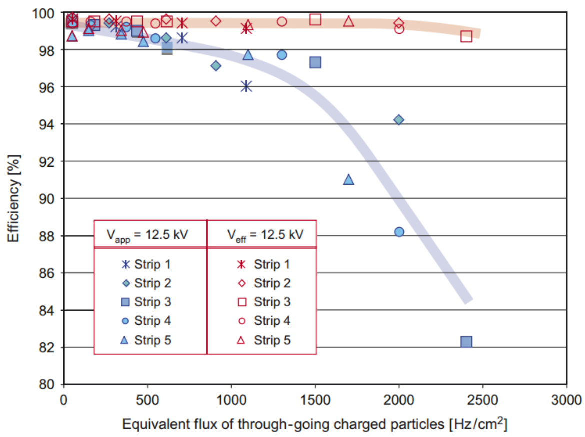

Figure 4.19: Comparison of the detector performance of ALICE ToF MRPC [236] at fixed applied voltage (in blue) and at fixed effective voltage (in red). The effective voltage is kept fixed by increasing the applied voltage accordingly to the current drawn by the detector.

4.2.3.3 Charge distribution and performance limitations

[This part could be moved in the next section of the chapter and deepened using the perspective of the avalanche physics.]

The direct consequence of the different RPC layouts is a variation of intrinsic time resolution of the RPC as the gap size decreases and of the rate capability when the deposited charge per event is spread over a larger number of amplification volumes, allowing for a reduction of the overall gain of the detectors which is replaced by an on-electronics pre-amplification of the signals. In this sense, an advantage is given to multigaps whose design use sub-millimeter gas volumes providing very consistent signals.

From the charge spectrum point of view, each layout has its own advantages. When the double-gap has the highest induced-over-drifting charge ratio, as seen in Figure 4.20, the multigap has a charge spectrum strongly detached from the origin, as visible in Figure 4.21. A high induced-over-drifting charge ratio means that the double-gap can be safely operated at a high threshold or that at a similar threshold it can be operated with a twice smaller drifting charge, meaning a higher rate capability if operated with sensitive enough electronics. On the other hand, the strong detachment of the charge spectrum from the origin in the MRPC case allows reaching a higher efficiency with increasing threshold as most of the induced charge is not low due to the convolution of several single-gap spectra. The range of stable efficiency increases with the number of gaps, as presented in Figure 4.22.

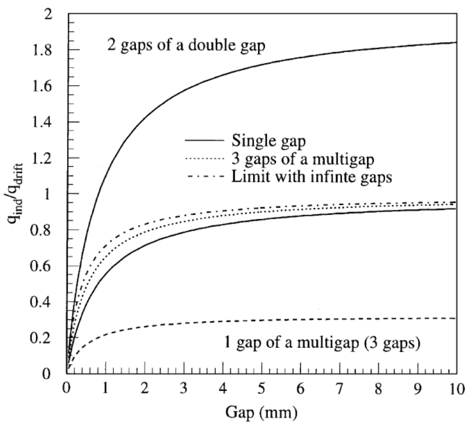

Figure 4.20: Ratio between total induced and drifting charge have been simulated for single-gap, double-gap and multigap layouts [237]. The total induced charge for a double-gap RPC is a factor 2 higher than for a multigap.

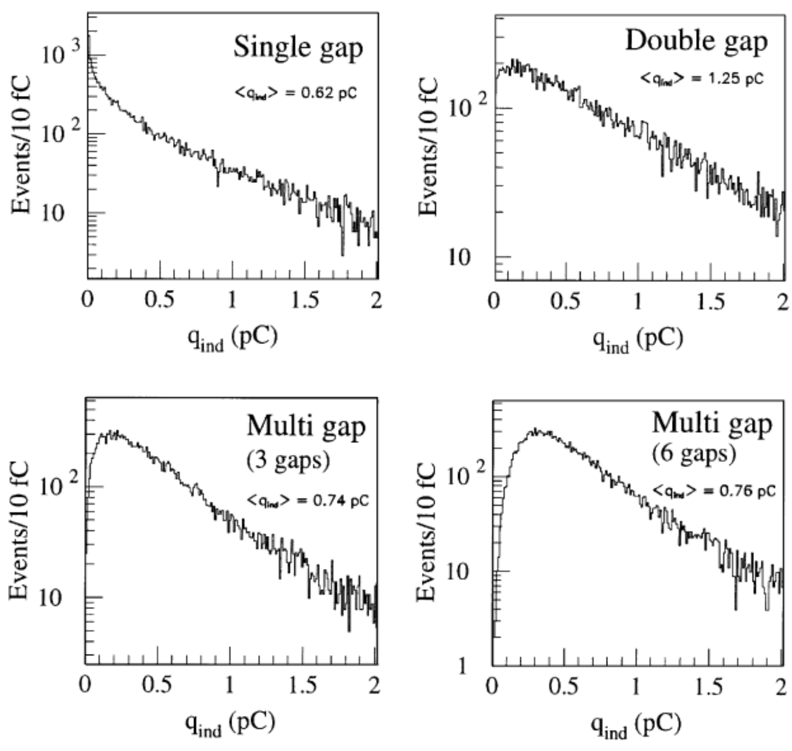

Figure 4.21: Charge spectra have been simulated for single-gap, double-gap and multigap layouts [237]. It appears that when single-gap shows a decreasing spectrum, double and multigap layouts exhibit a spectrum whose peak is detached from the origin. The detachment gets stronger as the number of gaps increases.

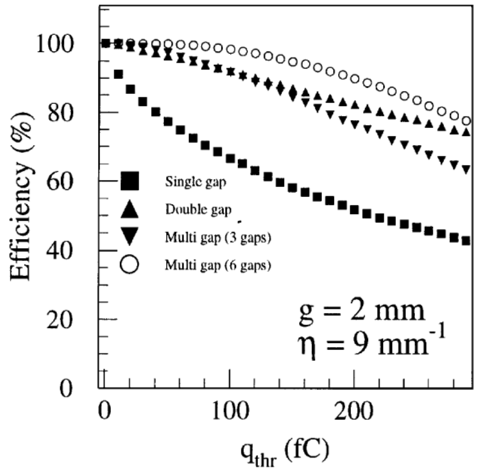

Figure 4.22: The maximal theoretical efficiency is simulated for single-gap, double-gap and multigap layouts [237] at a constant gap thickness of 2 mm *and using an effective Townsend coefficient of* $9\,\mathrm{mm}^{-1}$.

4.3 Signal formation

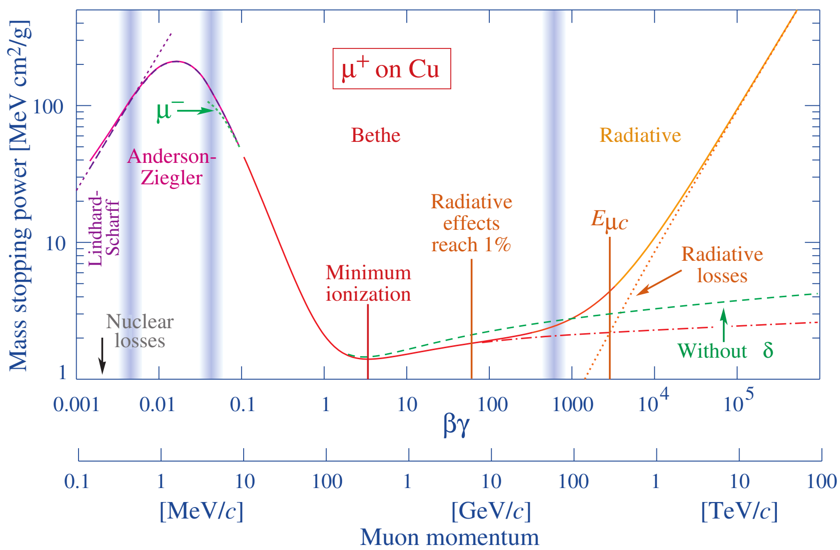

Figure 4.23: Mass stopping power as a function of $\beta\gamma = p/Mc$ *for positive muons in copper [115]. The total stopping power is indicated with a solid line and local components with dashed lines. The vertical bands are used to indicate boundaries between different approximations used at different energy range.*

The physics of Resistive Plate Chambers still is far from being fully understood and work is regularly being accomplished in trying to model these detectors the best way possible by phenomenological models using well-defined physics [221, 238, 239]. These theoretical works have nevertheless led to a better understanding of the key principles that account for RPCs signal formation. As previously discussed, the typical mixture of such a detector is in great majority composed by a ionizing gas with some quenching properties and a low ionization potential to easily produce electrons, with the addition of UV quencher and electronegative compounds. The electronic avalanche formation will be triggered by a charged particle passing through the gas, typically a muon in the case of most uses of RPCs. The production of electrons in the gas of a detector is related to the energy lost by the incoming particle traveling through a material medium. The example of the mass stopping power of copper on muons is given in Figure 4.23 on which the different energy loss mechanisms at different energy ranges are visible. Once primary electrons have been freed in the gas volume, the electric field applied in between the electrodes of the RPC will make the charges move and there will be a competition in the gas in between the Townsend and attachment coefficient which describe the evolution of the number of electrons in an avalanche. While drifting through the gas, the electrons are also subjected to diffusion that will affect the evolution of the avalanches. Finally, when the avalanche is big enough, the accumulation of negative (electrons) and positive (ions) charges in the gas volume will start affecting the local electric field. This effect is known as space charge effect.

4.3.1 Energy loss at intermediate energies

Intuitively, a particle traveling through a medium will interact with its components, losing energy. When a muon travels through the gas of a gaseous detector, at the energy range usually observed, it interacts with the molecules of the gas leading to dissipation of the transferred energy in the form of inelastic diffusion or ionization. The photons and electron-ion pairs resulting from these interactions can trigger avalanches in the gas which will contribute to feed the avalanche growth thanks to the strong electric field applied in between the two electrodes of an RPC.

The mass stopping power of moderately relativistic ($0.1 \lesssim \beta\gamma \lesssim 1000$) heavy particles ($M \gg m_e$) traveling through a medium via excitation and ionization processes was studied by Bethe in 1930 [240] and is well described by the so called the Bethe Formula given in Equation 4.5.

$$\left\langle -\frac{dE}{dx} \right\rangle = Kz^2 \frac{Z}{A} \frac{1}{\beta^2} \left(\frac{1}{2} ln \frac{2m_e c^2 \beta^2 \gamma^2 W_{max}}{I^2} - \beta^2 - \delta(\beta\gamma) \right) \tag{4.5}$$

The different parameters used in this equation are

E	-	incident particle energy $\gamma M c^2$	MeV
x	-	mass per unit area	$\mathrm{g\,cm^{-2}}$
N_A	-	Avogadro's number	6.022 140 857(74) $\times 10^{23} \mathrm{mol^{-1}}$
c	-	speed of light in vacuum	299 792 458$\mathrm{m\,s^{-1}}$
μ_0	-	permeability of free space	$4\pi \times 10^{-7} \mathrm{N\,A^{-2}}$
ϵ_0	-	permittivity of free space $\epsilon_0 = 1/\mu_0 c^2$	8.854 187 817 . . . $\times 10^{-12} \mathrm{F\,m^{-1}}$
α	-	fine structure constant $\alpha = e^2/4\pi\epsilon_0 \hbar c$	1/137.035 999 139(31)
r_e	-	classical electron radius $r_e = e^2/4\pi\epsilon_0 m_e c^2$	2.817 940 3227(19)fm
e	-	elementary charge of the electron	-1.6021766208(98) $\times 10^{-19}$C
$m_e c^2$	-	electron mass $\times c^2$	0.510 998 9461(31)MeV
K	-	constant defined as $K = 4\pi N_A r_e^2 m_e c^2$	0.307 075 $\mathrm{MeV\,mol^{-1}\,cm^2}$
z	-	charge number of incident particle	
Z	-	atomic number of absorbing medium	
A	-	atomic mass of absorbing medium	$\mathrm{g\,mol^{-1}}$
β	-	velocity of particle $\beta = v/c$	
γ	-	Lorentz factor $\gamma = (1-\beta^2)^{-1/2}$	

W_{max}	-	maximum energy transfer through a single collision	MeV
I	-	mean excitation energy of absorbing medium	eV
$\delta(\beta\gamma)$	-	density effect correction to ionization energy loss	

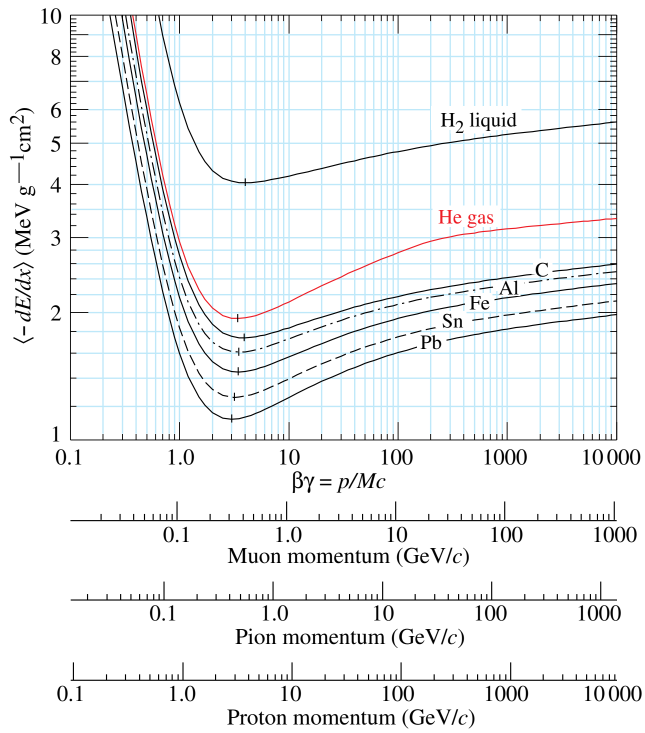

Figure 4.24: Mean mass stopping power for liquid hydrogen, as used in bubble chambers, gaseous helium, carbon, aluminum, iron, tin, and lead without the inclusion of radiative effect at higher $\beta\gamma$ necessary for pions and muons in denser materials [115].

In this equation, the maximum energy transfer W_{max} is defined as function of the incident particle mass M, expressed in $\mathrm{MeV/c^2}$

$$W_{max} = \frac{2m_e c^2 \beta^2 \gamma^2}{1 + 2\gamma m_e/M + (m_e/M)^2} \tag{4.6}$$

and the mean excitation energy I depends on the absorber. Its determination is non-trivial but recommendations are given by the International Commission on Radiation Units & Measurements (ICRU) based on experimental measurements and interpolations as showed in Figure 4.25.

For the case of copper, the mean stopping power is visible in Figure 4.23. The mean stopping power corresponding only to the Bethe range for other materials is given in Figure 4.24 and shows that $\langle -dE/dx \rangle$ is similar for each material with a slow decrease with Z. The factor affecting the equation the most is β as the dependence on M is introduced at higher energies in the logarithm via the max transfer energy per single collision but in most practicle cases, only the dependence on β is considered as most of the relativistic particles are closed to the lowest mean energy loss rate and are referred to as minimum ionizing particles (mip's). The almost logarithmic relation in between the mean energy loss rate for minimum ionizing particles and Z is showed in Figure 4.26.

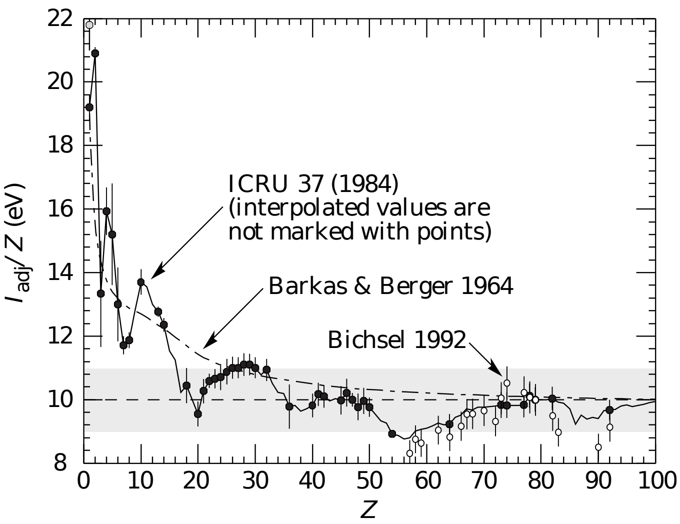

Figure 4.25: Mean excitation energies normalized to the atomic number as adopted by the ICRU [115, 241, 242].

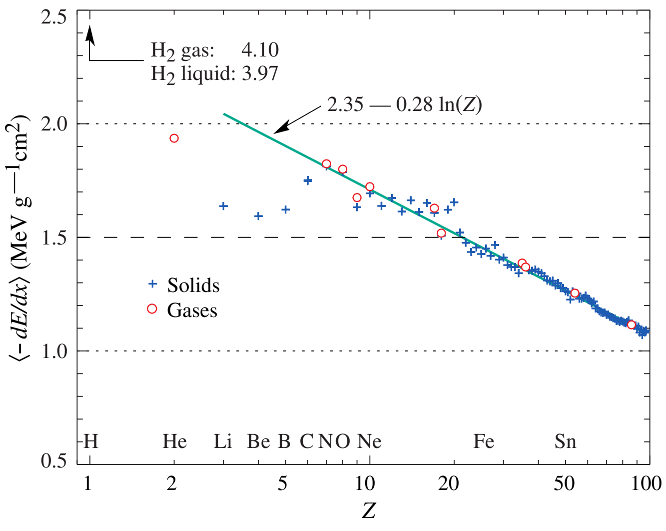

Figure 4.26: Mean mass stopping power at minimum ionization as a function of the atomic number [115].

Finally, the term $\delta(\beta\gamma)/2$ corresponds to the density effect correction introduced to account for the polarization of a real media that limits the spatial extension of the electric field of relativistic particles. Indeed, as the energy of a particle increases, the associated electric field will flatten and extend. Due to this effect, the distant collision contribution to Equation 4.5 will increase as $ln(\beta\gamma)$ but the polarization of the media truncates this rise. At high energies, the correction is given by

Equation 4.7

$$\delta/2 \longrightarrow ln(\hbar\omega_p/I) + ln(\beta\gamma) - 1/2 \tag{4.7}$$

where $\hbar\omega_p$ represents the plasma energy that depends on the electron density of the media and the electron mass and can be calculated as $\sqrt{\rho\langle Z/A\rangle} \times 28.816$ eV. The introduction of this correction term reduces the increase of the mean stopping power at higher energies as can be seen in Figure 4.23. Moreover, due to poorer electron density, the effect is less visible on gases than on liquids and solids has can be seen from Figure 4.24.

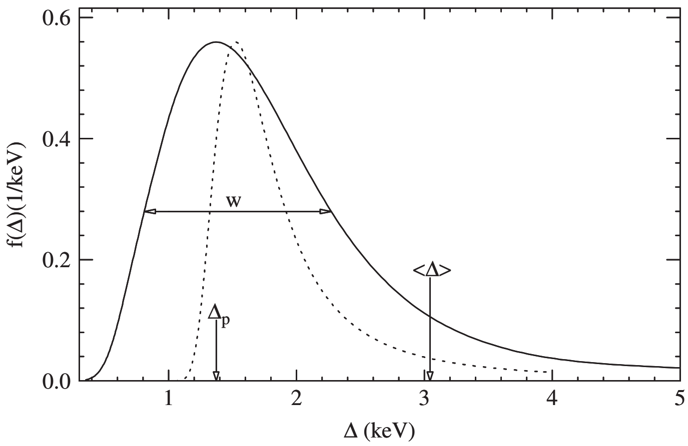

Figure 4.27: Example of straggling function $f(\Delta)$ of particles passing through $1.2\,\mathrm{cm}$ of Argon gas with a $\beta\gamma$ of 3.6 and represented with a solid line. The original Landau distribution is showed with a dashed line [243].

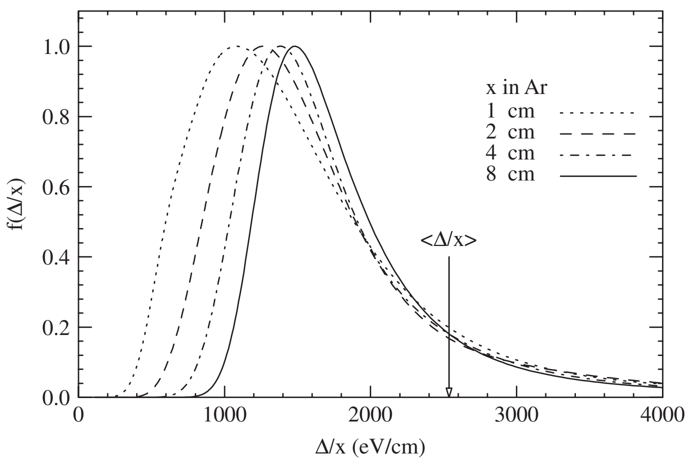

Figure 4.28: Evolution of straggling functions $f(\Delta)$ of particles passing through a volume of Argon gas with a $\beta\gamma$ of 3.6 with increasing thickness x [243].

The mean energy loss per collision can be difficult to measure for low data samples but is not always representative of the energy loss distribution for a given incident particle energy. Hence, it is easier to access the most probable energy loss which is a lower value than than the average loss due to the distribution of the energy transfer. This value is well described by a highly skewed Landau distribution for detectors with "moderate" thickness x, expressed in $\mathrm{g\,mol^{-1}}$. But for gas volumes, a Landau distribution greatly underestimates the width w of the distribution and only succeeds to provide with a correct value for the most probable energy loss, as showed in Figure 4.27. Thus, the energy loss distribution is better represented by its most probable energy loss Δ_p and its full-width-at-half-maximum (FWHM) w. As showed by Figure 4.28, the distribution is affected by the thickness of the gas volume and the most probable energy loss normalized to the thickness is increased and the width decreased, converging towards the Landau distribution, whereas the mean energy loss is unchanged. Corrections are brought to the original Landau equation in order to account better for the number of collisions leading to an increased width of the energy loss distribution [243].

In the case of gas mixtures, composed of several elements, using Bragg additivity it can be understood that the mean energy loss of the mixture is the sum of the mean energy losses in each individual element j layer of weight w_j.

$$\left\langle \frac{dE}{dx} \right\rangle = \sum w_j \left\langle \frac{dE}{dx} \right\rangle_j \tag{4.8}$$

4.3.2 Primary ionization

Using Bethe formula to understand the mean energy transfer of charged particles when traveling through a gas volume give an intuition of the physics that affect the particle but doesn't provide a detailed enough information about the individual ionizations along its tracks at a microscopic level. In order to simulate efficiently an RPC and hence understand the processes governing avalanches creation and growth, knowledge on the ionization process is necessary.

To convert the energy loss rate into a number of primary ionizations was developed in 1980 the Photo-Absorption Ionisation (PAI) model [244] based on the cross section of ionization of gas atoms to real photons and the dielectric constant of the medium through which the charged particles are going. Indeed, the interaction of charged particles with the gas molecules being of electromagnetic nature, it is mediated by quasi-real photons and, hence, the cross section to photon ionization is important to understand. This approach is nevertheless semi-classical as it relies on classical electrodynamics and it only gives access to the energy transfer to the gas atoms and no information on the energy dissipation and secondary emissions is available on the output of the model. The energy transferred to the medium is not all used for ionization. For an energy deposition Δ, the number of electron-ion pairs produced is:

$$\Delta = n_i W \tag{4.9}$$

W corresponds to the mean work per pair production that depends on the medium and is greater than the ionization potential leading to the conclusion that part of the transferred energy is dissipated through other processes [239, 245]. In order to understand the energy dissipation and the secondary emissions, the fine structure of each atom is taken into account. Through the PAI model, the incident charged particle interacts is assumed to interact with the full atom rather than with a single electron.

Although, considering that the particle interacts with a single electron, leads to the possibility to study the excited state of the atom once the photo-electron has been emitted with an energy corresponding to the transferred energy minus the binding energy of the electronic shell. The resulting vacancies in the electronic shell will be filled through emission of photons or Auger electrons and can contribute to further ionization or excitation in the gas volume. Fluorescence photons are usually not considered as they only constitute a very small fraction of secondary emissions [246]. Assuming that the transferred energy is absorbed in its totality by a single electronic shell, the PAI model was modified to include relaxations and constitute the new Photo-Absorption Ionisation with Relaxation (PAIR) model [246]. In this model, the cross section corresponding to the whole atom is re-expressed using a sum of partial cross sections corresponding to the different electronic shells. When one or more electrons are knocked out of the atom, the vacancies are filled by electrons of the shell above with relaxation by Auger electron emission. These processes happen in cascade from the inner shell to the outer one until all the vacancies are filled and the energy has been released.

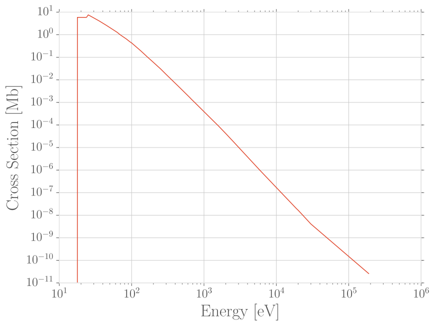

(a) Helium

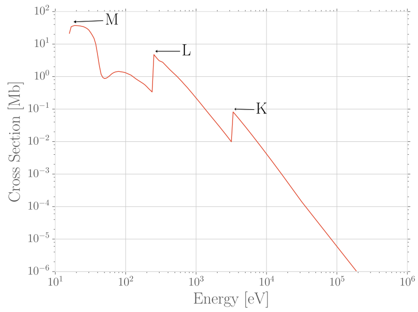

(b) Argon

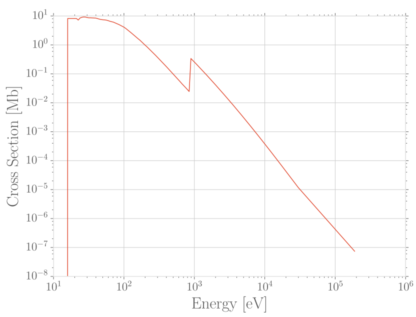

(c) Neon

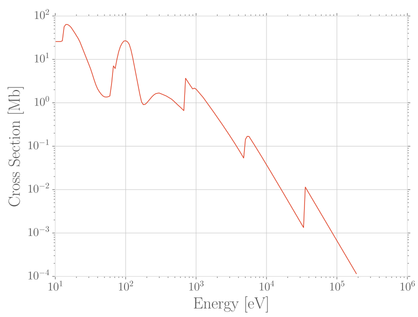

(d) Xenon

Figure 4.29: Photoabsorption cross section as computed by `HEED` *for nobles gases with different electric shell numbers [239].*

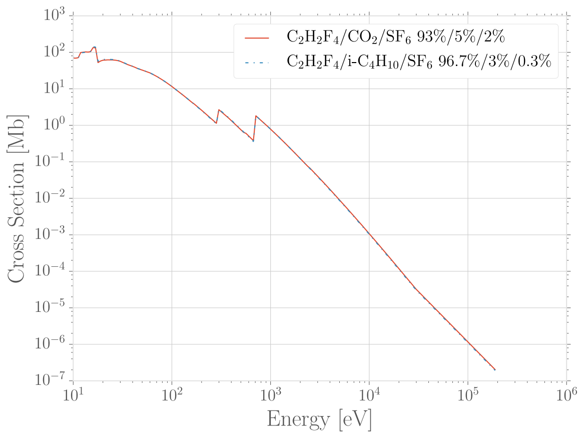

Figure 4.30: Photoabsorption cross section as computed by `HEED` *for typical RPC gas mixtures [239]. The RPC mixture with CO_2 corresponds to the mixture used by CALICE SDHCAL [247] while the other one was forseen for the experiment ATLAS [248] but has been changed since then.*

This model is included in the program `HEED` developed at CERN [249] and called by `Garfield`, a program developed for the simulation of gaseous detectors. The results for the cross section for a few noble gases are given in Figure 4.29. It can be seen that for each shell, the cross section is increased. More complex patterns are seen with bigger atoms such as Xenon on Figure 4.29d. For gas mixtures, like the typical RPC mixtures, the cross section is showed in Figure 4.30. Both mixtures being mainly composed of $C_2H_2F_4$, the variations in between the 2 cross section profiles are very subtle and depends on the concentration of the other compounds.

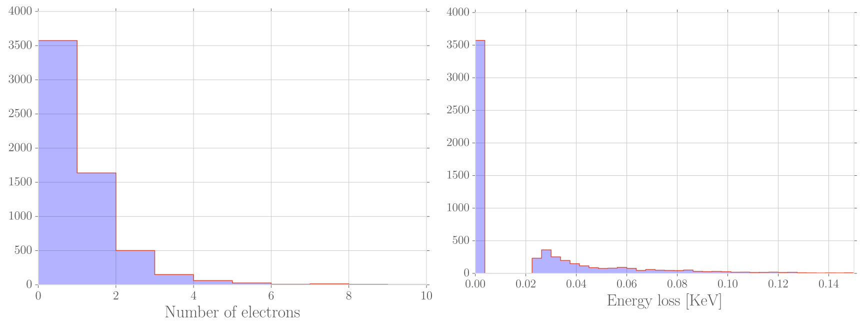

(a) Helium

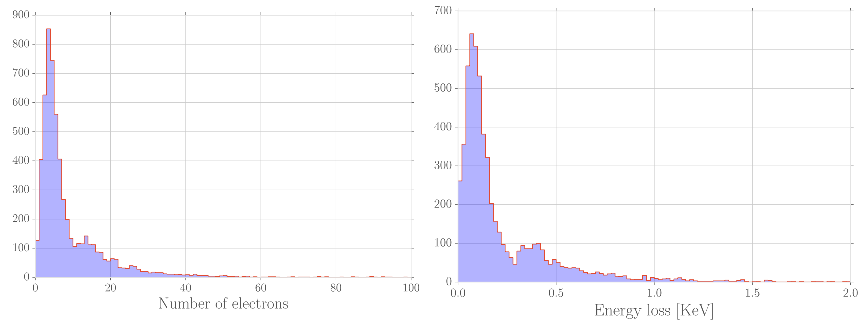

(b) Argon

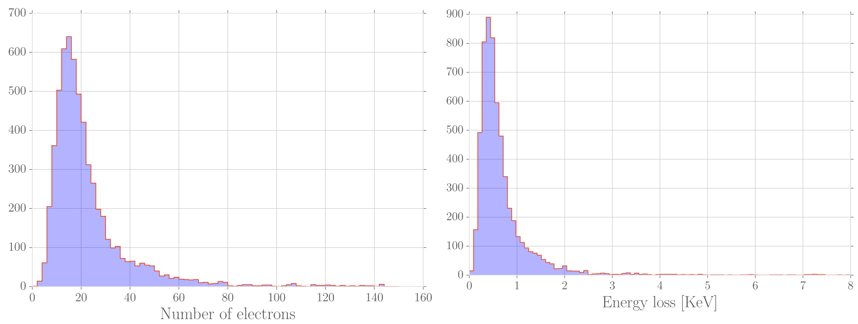

(c) 96.7% $C_2H_2F_4$, 3% i-C_4H_{10} and 0.3% SF_6 [248]

Figure 4.31: Distributions of number of electrons (left) and energy loss (right) for a $5\,\mathrm{GeV/c}$ *muon passing through* $1.2\,\mathrm{mm}$ *of Helium (Figure 4.31a), Argon (Figure 4.31b) or a typical RPC gas mixture (Figure 4.31c) [239].*

Once the cross section of interaction is known, it is possible to extract the distribution of energy loss and of the number of produced electrons, as showed in Figure 4.31 for Helium, Argon, which is used in gaseous detectors, and for a typical RPC mixture [239]. The distributions are computed using `HEED` and show typical straggling function profiles with some complex structures that can be related to interaction of the incoming particle with the different electronic shells. Helium does not have a great photoabsorption cross-section according to Figure 4.29a and a muon will not be likely to lose a lot of energy and to create a lot of electrons whereas in a more complex atom like Argon, the cross-section is greater and will lead to a greater energy loss of muons and more electron produced. Finally, a complex gas mixture used in RPCs will offer an even greater cross-section, a wider energy loss distribution and will be able to produce more electrons. The same information is seen by looking at the evolution of the mean number of clusters as a function of the lorentz factor associated to muons showed in Figure 4.32a. Indeed, the greater photoabsorption cross-section of RPC mixtures allows for a much greater number of clusters to be created by charged particles. The size of these clusters is studied through Figure 4.32b which shows that, in most of the cases (≈80%), the clusters only are composed of a single electron which is consistent with minimum ionizing particles.

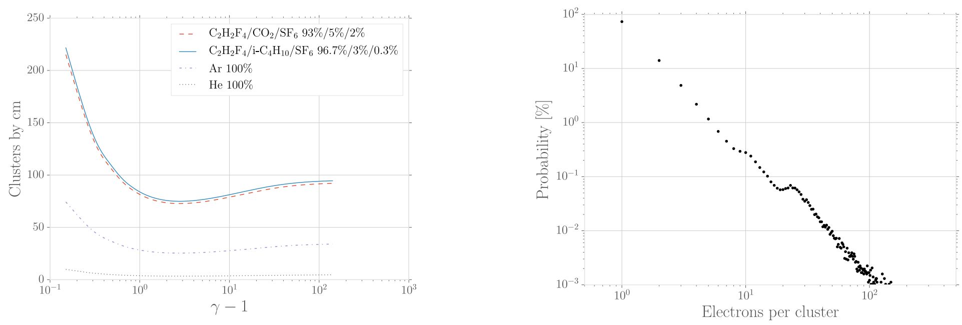

(a) (b)

Figure 4.32: Figure 4.32a: Mean cluster density for muons through different gas volumes [239]. Figure 4.32b: Distribution of the number of electrons per cluster for a $5\,\mathrm{GeV/c}$ *muon traveling through a mixture of 96.7%* $C_2H_2F_4$*, 3% i-*C_4H_{10} *and 0.3%* SF_6 *[239, 248].*

4.3.3 Development and propagation of avalanches

From the clusters released in the gas volume by the charged particles, free electrons will start drifting due to the electric applied in between the electrodes of the RPC. Gaining velocity and energy, these electrons in their turn will be able to ionize the gas. This process being repeated by all the produced electrons will trigger an avalanche to develop.

The growth of the avalanche can be intuitively understood as a competition between two effects. Due to their increasing energy, electrons have a probability to trigger new ionizations by interacting with gas molecules. On the other hand, before the minimal amount of energy is reached, the electrons can get attached to a gas molecule instead. These two effects can be described using a simple model in which the multiplication and attachment processes are given by the Townsend coefficient α and the attachment coefficient η, assuming that the history of previous interactions in the gas does not influence new interactions. This model simply takes into account probabilities to have at the gas depth z, for a given number n of free electrons in the gas, $n+1$ or $n-1$ electrons at the depth $z+\mathrm{d}z$ (respectively $n\alpha\mathrm{d}z$ and $n\eta\mathrm{d}z$). Then, the mean number of electrons $\bar{n}$ and cations $\bar{p}$ can be written for single compound gases as

$$\frac{\mathrm{d}\bar{n}}{\mathrm{d}z} = (\alpha - \eta)\bar{n}\,, \quad \frac{\mathrm{d}\bar{p}}{\mathrm{d}z} = \alpha\bar{n} \tag{4.10}$$

which, assuming the initial conditions $\bar{n}(0) = 1$ and $\bar{p}(0) = 0$, lead to the mean number of electrons and cations at a depth z

$$\bar{n}(z) = e^{(\alpha-\eta)z}\,,\ \bar{p}(z) = \frac{\alpha}{\alpha - \eta}\left(e^{(\alpha-\eta)z} - 1\right) \tag{4.11}$$

The Townsend and attachment coefficient as a function of the applied electric field are given in Figure 4.33 for a standard RPC gas mixture using `Magboltz` [250].

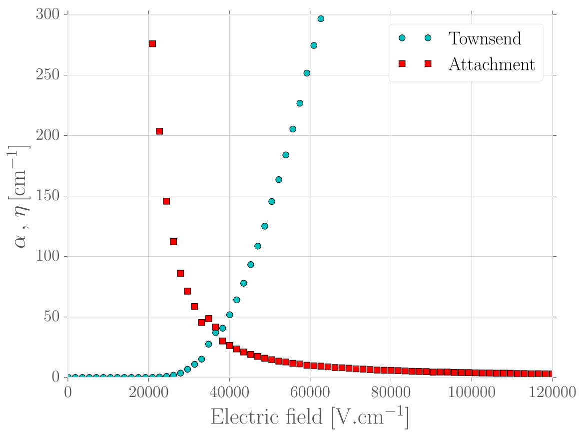

Figure 4.33: Townsend and attachment coefficient for a typical 96.7/3/0.3 mixture of $C_2H_2F_4$/i-C_4H_{10}/SF_6, at a temperature T =296.15 K and a pressure P =1013 hPa [239, 248].

Nevertheless, there are more to the avalanche growth than simply these two factors. Throughout the 20^{th} century, models have been developed to better understand the physics of discharges in gas. In 1937, Furry developed a model to describe electromagnetic cascades [251] that would be used for electron avalanches in gas during the 1950s. Furry realized that the use of a Poisson law to describe the distribution of shower sizes could not be accurate as he understood that the events occurring in the development of a cascade are not independent from each other, as a Poisson law would suggest. Indeed, part of the particles produce others and this process depends on both their original energy and energy lost. Experimental results showed excess of small showers and an under estimate of very large ones. To solve this problem, Furry proposed a distribution of sizes of following the likelihood described in Equation 4.12, in which $\bar{n} = e^{\alpha z}$, compared with a Poisson law in Figure 4.34.

$$P(n, \bar{n}) = \bar{n}^{-1}(1 - \bar{n}^{-1})^{n-1} \tag{4.12}$$

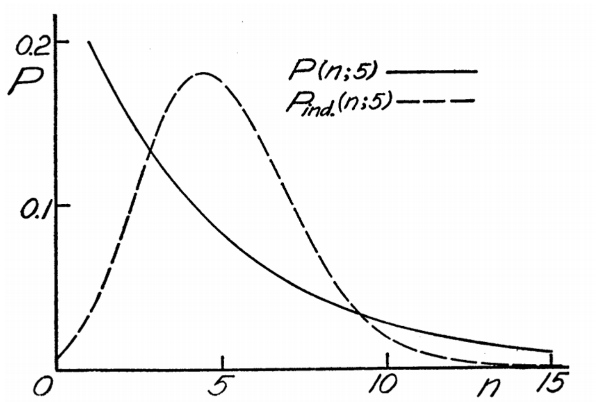

Figure 4.34: Comparison of the distribution law of Furry and the Poisson law for $\bar{n} = 5$ [251].

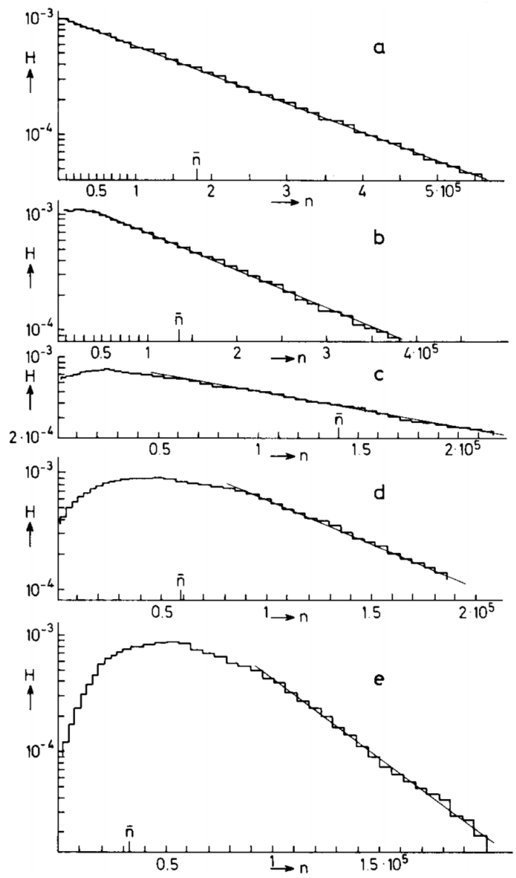

Figure 4.35: Single-electron avalanche size distribution in a proportional counter filled with methylal at different E/p values. (a) 70, (b) 76.5, (c) 105, (d) 186.5, (e) 426$\mathrm{V/cm\,torr}$ *[252].*

In this model, no extra energy is brought to the electrons in the showers, contrary to the case of a gaseous detector such as an RPC where an electric field accelerates them. Using the Furry model, Genz studied the fluctuations in electron avalanches in gaseous detectors [252]. Collisions leading to ionizations leave electrons with an energy much smaller than the ionization energy eU_i, where U_i is the ionization potential of a gas molecule. Hence, the electrons need to travel a distance $s = U_i/E$ along the electric field E to acquire a high enough energy to trigger a new ionization. For the probability of a new ionization to be independent from the path followed by the electrons since the previous ionization, the mean free path $1/\alpha$ of electrons in the gas has to be large compared to s and thus $E/\alpha \gg U_i$. The Townsend coefficient is related to the gas pressure leading to conditions on the value of E/p. Avalanches in gas are large compared to the showers Furry has studied in his original paper. For very large avalanche sizes, Equation 4.12 can be written as an exponential, as showed in Equation 4.13.

$$P(n, \bar{n}) = \bar{n}^{-1} e^{-n/\bar{n}} \tag{4.13}$$

This exponential behaviour is showed through Figure 4.35. In practice, to fully understand the avalanche growth, taking into account the path followed by electrons from one ionization to another will become necessary. In the same paper, Genz then discusses models using Polya distributions to estimate the multiplication by looking at the size of the avalanche it self. Indeed, the number of charge carriers in the avalanche might become important enough to have an effect on the multiplication process. To account for this, it was proposed to use a varying Townsend coefficient such as described by Equation 4.14 depending on the position x in which θ is an empirical parameter leading to the probability distribution of Equation 4.15. In the limit case where θ goes to 0, the formula describes again the Furry model. But the data deviates from this model as well at large n values. Moreover, the introduction of an empirical parameter makes the model hard to interpret physically.

$$\alpha(n,x) = \alpha(x)\left(1 + \frac{\theta}{n}\right), \quad n > 0 \tag{4.14}$$

$$P(n,x) = \frac{1+\theta}{\bar{n}}\frac{1}{\theta!}\left(\frac{n(1+\theta)}{\bar{n}}\right)^{\theta} e^{-\frac{n(1+\theta)}{\bar{n}}} \tag{4.15}$$

In order to have a model that describes reality better, the introduction of the attachment into the model is an important step. Despite its limitations, the Furry model had the advantage to well describe avalanches occurring when the attachment could be ignored. This is only natural that this model was then extended to included attachment. This was done by Riegler, Lippmann and Veenhof [248] which showed that was important was to consider both the Townsend coefficient describing the multiplication *and* the attachment coefficient, not only the effective multiplication coefficient $\bar{\alpha} = \alpha - \eta$. The probability to see an avalanche started by a single electron grow to a size n after having traveled a distance z through the gas is given by Equation 4.16.

$$\begin{aligned} P(n,z) = {} & P(n-1,z)\,(n-1)\alpha \mathrm{d}z\,(1-(n-1)\eta \mathrm{d}z) \\ & + P(n,z)\,(1-n\alpha \mathrm{d}z)\,(1-n\eta \mathrm{d}z) \\ & + P(n,z)\,n\alpha \mathrm{d}z\,n\eta \mathrm{d}z \\ & + P(n+1,z)\,(1-(n+1)\alpha \mathrm{d}z)\,(n+1)\eta \mathrm{d}z \end{aligned} \tag{4.16}$$

The first term of this probability that from a state with $n-1$ electrons, only 1 multiplies while the others don't get attached. Both the second and third terms describes the probability that from a state with already n electrons the total number of electrons stay the same. On the second term, no electron gets attached nor multiplies while on the third term, 1 electron gets multiplied and 1 gets attached to compensate. Finally, the fourth term describes the probability to fall from a state with $n+1$ to a state with n electrons due to the attachment of a single electron. At the first order, the evaluation of the previous expression leads to Equation 4.17 which general solution is given in Equation 4.18 in which are introduced the variables $\bar{n}(z)$, defined as in Equation 4.11, and $k = \eta/\alpha$ making explicit the fact that the distribution does not depend on the effective Townsend coefficient only.

$$\frac{\mathrm{d}P(n,z)}{\mathrm{d}z} = -P(n,z)n(\alpha+\eta) + P(n-1,z)(n-1)\alpha + P(n+1,z)(n+1)\eta \tag{4.17}$$

$$P(n,z) = \begin{cases} k\frac{\bar{n}(z)-1}{\bar{n}(z)-k}, & n = 0 \\ \bar{n}(z)\left(\frac{1-k}{\bar{n}(z)-k}\right)^2\left(\frac{\bar{n}(z)-1}{\bar{n}(z)-k}\right)^{n-1}, & n > 0 \end{cases} \tag{4.18}$$

The example given through Figure 4.36 shows the importance of each individual process in the growth of avalanches and the fluctuation of their size. The values of α and η will influence the probability distribution, as can be seen from Figure 4.36a. Then, Figure 4.36b shows that the fluctuation really takes place within the very first interactions. Indeed, when the avalanche contains a large enough number of charge carriers (a few hundreds), its size then increases like $e^{z(\alpha-\eta)}$.

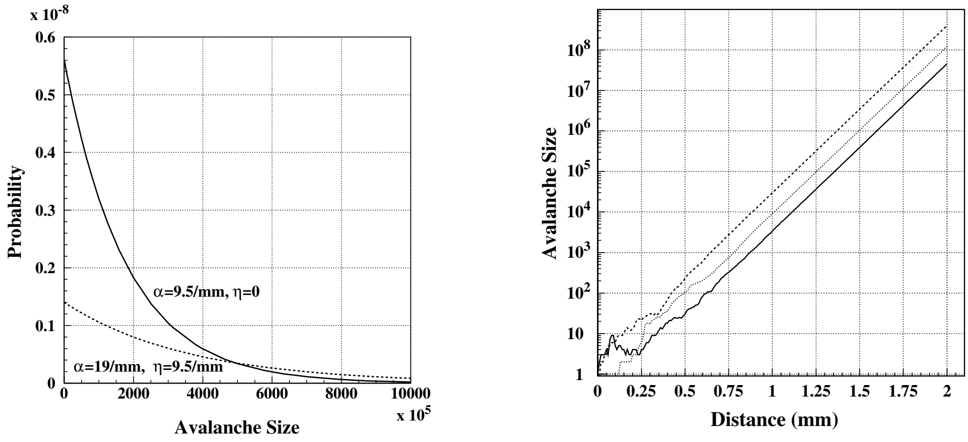

(a) *(b)*

Figure 4.36: Figure 4.36a: Comparison of avalanche size distributions for different values of Townsend and attachment coefficients. The effective Townsend coefficient is the same for both distributions. Figure 4.36b: Fluctuation in avalanches size for avalanche started by a single electron with $\alpha = 13\,\mathrm{mm}^{-1}$ *and* $\eta = 3.5\,\mathrm{mm}^{-1}$ *[248].*

4.3.4 Drift and diffusion of the electron cloud

During the growth of avalanches, an electron cloud drifting along the electric field through the gas will undergo thermal diffusion due to random collisions with the gas molecules. This phenomenon can be studied using Maxwell-Boltzmann distribution whose mean is defined by the thermal energy of the cloud $\langle E \rangle = 3/2kT$ with an extra component coming from the constant drift motion. The drift of electrons along the field lines is usually observed on a macroscopic scale through which the speed can be assimilated to a constant v_D which corresponds to the mean drift speed over a large number of collisions in the gas.

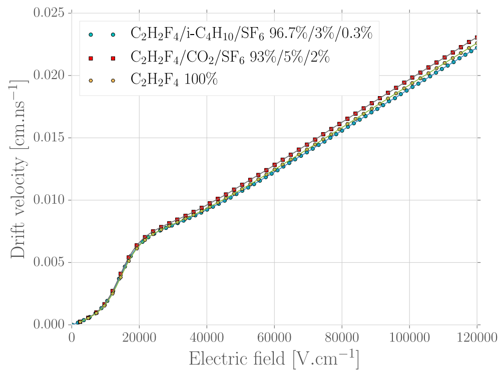

(a)

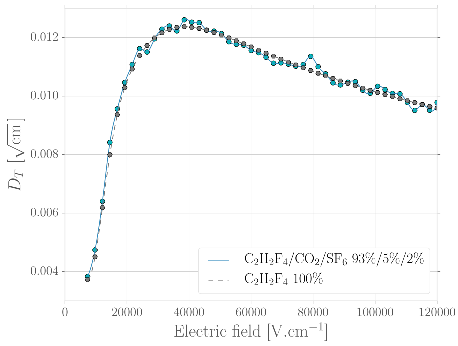

(b)

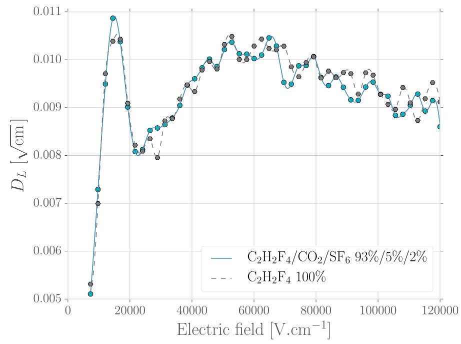

(c)

Figure 4.37: Figure 4.37a: Electrons mean drift velocity v_D in pure $C_2H_2F_4$ and typical RPC gas mixtures. Figure 4.37b: Transverse diffusion coefficient in pure $C_2H_2F_4$ and a typical RPC gas mixture. Figure 4.37c: Longitudinal diffusion coefficient in pure $C_2H_2F_4$ and a typical RPC gas mixture. All results are given with a pressure $P = 760\,\mathrm{Torr}$ and a temperature $T = 296.15\,\mathrm{K}$ [239].

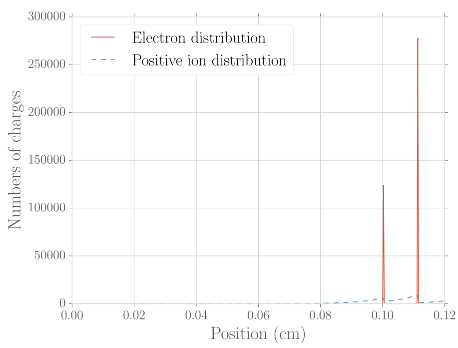

(a) $n_e = 4.01 \times 10^5$

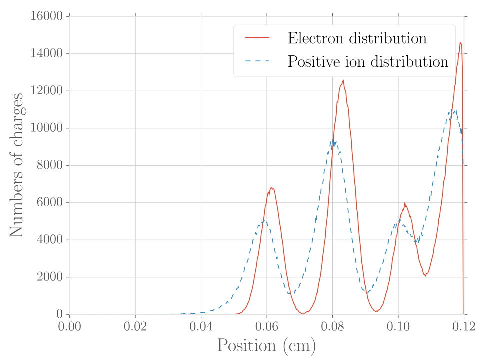

(b) $n_e = 1.25 \times 10^6$

Figure 4.38: Comparison of the free charge carriers in the gas after a time $t = 7.90\,\mathrm{ns}$ in the case where no diffusion is taken into account to simulate the avalanche (Figure 4.38a) and in the case where the diffusion is implemented (Figure 4.38b) [239].

Indeed, at the microscopic scale, the electrons are drifting over a distance δz while acquiring the corresponding kinetic energy $T = e_0|\overrightarrow{E}|\delta z$ until they are slowed down by a collision in which they lose part of their energy. This process is repeated as long as electrons are free carriers. Starting from a point-like electron cloud, the Gaussian density distribution at $\overrightarrow{r_0}$ will be described by Formula 4.19 in which the width of the isotropic distribution is $\sigma = 2\bar{D}t$, with $\bar{D}$ being a diffusion coefficient expressed in m^2/s [221].

$$\varphi(\overrightarrow{r}, t) = \frac{1}{\left(\sqrt{2\pi}\sigma(t)\right)^3} exp\left(-\frac{(\overrightarrow{r} - \overrightarrow{r_0})^2}{2\sigma^2(t)}\right) \tag{4.19}$$

Now, if the constant drifting motion is added, the distribution is anisotropic and can be divided onto transversal (Formula 4.20) and longitudinal (Formula 4.21) terms, $\varphi(r, z, t) = \varphi_T(r, t)\varphi_L(z, t)$, with a cylindrical symmetry around the field axis [221]. The variables t and $\sigma_{T,L}(t)$ can be hidden to the profit of the diffusion coefficients by using the relations $v_D = l/t$ and $\sigma^2_{T,L}(t) = 2\bar{D}_{T,L}l/v_D$ and introducing new diffusion coefficients $D_{T,L} = \sqrt{2\bar{D}_{T,L}/v_D}$ in order to explicitly show the dependence of the Gaussian width in drifted distance l.

$$\varphi_T(r, t) = \frac{1}{D_T^2 l} exp\left(-\frac{(r - r_0)^2}{2D_T^2 l}\right) \tag{4.20}$$

$$\varphi_L(z, t) = \frac{1}{\sqrt{2\pi l}D_L} exp\left(-\frac{(z - z_0)^2}{2D_L^2 l)}\right) \tag{4.21}$$

These coefficients, as well as the drift velocity of the electrons, can be calculated thanks to `Magboltz` as showed in Figure 4.37. The influence of the diffusion on the distribution of charge carriers throughout the gas volume is depicted in Figure 4.38. From very localised electron clusters in the gas in Figure 4.38a, a Gaussian diffusion is then visible in Figure 4.38b. Due to the interactions with gas molecules during the drift, diffusions can occur in the forward and backward direction. Electrons diffused backward will effectively drift over a longer distance and multiply more than electrons diffused forward that will see a shorter drift length. As an effect, the avalanche develops over a longer time and extends over a greater gas volume than in the case the electron cloud is considered as point like and without diffusion. Moreover, as a side effect to the longer growth of the avalanche due to backward longitudinal diffusion, the total production of electrons is increased.

4.3.5 Space charge effect & streamers

Now that has been considered the basic processes that influence the development of avalanches in a gaseous detector in the previous sections, it is now important to consider the influence of the charge carriers present in the avalanche on the electric field seen by the avalanche. Indeed, each charged particle induces an electric field and it is only natural that the increasing density of electrons and ions in the detector volume will affect the electric field. Thus, parameters such as the Townsend and attachment coefficients, drift velocity or diffusion coefficients will find themselves to be modified along the gas gap length due to this effect referred to as *space charge effect*. Figure 4.39 is a more detailed version of Figure 4.1 *(b)* in which three electric regions are distinguished [221]. When compared to the linear electric field of strength E_0 that is developed in between the detector's electrodes, the accumulation of negative charges (electrons) on the front of the avalanche will reinforce the effective electric field in between the anode and the avalanche front. Deeper in the gas volume, the positive charges (cations) slowly drift towards the cathode and can induce together with the avalanche front opposite electric field loops. Finally, due to the density of positive charges, the electric field seen in between the ions tails and the cathode charged with negative charges is on average stronger than E_0 and compensate for the locally reversed field E_2. Lippmann roughly estimated by considering that 10^6 charges were contained in a sphere of radius $r_d = 0.1\,\mathrm{mm}$ that the space charge effect could change the electric field by 3% and the Townsend and attachment coefficient up to 14% [221, 239].

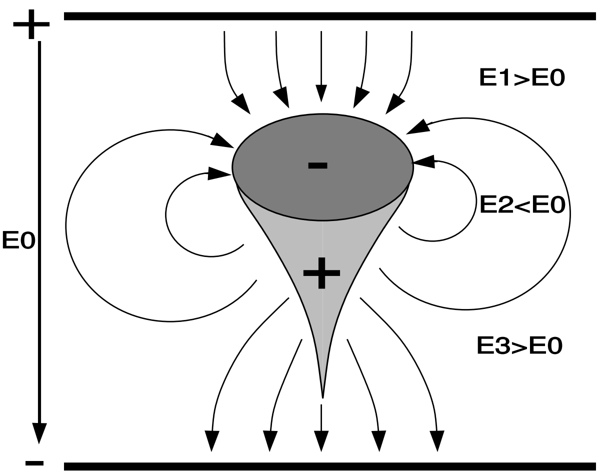

Figure 4.39: Schematic representation of an avalanche and of the electric field deformation it causes due to the local concentration of charge carriers [221].

To account for the space charge effect, the electric potential and field of free charges are solved and applied to each charge in the avalanche [221, 239]. As discussed by Français who has been working on simulating RPCs similar to that used by the SDHCAL project of ILC, the computation of these equations for each individual charge carrier to dynamically know the space charge field at every stage of an avalanche development is a difficult task and would require far too much computation time and a solution is to pre-compute an interpolation table keeping an adequately large number of values of the space charge field for each position in space thanks to which the values stored in the interpolation table become very close to the analytic solution and allow for a much faster simulation.

The study of space charge effect through simulation shows that the it can lead to a saturation of the avalanche growth due to the deformation of the electric field, as showed through Figure 4.40. Additionally, a more precise understanding of the space charge effect is given through Figure 4.41 which looks at the distribution of charges and the distortion of the electric field at different steps of the evolution of an avalanche in a RPC. At the moment a $5\,\mathrm{GeV}$ muon ionizes the gas, electron-ion pairs are created in the gas in different clusters (Figure 4.41a). Later, the first clusters have reached the anode while the clusters that where created the closest to the cathode are now big enough to start influencing the electric field in the gap (Figure 4.41b). When a cluster is big enough, the electric field in front of it locally increases a lot and contributes to a stronger but very localised multiplication. At the same moment, the positive ions right behind the cluster avalanche front decrease the electric field, saturating the electron multiplication on the tail of the electron cloud (Figure 4.41c).

3054 Finally, when all the electrons have reached the anode and are relaxing, the electric field still is very
3055 deformed by the distribution of both positive and negative ions in the gas volume closest to the anode
3056 (Figure 4.41d).

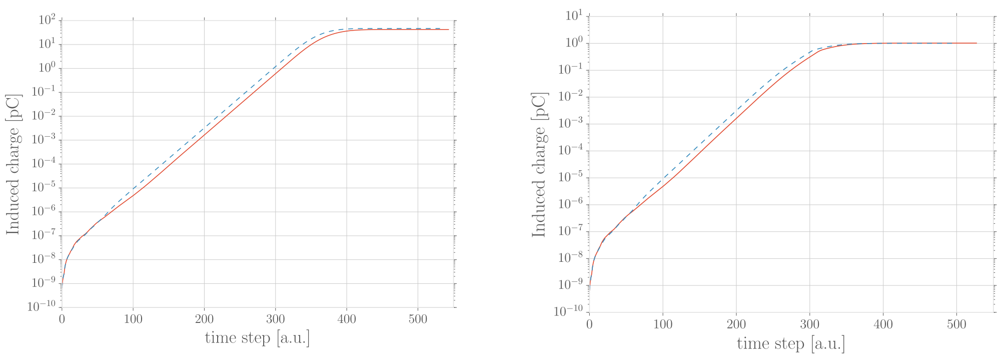

(a) *(b)*

Figure 4.40: Evolution of the charge induced by an avalanche started by a single electron in a $1.2\,\mathrm{mm}$ *thick RPC with an applied electric field of* $54\,\mathrm{kV}/\mathrm{cm}$ *in the case space charge is not taken into account (Figure 4.40a) and in the case it is implemented into the simulation (Figure 4.40b). The total induced charge is correlated to the size of the avalanche [239].*

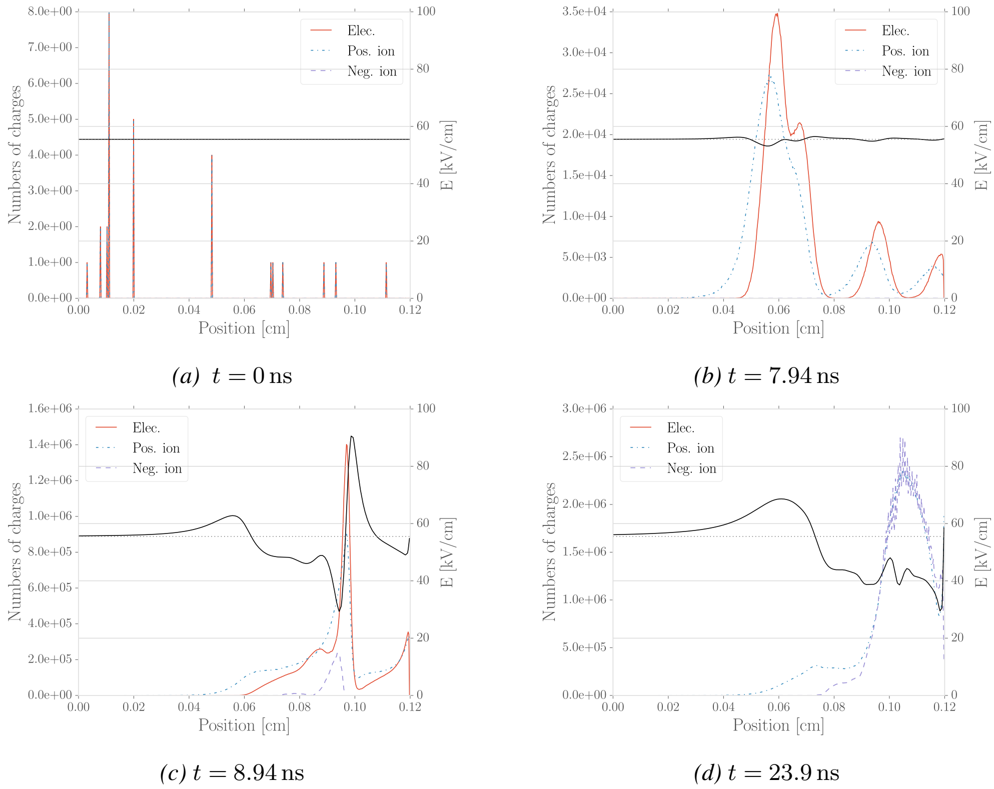

(a) $t = 0\,\mathrm{ns}$

(b) $t = 7.94\,\mathrm{ns}$

(c) $t = 8.94\,\mathrm{ns}$

(d) $t = 23.9\,\mathrm{ns}$

Figure 4.41: Distributions of charge carriers within the gas volume of a $1.2\,\mathrm{mm}$ *thick RPC and the corresponding deformation of the electric field at different time steps with an applied electric field of* $55.5\,\mathrm{kV/cm}$ *[239].*

The electric field following the development of an avalanche can stay perturbed for a long time with respect to the avalanche development due to the slow drift of the much heavier ions. This can result in powerful secondary avalanches triggered by the fluctuation of the electric field together with the emission of UV-photons leading to emission of electrons at the surface of the electrode. This is a slow phenomenon compared to the development of avalanches. Experimentally, it is observed that the stronger the electric field applied over the gap, the sooner after the avalanche, referred to as *precursor signal* in this context, and the stronger will the secondary avalanche be, possibly reaching the streamer regime. This could be due to the amount of UV-photons emitted by the growing precursor. These photons will be able to trigger new avalanches in a radius of a few mm around the precursor by knocking electrons from the cathode by photoelectric effect. The strong distortions of the electric field due to a large avalanche will be more likely to emit UV-photons as the electric field at the front of the precursor avalanche will be large, providing the electrons with a larger energy. Eventually, the new avalanches can grow to form streamers.

4.4 Effect of atmospherical conditions on the detector's performance

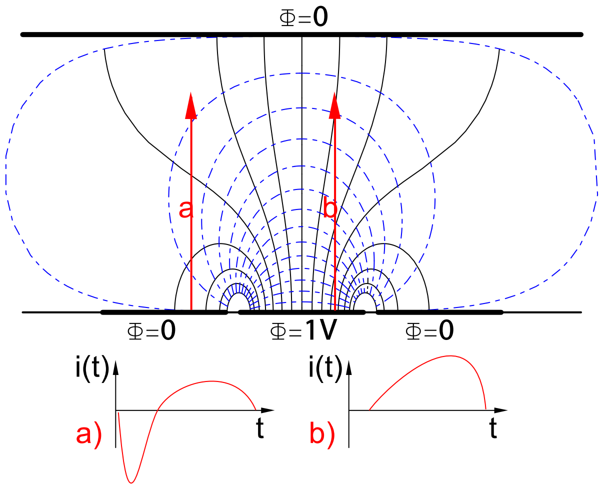

Figure 4.42: Representation of the weighting field in the volume of an RPC and the resulting induced current in the strip placed at $1\,\mathrm{V}$ *and its neighbour connected to the ground. The induced current corresponds, as can be understood from Formula 4.22 [221].*

Accordingly to Ramo's theorem, the movement of charge carriers, and in particular, the movement of a dense electron cloud toward the anode induces a current signal on one or more of the readout electrodes (strips or pads). The ions on the other hand induce only a very small current as their movement is much slower than which of the electrons. The current induced by $n_C l$ clusters of $N_j(t)$ charge carriers drifting at velocities $\overrightarrow{v_{Dj}}(t) = \overrightarrow{\dot{x}_j}(t)$ at a time t is given by Formula 4.22 in which e_0 is the unit charge and $\overrightarrow{E_w}$ is the *weighting field*.

$$i(t) = \sum_{j=1}^{n_C l} \overrightarrow{E_{wj}}(\overrightarrow{x_j}(t)) \cdot \overrightarrow{v_{Dj}}(t) e_0 N_j(t) \tag{4.22}$$

The weighting field, that has been schematized in Figure 4.42, corresponds to the electric field that would be observed in the gas gap if a readout electrode is placed at a potential of $1\,\mathrm{V}$ while keeping all the other electrodes grounded. Then the induced charge in the readout can be simply obtained by integrating Formula 4.22 over the duration T of the signal, as given by Formula 4.23.

$$Q(t) = \int_0^T \sum_{j=1}^{n_C l} \overrightarrow{E_{wj}}(\overrightarrow{x_j}(t)) \cdot \overrightarrow{v_{Dj}}(t) e_0 N_j(t) \tag{4.23}$$

The signal induced in the readout of RPCs operated in avalanche mode is then sent into Front-End Electronics in which they will be pre-amplified and discriminated. The discrimination and digitization of signals in CMS FEE are described through Figure 4.43. On a first stage, analogic signals are amplified, following the curve given on Figure 4.44, and then sent to the Constant Fraction Discriminator (CFD) described in Figure 4.45. At the end of the chain, $100\,\mathrm{ns}$ long pulses are sent in the LVDS output. The digital signals are both used as trigger for CMS and to evaluate the performance of the detectors. The performance will depend on the applied HV, i.e. on the electric field inside of the gas volume, but also on the threshold applied on the CFDs. Indeed, in order to reduce the probability to measure noise, the threshold is set to a level where the noise is strongly suppressed while the signals are not too affected. Typically, CMS FEEs are set to a threshold of $215\,\mathrm{mV}$ after pre-amplification, corresponding to an input charge of about $140\,\mathrm{fC}$.

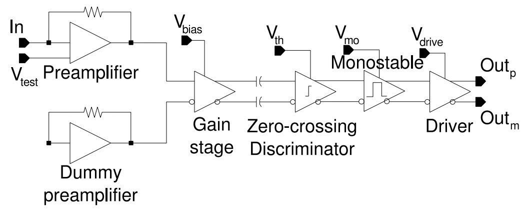

Figure 4.43: Schematics of CMS RPC FEE logic.

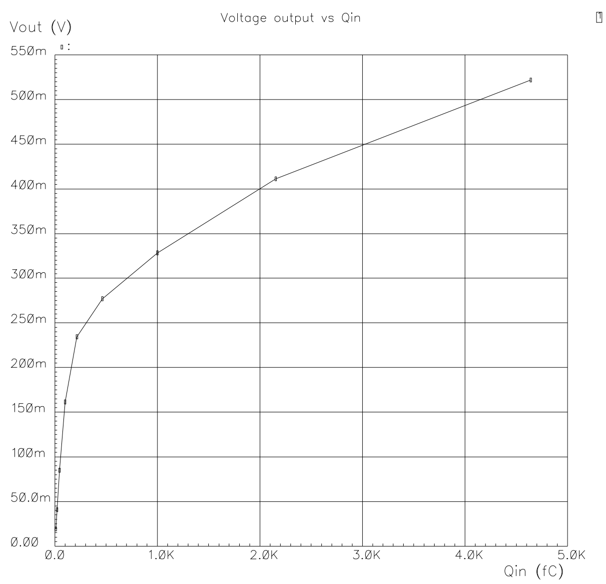

Figure 4.44: Equivalence in between the charge of the induced signal in input of the CMS FEE and the signal strength on the output of the pre-amplifier.

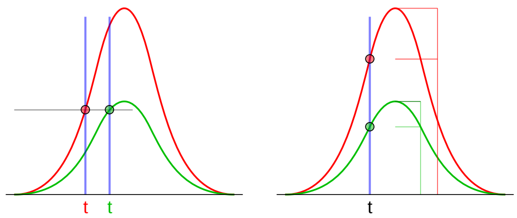

(a)

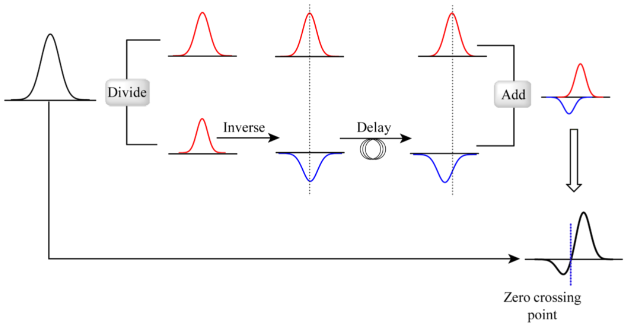

(b)

Figure 4.45: Description of the principle of a CFD. A comparison of threshold triggering (left) and constant fraction triggering (right) is shown in Figure 4.45a. Constant fraction triggering is obtained thanks to zero-crossing technique as explained in Figure 4.45b. The signal arriving at the input of the CFD is split into three components. A first one is delayed and connected to the inverting input of a first comparator. A second component is connected to the noninverting input of this first comparator. A third component is connected to the noninverting input of another comparator along with a threshold value connected to the inverting input. Finally, the output of both comparators is fed through an AND gate.

The performance of a detector is then simply measured relatively to which of a reference detector used as trigger as the ratio in between the number of events recorded in coincidence in the detector and the reference and the total number of trigger events, $\epsilon = n_{events}/n_{triggers}$. An example of efficiency measured as a function of the effective voltage HV_{eff} is given in Figure 4.46 and can be fitted thanks to a sigmoidal function described as in Formula 4.24 and where ϵ_{max} is the maximal efficiency of the detector, λ is proportional to the slope at half maximum and HV_{50} is the value of the voltage when the efficiency reaches half of the maximum.

$$\epsilon(HV_{eff}) = \frac{\epsilon_{max}}{1 + e^{-\lambda(HV_{eff} - HV_{50})}} \tag{4.24}$$

CMS RPC also define two points on this sigmoid that called *knee* and *working point*. The corresponding voltages HV_{knee} is defined as the voltage at 95% of the maximum efficiency, and HV_{WP} is defined as in Formula 4.25.

$$HV_{WP} = HV_{knee} + \begin{cases} 100\text{V} & \text{(barrel)} \\ 150\text{V} & \text{(endcap)} \end{cases} \tag{4.25}$$

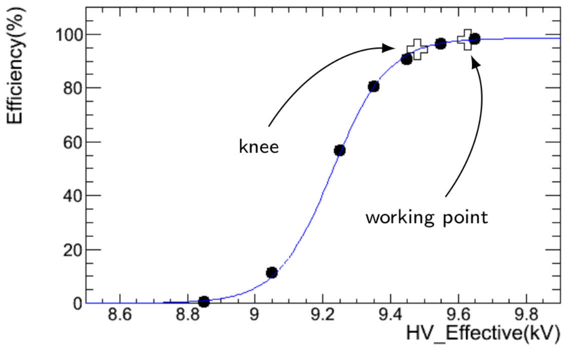

Figure 4.46: Typical efficiency sigmoid of a CMS RPC detector. The black dots correspond to the data, the blue line to the sigmoid fit and the opened cross to the knee and working extracted from the fit line.

Nevertheless, the voltage applied on a detector may vary due to a change in environmental conditions. Indeed, the variation of temperature and/or pressure will have effect on the gas density and the electrodes' resistivity which can be overcome by changing the electric field accordingly. The variation in temperature and pressure are depicted respectively in Figure 4.47 and Figure 4.48. A standard procedure to correct for temperature and pressure variations is to keep the factor $HV \cdot T/P$ constant using Formula 4.26 [253, 254] with reference values for T_0 and P_0. For example, CMS uses $T_0 = 293.15\,\mathrm{K}$ and $P_0 = 965\,\mathrm{hPa}$.

$$HV_{app} = HV_{eff} \frac{P_0}{P} \frac{T}{T_0} \tag{4.26}$$

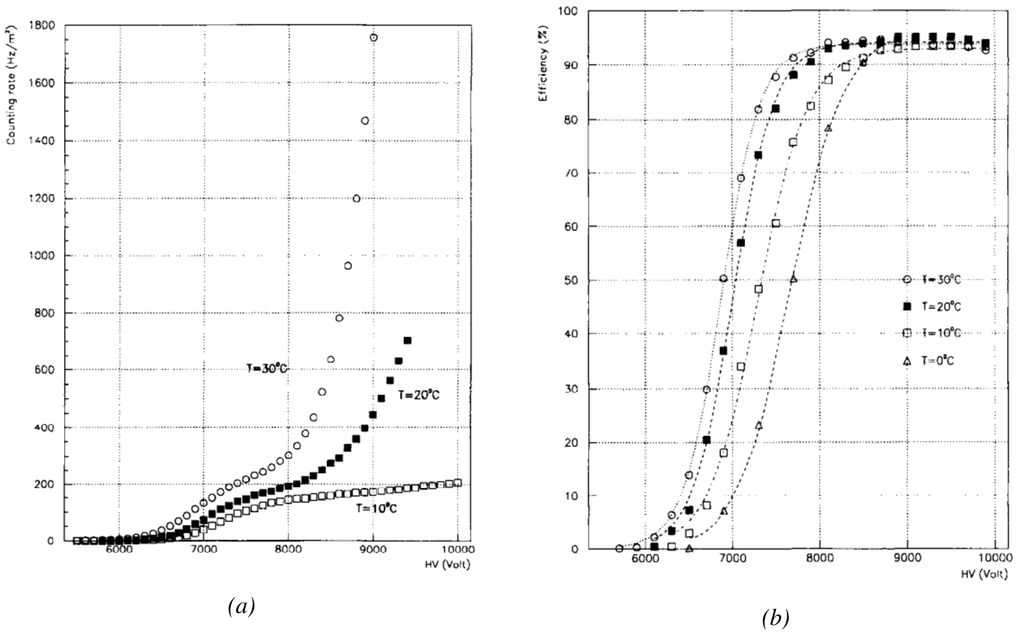

Figure 4.47: Effect of the temperature variation on the rate (Figure 4.47a) and the efficiency (Figure 4.47b) of an RPC [253].

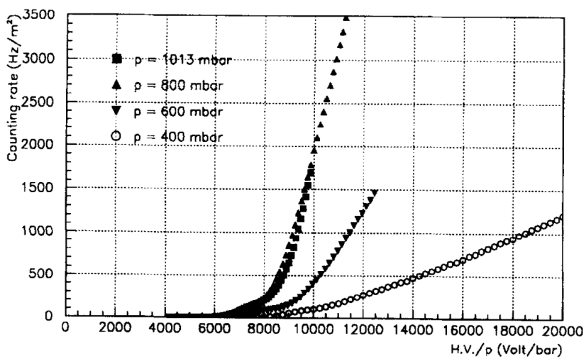

(a)

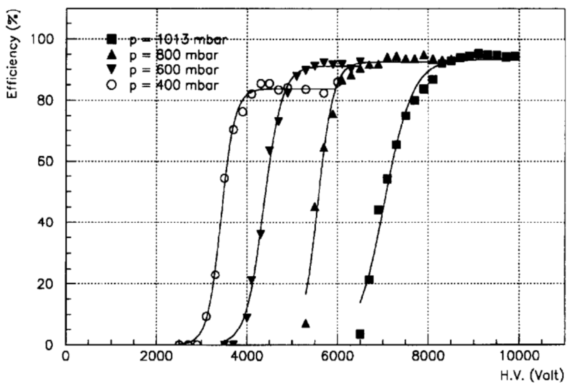

(b)

Figure 4.48: Effect of the pressure variation on the rate (Figure 4.48a) and the efficiency (Figure 4.48b) of an RPC [254].

It was actually found that such a simple procedure would overcorrect the applied voltage in the case the variations of temperature or pressure were too important [255–258]. CMS, considering that the temperature variations in the detector cavern were very small, decided only to improve the pressure correction, giving rise to Formula 4.27 [255] while on the other hand, ATLAS decided to have a more robust correction for both parameters and uses Formula 4.28 instead [258]. The coefficients α, in the case of CMS, and α, β, in the case of ATLAS, are extracted from fit on available dataset obtained during the operation of the detectors.

$$HV_{app} = HV_{eff}\left(1-\alpha+\alpha\frac{P_0}{P}\right)\frac{T}{T_0}\ , \quad \alpha = 0.8 \tag{4.27}$$

$$HV_{eff} = HV_{app}\left(1+\alpha\frac{\Delta T}{T_0}\right)\left(1-\beta\frac{\Delta P}{P_0}\right)\ , \quad \alpha = 0.5\ ,\ \beta = 0.71 \tag{4.28}$$

5

Longevity studies and Consolidation of the present CMS RPC subsystem

The RPC system, located in both barrel and endcap regions, provides a fast, independent muon trigger with a looser $p_T$threshold over a large portion of the pseudo-rapidity range ($|\eta| < 1.6$). During HL-LHC operations the expected conditions in terms of background and pile-up will make the identification and correct $p_T$assignment a challenge for the muon system. The goal of RPC upgrade is to provide additional hits to the Muon System with more precise timing. All this information will be elaborated by the Trigger System in a global way enhancing the performance of the trigger in terms of efficiency and rate control. The RPC Upgrade is based on two projects: an improved Link Board System and the extension of the RPC coverage up to $|\eta| = 2.4$.

The Link Board System is responsible for the processing, the synchronization and the zero-suppression the signals coming from the RPC FEBs. The Link Board components have been produced between 2006 and 2007 and will be subjected to ageing and failure on a long term scale. An upgraded Link Board System will overcome the ageing problems and will allow for a more precise timing information to the RPC hits from 25 to $1.5\,\mathrm{ns}$.
In order to develop an improved RPC that fulfills CMS requirements, an extensive R&D program is being conducted. The benefits of adding two new RPC layers in the innermost ring of stations 3 and 4 will be mainly observed in the neutron-induced background reduction and efficiency improvement for both trigger and offline reconstruction.

The coverage of the RPC System up to higher pseudo-rapidity $|\eta| = 2.1$ was part of the original CMS TDR. Nevertheless, the expected background rates being higher than the certified rate capability of the present CMS RPCs in that region and the budget being limited, RPCs were restricted to a shorter range. Even though the iRPC technology that will equip the extension of the Muon System will be different than the current CMS RPC technology, it is necessary to certify the rate capability and longevity of the existing detectors as the radiation level will increase together with the increase of instantaneous luminosity of the LHC. For this purpose, spare RPC detectors built but not installed in CMS have been installed in different irradiation facilities, first of all, to certify the detectors to the new levels of irradiation they will be subjected to and, finally, to study their ageing and certify their good operation throughout the HL-LHC program.

5.1 Testing detectors under extreme conditions

The upgrade from LHC to HL-LHC will increase the peak luminosity from 10^{34} cm^{-2} s^{-1}to reach 5×10^{34} cm^{-2} s^{-1}, increasing in the same way the total expected background to which the RPC System will be subjected to. Mainly composed of low energy gammas, neutrons, and electrons and positrons from p-p collisions, but also of low momentum primary and secondary muons, punch-through hadrons from calorimeters, and particles produced in the interaction of the beams with collimators, the background will mostly affect the regions of CMS that are the closest to the beam line, i.e. the RPC detectors located in the endcaps.

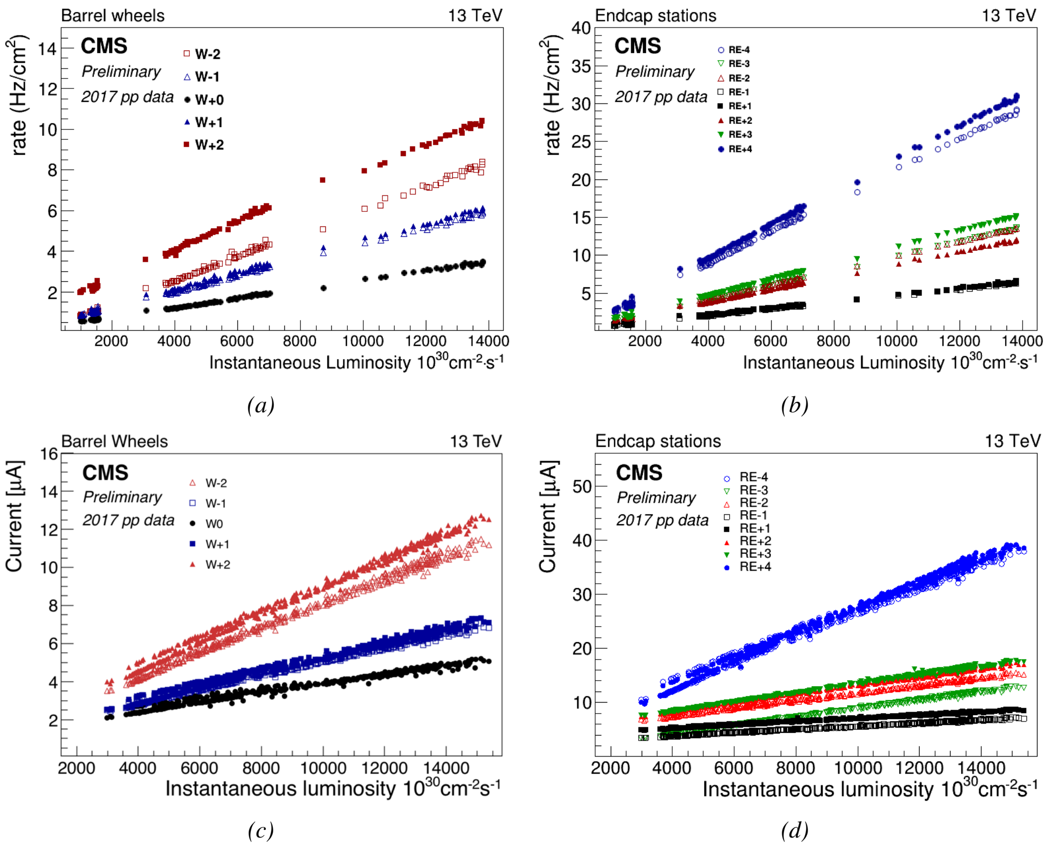

Figure 5.1: Mean RPC Barrel (left column) and Endcap (right column) rate (top row) and current (bottom row) as a function of the instantaneous luminosity as measured in 2017 p-p collision data.

Data collected over 2017, presented through Figure 5.1, allows to study the values of the background rate in all the RPC System. This was achieved thanks to a monitoring of the rates in each RPC rolls, where rolls correspond to the pseudo-rapidity partitioning of the readout electronics, and of the current in each HV channel. A linear dependence in between the mean rate or current with instantaneous luminosity is showed in selected runs with identical LHC running parameters. In Figure 5.2, a linear extrapolation of the distribution of the background hit rate per unit area as well as the integrated charge is showed at a HL-LHC condition. The maximum rate per unit area in the endcap detectors at HL-LHC conditions is expected to be of the order of $600\,\mathrm{Hz/cm^2}$ while the charge deposition should exceed $800\,\mathrm{mC/cm^2}$. The detectors will then be certified up to an irradiation of $840\,\mathrm{mC/cm^2}$. These extrapolations are provided with a required safety factor 3 for the certification study.

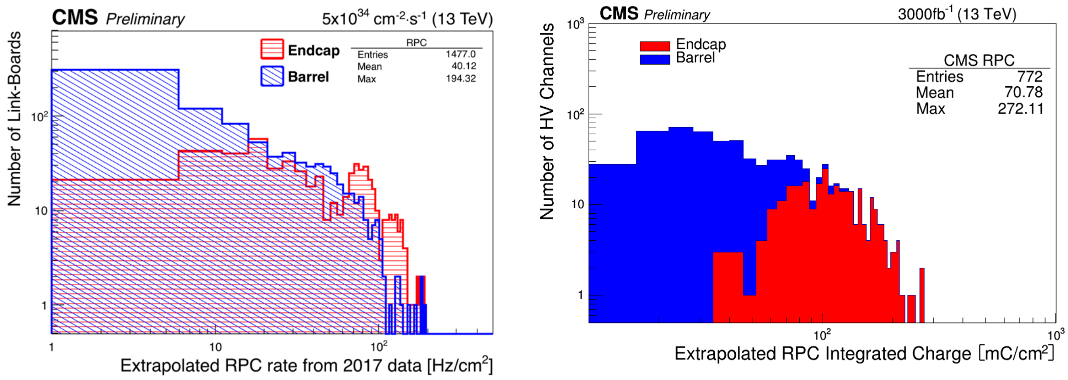

(a) *(b)*

Figure 5.2: Figure 5.2a: The hit rate per region (Barrel, Endcap) is linearly extrapolated to HL-LHC highest instantaneous luminosity ($5\times10^{34}\,\mathrm{cm^{-2}\,s^{-1}}$) using the rate as a function of instantaneous luminosity recorded by RPCs in 2017 showing a linear dependence. Figure 5.2b: The integrated charge per region (Barrel, Endcap) is extrapolated to HL-LHC integrated luminosity ($3000\,\mathrm{fb^{-1}}$) using the data accumulated in 2016 in every HV channel.

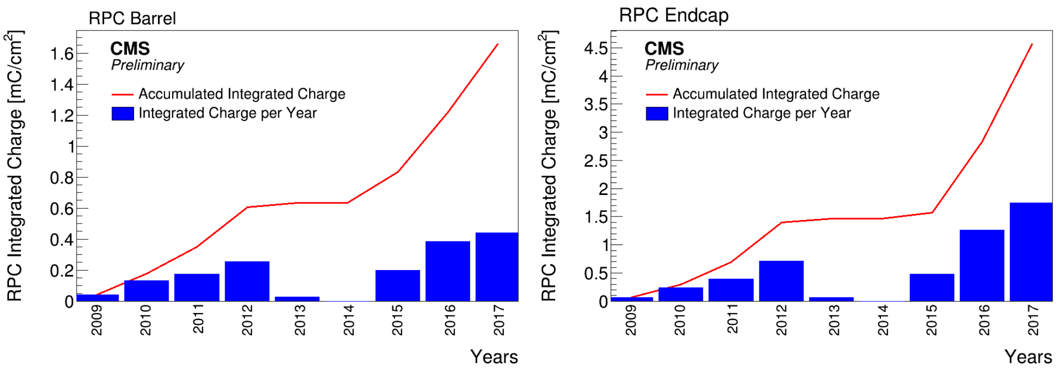

(a) *(b)*

Figure 5.3: CMS RPC mean integrated charge in the Barrel region (Figure 5.3a) and the Endcap region (Figure 5.3b). The integrated charge per year is shown in blue. The red curve shows the evolution of the accumulated integrated charge through time. The blank period in 2013 and 2014 corresponds to LS1. The total integrated charge for the entire operation period (Oct.2009 - Dec.2017) is estimated to be about $1.66\,\mathrm{mC/cm^2}$ in the Barrel and $4.58\,\mathrm{mC/cm^2}$ in the Endcap.

In the past, extensive long-term tests were carried out at several gamma and neutron facilities certifying the detector performance. Both full size and small prototype RPCs have been irradiated with photons up to an integrated charge of $\sim 0.05\,\mathrm{C/cm^2}$ and $\sim 0.4\,\mathrm{C/cm^2}$ respectively and were certified for rates reaching $200\,\mathrm{Hz/cm^2}$ [259, 260]. Since the beginning of Run-I until December 2017, the RPC system provided stable operation and excellent performance and did not show any ageing effects for a maximum integrated charge in a detector of the order of $0.01\,\mathrm{C/cm^2}$ - the average being of the order of $2\,\mathrm{mC/cm^2}$ in the Barrel and $5\,\mathrm{mC/cm^2}$ in the Endcap, closer to the beam line, as can be seen from Figure 5.3 - and a peak luminosity reaching $1.4 \times 10^{34}\ \mathrm{cm^{-2}\,s^{-1}}$during 2017 data taking period.

To perform the necessary studies on the present CMS RPC detectors, facilities offering the possibility to irradiate the chambers are necessary in order to recreate HL-LHC conditions or stronger and study their performance through time. Such facilities exist at CERN and were exploited to conduct this study. A first series of preliminary studies was conducted in the former gamma facility of CERN (GIF) before its dismantlement. This preliminary study was used as a stepping stone towards the building of a more powerful irradiation fully dedicated to longevity studies of CMS and ATLAS subsystems in the perspective of HL-LHC. The period of preliminary work has also been a key moment in the elaboration and improvement of data acquisition, offline analysis and online monitoring tools that are extensively used in the new gamma irradiation facility.

5.1.1 GIF

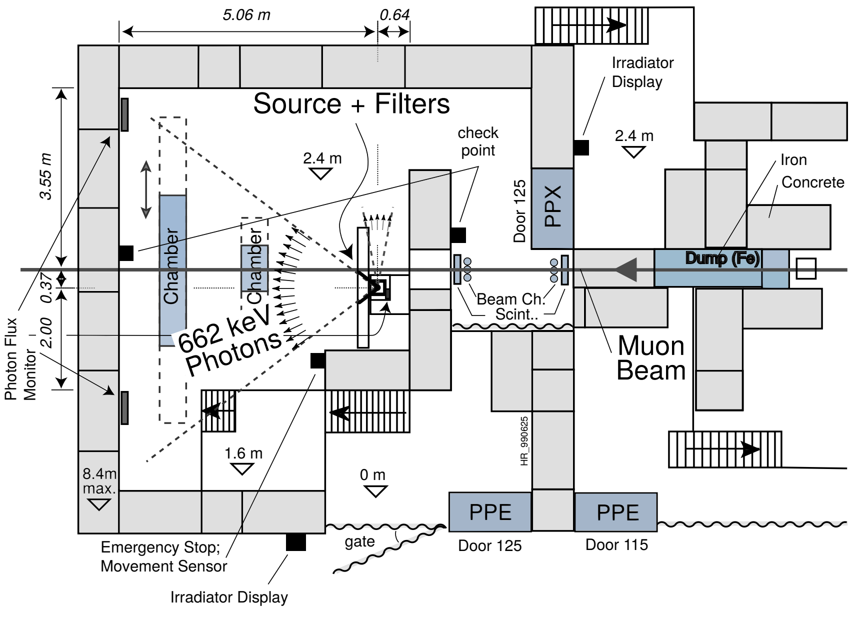

Figure 5.4: Layout of the test beam zone called X5c GIF at CERN. Photons from the radioactive source produce a sustained high rate of random hits over the whole area. The zone is surrounded by $8\,\mathrm{m}$ *high and* $80\,\mathrm{cm}$ *thick concrete walls. Access is possible through three entry points. Two access doors for personnel and one large gate for material. A crane allows installation of heavy equipment in the area.*

Located in the SPS West Area at the downstream end of the X5 test beam, the Gamma Irradiation Facility (GIF) was a test area in which particle detectors were exposed to a particle beam in presence of an adjustable gamma background [261]. Its goal was to reproduce background conditions these detectors would suffer in their operating environment at LHC. GIF layout is showed in Figure 5.4. Gamma photons are produced by a strong ^{137}Cs source installed in the upstream part of the zone inside a lead container. The source container includes a collimator, designed to irradiate a $6 \times 6\,\mathrm{m}^2$ area at $5\,\mathrm{m}$ maximum to the source. A thin lens-shaped lead filter helps providing with a uniform out-coming flux in a vertical plane, orthogonal to the beam direction. The photon rate is controlled by further lead filters allowing the maximum rate to be limited and to vary within a range of four orders of magnitude. Particle detectors under test are then placed within the pyramidal volume in front of the source, perpendicularly to the beam line in order to profit from the homogeneous photon flux. Adjusting the background flux of photons can then be done by using the filters and choosing the position of the detectors with respect to the source.

As described on Figure 5.5, the ^{137}Cs source emits a $662\,\mathrm{keV}$ photon in 85% of the decays. An activity of $740\,\mathrm{GBq}$ was measured on the 5^{th} of March 1997. To estimate the strength of the flux in 2014, was considered the nuclear decay through time associated to the Cesium source whose half-life is well known ($t_{1/2} = (30.05 \pm 0.08)\,\mathrm{y}$). The GIF tests where done in between the 20^{th} and the 31^{st} of August 2014, i.e. at a time $t = (17.47 \pm 0.02)\,\mathrm{y}$ resulting in an attenuation of the activity from $740\,\mathrm{GBq}$ in 1997 to $494\,\mathrm{GBq}$ in 2014.

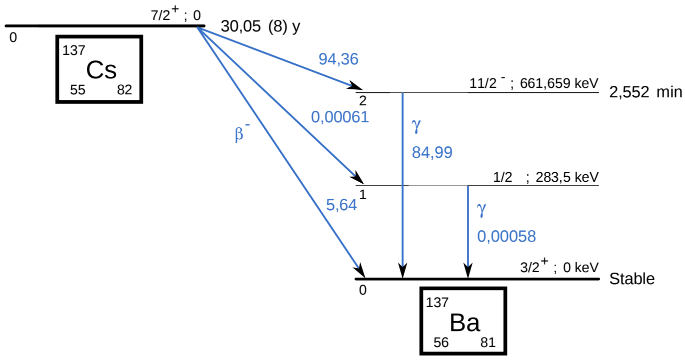

Figure 5.5: ^{137}Cs decays by β^- emission to the ground state of ^{137}Ba (BR = 5.64%) and via the $662\,\mathrm{keV}$ isomeric level of ^{137}Ba (BR = 94.36%) whose half-life is 2.55min.

5.1.2 GIF++

The new Gamma Irradiation Facility (GIF++), located in the SPS North Area at the downstream end of the H4 test beam, has replaced its predecessor during LS1 and has been operational since spring 2015 [262]. Like GIF, GIF++ features a ^{137}Cs source of $662\,\mathrm{keV}$ gamma photons, their fluence being controlled with a set of filters of various attenuation factors. The source provides two separated large irradiation areas for testing several full-size muon detectors with homogeneous irradiation, as presented in Figure 5.6.

The source activity was measured to be about $13.5\,\mathrm{TBq}$ in March 2016. The photon flux being far greater than HL-LHC expectations, GIF++ provides an excellent facility for accelerated ageing tests of muon detectors. The source is situated in a bunker designed to perform irradiation test along a muon beam line, the muon beam being available during selected periods throughout the year. The H4 beam, providing the area with muons with a maximum momentum of about $150\,\mathrm{GeV/c}$, passes through the GIF++ zone and is used to periodically study the performance of the detectors placed under long term irradiation. Its flux is of $104\,\mathrm{particles/s/cm^2}$ focused in an area similar to

$10 \times 10\,\mathrm{cm}^2$. Therefore, with properly adjusted filters, one can simulate the background expected at HL-LHC and study the performance and ageing of muon detectors in HL-LHC environment.

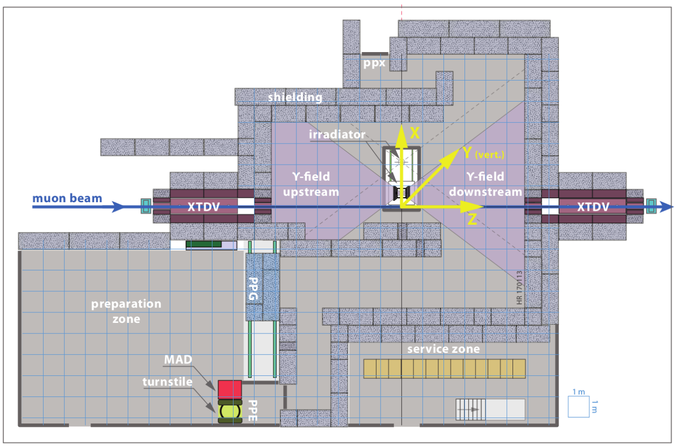

Figure 5.6: Floor plan of the GIF++ facility. When the facility downstream of the GIF++ takes electron beam, a beam pipe is installed along the beam line (z-axis). The irradiator can be displaced laterally (its center moves from $x = 0.65\,\mathrm{m}$ to $2.15\,\mathrm{m}$), to increase the distance to the beam pipe.

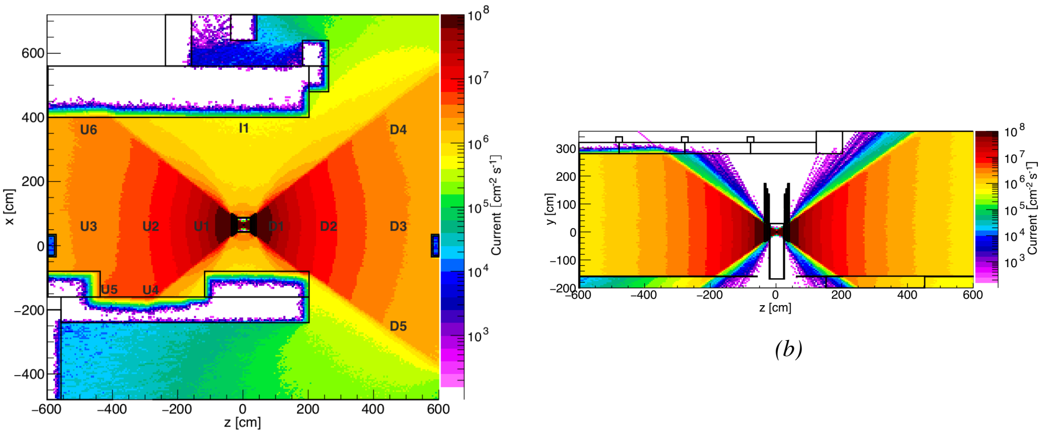

(a) *(b)*

Figure 5.7: Simulated unattenuated current of photons in the xz plane (Figure 5.7a) and yz plane (Figure 5.7b) through the source at $x = 0.65\,\mathrm{m}$ and $y = 0\,\mathrm{m}$ [263]. With angular correction filters, the current of $662\,\mathrm{keV}$ photons is made uniform in xy planes.

The gamma current as simulated with GEANT4 is presented in Figure 5.7 in which the labels UN, DN, with $N \in [1 : 5]$ and I1 correspond to the position of different Radiation Monitoring (RADMON) sensors dedicated to measuring the irradiation in the bunker area [263]. According to the simulation results, that agree within 12% to the doses measured with the RADMONs, the RPCs that will be tested in GIF++ can expect a maximal gamma current of the order of 2 to 5×10^6

$\mathrm{cm}^{-2}\,\mathrm{s}^{-1}$assuming they will always stay in a region in between sensor U5 and the back wall of the upstream area.

5.2 Preliminary studies at GIF

5.2.1 RPC test setup

During summer 2014, preliminary tests have been conducted in the GIF area on an endcap chamber of type RE4/2 and labeled `RE-4-2-BARC-161` produced for the extension of the endcap with a fouth disk in 2013. This chamber has been placed into a trolley covered with a tent. The positions of the RPC inside the tent and of the tent with respect to the source in the bunker are described in Figure 5.8. The goal of the study was to have a preliminary understanding of the rate capability of the present technology used in CMS. It was decided to measure the efficiency of the RPC under irradiation at detecting cosmic muons as, at the time of the tests, the beam not operational anymore. Three different absorber settings were used and compared to the case where the detector was not irradiated in order to study the evolution of the performance of the detector with increasing exposition to gamma radiation. First of all, measurements were done with the fully opened source. To complete this preliminary study, the gamma flux has been attenuated by a factor 2, a factor 5 and finally the source was shut down. The efficiency of the RPC at detecting the cosmic muons in coincidence with a cosmic trigger as well as the background rate as seen by the detectors were measured.

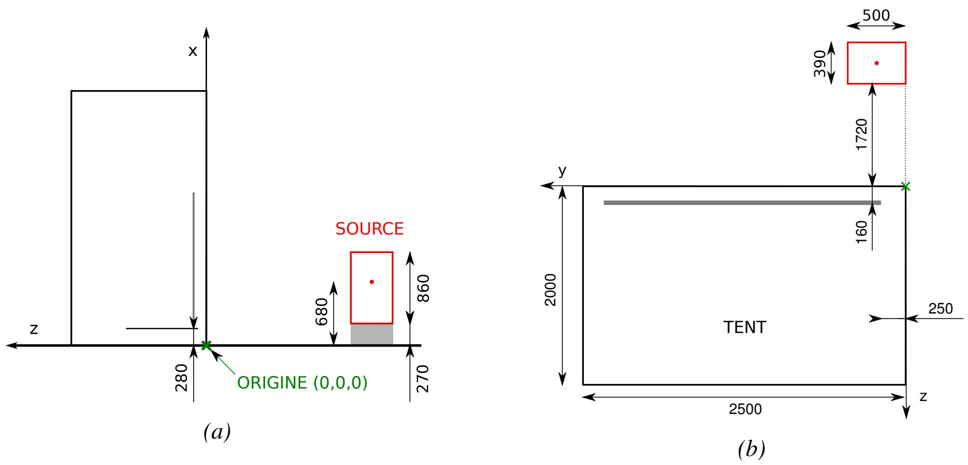

Figure 5.8: Description of the RPC setup. Dimensions are given in mm. *A tent containing RPCs is placed at* 1720 mm *from the source container. The source is situated in the center of the container. RE-4-2-BARC-161 chamber is* 160 mm *inside the tent. This way, the distance between the source and the chambers plan is* 2060 mm. *Figure 5.8a provides a side view of the setup in the xz plane while Figure 5.8b shows a top view in the yz plane.*

The trigger system was composed of two plastic scintillators and was placed in front of the setup with an inclination of 10° with respect to the detector plane in order to look at cosmic muons. Using this particular trigger layout, showed in Figure 5.9, leads to a cosmic muon hit distribution into the chamber similar to the one of Figure 5.10. Measured without gamma irradiation, two peaks can be seen on the profile of readout partition B, centered on strips 52 and 59. Section 5.2.2 will help us understand that these two peaks are due respectively to forward and backward coming cosmic particles where forward coming particles are first detected by the scintillators and then the RPC while the backward coming muons are first detected in the RPC.

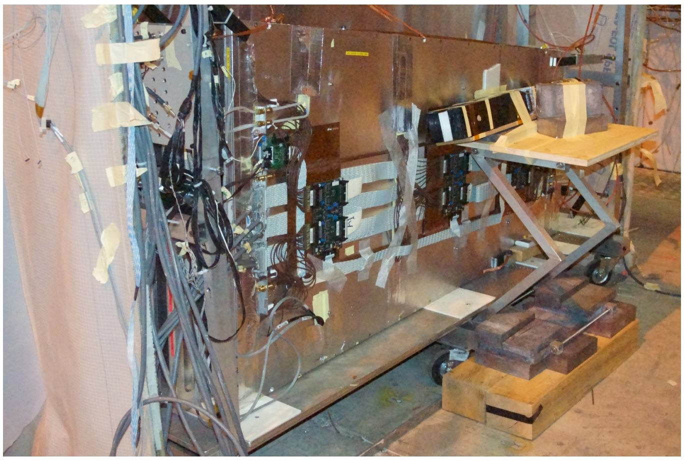

Figure 5.9: `RE-4-2-BARC-161` chamber is inside the tent as described in Figure 5.8. In the top right, the two scintillators used as trigger can be seen. This trigger system has an inclination of 10° *relative to horizontal and is placed above half-partition B2 of the RPCs. PMT electronics are shielded thanks to lead blocks placed in order to protect them without stopping photons from going through the scintillators and the chamber.*

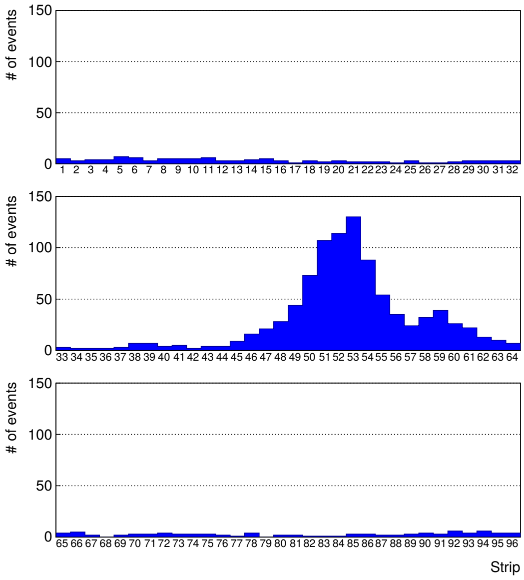

Figure 5.10: Hit distributions over all three partitions of `RE-4-2-BARC-161` chamber is showed. Top, middle and bottom figures respectively correspond to partitions A, B, and C. The profiles show that some events still occur in other half-partitions than B2, which corresponds to strips 49 to 64, in front of which the trigger is placed, contributing to the inefficiency of detection of cosmic muons. In the case of partitions A and C, the very low amount of data can be interpreted as noise. On the other hand, it is clear that a little portion of muons reach the half-partition B1, corresponding to strips 33 to 48.

The data taking is then performed thanks to a `CEAN` TDC module of type `V1190A` [264] to which is connected the digitized output of the RPC Front-End Board, as described in Figure 5.11a and the trigger signal from the telescope. The communication with the computer is performed thanks to a `CAEN` communication module of type `V1718` [265]. In order to control the rates recorded by the detector, the digitized RPC signals are also sent to scalers as described in Figure 5.11b. The `C++` DAQ software used in GIF was developed as an early attempt towards the understanding of the `CAEN` libraries and the data collected by the TDCs was saved into `.dat` files is analysed with an algorithm computing parameters such as efficiency, hit profile, cluster size, or gamma and noise rates which was developed with `C++` as well. Finally, histograms and curves are produced using `ROOT`.

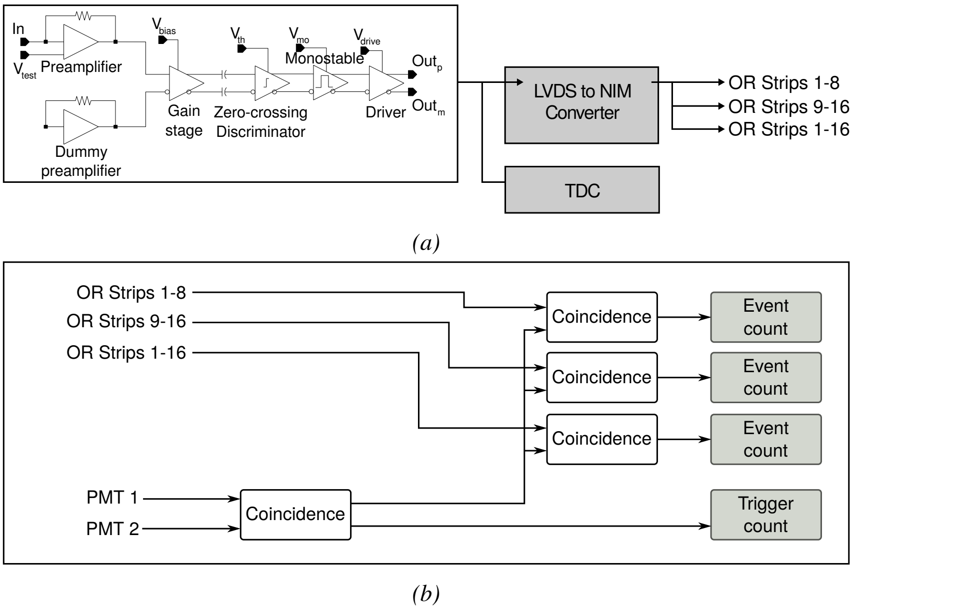

Figure 5.11: Signals from the RPC strips are shaped by the FEE described on Figure 5.11a. Output LVDS signals are then read-out by a TDC module connected to a computer or converted into NIM and sent to scalers. Figure 5.11b describes how these converted signals are put in coincidence with the trigger.

5.2.2 Geometrical acceptance of the setup layout to cosmic muons

In order to profit from a constant gamma irradiation, the detectors inside of the GIF bunker need to be placed in a plane orthogonal to the beam line. The muon beam that used to be available was meant to test the performance of detectors under test. This beam being not active anymore, another solution to test detector performance had to be used. Thus, it has been decided to use cosmic muons detected through a telescope composed of two scintillators. Lead blocks were used as shielding to protect the photomultipliers from gammas as can be seen from Figure 5.9.

An inclination of $\sim 10°$ has been given to the cosmic telescope to maximize the muon flux. A good compromise had to be found between good enough muon flux and narrow enough hit distribution to be sure to contain all the events into only one half partitions as required from the limited available readout hardware. It was then foreseen to detect muons and read them out only from half-partition B2, the last 16 channels of readout partition B (i.e. strips 49 to 64). Nevertheless, a consequence of the misplaced trigger, that can be seen as a loss of events in half-partition B1 (strips 33 to 48) in Figure 5.10, is an inefficiency. The observed inefficiency of approximately 20% highlighted in Figure 5.12 by comparing the performance of chamber `RE-4-2-BARC-161` as measured prior to the study at GIF and at GIF without irradiation seems too important, compared to the 12.7% of data contained into the first 16 strips observed on Figure 5.10, to only be explained by the geometrical acceptance of the setup itself. Simulations have been conducted to show how the setup brings inefficiency.

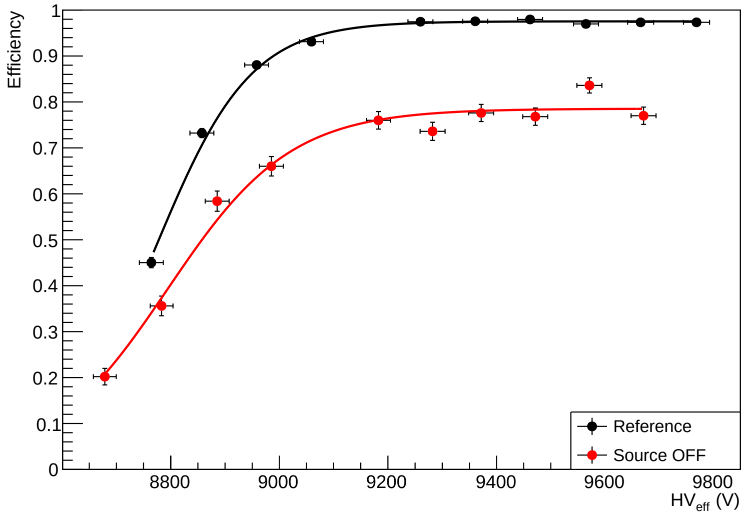

Figure 5.12: Results are derived from data taken on half-partition B2 only. On the 18th of June 2014, data has been taken on chamber `RE-4-2-BARC-161` at CERN building 904 (Prevessin Site) with cosmic muons providing us a reference efficiency plateau of (97.54 ± 0.15)*% represented by a black curve. A similar measurement has been done at GIF on the 21st of July with the same chamber giving a plateau of* (78.52 ± 0.94)*% represented by a red curve.*

5.2.2.1 Description of the simulation layout

The layout of GIF setup has been reproduced, only roughly using Figure 5.9 due to the lack of measures, and incorporated into a `C++` Monte Carlo (MC) simulation to study the geometrical acceptance of the telescope projected onto the readout strips [266]. A 3D view of the simulated layout is given into Figure 5.13. Muons are generated randomly in a horizontal plane located at a height corresponding to the lowest point of the PMTs. This way, the needed size of the plane in order to simulate events happening at very large azimuthal angles (i.e. $\theta \approx \pi$) can be kept relatively small while the total number of muon tracks to propagate is kept relatively small. The muon flux is designed to follow the usual $cos^2\theta$ distribution for cosmic particles. The goal of the simulation is to look at muons that pass through the telescope composed of the two scintillators and define their distribution onto the RPC read-out plane. During the reconstruction, the read-out plane is then divided into read-out strips and each muon track is assigned to a strip.

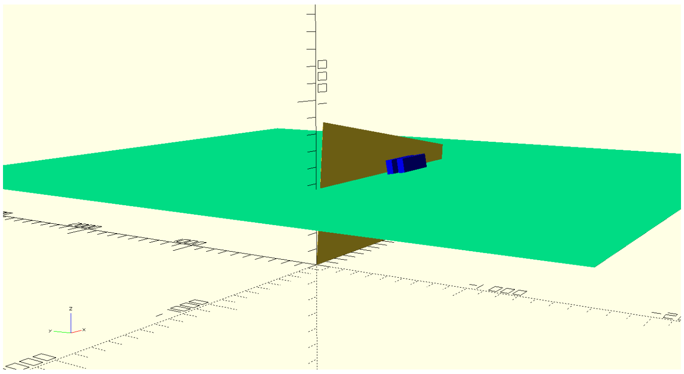

(a)

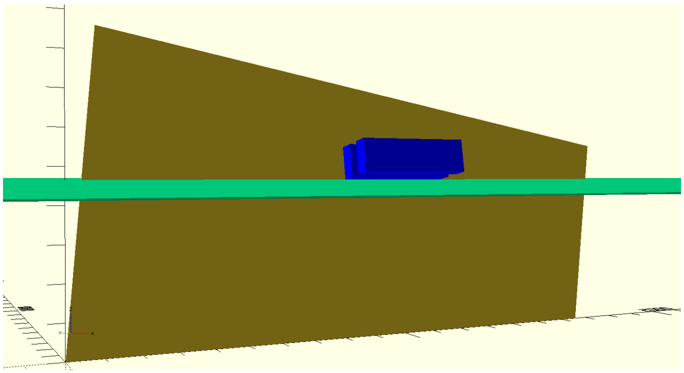

(b)

Figure 5.13: Representation of the layout used for the simulations of the test setup. The RPC read-out plane is represented as a yellow trapezoid while the two scintillators as blue cuboids looking at the sky. The green plane corresponds to the muon generation plane within the simulation. Figure 5.8a shows a global view of the simulated setup. Figure 5.8b shows a zoomed view that allows to see the two scintillators as well as the full RPC plane.

5.2.2.2 Simulation procedure

$N_\mu = 10^8$ muons are randomly generated inside the muon plane with an azimuthal angle θ chosen to follow a $cos^2\theta$ distribution. Infinite planes are associated to each surface of the scintillators. Knowing the muon position into the muon generation plane and its direction allows, by assuming that muons travel in a straight line, to compute the intersection of the muon track with these planes. Applying conditions to the limits on the contours of the scintillators' faces then gives an answer to weither or not the muon passed through the scintillators. In the case the muon was not *detected* into both scintillators, the simulation discards the muon and generates a new one.

On the contrary, if the muon is labeled as good, its position within the RPC read-out plane is computed and the corresponding strip, determined through geometrical tests, gets a *hit*. Muon hits fill different histograms whether they are associated to forward or backward coming muons. A discrimination is performed according to their direction components. An (x, y, z) position into the generation plane as well as a $(\theta;\phi)$ pair are associated to each generated muon providing with information on the direction the track follows. This way, muons satisfying the condition $0 \leq \phi < \pi$ are labeled as *backward* coming muons while muons satisfying $\pi \leq \phi < 2\pi$ as *forward* coming muons.

5.2.2.3 Results and limitations

The output from the simulation is given in Figure 5.14 in which the distribution is showed for all muons but also for the separate contributions of forward and backward coming muons. The strip number is here given in a range of 1 to 32 corresponding to the 32 strips contained in each RPC read-out partition, without taking into account the fact that partition B of an RPC correponds, by convention, to strips 33 to 64. Comparing the number of muons recorded respectively in the first 16 strips and the in all of the 32 strips of the RPC read-out panel, it can be established than, out of the total amount of muons that have passed through the telescope and reached the RPC, 16.8% where to be detected in the 16 first strip of the read-out plane corresponding to half partition B1. This brings a geometrical inefficiency of the same amount that can then be used to correct the data by scaling up by a factor $c_{geo} = 1/(1 - 0.168)$ the maximum efficiency measured during data taking.

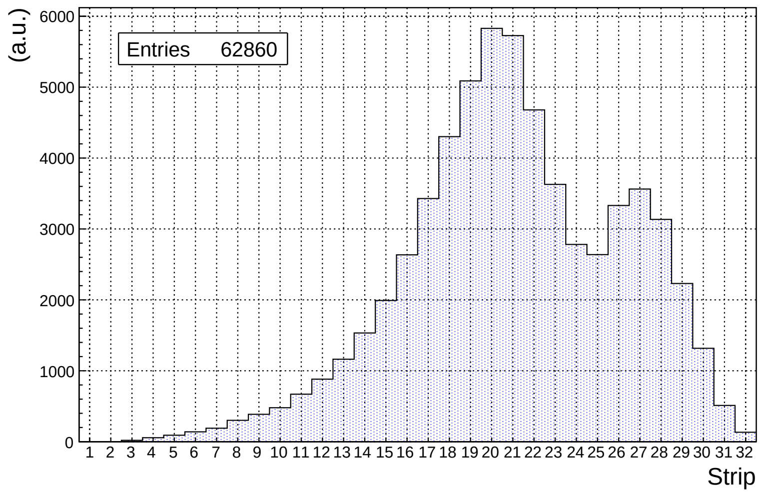

(a) Full acceptance distribution

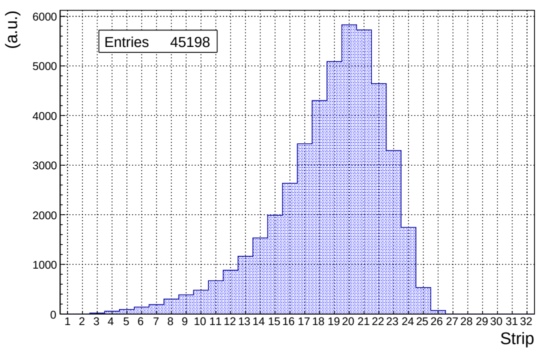

(b) Forward acceptance

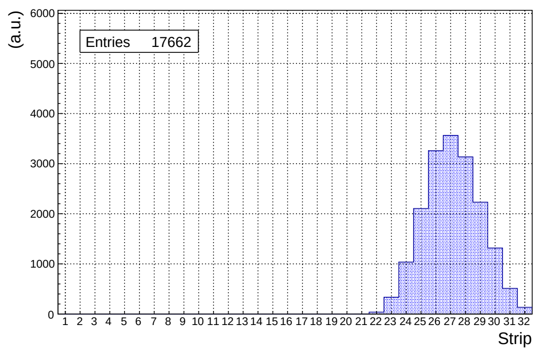

(c) Backward acceptance

Figure 5.14: Geometrical acceptance distribution as provided by the Monte Carlo simulation.

Nevertheless, it is difficult to evaluate a systematic uncertainty on this geometrical correction for different reasons. First of all, even though the dimensions of the scintillators and of the RPC are well known, the position of each element of the setup with respect to one another was not measured. It was then necessary, using known dimensions, to extract the positions of each element from Figure 5.9 with unknown uncertainty. The inclination is also roughly measured to be $10°$ and even if the position of each peak, distant in the simulation of 7 strips, tends to confirm this assumption, the geometrical inefficiency would be affected by a variation of the inclination angle. Introducing in the simulation an error of $\pm 2°$ would lead to a correction factor $c_{geo} = 1.20^{+0.04}_{-0.03}$ that allows for a good improvement of the efficiency measured in GIF, as can be seen from Figure 5.15. GIF measurement is in agreement with the reference curve within statistical errors.

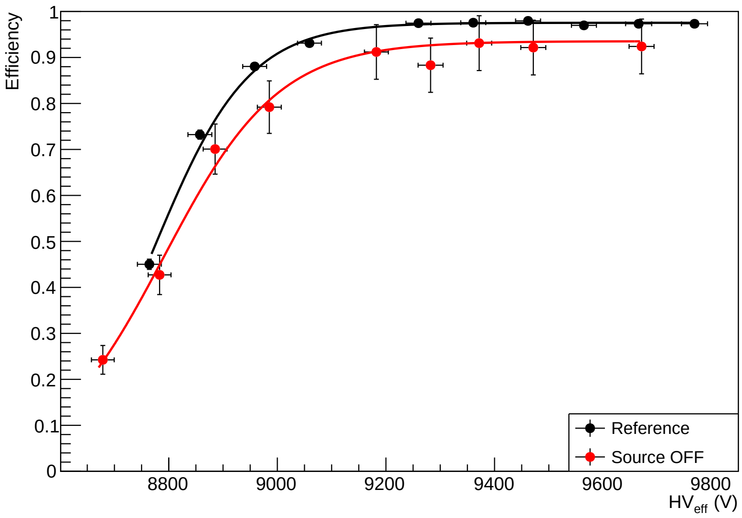

Figure 5.15: Correction of the efficiency without source. The efficiency after correction gets much closer to the Reference measurement performed before the study in GIF by reaching a plateau of (93.52 ± 2.64)*%.*

Further corrections could be also be brought as it can easily be understood that the distribution showed through Figure 5.14a differs from the measured hit profile showed in Figure 5.10. The contributions of forward and backward muon indicate that 28.1% of the total geometrical acceptance should contribute to detecting backward muons whereas it is measured that the hit profile contains 22.0% of backward data only. This estimation of the backward versus forward content in the data was done through a fit using a sum of two skew distribution, one acting on the forward muon peak while the other acts on the backward muon fit, as showed in Figure 5.16. Although a skew distribution lacks physical interpretation, it allows fitting easily such kind of data. A description of a skew distribution, as the product of a gaussian and a sigmoid (Formula 5.1), is given through Formula 5.2.

$$g(x) = A_g e^{\frac{-(x-\bar{x})^2}{2\sigma^2}} \quad , \quad s(x) = \frac{A_s}{1 + e^{-\lambda(x - x_i)}} \tag{5.1}$$

$$sk(x) = g(x) \times s(x) = A_{sk} \frac{e^{\frac{-(x-\bar{x})^2}{2\sigma^2}}}{1 + e^{-\lambda(x - x_i)}} \tag{5.2}$$

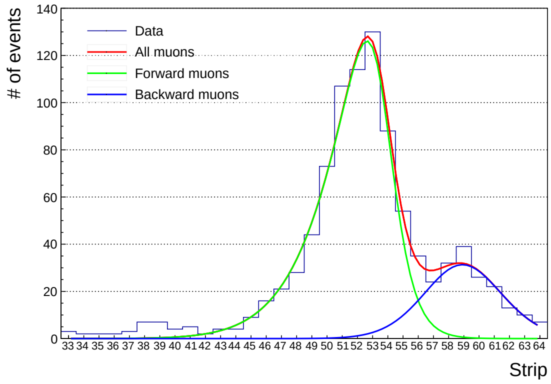

Figure 5.16: Hit distributions over read-out partition B of `RE-4-2-BARC-161` *chamber together with skew distribution fits corresponding to forward and backward coming muons.*

From the obvious difference in between geometrical simulation and data, it is necessary to realize that the geometrical acceptance and the hit profile are two distinct information. When the geometrical acceptance only provides with the information about what the detector can expect to see in a perfect world where all muons are detected in the exact same way independently from their energy, angle of incidence, fluctuation of the detector gain due to complex avalanche development, thresholds applied on the scintillators and on the RPC FEEs to reduce the noise, the cross-talk and corresponding spread of the induced charge observed on the read-out strips, the hit profile provides the final product of all the previously mentioned contributions and can greatly differ from purely geometrical considerations. A full physics analysis involving softwares such as `GEANT` would be required to further refine the correction on the measured efficiency at GIF.

5.2.3 Photon flux at GIF

In order to understand and evaluate the γ flux in the GIF area, simulations had been conducted at the time GIF was opened for research purposes [261]. Table 5.1 presented in this article gives the γ flux for different distances D to the source. The simulation was done using GEANT and a Monte Carlo N-Particle (MCNP) transport code, and the flux F is given with the estimated error from these packages expressed in $\%$.

Nominal ABS	Photon flux F [$\mathrm{cm^{-2}\,s^{-1}}$]			
	at $D = 50\,\mathrm{cm}$	at $D = 155\,\mathrm{cm}$	at $D = 300\,\mathrm{cm}$	at $D = 400\,\mathrm{cm}$
1	$0.12 \times 10^{8} \pm 0.2\%$	$0.14 \times 10^{7} \pm 0.5\%$	$0.45 \times 10^{6} \pm 0.5\%$	$0.28 \times 10^{6} \pm 0.5\%$
2	$0.68 \times 10^{7} \pm 0.3\%$	$0.80 \times 10^{6} \pm 0.8\%$	$0.25 \times 10^{6} \pm 0.8\%$	$0.16 \times 10^{6} \pm 0.6\%$
5	$0.31 \times 10^{7} \pm 0.4\%$	$0.36 \times 10^{6} \pm 1.2\%$	$0.11 \times 10^{6} \pm 1.2\%$	$0.70 \times 10^{5} \pm 0.9\%$

Table 5.1: Total photon flux ($E\gamma \leq 662\,\mathrm{keV}$) with statistical error predicted considering a ^{137}Cs activity of $740\,\mathrm{GBq}$ at different values of the distance D to the source along the x-axis of irradiation field [261].

The simulation does not provide with an estimated flux at the level of the RPC under test. First of all, it is necessary to extract the value of the flux from the available data contained in the original paper and then to estimate the flux in 2014 at the time the experimentation took place. In the case of a pointlike source emitting isotrope and homogeneous gamma radiations, the gamma flux F at a distance D from the source with respect to a reference point situated at D_0 where a known flux F_0 is measured will be expressed like in Formula 5.3, assuming that the flux decreases as $1/D^2$, where c is a fitting factor that can be written from Formula 5.3 as Formula 5.4. Finally, using Equation 5.4 and the data of Table 5.1, with $D_0 = 50\,\mathrm{cm}$ as reference point, Table 5.2 can be built. It is interesting to note that c for each value of D doesn't depend on the absorption factor.

$$F^{ABS} = F_0^{ABS} \times \left(\frac{cD_0}{D}\right)^2 \tag{5.3}$$

$$c = \frac{D}{D_0}\sqrt{\frac{F^{ABS}}{F_0^{ABS}}}\ , \quad \Delta c = \frac{c}{2}\left(\frac{\Delta F^{ABS}}{F^{ABS}} + \frac{\Delta F_0^{ABS}}{F_0^{ABS}}\right) \tag{5.4}$$

Nominal	Correction factor c		
ABS	at $D = 155\,\mathrm{cm}$	at $D = 300\,\mathrm{cm}$	at $D = 400\,\mathrm{cm}$
1	$1.059 \pm 0.70\%$	$1.162 \pm 0.70\%$	$1.222 \pm 0.70\%$
2	$1.063 \pm 1.10\%$	$1.150 \pm 1.10\%$	$1.227 \pm 0.90\%$
5	$1.056 \pm 1.60\%$	$1.130 \pm 1.60\%$	$1.202 \pm 1.30\%$

Table 5.2: Correction factor c is computed thanks to Formula 5.4 taking as reference $D_0 = 50\,\mathrm{cm}$ *and the associated flux* F_0^{ABS} *for each absorption factor available in table 5.1.*

For the range of D/D_0 values available, it is possible to use a simple linear fit to get the evolution of c that can be expressed as $c(D/D_0) = aD/D_0 + b$. Using Formula 5.5, but neglecting the incertainty on D that will only be used when extrapolating the values for the position of the RPC under test whose position is not perfectly known, the results showed in Figure 5.17 is obtained. Figure 5.17b confirms that using only a linear fit to extract c is enough as the evolution of the rate that can be obtained superimposes well on the simulation points.

$$F^{ABS} = F_0^{ABS}\left(a + \frac{bD_0}{D}\right)^2\ , \quad \Delta F^{ABS} = F^{ABS}\left[\frac{\Delta F_0^{ABS}}{F_0^{ABS}} + 2\frac{\Delta a + \Delta b\frac{D_0}{D} + \Delta D\frac{bD_0}{D^2}}{a + \frac{bD_0}{D}}\right] \tag{5.5}$$

In the context of the 2014 GIF tests, the RPC read-out plane is located at a distance $D = 206\,\mathrm{cm}$ from the source. Moreover, to estimate the strength of the flux in 2014, it is necessary to consider the nuclear decay through time associated to the Cesium source whose half-life is well known ($t_{1/2} = (30.05 \pm 0.08)\,\mathrm{y}$). The very first source activity measurement has been done on the 5^{th} of March 1997 while the GIF tests where done in between the 20^{th} and the 31^{th} of August 2014, i.e. at a time $t = (17.47 \pm 0.02)\,\mathrm{y}$ resulting in an attenuation of the activity from $740\,\mathrm{GBq}$ in 1997 to $494\,\mathrm{GBq}$ in 2014. All the needed information to extrapolate the expected flux through the detector at the moment of GIF preliminary tests has now been assembled, leading to Table 5.3. By assuming a sensitivity of the RPC to γ of 2×10^{-3}, the order of magnitude of the expected hit rate per unit area would be of the order of the kHz for the fully opened source, as reported in the last column of the table.

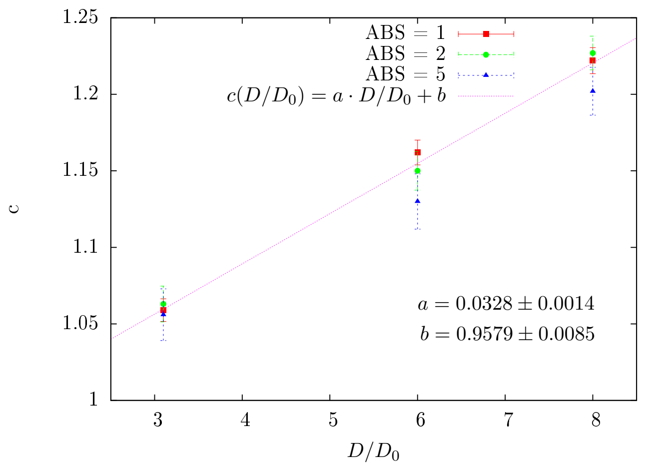

(a)

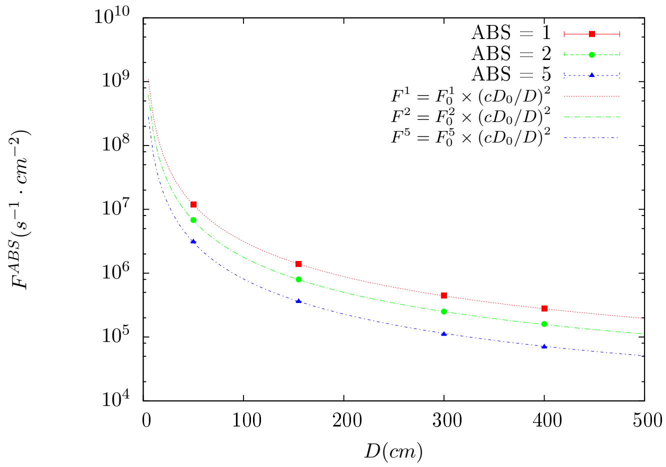

(b)

Figure 5.17: Figure 5.17a shows the linear approximation fit performed on data extracted from table 5.2. Figure 5.17b shows a comparison of Formula 5.5 with the simulated flux using a and b given in figure 5.17a in formulae 5.3 and the reference value $D_0 = 50\,\mathrm{cm}$ and the associated flux for each absorption factor F_0^{ABS} from table 5.1.

Nominal ABS	Photon flux F [$\mathrm{cm}^{-2}\,\mathrm{s}^{-1}$] at $D_0^{97} = 50\,\mathrm{cm}$	at $D^{97} = 206\,\mathrm{cm}$	at $D^{2014} = 206\,\mathrm{cm}$	Rate [$\mathrm{Hz/cm}^2$] at $D^{2014} = 206\,\mathrm{cm}$
1	$0.12 \times 10^8 \pm 0.2\%$	$0.84 \times 10^6 \pm 1.2\%$	$0.56 \times 10^6 \pm 1.2\%$	1129 ± 14
2	$0.68 \times 10^7 \pm 0.3\%$	$0.48 \times 10^6 \pm 1.2\%$	$0.32 \times 10^6 \pm 1.2\%$	640 ± 8
5	$0.31 \times 10^7 \pm 0.4\%$	$0.22 \times 10^6 \pm 1.2\%$	$0.15 \times 10^6 \pm 1.2\%$	292 ± 4

Table 5.3: The data at D_0 in 1997 is taken from [261]. Using Formula 5.5, the flux at D, including an error of $1\,\mathrm{cm}$, can be estimated in 1997. Then, taking into account the attenuation of the source activity, the flux at D can be estimated at the time of the tests in GIF in 2014. Assuming a sensitivity of the RPC to γ $s = 2 \times 10^{-3}$, an estimation of the hit rate per unit area is obtained.

The goal of the study will be to have a good measurement of the intrinsic performance without source irradiation. Then, taking profit of the two working absorbers, at absorption factors 5 (300 Hz) and 2 ($\sim$600 Hz) the goal will be to show that the detectors fulfill the performance certification of CMS RPCs. Finally, a first idea of the performance of the detectors at higher backgrounds will be provided with absorbtion factor 1 (no absorption and $>$1 kHz)).

5.2.4 Results and discussions

The data taking at GIF has been conducted in between the 21st and the 31st of August, 2014. Data has been collected with source both ON and OFF using three different absorber settings (ABS 5, 2 and 1) in order to vary the irradiation on the RPC. For each source setting, two HV scans have been performed with two different trigger settings. During a first scan the trigger sent to the TDC module was the coincidence of the two scintillators composing the telescope while during a second scan the trigger was a pulse coming from a pulse generator in order to measure the noise or gamma rate seen by the chamber. Indeed, using a pulse allows to trigger at moments not linked to any physical event and, hence, to obtain a *RANDOM* trigger on noise and gamma events to measure the associated rates, the probability to have a pulse in coincidence with a cosmic muon being negligible.

From the cosmic trigger scans, a summary of the efficiencies and corresponding cluster sizes is showed in Figure 5.18. The efficiency curves with Source ON show a shift with respect to the case without irradiation. With ABS 5, the general shape of the efficiency curve stays unchanged whereas a clear alteration of the performance is observed at ABS 2 and ABS 1. From the cluster size results, a reduction of the cluster size under irradiation can be observed at equivalent efficiency. This effect can be due to the perturbation of the electric field by the strong rate of gamma particles starting avalanches in the gas volume of the detector.

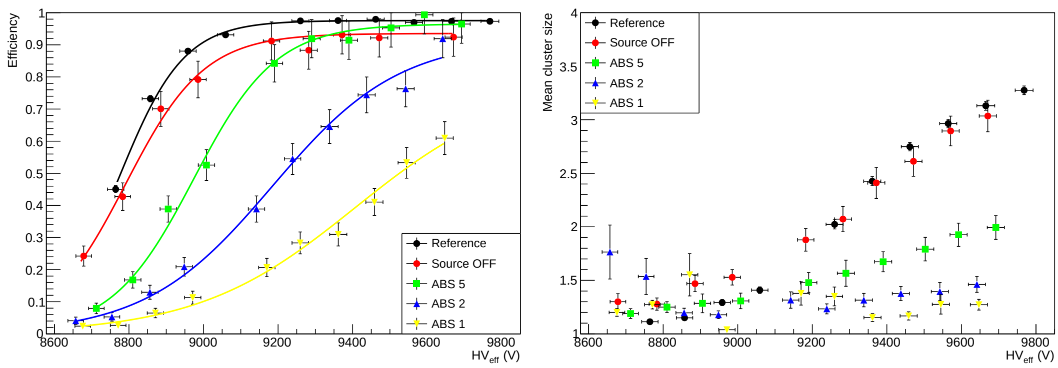

(a) *(b)*

Figure 5.18: Efficiency (Figure 5.18a) and cluster size (Figure 5.18b) of chamber `RE-4-2-BARC-161` *measured at GIF with Source OFF (red) and Source ON using different absorber settings: ABS 5 (green), ABS 2 (blue) and ABS 1 (yellow). The results are compared to the Reference values obtained with cosmics.*

It is necessary to study the evolution of the performance of the chamber with the increasing rate. In Figure 5.19a, the noise rate when the source is OFF stays low but increases at voltages above 9500 V. The rise of the noise rate in the detector can be related to the increased streamer probability observed with such a large electric field. The rates with source ON measured at GIF all show a similar behaviour until a high voltage of approximately 9400 V at which the rate of ABS 5 saturates, corresponding to the chamber reaching full efficiency. It is important to note that, even though the rates look similar independently from the gamma flux, relatively to the efficiency of the chamber, the rate actually increases with increasing flux at equivalent efficiency. A rough way to measure the rate effectively observed by the detector for each source setting would be to normalize the measured rates to the efficiency of the detector. This exercise was done with Figure 5.19b from which constant fits where done on Source ON data in order to extract the rate the chamber was subjected to.

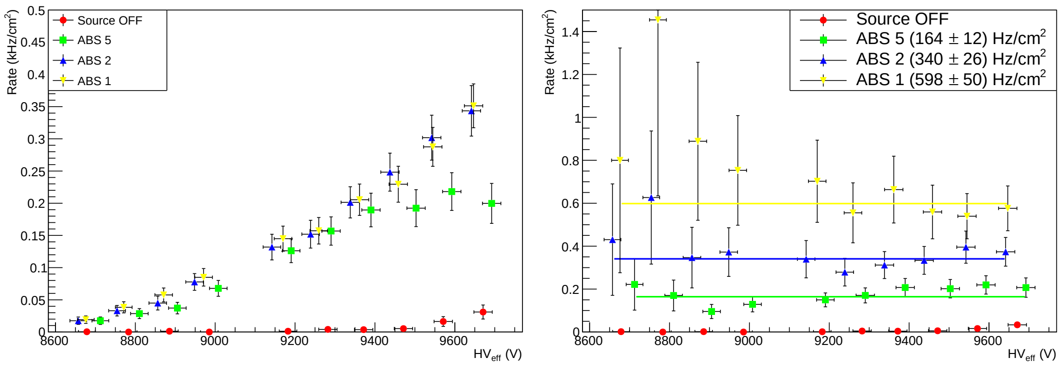

(a) *(b)*

Figure 5.19: Rates in chamber `RE-4-2-BARC-161` measured at GIF with Source OFF (red) and Source ON using different absorber settings: ABS 5 (green), ABS 2 (blue) and ABS 1 (yellow). On Figure 5.19b, the rates of Figure 5.19a were normalized to the measured efficiency, and constant fits are performed on Source ON data showing the gamma rate in the chamber.

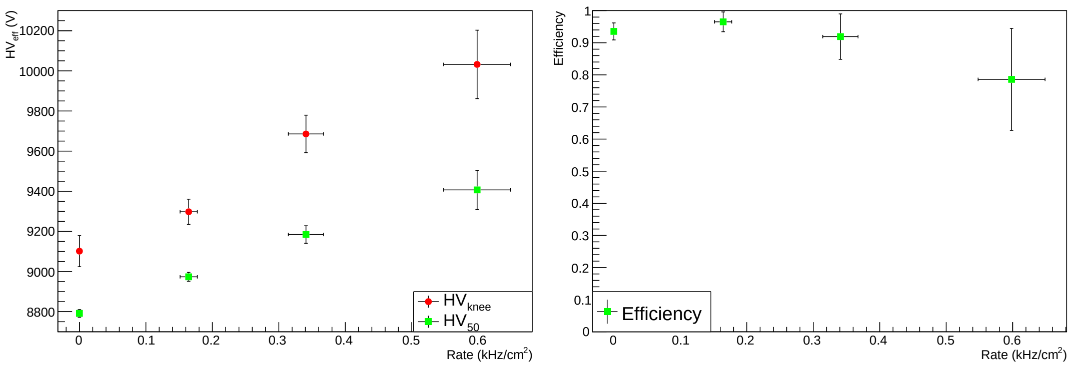

(a) *(b)*

Figure 5.20: Evolution of the voltages at half maximum and at 95% of the maximum efficiency (Figure 5.20a), and of the maximum efficiency (Figure 5.20b) as a function of the rate in chamber `RE-4-2-BARC-161`. The data is extracted from the fits in Figures 5.18a and 5.19b.

The results need to be taken with care as a better estimation of the rate would have been to push the detector towards higher voltages to reach the efficiency plateau for each absorber configuration and only then extract the measured rate at working voltage, defined as in Formula 4.25. Nevertheless, using this method to estimate the rate to which the chamber is subjected, it is possible to look at the evolution of the HV_{50} and HV_{knee} (the working voltage being defined to be $150\,\mathrm{V}$ above the knee in the endcap) as a function of the increasing rate as showed in Figure 5.20. The results from GIF suggest that at a rate of $600\,\mathrm{Hz/cm^2}$ the working voltage of the chamber is increased by a thousand V while the efficiency is reduced to approximately 80%, although the result still is consistent with an efficiency better than 90% due to the large error on the measurement. Moreover, it is likely that the rates obtained through fitting on normalized values is underestimated. Indeed, monitoring the current in the three gaps composing a CMS endcap RPC (Figure 5.21) while knowing the rate, the charge deposition per avalanche q_γ can be computed.

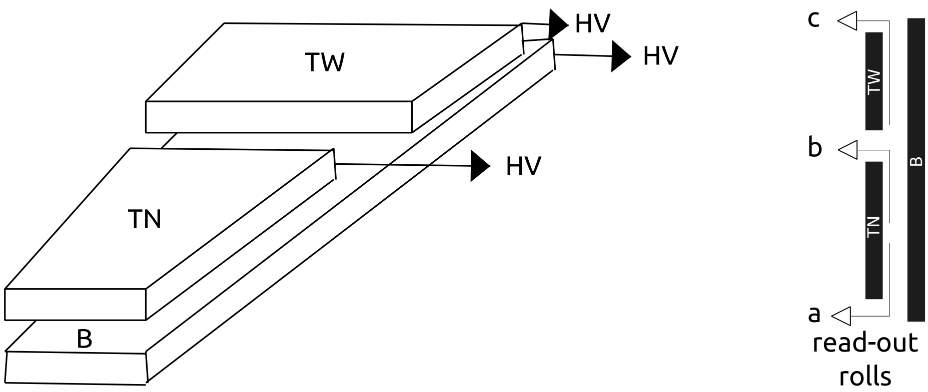

(a) *(b)*

Figure 5.21: Presentation of a double-gap endcap RPC with its three RPC gaps. Due to the partitioniing of the read-out strips into three rolls, the TOP layer of gap is divided into two gaps: TOP NARROW (TN) and TOP WIDE (TW). The BOTTOM (B) only consists in one gap.

A charge is expressed in C which is consistent with a current density, expressed in $\mathrm{A/cm^2}$, divided by a rate per unit area, expressed in $\mathrm{Hz/cm^2}$. The current driven by the RPC is assumed to be due to the irradiation, hence, to the avalanches developing in the gas volume due to the photons of the Cesium source. On the other hand, the rate is supposed to be a measure of the number of photons interacting with the detector. This way, it comes that the charge deposition per avalanche is expressed like $q_\gamma = J_{mon}/R_\gamma$, J_{mon} being the monitored current density and R_γ the measured γ rate. The current density is computed as the sum of the current density measured on the top gap layer and of which measured in the bottom gap layer, $J_{mon} = (I^{TW}_{mon}+I^{TW}_{mon})/(A_{TW}+A_{TN})+I^{B}_{mon}/A_B$, $A_{B,TN,TW}$ being the active area and $I^{B,TN,TW}_{mon}$ the monitored currents of the gaps. According to Figure 5.22, the charge deposition per avalanche consistently converges to a value of the order of $50\,\mathrm{pC}$ for each absorber setting which corresponds to a value more than twice greater than what reported in literature for CMS detectors [267, 268] indicating that the rates could have been wrongly evaluated during the short study performed at GIF. An increase of the γ rate by a factor 2 would be consistent with the expected rates calculated in Table 5.3, assuming the sensitivity to γ to be of the order of 2×10^{-3}.

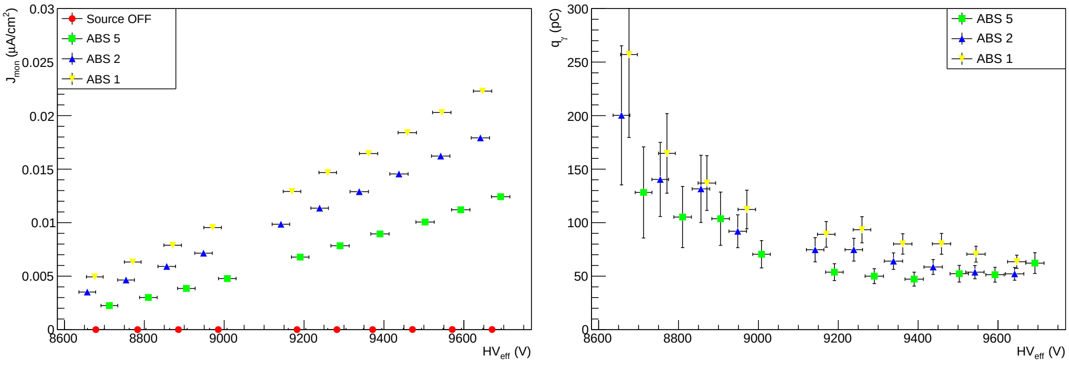

(a) *(b)*

Figure 5.22: Current density and charge deposition per gamma avalanche, defined as the current density normalized to the measured rate taken from Figure 5.19a as a function of the effective high voltage in chamber `RE-4-2-BARC-161` *measured at GIF with Source ON using different absorber settings: ABS 5 (green), ABS 2 (blue) and ABS 1 (yellow).*

Overall, working at GIF has been a rewarding experience as it offered CMS RPC R&D team the possibility to start developing the necessary skills and tools that would become the core of GIF++ experiment. The quality of the results can be argued both due to the little robustness of the experimental setup and the lack of available statistics to draw conclusions from, bringing large errors on the final result. The confrontation of the data to known results pointed to a failure in correctly measuring the γ rate at working voltage and, hence, to an overestimation of the charge per avalanche and of the drift of working voltage with increasing rate. Nevertheless, the prototypes of DAQ and offline analysis tools proved to be reliable.

5.3 Longevity tests at GIF++

5.3.1 Selection and characterization of CMS RPCs for longevity at GIF++

First proposed in 2009 [269], the new Gamma Irradiation Facility of CERN was thought in the perspective of future upgrades of LHC that would bring detectors to be operated in a high irradiation environment. GIF++ would thus provide all LHC R&D teams working on behalf of the different LHC experiment with a facility to perform longevity studies using a very intense Cesium gamma source.

In the specific case of CMS RPC, the longevity studies imply a constant irradiation of selected detectors in order to accumulate a charge equivalent to what is expected during HL-LHC, i.e. a charge of $0.8\,\mathrm{C/cm^2}$ according to Figure 5.2 including a safety factor 3, while other detectors are left non-irradiated to be used as references. Throughout the irradiation campaign, the performance of the irradiated and reference detectors will be periodically probed using the high intensity H4 muon beam. Dedicated test beam periods will be used to measure the efficiency and γ rate at the level of the detectors with different source absorber settings to have access to the rate capability of CMS RPCs, that needs to be certified above $600\,\mathrm{Hz/cm^2}$, and to identify signs of ageing in the case the performance of the irradiated detectors diverges from those of the reference detectors with increasing accumulated charge. Other than the performance of the detectors, signs of ageing could come from increasing dark current that would be related to local ageing of the electrodes triggered by the hydrofluoric acid (HF) production in an irradiated environment. HF is produced by the decomposition of $C_2H_2F_4$ molecules during the charge multiplication process and leads to increased dark current and noise in Bakelite RPCs treated with linseed oil. This effect is strongly reinforced by the presence of UV photons [270, 271]. A close monitoring of the current driven by the detectors will then be necessary as well as dedicated periodical electrode resistivity measurement and chromatography measurement on the gas exhaust.

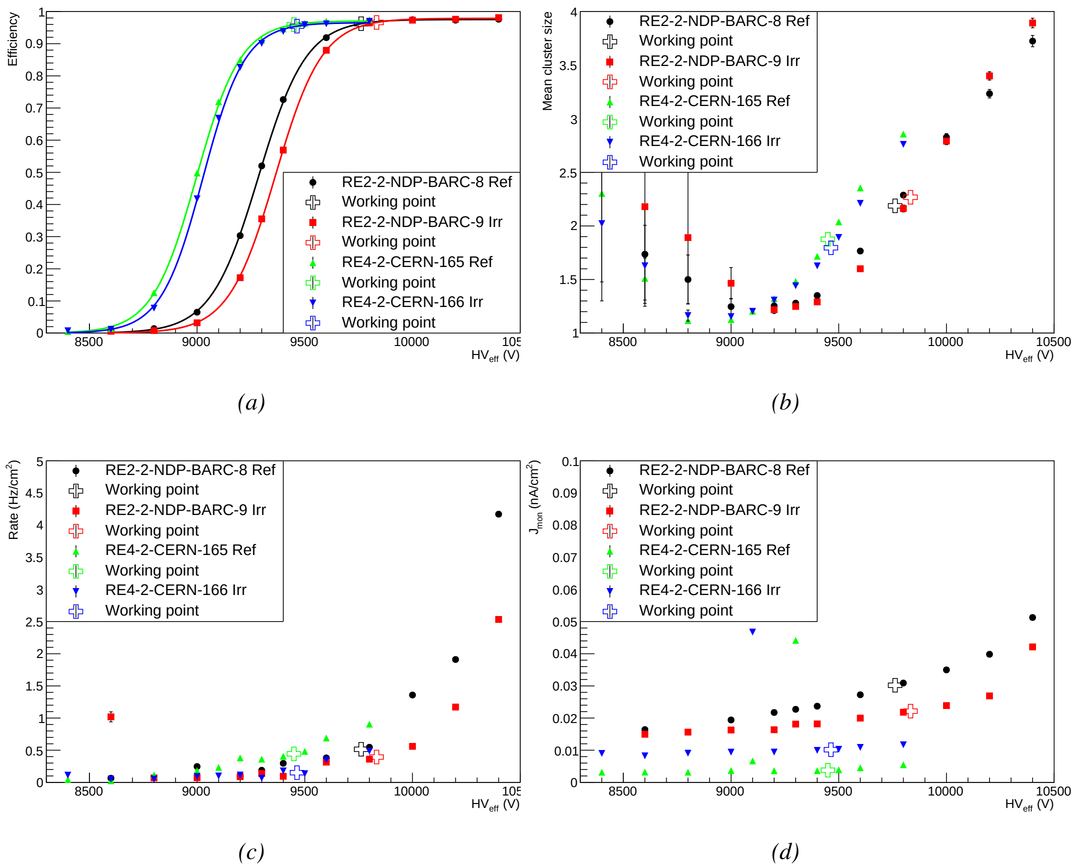

(a) *(b)*

(c) *(d)*

Figure 5.23: Characterization of CMS RPC detectors foreseen to be used at GIF++ for longevity studies of the present system. Using cosmic muons, efficiency (Figure 5.23a) and cluster size (Figure 5.23b) were measured as well as noise rate (Figure 5.23c) and current density (Figure 5.23d). For each detector, the working voltage, defined as in Formula 4.25, was extracted from sigmoid fits performed in Figure 5.23a and the values of efficiency, cluster size, noise rate and current density at this voltage are reported using open crosses.

As the maximum background is found in the endcap, the choice naturally was made to focus the GIF++ longevity studies on endcap chambers. Most of the RPC system was installed in 2007. Nevertheless, the large chambers in the fourth endcap (RE4/2 and RE4/3) have been installed during LS1 in 2014. The Bakelite of these two different productions having different properties, four spare chambers of the present system were selected. From the original CMS RPC system, two RE2/2 spares were selected along two RE4/2 spares from the newest detectors. Having two chambers of each type allows to always keep one of them non-irradiated as reference. Due to the limited gas flow in GIF++, the RE4 chamber remained non-irradiated until end of November 2016 where the longevity studies could finally be started on those chambers.

The performance of the chambers prior to the start of the longevity campaign has been characterized in Ghent before being shipped to CERN to be installed in GIF++. The results of the characterization are showed in Figure 5.23 and summarized in Table 5.4. A clear difference in performance for both types of chambers is observed as the working voltages of the newest chambers, of type RE4, are 300 to 400 V lower to the older chambers indicating that the gap thickness of RE4 detectors could be thinner. This conclusion could as well be supported by the lower cluster size at working voltages that also are smaller in RE4 chambers. Even though the measured currents are low, RE4 detectors draw less current without irradiation than RE2 detectors pointing to a difference in electrode resistivity that were produced at different moments. Efficiency and noise rate levels are of the same order of magnitude for both type of RPCs.

RPC	RE2-2-NPD-BARC-08	RE2-2-NPD-BARC-09	RE4-2-CERN-165	RE4-2-CERN-166
Used as	Reference	Irradiation	Reference	Irradiation
HV_{WP} [V]	(9762 ± 6)	(9833 ± 6)	(9449 ± 5)	(9464 ± 5)
Efficiency at WP	(96.2 ± 0.3)	(96.6 ± 0.3)	(95.9 ± 0.3)	(95.5 ± 0.3)
Cluster size at WP	(2.19 ± 0.04)	(2.27 ± 0.05)	(1.88 ± 0.04)	(1.80 ± 0.04)
Noise at WP [Hz/cm^2]	(0.51 ± 0.01)	(0.39 ± 0.01)	(0.44 ± 0.00)	(0.15 ± 0.01)
J^{WP} [pA/cm^2]	(30.1 ± 0.1)	(22.2 ± 0.1)	(3.8 ± 0.0)	(10.2 ± 0.0)

Table 5.4: Summary of the characterization measurement performed in Ghent on CMS RPC detectors foreseen to be used at GIF++ for longevity studies of the present system. For each detector, the working voltage, defined as in Formula 4.25, was extracted from sigmoid fits performed in Figure 5.23a and the values of efficiency, cluster size, noise rate and current density at this voltage are reported.

5.3.2 RPC test setup

For an easy manipulation of the detectors, a trolley with a structure containing slots in which the RPCs can be slid vertically and referred to as `T1` was used. In this position, each chamber is in a plane perpendicular to the beam line and the source flux as can be seen through Figure 5.24, receiving a uniform irradiation. Moreover the trolley allows for easy movement of the system. Indeed, the position of the trolley varies according to the period of the year.

During the dedicated test beam periods during which GIF++ longevity experiments are in control of the muon beam, the trolley is placed in the upstream region of the bunker, in the beam line, as described through Figure 5.24a. The CMS RPC detectors are the ones being farther away from the source on this side of the source as other detectors need to be certified at higher background rates. An additional trolley, reffered to as `T3`, containing iRPCs and tracking RPCs is placed in between the source and the trolley containing present CMS RPCs. Indeed, iRPCs need to be certified at higher rates and thus need to be placed closer to the source to receive a stronger irradiation using the same absorber settings. The space on `T1` being limited, the tracking RPCs used for extra offline information during the analysis are placed on the same trolley than iRPCs and are kept at full efficiency at all time to reconstruct muon tracks in correlate them with hits recorded in `T1` chambers. The beam trigger system is composed of 2 scintillators placed outside on each side of the bunker and of a third scintillator placed in between `T1` and the wall of the bunker along the beam line.

However, most of the year, `T1` is placed in the so called *ageing position* corresponding to the furthest position from the source outside of the beam line, which needs to stay clear during periods where GIF++ doesn't have the control of the beam so that a beam tube can be installed through the bunker, as can be seen in Figure 5.24b. The reason for placing the chambers as far as possible from the source comes from the too high irradiation delivered by the source during the irradiation periods where all the other experiment having placed detectors into the bunker requires to integrate as much charge as possible. Hence, the source is operated with any absorbers. On the contrary, during the test beam periods, all the groups working in GIF++ are interested in operating the source using various absorber settings to study the performance of their detectors under different irradiation conditions. The time spent with a source fully opened and during which the RPCs of `T1` are kept at a standby voltage of 6500 V much lower than what necessary to grow avalanches in the gas is then small compared to the time spent with other source settings and during which data can be taken.

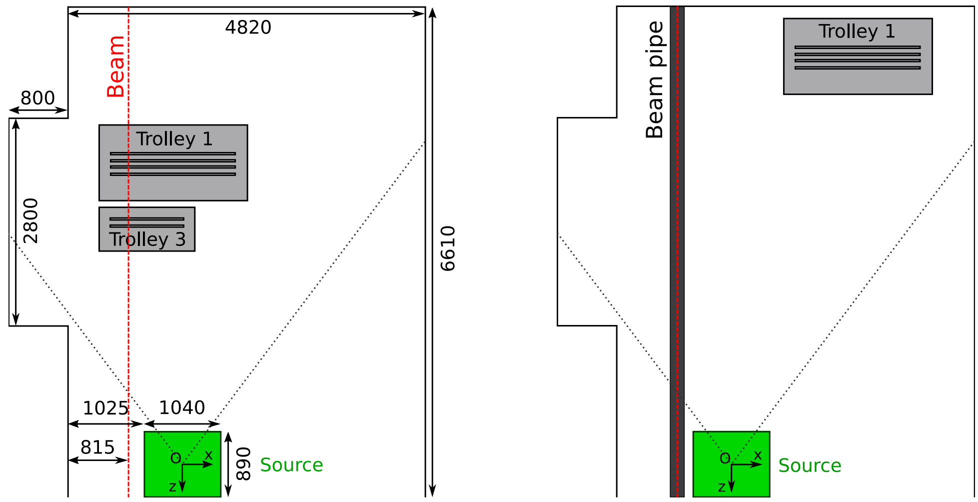

(a) Test beam position *(b) Ageing position*

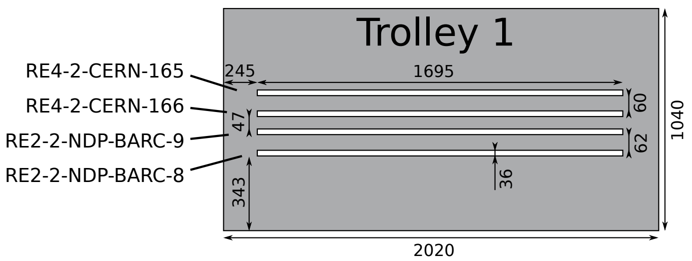

(c)

Figure 5.24: CMS RPC setup inside of GIF++ bunker during test beam (Figure 5.24a) and ageing periods (Figure 5.24b). The space in between the RPCs and the source is usually used by other detectors while the space in between `T1` and the upstream wall is not filled. Due to the presence of the beam pipe, the trolley is moved away from the beam line during irradiation periods and placed farther away from the source for less intense irradiation. The position of the trolley can vary due to the use of the space by other setups and is then not exact. In the contrary, the position of the chambers in the trolley is fixed and given in Figure 5.24c.

From the bunker area, the detectors are connected to the service area, visible in Figure 5.6, through the wooden floor thanks to long cable. The service area hosts all the high and low voltage power supplies, the TDCs and computers used for data acquisition and preliminary offline analysis used to fill the Detector Control Software (DCS) webpage, referred to as WebDCS, with Data Quality Monitoring (DQM) histograms useful for the shifters on duty in the control room located farther in the building, away from the beam lines, as well as the gas system required for the gaseous detectors installed in GIF++ [272]. The detectors read-out is, as in the case of GIF, connected to `V1190A` VME TDCs communicating with the DAQ computer thanks to a `V1718` VME bridge manufactured by `CAEN`. Moreover, a constant monitoring of all the environmental parameters, in different points of the bunker area, gas parameters, to control its composition, temperature and pressure, and of the voltages and currents delivered by the power supplies is performed and displayed on the homepage of the WebDCS interface.

5.3.3 GIF++ data flow

At GIF++, the CMS RPC R&D experiment collects different types of data coming from the detectors monitored parameters, such as voltage and currents, the gas, source, and environmental parameters, and, of course, the TDC data in which are collected the actual muon and gamma physics. These different data sources compose three different data flows as presented in Figure 5.25.

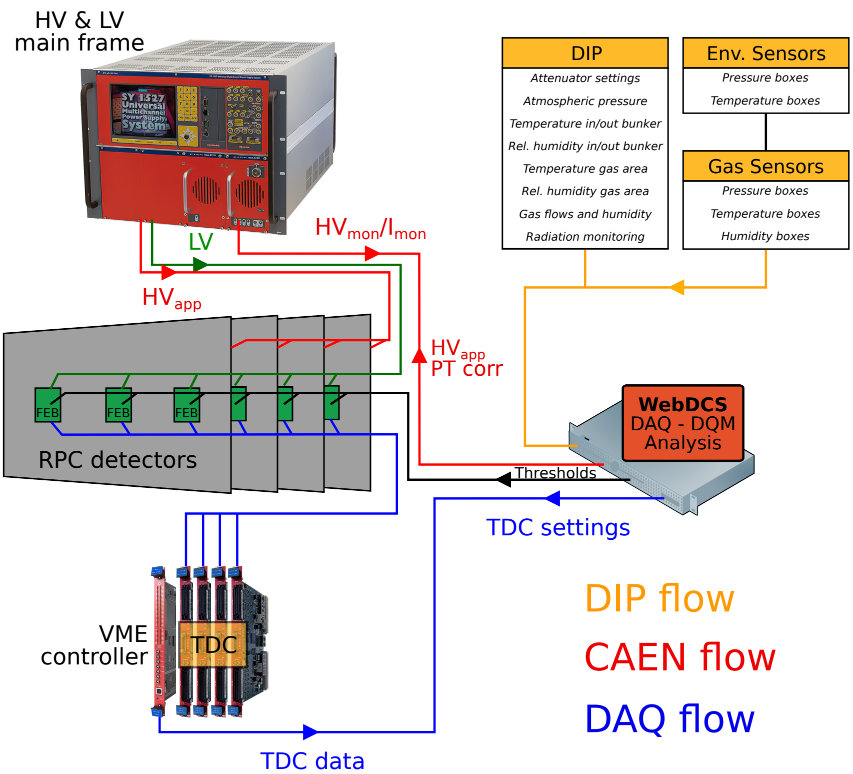

Figure 5.25: Visualisation of the main data flows in GIF++. The yellow flow lines correspond to the DIP flow used for source, environmental and gas information. The red flow lines are for the CAEN flow through which the WebDCS communicates the voltages to be applied on the detectors using pressure and temperature information and retrieves the monitored voltages and currents. Finally, the blue flow lines correspond to the DAQ flow through which the RPC data is collected from the TDCs by the computer.

The *DIP flow*, DIP being a communication system allowing for exchange of real-time information between systems, concerns all the data coming from the gas composition, temperature and humidity, the environmental temperature and pressure, the source settings and the radiation monitoring sensors. The experimental area is in charge of measuring, storing and distributing the data of interest for all of the users of the facility (source settings, radiation monitoring, gas composition at the exit of the gas mixer and general environmental information). Retrieving this data is done by accessing to the database of the experimental hall in which GIF++ is located through DIP communication. More specific data such as gas flow, temperature and humidity at the level of the detectors (upstream and downstream of the detectors) as well as environmental parameters are at the charge of the users. For this reason, several pressure, temperature and humidity sensors were installed on the gas distribution system of the RPC trolleys. The corresponding data flow, although not related to DIP itself, is saved together with the DIP data into the local CMS RPC database and displayed on the front page of the WebDCS together with alerts in the case the values measured are out of optimal working range. The data is particularly important to perform the PT correction described in Section 4.4 of Chapter 4 and keep stable the effective voltage of the detectors. Monitoring history plots are made using `JavaScript` are also displayed for an easy access to past information, as showed in Figure 5.26.

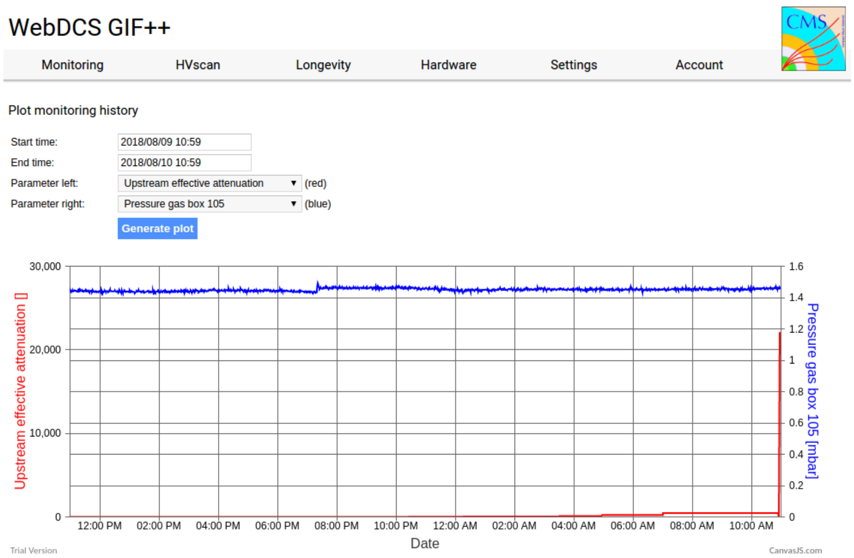

Figure 5.26: DIP monitoring history accessed through GIF++ WebDCS interface.

The data flow related to the monitoring of the detector high voltages and currents, referred to as *CAEN flow* as a reference to the manufacturer of power supplies, is retrieved thanks to computer to main frame communications. Indeed, during the operations (irradiation or beam period), these values can be accessed directly through the bus of the main frame hosting the high voltage supplies. Finally, the DAQ flow concerns all data acquired through the use of the TDCs, i.e. all the muon or gamma data recorded by the detectors under test at GIF++.

5.3.4 Measurements performed during beam periods

As previously described, two types of measurement are performed on the chambers during beam periods. On one hand, it is interesting to measure the efficiency of the RPCs with increasing voltage with different source absorber settings but on the other hand, it is important to correlate the efficiency information to the gamma rate seen by the chambers at the voltages that were scaned for efficiency. The choice was made to separate efficiency measurements from rate measurements to better manage time and data volume. In both cases, TDC data recorded during so called *HV scans* is divided into *runs*, one for each high voltage point, whose data is stored into ROOT files. The TDC settings used during both these scans as well as the ROOT data structure are detailed in Section A.4.2 of Appendix A.

The goal of both efficiency and rate scans is to measure the rate capability of the detectors but also to monitor any degradation of the performance due to ageing. This way, during test beam periods the efficiency and corresponding gamma background are measured to correlate the evolution of rate capability at different stages of irradiation. In the absence of other signs of ageing, a reduction of the rate capability could be related to an increase of the electrodes resistivity.

5.3.4.1 Efficiency scans

The HV scans performed to specifically measure the muon detection efficiency under different irradiation conditions follow a standardized procedure. Data using the DAQ is taken at the same 12 HV points for all chambers, ranging from $9\,\mathrm{kV}$ to $10.1\,\mathrm{kV}$ by steps of $100\,\mathrm{V}$. For each HV run, a minimum of 5000 muon beam triggers, provided by the coincidence of the three scintillators, is required in order to accumulate enough statistics for a reliable computation of the efficiency of the detectors. In addition to the four RPCs held on `T1`, two tracking RPCs installed on `T3` are kept at a fixed voltage of $9.7\,\mathrm{kV}$ to provide the analysis software [273] with beam position information to exclude off-track signals. The tracking RPCs, whose design is based on which of CMS RPCs, are double gap detectors featuring $2\,\mathrm{mm}$ HPL electrodes and $2\,\mathrm{mm}$ gas gaps. Finally, the monitored currents and voltages are recorded in histograms along the TDC data in a different ROOT file for each run.

HV scans are taken for different source settings as the goal is to irradiate all the detectors with a minimal rate of $600\,\mathrm{Hz/cm^2}$. Usually, a full study of the performance of the detectors is performed with Source OFF, and then with nine absorber settings that attenuate the nominal gamma flux by factors from more than 200 to only 3, settings with fully opened source being avoided with RPCs in test beam position. Adjusting the gamma flux is possible thanks to the three layers of absorbers featured on the Cesium source [274].

5.3.4.2 Rate scans

These background measurements are performed using a similar HV scan procedure than in the case of efficiency measurements. The HV scan in test beam period will be taken fewer HV points than for the efficiency scans as the region of interest is located around the knee and efficiency plateau of the detectors in order to extract through linear interpolation the value of the rate at the working voltage deduced from the efficiency scan. Thus, these scans are performed only on six HV points ranging from $9.5\,\mathrm{kV}$ to $10\,\mathrm{kV}$. Rate scans are substantially heavier than efficiency scans. Indeed, a good estimation of the rate requires a long enough integrated time worth of data. The way data is collected, detailed in Appendix A, makes the DAQ search for data stored in the TDC buffers prior to the trigger signal. The time window from which the data is collected ranges in between only 25 ns to more than 50 μs. The Cesium source delivering a consistent gamma flux, it was decided than a total integrated time of 0.2 s would be enough to have a reliable calculation of the γ rate. This is achieved by taking 20,000 random trigger pulses delivered by a pulse generator at a frequency of 300 Hz while extracting 10 μs of data from the buffers for each trigger.

Separating rate measurements from efficiency measurement was motivated by the inconsistency of the muon beam provided in GIF++. Using periods without beam to measure rates with a good statistics allows for faster study programs. Moreover, depending on the muon strength that can strongly vary due to users placed upstream of GIF++ and using magnets, the number of muon delivered per beam spill can make the accumulation of 20,000 events too long for the other users of GIF++. Hence, efficiency scans are performed with lower statistics, and the time window from which the data is extracted is strongly reduced (400ns for efficiency scans versus 10 μs for rate scans) to keep the data size to its bare minimum.

5.3.4.3 Offline analysis and Data Quality Monitoring

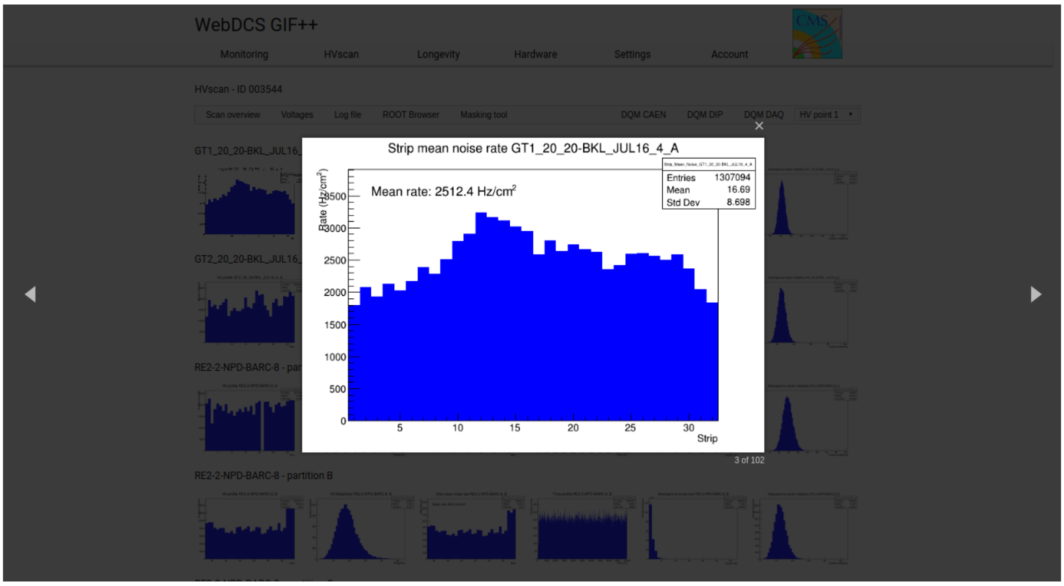

Figure 5.27: Example of DQM page available on CMS RPC WebDCS in GIF++. The rate measured in one of the tracking chambers, namely `GT1_20_20-BKL_JUL16_4`*, is presented here. The DQM page allows clicking on each histogram to extend its view and to navigate through the histograms thanks to the left and right arrows.*

The data recorded during efficiency and rate scans always consist in two ROOT files per run, a run corresponding to a HV point. One of the files corresponds to the TDC data, a collection of hits per active channel on the read-out of the RPCs, while the second is the CAEN main frame data, offering a monitoring of the currents and high voltages. This data is systematically analysed at the end of each scan thanks to the Offline Analysis tool of GIF++, detailed in Appendix B, that produces histograms such as hit, rate and time profiles, hit multiplicities, gamma cluster sizes or nultiplicities for the DQM display of the WebDCS, as showed in Figure 5.27. More histograms can be accessed through the ROOT browser included in the WebDCS, as showed in Figure 5.28. Moreover, the analysis performed thanks to the Offline tool is definitive in the case of evaluating the rates from rate scans. On the contrary, the algorithm for efficiency calculation is kept simple and approximative in the tool as including tracking into the analysis requires manual adjustment for each individual scan.

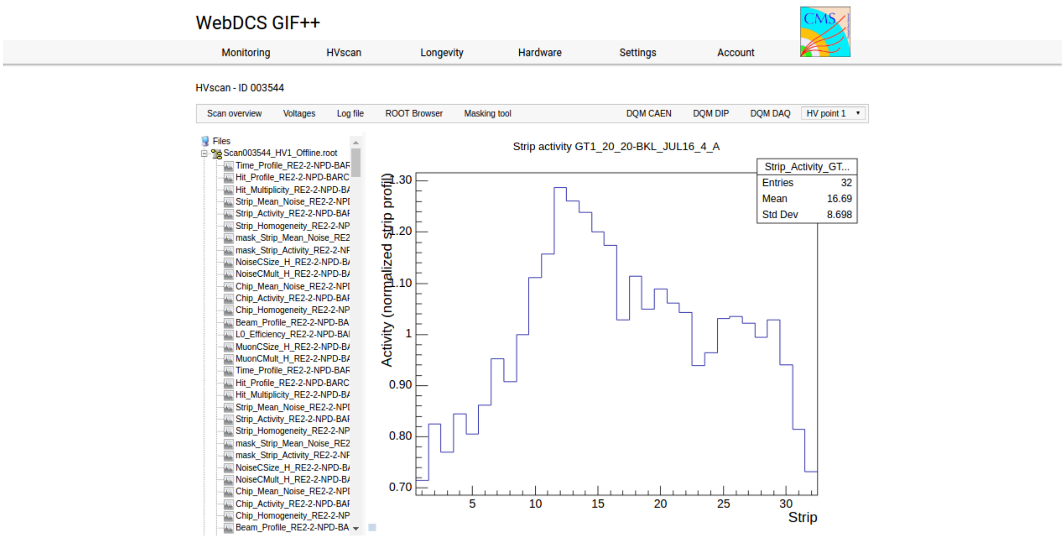

Figure 5.28: Example of DQM ROOT Browser page available on CMS RPC WebDCS in GIF++. The strip activity profile, defined as the rate profile normalized to the mean rate, in one of the tracking chambers, namely `GT1_20_20-BKL_JUL16_4`*, is presented here. Available ROOT files and histograms can be browsed thanks to the left panel showing the directory and files structures.*

5.3.5 Measurements performed during irradiation periods

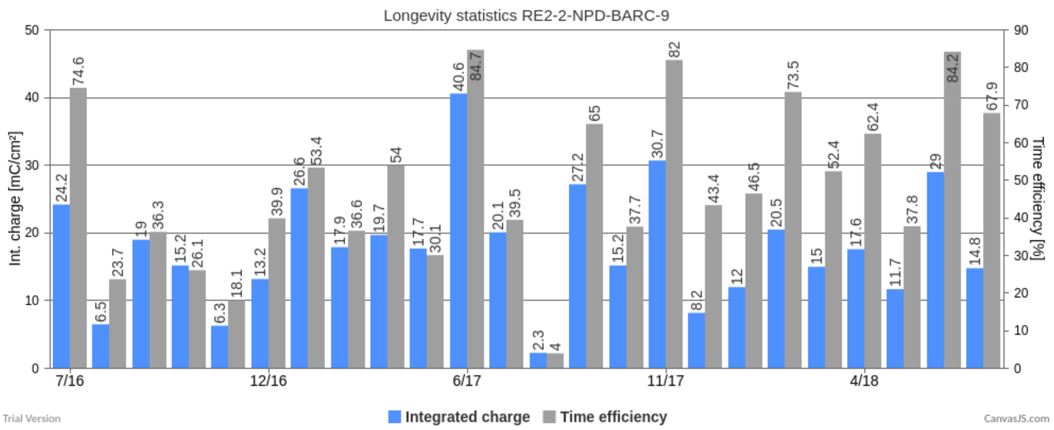

Figure 5.29: Longevity statistics of chamber `RE2-2-NPD-BARC-9` *in GIF++. For each month since July 2017, the integrated charge (in blue) as well as the time efficiency of irradiation (in gray) is reported.*

Even though test beam periods are stressful times has an extensive data taking planing needs to be finalized in a short amount of time, the biggest amount of data comes from irradiation periods. Indeed, when `T1` is moved back to its ageing position in between each test beam periods, data is recorded at any time the source can be switched ON for irradiation. Indeed, other experiments in the area might prevent the source from staying opened continuously. As an example, the time efficiency of irradiation of CMS RPC detectors in GIF++ is presented in Figure 5.29.

Several types of measurement are performed throughout the irradiation period. Indeed, as long as the detectors are being irradiated, a monitoring of the currents is performed to evaluate the corresponding integrated charge considering the irradiation time. Moreover, the corresponding gamma rates need to be measured on a regular basis. Ageing signs can be understood through an increase of the detector noise correlated with an increased dark current. For this purpose, HV scans are performed to measure the noise with increasing voltage and the dark currents. Another way to highlight ageing is through the loss of rate capability of the detectors. During irradiation periods this can be looked through thanks to HV scans performed at various source settings, which are referred to as *source scans*. The loss in rate capability could be understood by a saturation of the measured at higher gamma flux. This effect could be correlated with an increase of the electrodes resistivity. The resistivity is then measure periodically during the year, generally before or after test beam periods by the use of Argon breakdown technic.

5.3.5.1 Longevity scans

The main activity of irradiation periods consists in the *longevity scans* during which the currents of the irradiated chambers are continuously monitored. The two irradiated chambers, `RE2-2-NPD-BARC-09` and `RE4-2-CERN-166`, are both brought to a voltage of 9.8 kV while the source flux can vary depending on the need of experiments using the facility. The currents are recorded on each active gas volume and each gap contribution is then translated into the mean chamber integrated charge as can be seen from Figure 5.30. At the end of each longevity scan the integrated charge accumulated in each chamber is used to update the summary plots providing the collaboration with official results to be spread.

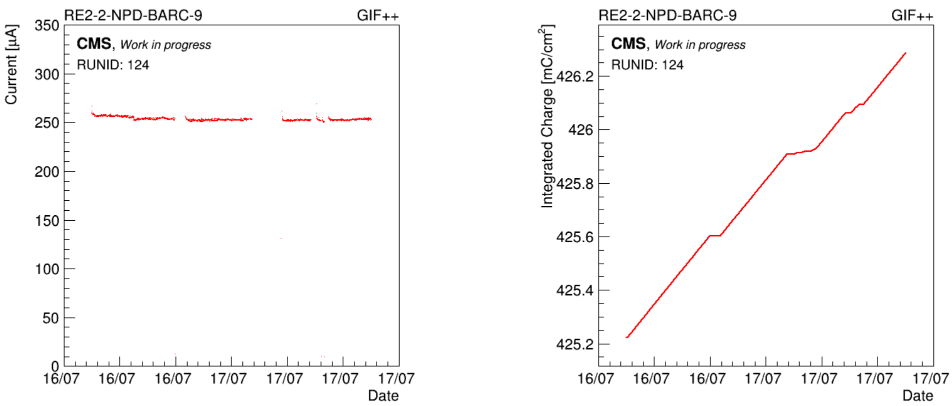

(a) *(b)*

Figure 5.30: Example of current monitoring (Figure 5.30a) and of corresponding integrated charge (Figure 5.30b) of chamber `RE2-2-NPD-BARC-09`. The decrease of current is related to a decrease of the voltage due to the daily rate scan procedure or to periods during which the source was turned OFF.

5.3.5.2 Daily rate monitoring scans

Every night during longevity scans, the DAQ is used to perform *daily rate scans*. These scans aim at keeping track of the gamma rate measured in the irradiated RPCs during longevity but is also measured the noise rate at standby voltage and this, for each gap individually. The procedure for these HV scans consist in 9 runs for which 50,000 random triggers are requested, corresponding to $0.5\,\mathrm{s}$ of total integrated time.

1- All gaps are first left at the irradiation voltage of $9.8\,\mathrm{kV}$ to measure the γ rate.

2- Then all gaps are brought to the standby voltage of $6.5\,\mathrm{kV}$ to measure the noise rate of the full detectors.

3- Both top gaps (TW and TN) are brought to a voltage equivalent to an OFF status, i.e. $1\,\mathrm{kV}$ so that the noise contribution of only the bottom gap at standby voltage can be measured.

4- The bottom gaps are ramped up toward the working voltage of $9.8\,\mathrm{kV}$ to measure their contribution to the gamma rate estimation.

5-8 The steps 3 and 4 are repeated on TN and then on TW, keeping the bottom and the top gap which is not of interest at a voltage of $1\,\mathrm{kV}$. This way, the individual contribution to the noise and gamma rates are known.

9- Finally, both TW and TN are brought to working voltage while the bottom gap is left at $1\,\mathrm{kV}$ to measure the gamma rate for the full top layer at once.

Finally, the voltages of all gaps are brought back to working voltage for the longevity program to continue until the next daily scan.

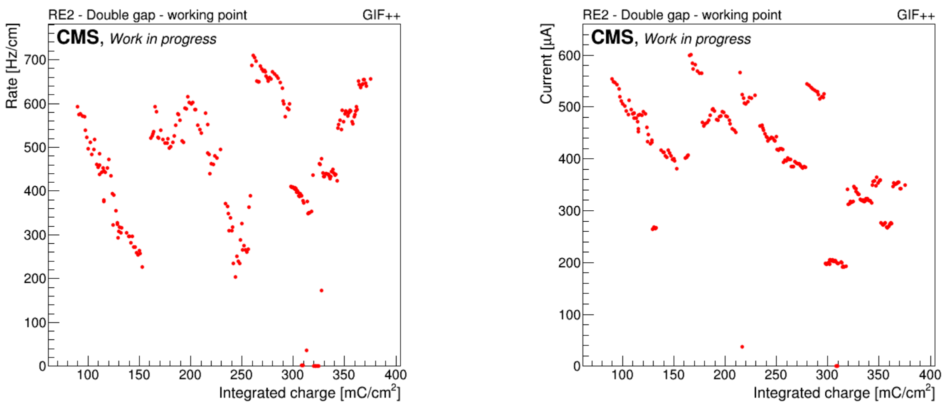

(a) *(b)*

Figure 5.31: Example of rate (Figure 5.31a) and current (Figure 5.31b) monitoring of chamber `RE2-2-NPD-BARC-09` *with increasing integrated charge. The variations of the rate and current are correlated and corresponds to change of source irradiation, gas flow, gas humidity, or environmental conditions.*

Naturally, as this data is taken using GIF++ DAQ, two ROOT files containing the DAQ data and CAEN data are created for each runs in the exact same way than for efficiency or rate scans taken during test beam periods but while the currents are still monitored by the longevity scan and saved into GIF++ database for an easy evaluation of the currents to the integrated charge. The Offline Analysis tool provides then the DQM page with histograms and daily values can be assembled in long term monitoring plots to study the variations of rate and current with increasing integrated charge, as presented in Figure 5.31. The rates on every single read-out channel are also tracked to control their activity with increasing integrated charge and, this way, understand the appearance of hot spots through noisy channels, as showed in Figure 5.32.

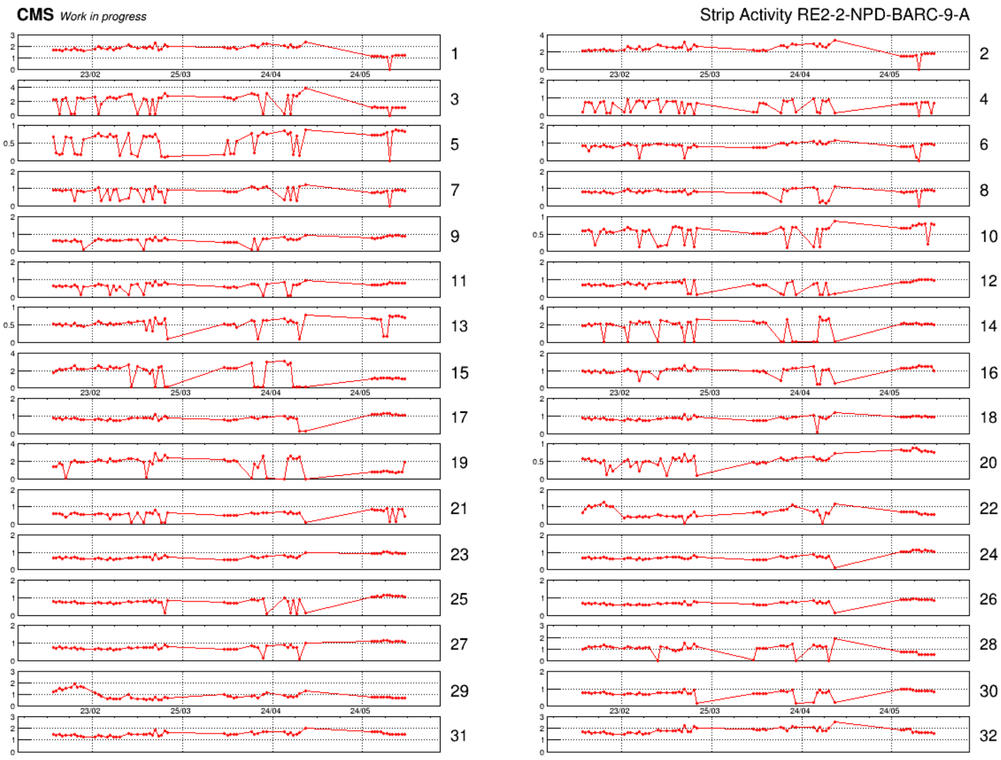

Figure 5.32: Example of strip activity of chamber `RE2-2-NPD-BARC-09` *monitoring through time. The activity of a strip is defined as the rate of the individual channel normalized to the mean rate measured in the corresponding read-out partition.*

5.3.5.3 Weekly noise monitoring scans

Once a week, the source is turned OFF for the CMS RPC to make a noise scan, which consist into a HV scan composed of seven runs and involving both the irradiated but also the reference chambers, providing with a weekly monitoring of the evolution of the irradiated chambers noise and dark current. The first run is taken at standby voltage for all chambers while the next 6 runs are taken with voltages ranging from 9.4 to 9.9 kV inorder to have for both type of chambers, RE2 and RE4, a coverage of the noise rate in the voltage region in which the efficiency rises and reaches the plateau.

5.3.5.4 Weekly source scans

Directly following the weekly noise scans, HV rate scans are organised at three different source settings, usually corresponding to ABS 6.8, 4.6 and 3.3. The procedure of these HV scans is strictly similar to which of weekly noise scans, involving the four RPCs in order to have a weekly comparison of the values recorded in every chamber. Measuring with all detectors at the same time allows getting rid of potential systematics that might make the rates (noise or gamma) vary from one measurement to another. If such systematic effect occurs, it will be observed in all detectors.

5.3.5.5 Weekly current scans

The previously detailed daily rate scans, but also the weekly noise and source scans are interesting tools to look at an increase of noise rates and dark currents or at a loss of rate capability and point to an increase of surface resistivity of the electrodes through the absorption of hydrofluoric acid. Nevertheless, periodically measuring the currents on wider high voltage ranges allows to have access to the ohmic part of the current driven by the detectors related to the electrodes resistance. This is why precise current scans, consisting only in measuring the current driven through the four detectors, are performed each week. The scan procedure consists in 131 high voltage steps in between $500\,\mathrm{V}$ and $10\,\mathrm{kV}$ by steps of $100\,\mathrm{V}$ until the standby voltage of $6.5\,\mathrm{kV}$ is reached and then by steps of $50\,\mathrm{V}$. The current increase in between $500\,\mathrm{V}$ and the voltage where charge multiplication starts to occur is only driven by the resistance of the detector to current and thus increases linearly. A fit on this linear increase of the currents in the range before charge multiplication occurs gives access to the resistance of the system electrodes/gas. If any variation of the electrode resistance occurs, the global resistance will increase and so will the current. Technically, these scans will record a ROOT file per HV step that will have the same format than the CAEN ROOT file saved during other HV scans and is also analysed using the Offline Analysis tool to provide with DQM histograms as well as standardised I/V tables.

5.3.5.6 Resistivity measurements

Aside of the parameters monitored to spot ageing, the resistivity of the HPL planes is measured regularly before or after test beam periods through high voltage scans of the detectors operated with pure Argon. The electric field strength at which Argon breaks down being well known, the breakdown voltage in the detectors is measured and gives an information about the resistance of the electrodes, as above the breakdown voltage Argon turns into a conductive plasma and thus does not offer electric resistance anymore, which then can be used to calculate the resistivity of the electrode material. The Argon line in GIF++ are not kept humid and thus this measurement is not performed too often to make sure the electrodes don't dry out, leading to an increase of the electrode resistivity.

5.3.6 Results and discussions

Since 2015, CMS RPCs have been irradiated in GIF++ with the goal to reach a total integrated charge per irradiated detector of $0.84\,\mathrm{C/cm^2}$ while certifying the detectors to a rate capability of $600\,\mathrm{Hz/cm^2}$. As of today, the RE2 and RE4 chambers respectively achieved 51 and 26% of the total irradiation program. A few years of irradiation are expected before reaching the end of the longevity study and a final answer on whether the detector will be able to live through HL-LHC or not. A negative answer to this question would probably lead to solutions to replace the detectors before HL-LHC or to improve the shielding of these detectors against background radiation in the experimental cavern, which could be a more sustainable solution.

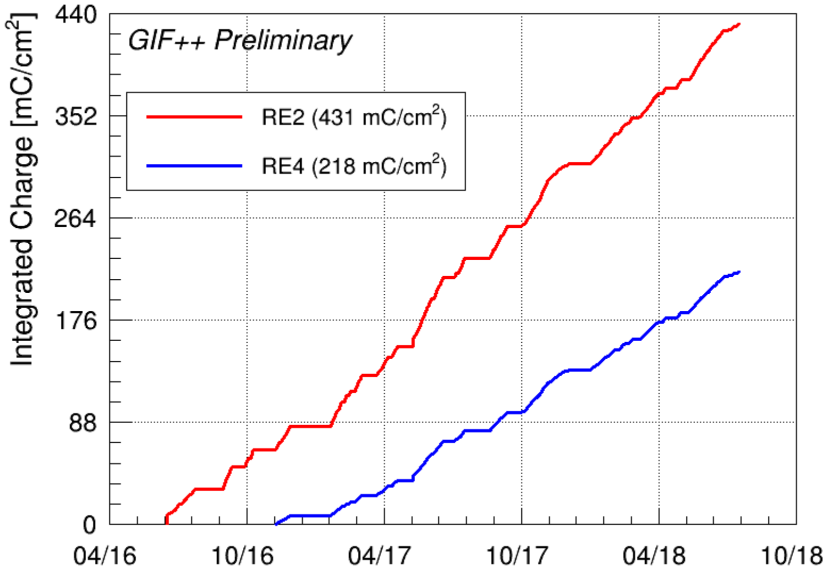

Figure 5.33: Total integrated charge in the irradiated RPCs, `RE2-2-NPD-BARC-9` *and* `RE4-2-CERN-165`*, before starting August 2018 test beam period. The irradiation of the RE2 chamber started in June 2016 while the RE4 chamber couldn't be irradiated before November 2016.*

6

Improved RPC investigation and preliminary electronics studies

The extension in the endcap of the RPC sub-system towards higher pseudo-rapidity will bring the new detectors to be exposed to much more intense background radiations due to the proximity of the detectors with the beam line (Figure 3.5). The challenge will be to produce high counting rate detectors with limited ageing rate to ensure a stable operation of the detector over a period longer than ten years. In Chapter 4 was discussed the influence of the detector design (number and thickness of gas volumes, OR system, etc...) on the charge deposition and rate capability. Nevertheless, this question can also be addressed from the electronics point of view as a better signal-to-noise ratio would also mean the possibility to greatly lower the charge threshold on the signals to be detected, allowing to use the detector at lower gain, hence lowering the charge deposition per avalanche in the gas volume. Cardarelli showed that the production of low-noise fast FEEs could help decreasing the charge deposition per avalanche at working voltage by an order of magnitude, virtually increasing the life expectancy of such a detector in the same way [275].

6.1 FEE candidates for the production of iRPCs

The extension of the third of fourth endcap disks with improved RPCs has been presentated in Chapter 3 together with the expected background levels (Figure 3.23). An important piece of these iRPCs will be the Front-End Electronics that will equip the chambers. A fast, low-jitter and low-charge sensitive electronics will help reducing further the charge deposition in the detector by making it possible to operate at lower gain.

In the context of the CMS Muon Upgrade, two FEE solutions have been considered to equip the iRPCs. The baseline for the RPC upgrade is based on the PETIROC ASIC, initially for Time-of-flight (ToF) applications. A back-up solution is also under study and focusses on a new low-noise preamplifier designed in INFN laboratories in Rome to replace the preamplification stage of the already existing CMS RPC Front-End Board.

The FEEs that are foreseen to equip the new RPCs need to be able to detect charges as small as $10\,\mathrm{fC}$. Not only the new electronics need to be fast and reliable, they also should be able to sustain the high radiation the detectors will be subjected to in the region closest to the beam.

6.1.1 CMS RPCROC: the RPC upgrade baseline

Designed by Weeroc, a spin-off company from the french OMEGA laboratory, the PETIROC 2A consits in a fast and low jitter 32-channel ASIC originally developed to read-out Silicon Photomultiplier (SiPM) in ToF applications and that allows for precise time measurements [198, 199]. The ASIC uses an AMS $350\,\mathrm{ns}$ SiGe technology. The block diagram of the ASIC is showed on Figure 6.1. A 10-bit DAC allows to adjust the trigger level in a dynamical range spanning from 0.5 to a few tens of photoelectrons and a 6-bit DAC to adjust the response of each individual channel to similar a level.

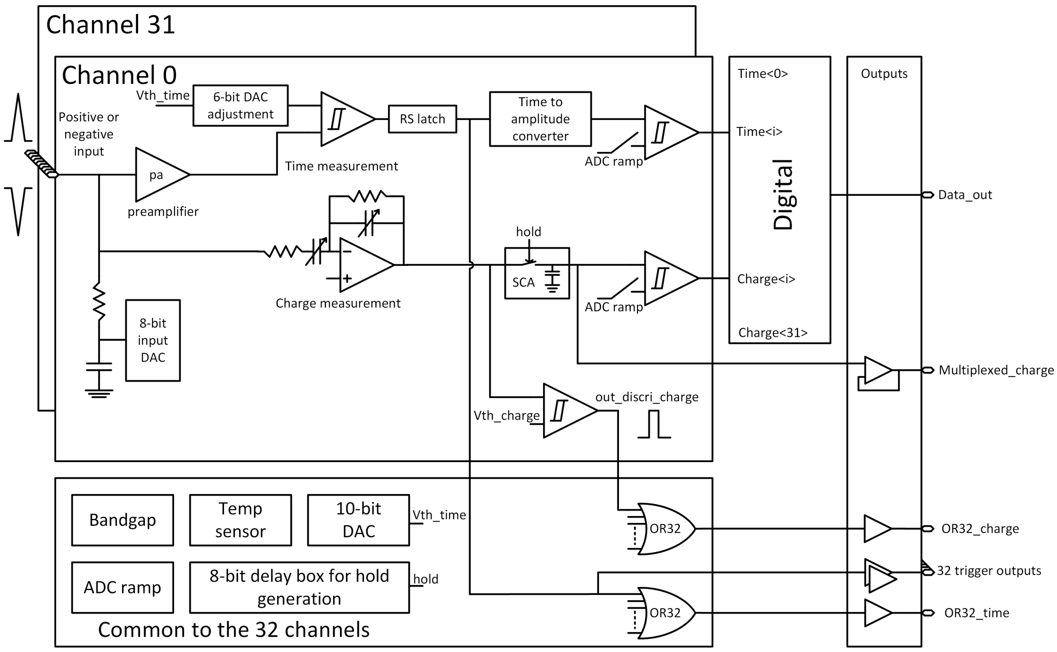

Figure 6.1: PETIROC 2A block diagram.

Nevertheless, in order to adapt this ASIC to CMS, modifications were brought to the PETIROC [177] and not all its functions will be used [276]. In the new CMS RPCROC, showed in Figure 6.2, the measurement of the charge will be performed by a Time-over-Threshold (ToT) technic, taking profit of the capacity the ASIC has in measuring both the leading and trailing edges of the input signals. The dynamic range will be expanded towards lower values to allow for the detection of charges as low as $10\,\mathrm{fC}$. Due to the radiation levels that are foreseen at the level of the iRPCs, the SiGe technology will be replaced by the Taiwan Semiconductor Manufacturing Company (TSMC) $130\,\mathrm{nm}$ CMOS, to increase its radiation hardness while keeping fast pre-amplification and discrimination with a very low jitter that can reach less than $20\,\mathrm{ps}$ if no internal clock is used, as can be seen from Figure 6.3. The ASIC is associated with an FPGA which purpose is to measure time of the signals. The FPGA is equipped with a TDC with a time resolution of 50-100 ps developed by Tsinghua

University. The full system will provide a measurement of the signal position along the strip with a precision of a few cm by measuring the signal timing on both ends of the strips.

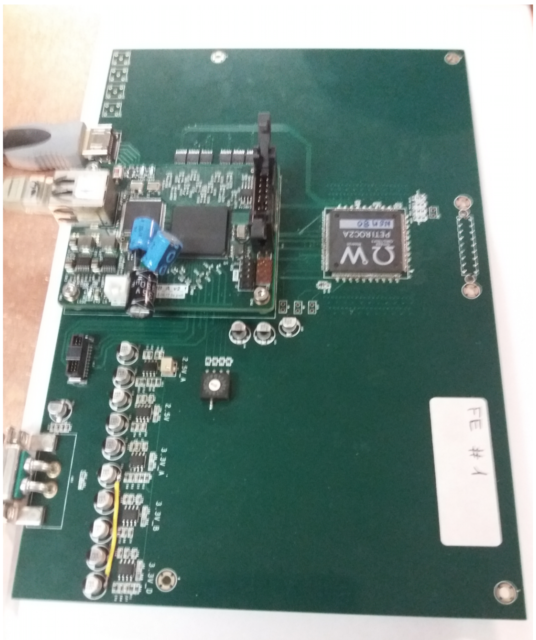

Figure 6.2: View of the RPCROC Front-End Electronics in which the PETIROC 2A ASIC is visible as well as the FPGA on which the TDC is hosted.

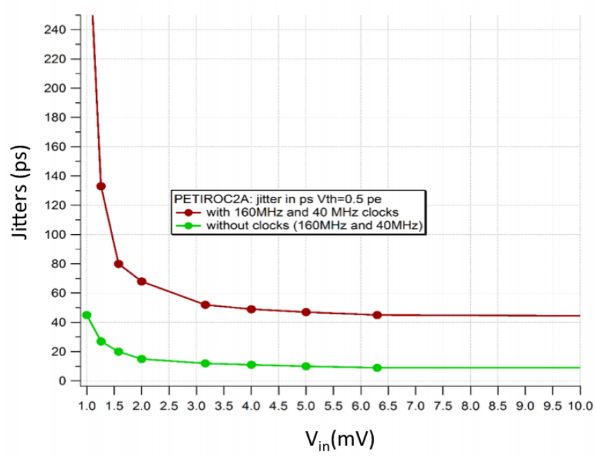

Figure 6.3: The PETIROC time jitter as a function of the input signal amplitude, measured with and without internal clocks.

In order to read-out all 96 strips, 3 ASICs and 3 TDCs, each having an increased number of 64-channels, are hosted on a FEB attached to the chamber. Two scenarios are being studied to connect the ASICs to the read-out strips [276]. The correspponding read-out panels are showed in Figure 6.4.

On the one hand there is the possibility to design a standard trapezoidal strip panel and to directly connect the strips to the ASICs using coaxial cables of similar impedance than the strips. On the other hand, the return lines could be embeded directly in extra layers of the strip panel to offer the possibility to minimize the amount of on-detector cables by using a single connector to send the signals to the FEB's inputs. The first version of the panel is refered to as *coaxial design* while the second as *return design*. In the case of the return design panel, the read-out area is a little smaller than in the case of the coaxial panel. This was motivated by the need to shield the return strips beneath the copper ground plane visible on the side of the PCB.

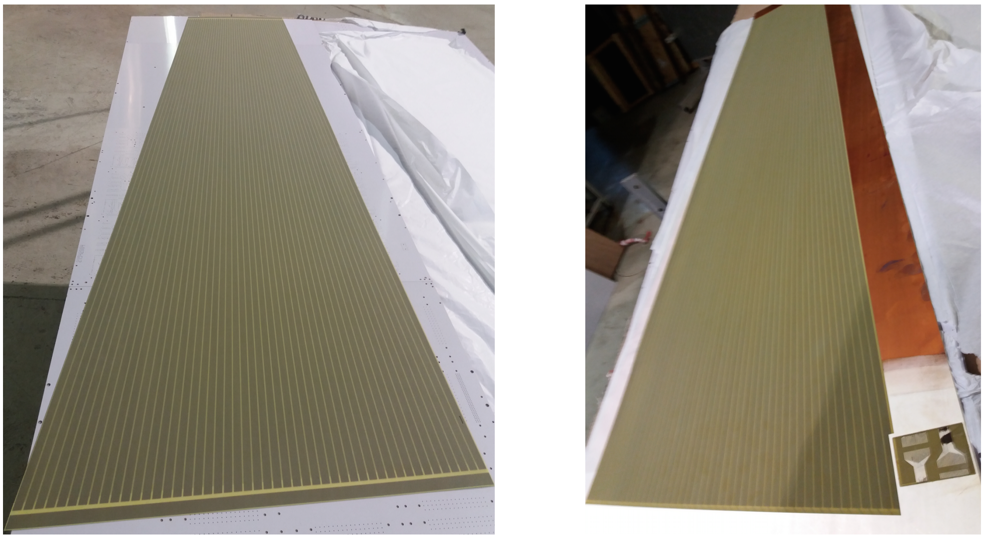

(a) *(b)*

Figure 6.4: View of the coaxial design (Figure 6.4a) and of the return design (Figure 6.4b) of read-out panels used in the iRPC prototypes. Only half PCBs with 48 strips are showed.

6.1.2 INFN Front-End Board: a robust back-up solution

Even though the baseline for the electronics that will equip the iRPCs will be the CMS RPCROC, a back-up solution needs to be certified. The back-up has been found in a Front-End Electronics featuring a fast and low-noise (1000 e^- rms) Silicon (Si) preamplifier and a Silicon-Germanium (SiGe) discriminator [277] associated with an optimized read-out panel [278]. The low-noise preamplifier is a new version of a preliminary production of a SiGe preamplifier by the team of Cardarelli working with INFN Roma with the purpose of equipping the new generation of ATLAS RPCs [279].

The FEB is equipped with eight channels of preamplifiers using a Bipolar Junction Transistor (BJT) technology and two discriminator ASICs of four channels using Hetero Junction bipolar Transistor (HJT) technology. The input signals are amplified at an amplification factor of 0.2 to $0.4\,\mathrm{mV/fC}$ and are then discriminated with a threshold of $0.5\,\mathrm{mV}$ at minimum. For each channel, the LVDS output is proportional in width to the Time-over-Threshold in the discriminator of the amplified signal with a minimum width of $3\,\mathrm{ns}$. This method allows for an estimation of the avalanche charge as the width of the signals usually is consistent and proportionnal to the amount of charge released in the gas volume.

The read-out panel feautures 96 trapezoidal copper strips and has a similar design to the read-out panels used for the CMS RPCROC. As for now, the strips are only read-out from one end.

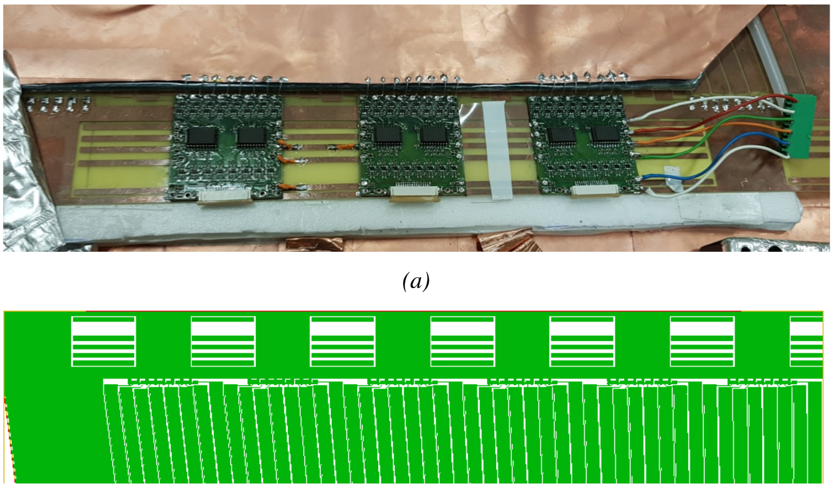

(a)

(b)

Figure 6.5: Experimental setup used to test the INFN preamplifier with respect to the CMS FEEs.

6.2 Preliminary electronics tests at CERN

6.2.1 INFN preamplifiers as upgrade candidates

INFN electronics were the first ones to be tested by CMS RPC group in collaboration with colleagues from INFN Roma working in the ATLAS RPC group. The tests with CMS RPCs were performed in February 2013 outside of the old GIF facility presented in Chapter 5.1.1. Four preamplifier channels were lended by Cardarelli to equip four CMS RPC channels as presented in Figure 6.9. They were directly connected to the strips for the signals induced by muons passing through the gas volume of the chamber to be amplified. The output was then sent to a discriminator to digitize the signals and filter out the noise by tuning the threshold level. The NIM quad discriminator 821 manufactured by LECROY used during this experiment only allows at minimum to set the threshold at a voltage of approximately $30\,\mathrm{mV}$ on the input signals. Thus, two values of discrimination were used ($\sim 75\,\mathrm{mV}$ and $\sim 30\,\mathrm{mV}$).

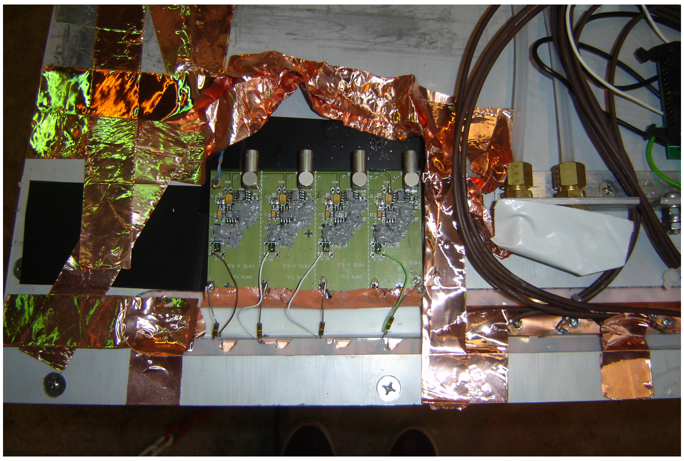

Figure 6.6: The four channels of INFN preamplifiers are mounted directly on a CMS RPC and connected to the four outermost read-out strips of the detector.

The performance of the chamber equipped with these new preamplifiers was compared to the performance of CMS FEEs. The experimental setup used is described in Figure 6.7. PMTs a little less wide than four strips were used to trigger the data tacking. Two pairs were used in coïncidence on both the strips connected to the INFN preamplifiers and to the ones connected to the CMS FEEs. An extra PMT, placed perpendicularly to the rest of the setup at the bottom of the setup was used to detect potential showers and send VETO signals if necessary. A last PMT was used close to the power supplies to measure and discard signals due to electromagnetic noise and is not visible on the pictures. Finally, after discrimination, the output of the INFN preamplifiers together with the signals from the CMS FEEs were sent to scalers to count the detected signals versus the number of trigger coïncidences as no DAQ software was available at the time. The full pulse processing for this experiment is shown in Figure 6.8.

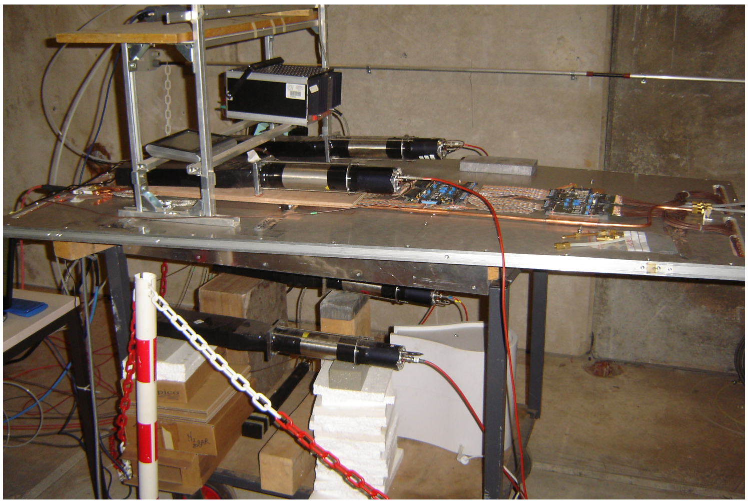

(a)

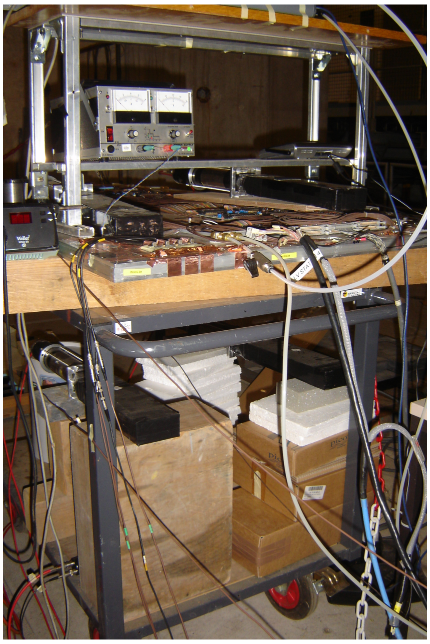

(b)

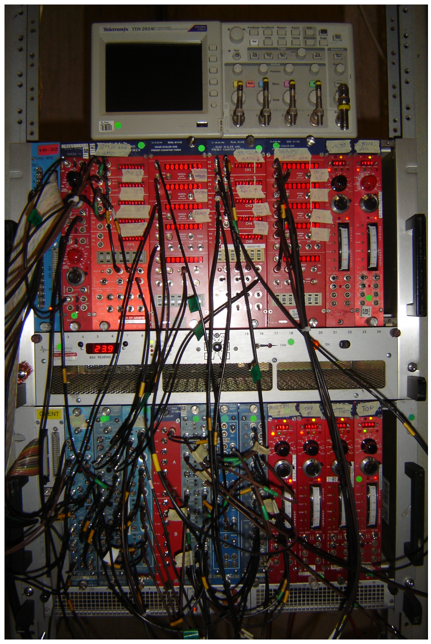

(c)

Figure 6.7: Experimental setup used to test the INFN preamplifier with respect to the CMS FEEs.

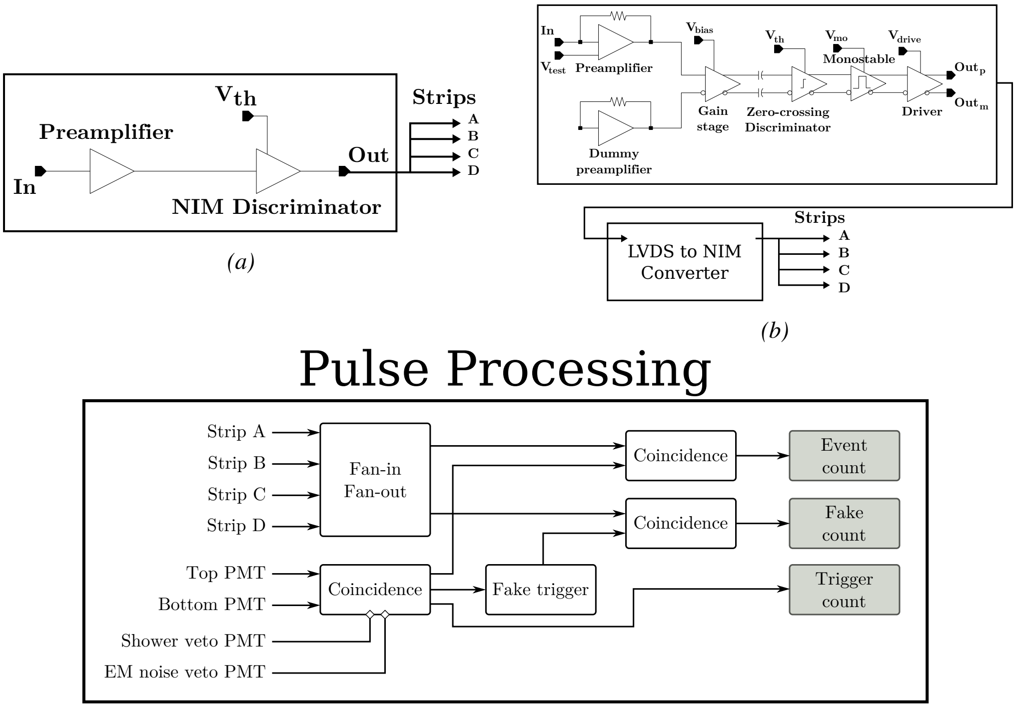

(c)

Figure 6.8: The block diagrams corresponding to the signal treatment for both INFN preamplifier (Figure 6.8a) and CMS FEEs (Figure 6.8b) are shown. The digitized signals are then counted in coïncidence with the trigger signals provided by PMTs (Figure 6.8c).

The data taking program consisted in High Voltage scans. A first point was taken at 0 V to only measure noise. Then the HV was increased to an applied value of 7 kV. The voltage was increased in steps of 500 V until 8 kV from where it was increased in steps of 100 V until an upper limit of 10 kV. After rising the voltage over the electrodes of the RPC, a waiting period of 15 minutes was observed to leave time to the electrodes to charge and to the currents to stabilize. The currents were reported at the moment the data taking was started. At each HV step, except at 0 V, approximatively 300 triggers were taken to estimate the efficiency of the detector by counting the number of hits in the system (A or B or C or D), referring to the strips. The noise rate per unit area was measured during the first 100 s of data taking by counting the number of hits recieved in each read-out strip. The cluster size, the average number of adjacent strips fired during a muon event, could not be measured due to the lack of available scalers.

During the data acquisition, in addition to counting the number of signals with respect to the number of triggers, the current or the noise rate per unit area as a function of the increasing voltage, the environmental parameters were monitored. Using the information provided by a humidity and temperature sensor on the gas input line together with the environmental pressure given by a weather station, the applied voltage could be corrected following Formula 4.27. Moreover, the voltage line was filtered to prevent noise and higher currents in the RPC under test.

The results of the preliminary tests are presented in Figure 6.9. More details on the fit performed on the data are provided in Table 6.1. As can be seen, being able to use electronics with a much higher sensitivity allows for a HV shift of up to 475 V with a threshold as low as 3 fC corresponding to the lowest threshold available on the discriminator modules. On the other hand, the higher charge sensitivity also brings a higher noise level. After a first series of measurement performed with a bad grounding leading to grounding loops and hence an artificially higher noise, it can be concluded that the noise rate per unit area of such electronics is approximately one of manitude higher than the noise rate measured with the CMS FEB. The noise reaches approximately $2\,\mathrm{Hz/cm^2}$ at the level of the working in the case of the INFN preamplifier while it is lower than $0.2\,\mathrm{Hz/cm^2}$ for the CMS FEB. It is likely that the higher sensitivity also brings a higher sensitivity to local discharges happening in the gas due to fluctuations of the electric field. The surface of the electrodes not being perfectly smooth, the local electric field may vary quickly. The gas molecules circulating in the gas could then be ionised by the fast variation of the field and trigger an avalanche that can then be detected. Reducing the noise rate per unit area would then come from an improvement of the detector itself rather than from a reduction of the electronic noise of the INFN preamplifier.

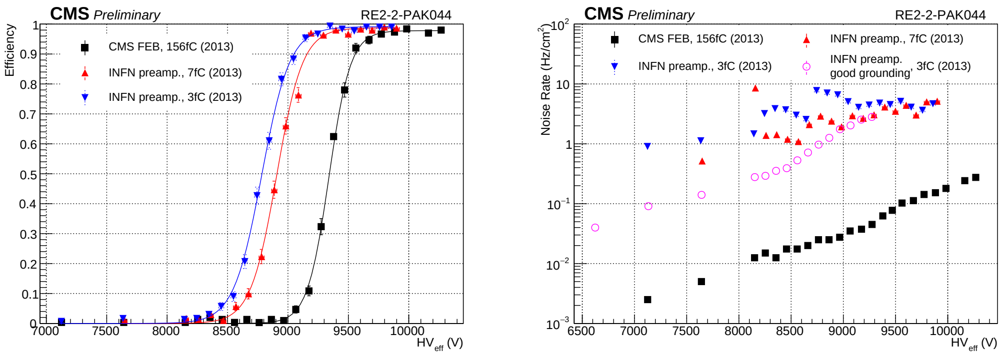

(a) *(b)*

Figure 6.9: Efficiency (Figure 6.9a) and noise rate per unit area (Figure 6.9b) of the CMS RE2-2 detector tested with the standard CMS FEBs (black) and with the INFN preamplifier at different thresholds (red and blue). An extra HV scan was performed with better conditions to measure the noise with a threshold of $3\,\mathrm{fC}$ *on the INFN preamplifiers.*

Data	ϵ_{max}	$\lambda\,(\times 10^{-2}\,\mathrm{V}^{-1})$	HV_{50} (V)	ϵ_{WP}	HV_{WP} (V)
CMS FEB, 156fC (2013)	(0.978 ± 0.004)	(1.12 ± 0.07)	(9339 ± 11)	(0.97 ± 0.01)	(9752 ± 27)
INFN preamp., 7fC (2013)	(0.987 ± 0.003)	(0.93 ± 0.05)	(8907 ± 11)	(0.97 ± 0.01)	(9374 ± 27)
INFN preamp., 3fC (2013)	(0.991 ± 0.003)	(0.86 ± 0.04)	(8783 ± 11)	(0.98 ± 0.01)	(9276 ± 27)

Table 6.1: Results of the sigmoid fit (Formula 4.24) performed on the data presented in Figure 6.9a. The working point and its corresponding efficiency are computed using Formulas 4.24 and 4.25.

6.2.2 INFN preamplifiers mounted onto CMS Front-End Board

Following the first experiment performed in the experimental hall aside of the old GIF, a new series of tests has been done in the CMS RPC assembly laboratory at CERN. For this purpose, the preamplifiers have been designed to be standalone single channels. To have a consistent comparison with the CMS FEB, a FEB prototype has been built based on the current CMS design. As shown in Figure 6.10, the preamplifiers are meant to be plugged in one of the available 16 channels of the board that produces an LVDS output with similar characteristics than the CMS FEB.

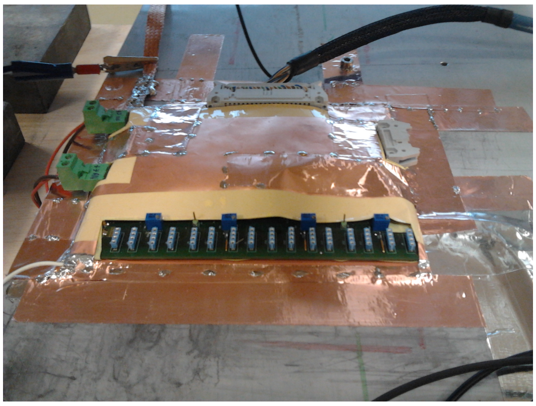

(a)

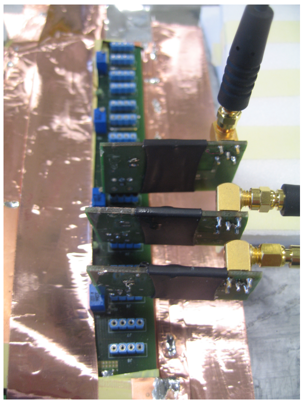

(b)

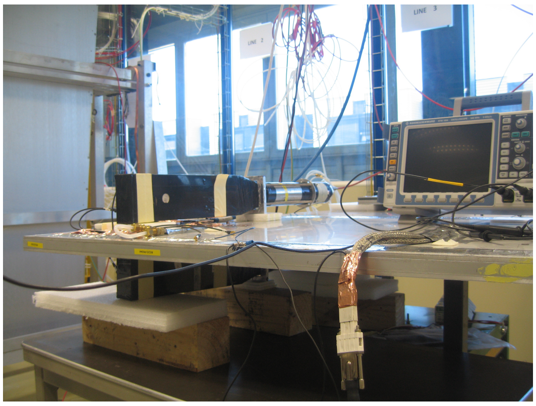

(c)

Figure 6.10: Figure reffig:Setup-INFN-904:A: Shielded Front-End Board on which the INFN preamplifiers are to be mounted. Figure reffig:Setup-INFN-904:B: Three INFN preamplifiers connected onto the test FEB. Figure reffig:Setup-INFN-904:C: Experimental setup used to test the INFN preamplifier single mounted on a FEB similar to the CMS FEB.

At the time of the second experiment, only three channels could be lended by the team of INFN Roma. The impedance of the preamplifiers was set to $100\,\Omega$ at delivery. The strips are then connected to the preamplifiers using $50\,\Omega$ coaxial cables equipped with SMC connectors, known for their good transmission. To match the impedance of the preamplifier input with the signal cable, a $100\,\Omega$ resistor was added in parallel of the input line. In CMS endcap RPCs, the strips are left floating. For the purpose of this test, it was necessary to terminate the strips on both ends to prevent reflections in the transmission line. The impedance of the strips being approximately $25\,\Omega$, the strips were terminated with $50\,\Omega$ resistors on the signal cable side, and with $25\,\Omega$ resistors on the end side.

The threshold of the zero-crossing discriminators used on the FEB is controled via a labview interface similar to the one used to control the threshold of the CMS FEB. Various thresholds were used in a range in between 7 and 5 fC. These values are a little higher than the minimal threshold of about 3 fC used during the first experiment due to limitations of the FEB itself.

Finally, it was decided to use the same PMTs than in the first experiment as trigger. This time, they were placed on their narrow side to only cover an area on the detector smaller than three strips. On the data acquisition side, no DAQ software was available yet at the time of experimentation and scalers were once again used. As can be seen from Figure 6.11, the pulse processing has been inspired by the previous scheme. Thanks to the lower number of channels to monitor, the cluster size could be estimated by counting the signals on single channels (A, B and C on their own) but also on groups of two (A and B, B and C) and three channels (A and B and C) in coincidence with the trigger.

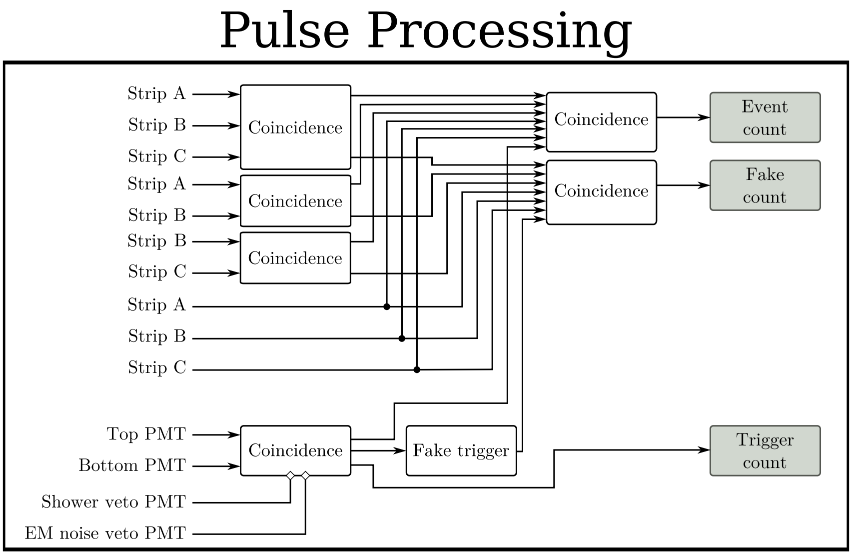

Figure 6.11: Similarly to Figure 6.8c, the signals are counted in coïncidence with the trigger signals provided by PMTs. To estimate the cluster size, the channels are counted by groups of three, two but also alone.

The results of the second round of tests with INFN preamplifiers are presented in Figure 6.12 and Table 6.2. These results are consistent with what was measured with the first tested prototypes. The efficiency sigmoid has been measured once again with the CMS FEB, using a threshold of $170\,\mathrm{fC}$ and is in agreement with the data collected in 2013. The performance of the detector with the preamplifiers tuned at 7.2 and $6.4\,\mathrm{fC}$ falls in the very same values than the setting at $7\,\mathrm{fC}$ according to the table. A maximum shift of $410\,\mathrm{V}$ is observed for a threshold of $5\,\mathrm{fC}$.

With the care placed into having a good grounding of the setup as well as a good impedance matching, the noise rate per unit area is this time lower than what previously measured. Nevertheless, it still is more than one order of magnitude higher than in the case of the CMS FEB with a threshold set at $170\,\mathrm{fC}$. The noise rate is measured to be at lowest around $0.7\,\mathrm{Hz/cm^2}$ when measured to be approximately $0.05\,\mathrm{Hz/cm^2}$ for the CMS FEB. At such high threshold values, the noise rate per unit area is not expected to vary much. The data collected at the RPC assembly laboratory then displays much better data tacking conditions with both electronics.

Finally, the cluster size is measured to be similar for both electronics at the level of the working point and is in between 2.2 and 2.4 strips on average. The spatial resolution of both devices would then be the same.

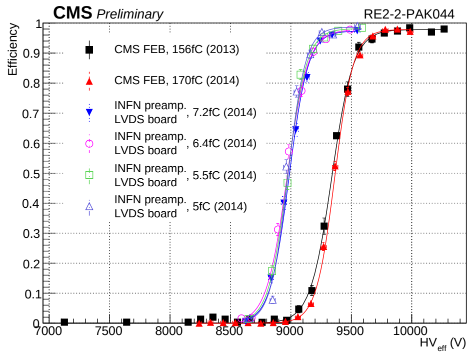

(a)

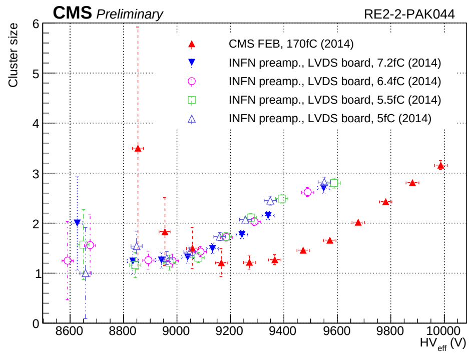

(b)

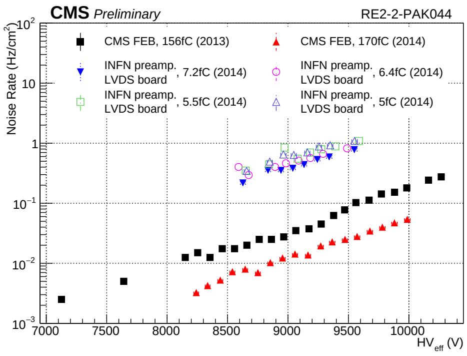

(c)

Figure 6.12: Efficiency (Figure 6.12a), cluster size (Figure 6.12b) and noise rate per unit area (Figure 6.12c) of the CMS RE2-2 detector tested with the standard CMS FEBs (black and red) and with the INFN preamplifier mounted onto the CMS FEB at different thresholds (blue, pink, green and purple).

Data	ϵ_{max}	$\lambda\,(\cdot 10^{-2}\ \mathrm{V}^{-1})$	HV_{50} (V)	ϵ_{WP}	HV_{WP} (V)
CMS FEB, 156fC (2013)	(0.978 ± 0.004)	(1.12 ± 0.07)	(9339 ± 11)	(0.97 ± 0.01)	(9752 ± 27)
CMS FEB, 170fC (2014)	(0.978 ± 0.003)	(1.30 ± 0.06)	(9364 ± 9)	(0.97 ± 0.01)	(9740 ± 19)
INFN/CMS FEB, 7.2fC (2014)	(0.973 ± 0.006)	(1.26 ± 0.09)	(8985 ± 10)	(0.97 ± 0.01)	(9368 ± 26)
INFN/CMS FEB, 6.4fC (2014)	(0.978 ± 0.007)	(1.16 ± 0.08)	(8969 ± 11)	(0.97 ± 0.01)	(9372 ± 28)
INFN/CMS FEB, 5.5fC (2014)	(0.981 ± 0.005)	(1.26 ± 0.09)	(8973 ± 12)	(0.97 ± 0.01)	(9357 ± 28)
INFN/CMS FEB, 5fC (2014)	(0.987 ± 0.004)	(1.37 ± 0.10)	(8976 ± 12)	(0.98 ± 0.01)	(9342 ± 28)

Table 6.2: Results of the sigmoid fit (Formula 4.24) performed on the data presented in Figure 6.12a. The working point and its corresponding efficiency are computed using Formulas 4.24 and 4.25.

In addition to the tests performed on the electronics with the CMS RPC, the electronics also have been tested on a gRPC designed in Ghent. The gRPC used for this experiment is described in Figure 6.13. The detector, showed on Figure 6.14, uses a double-gap layout with float glass electrodes of 1.1 mm and a gas gap of 1.2 mm. The electrodes themselves are made out of four pieces of glass glued together. Such a design was studied for high-rate detection purposes and aimed to serve as a proof of concept for RPCs built using small pieces assembled together to produce a larger detection area. Indeed, in the context of R&D in the field of high-rate RPCs, most low resistivity materials are custom made dopped glass or ceramics plates. These materials can't be produced in large areas as they are not manufactured on a large enough scale. Thus, building large detectors requires using such methods.

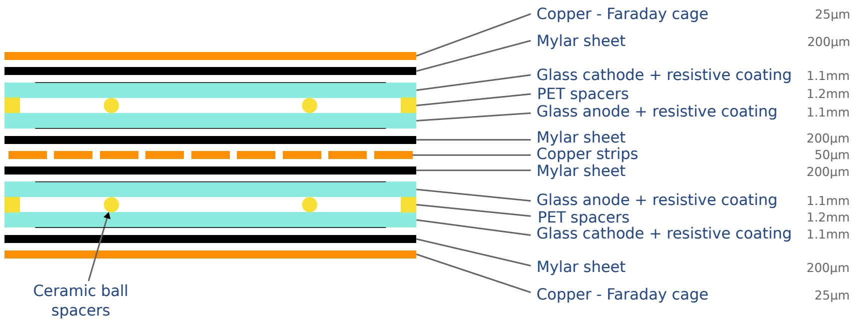

(a)

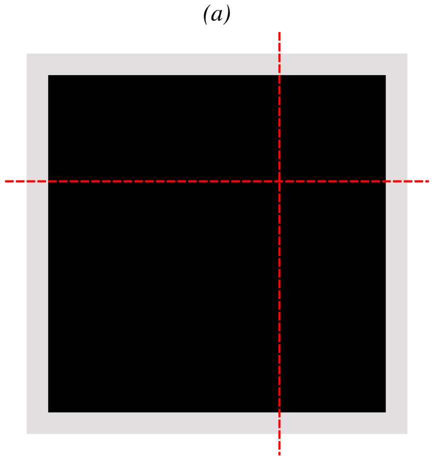

(b)

Figure 6.13: The glass RPC developped by Ghent uses a double-gap design (Figure 6.13a). The electrodes are made of four pieces of float glass glued into a single plate (Figure 6.13b). Indeed a gluing technique has been investigated as most new low resistivity materials foreseen for RPCs of the new generation are not available in large areas.

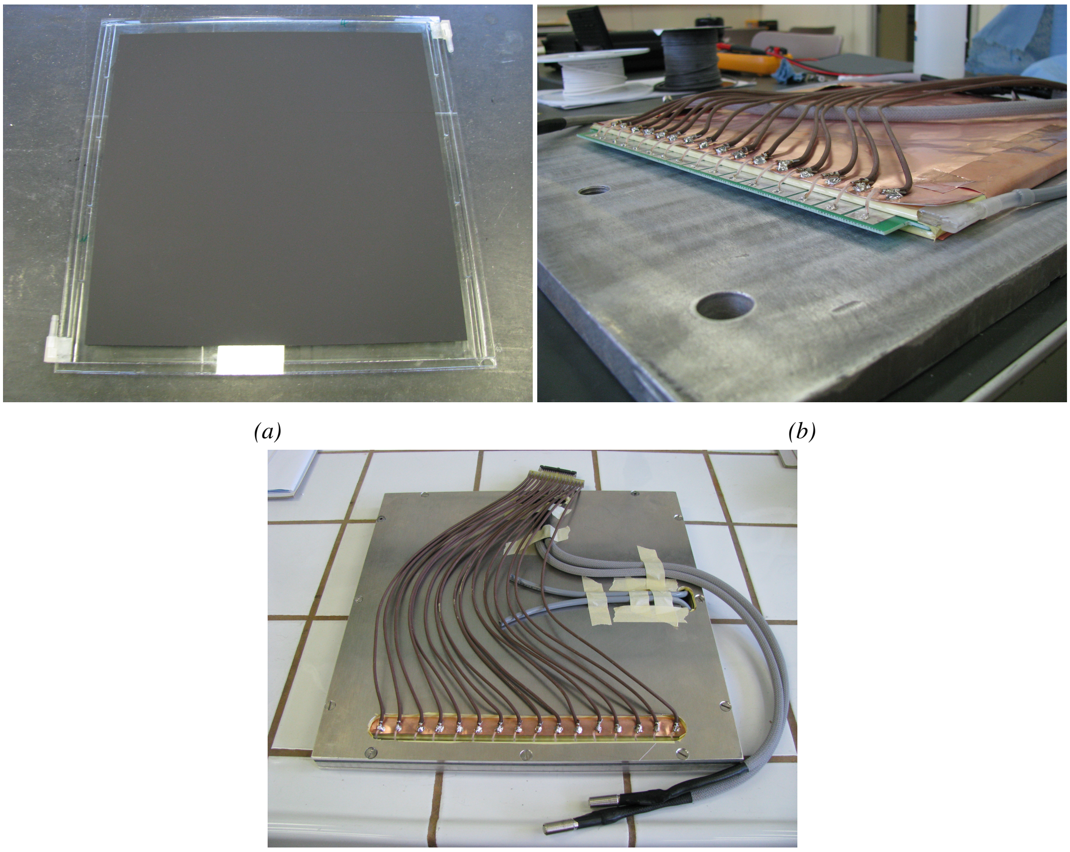

(a) *(b)*

(c)

Figure 6.14: Figure 6.14a: A gap used to concieve the gRPC tested at CERN. Figure 6.14b: Both gaps with their read-out panel are placed into a faraday made out of copper. Figure 6.14c: The faraday cage containing the double-gap gRPC is finally placed into its aluminium case.

The tests involving this detector were conducted in 2015 with the setup described by Figure 6.15. The photomultipliers used to trigger the data taking were a little larger than the detector and the strips themselves. Similarly to the case of the GIF experiment described in Section 5.2.2 of Chapter 5, it has been necessary to evaluate the geometrical acceptance of the setup to detect cosmic muons. This way, a C++ Monte Carlo simulation has been written using the dimensions of the experimental setup. By running 1000 simulations in which a million muons were generated in a source plane much larger than the experimental setup itself to reach high wenith angles, the geometrical acceptance was measured to be (0.9835 ± 0.0014). This factor has then been used to correct the measured efficiency of the detector.

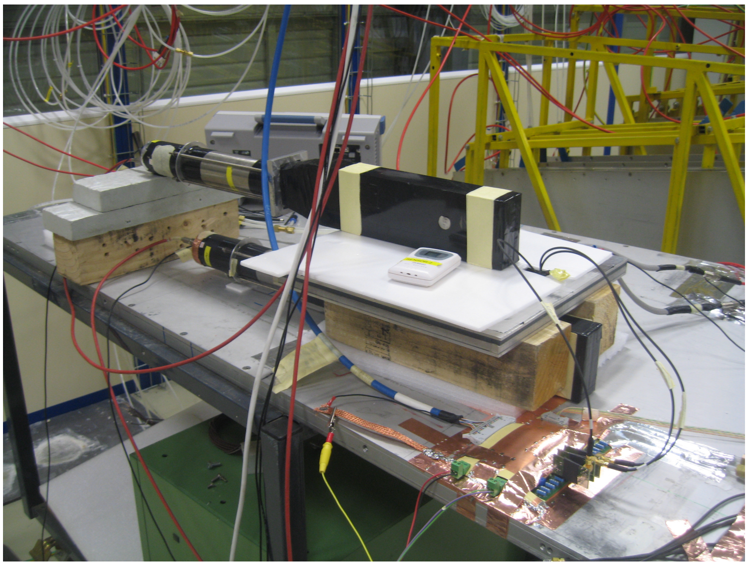

Figure 6.15: Experimental setup used to test the INFN preamplifier mounted on the CMS like FEB with the glass RPC build by Ghent.

Thanks to the activities ongoing for the preparation of the CMS RPC experiment taking place at GIF++ and detailed in Chapter 5, a first prototype of DAQ software was available to automate the data tacking process. Thanks to this early version of the software, the pulse processing was made more simple. The three channels connected to the preamplifiers were sent directly into a V1190A TDC manufactured by CAEN. The trigger was provided by the same trigger pulse processing described in Figure 6.11. The output of the coincidence of both scintillators was sent into the *TRIGGER* input of the TDC. The communication with the computer was done thanks to a V1718 module. More details on the DAQ can be found in Appendix A. Contrary to the data now collected at GIF++, the output of the first DAQ script consisted in a simple text file using a format described in Source Code 6.1. The analysis is then performed using a loop through the data file.

```
Evt0        nHits
ChHit1        THit1
ChHit2        THit2
ChHit3        THit3
ChHit4        THit4
ChHit5        THit5
...
Evt1        nHits
ChHit1        THit1
ChHit2        THit2
ChHit3        THit3
...
```

Source Code 6.1: Description of the format used to store the data collected during the experiment aiming at testing the INFN electronics with a gRPC built by Ghent. For each trigger recieved in the TDC module, an event is created. A first line containing two columns is written in the output file with the event number `EvtX` and the recorded number of hits `nHits`. This line is directly followed by the list of hits in each channel `ChHitX` and their corresponding time stamp `THitX` organized into two columns.

The results of the experiment with the gRPC are provided in Figure 6.16 and Table 6.3. The efficiency of the detector reaches 95% at working voltage, indicating that such a detector using electrodes composed of several glued pieces can be an option for the future of RPC technologies. The benefits of the preamplifiers is once again visible through the huge efficiency shift towards lower voltages. The shift reaches almost 470 V for thresholds lower than 6 fC.

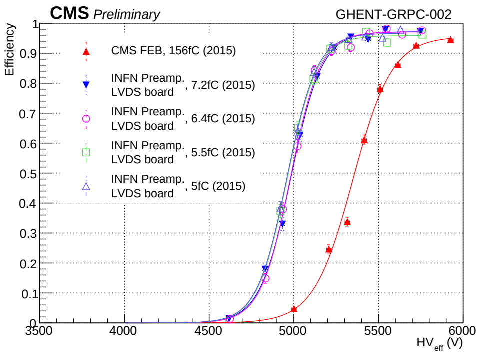

(a)

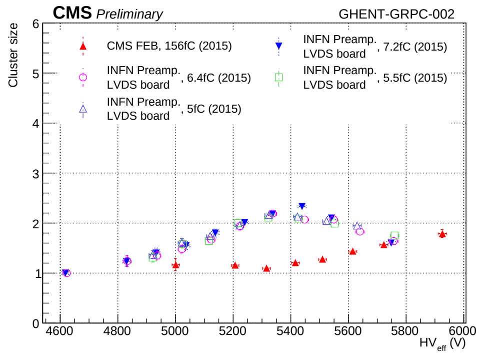

(b)

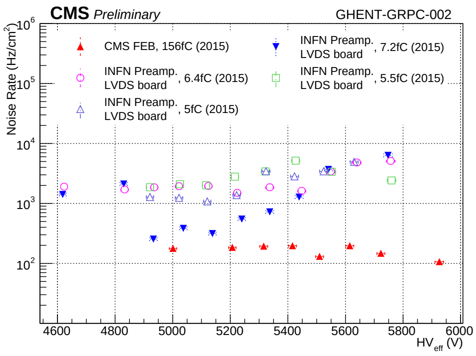

(c)

Figure 6.16: Efficiency (Figure 6.16a), cluster size (Figure 6.16b) and noise rate per unit area (Figure 6.16c) of the Ghent gRPC detector tested with the standard CMS FEBs (red) and with the INFN preamplifier mounted onto the CMS FEB at different thresholds (blue, pink, green and purple).

Data	ϵ_{max}	λ ($\cdot 10^{-2}$ V^{-1})	HV_{50} (V)	ϵ_{WP}	HV_{WP} (V)
CMS FEB, 156fC (2015)	(0.956 ± 0.007)	(0.86 ± 0.04)	(5349 ± 8)	(0.94 ± 0.01)	(5839 ± 23)
INFN/CMS FEB, 7.2fC (2015)	(0.972 ± 0.006)	(1.09 ± 0.06)	(4983 ± 8)	(0.96 ± 0.01)	(5403 ± 22)
INFN/CMS FEB, 6.4fC (2015)	(0.971 ± 0.005)	(1.13 ± 0.06)	(4981 ± 8)	(0.96 ± 0.01)	(5391 ± 22)
INFN/CMS FEB, 5.5fC (2015)	(0.959 ± 0.006)	(1.13 ± 0.11)	(4960 ± 11)	(0.95 ± 0.02)	(5371 ± 37)
INFN/CMS FEB, 5fC (2015)	(0.967 ± 0.006)	(1.12 ± 0.11)	(4959 ± 11)	(0.96 ± 0.02)	(5371 ± 38)

Table 6.3: Results of the sigmoid fit (Formula 4.24) performed on the data presented in Figure 6.16a. The working point and its corresponding efficiency are computed using Formulas 4.24 and 4.25.

The cluster size also shows a shift but its value suddenly dicreases after 5.4 kV. After a rise above 2, the cluster size drops when the detector reaches the plateau. A first idea to explain this phenomenon would be to check the cluster algorithm to make sure that it is not biased and does not introduce a fake split of the clusters due to arbitrarily strict selection rules. Clusters are always made of neighbour strips getting a hit within a certain time window. In the algorithm written to analyse the data, it is required for the maximum time difference between the earliest hit and the latest hit in a cluster to be smaller than $10\,\mathrm{ns}$. Physically, assuming of drift velocity of the electrons in the gas of the order of $0.1\,\mathrm{mm/ns}$ [280], the growth of an avalanche only takes a few ns. This effect is visible in Figure 6.17a in which the maximum time difference has been artificially increased to $300\,\mathrm{ns}$. The peak reaveals that the avalanches are not expected to grow over a time period longer than $10\,\mathrm{ns}$. No peak emerges at time differences longer than $10\,\mathrm{ns}$ indicating that the choice of a short time development within the algorithm was justified. This conclusion is supported by Figure 6.17b in which the evolution of the reconstructed cluster size with increasing maximum time difference shows no effect.

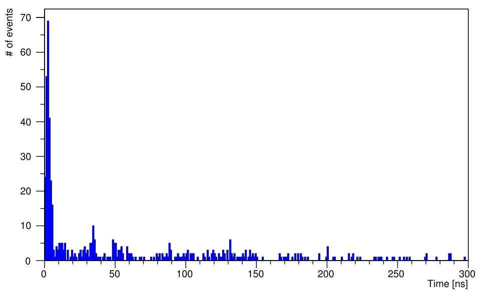

(a)

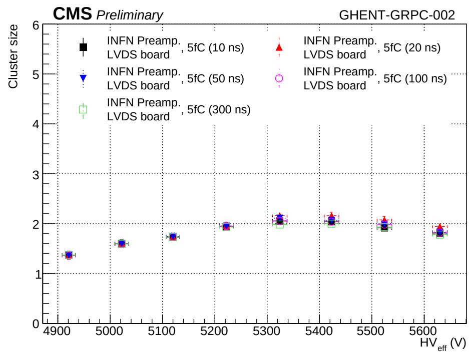

(b)

Figure 6.17: Figure 6.17a: Time difference between the first and last hit composing a cluster in the gRPC. The maximum time difference is set to $300\,\mathrm{ns}$*. Figure 6.17b: Variation of the reconstructed average cluster size as a function of the time constraint used in the algorithm.*

Due to the available number of channels, the cluster size is limited to 3. It is reasonable to assume that this only is the cause of the fall of cluster size beyond $5.4\,\mathrm{kV}$. Indeed looking closely at both Figure 6.18 and Figure 6.19, the link between increasing HV and decreasing cluster size can be understood. On the one hand, Figure 6.18 indicates that the cluster size features at first a maximum at 1. The maximum moves then from 1 to 3 over the points at $5120\,\mathrm{V}$, $5222\,\mathrm{V}$ and $5324\,\mathrm{V}$. Then over the last three voltage points, the bin at 2 drops to the profit of the bin at 1, the bin at 3 staying more or less stable. On the other hand, Figure 6.19 provides us more information about the localisation of the clusters among the three read-out strips. At the lowest two voltages, most of the data is contained in the central strip. At $5120\,\mathrm{V}$, the highest bin is the one corresponding to the central strip with a cluster size of 1. Already at $5222\,\mathrm{V}$, the balance changes towards the central strip with 3 strips in the clusters. At $5324\,\mathrm{V}$, even more events happen with clusters of all 3 strips while the events with a single hit in the side strips starts to increase. The number of events with cluster made of all 3 strips will not vary much anymore while the number of events with clusters made of 2 strips will dicrease and the single hits in the side strips will continue rising. This information indicates that the avalanches in the gap start to get stronger. Indeed, the increase of the events containing single hits mainly increases on the side strips points to an intensification of the avalanche gain on the strip adjacent to the three channels connected to the read-out setup. Only a single hit is read-out while in reality this was the contribution of bigger avalanches. The events with clusters of size 2 tend to dicrease due to the stronger gain that should normally be triggering wider avalanches. The cluster size distribution of Figure 6.18 gives the impression that the distribution is moving towards higher values but the geometrical limitation of the system due to the very low number of channels makes it impossible to measure.

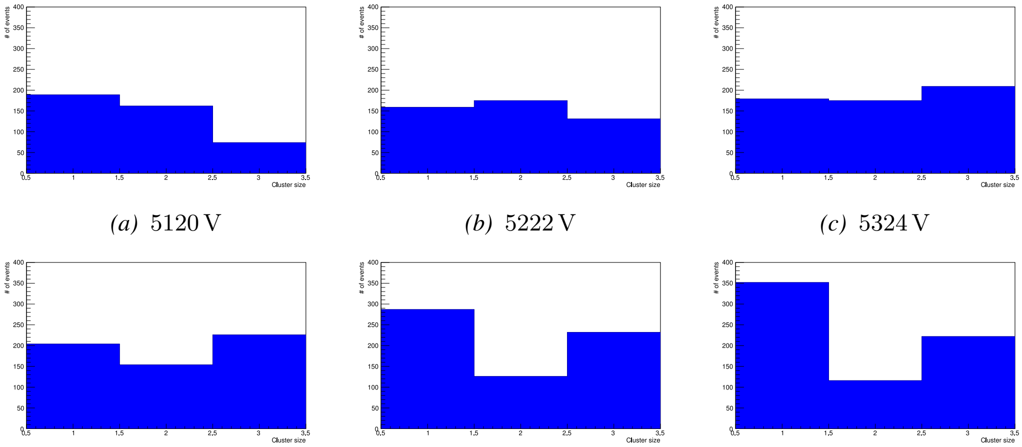

(a) 5120 V *(b)* 5222 V *(c)* 5324 V

(d) 5423 V *(e)* 5524 V *(f)* 5630 V

Figure 6.18: Evolution of the cluster size distribution with increasing voltage for the gRPC tested with the INFN preamplifiers using a threshold of 5 fC.

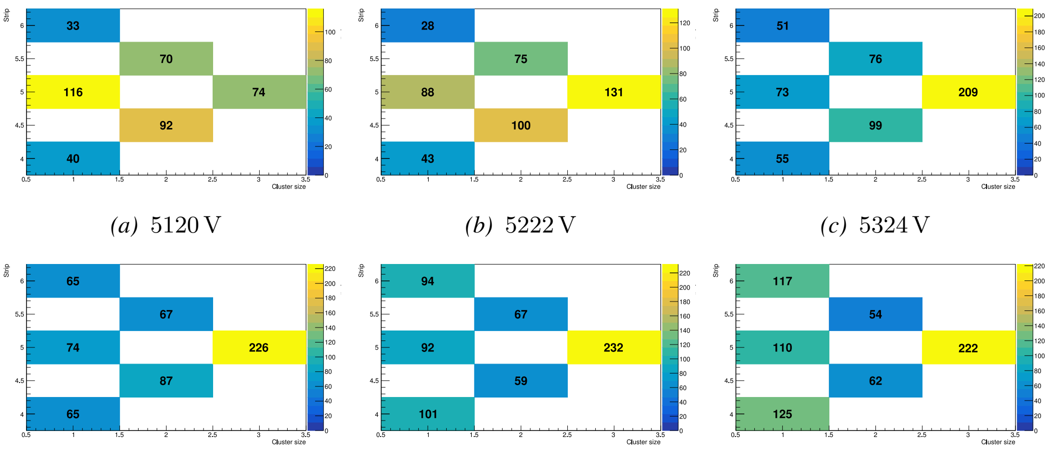

(a) 5120 V *(b)* 5222 V *(c)* 5324 V

(d) 5423 V *(e)* 5524 V *(f)* 5630 V

Figure 6.19: Map of the cluster size distribution as a function of the cluster position with increasing voltage for the gRPC tested with the INFN preamplifiers using a threshold of 5 fC.

Eventhough the performance of the detector are promising, the results concerning the noise rate per unit area seem to indicate that the detector and its combination with the electronics in the case of this experiment produces very high levels of noise, if compared to the noise measured in the RE4 detector. With each type of electronics, the noise doesn't indicate a clear correlation with increasing voltage. The hypothesis at this stage would be that the noise is not created inside of the gas volume by avalanches triggered along the glueing lines, where the electric field could be abruptly pertubated. It would rather come from the read-out channel itself, and from its connection to the electronics. Indeed, looking at the noise profile measured in the detector and presented in Figure 6.20a, it is clear that the noise is localised in two areas corresponding to the HV connectors in the case of the HV scan performed with the CMS FEB. Moreover, contrary to the very careful work performed on the RE2 chamber to match the impedance of the strips with the read-out cables connected to the board on which the INFN preamplifers are mounted, no matching was done on the gRPC due to a lack of time. The noise measured in the tested three channels is showed in Figure 6.20b. This region of the detector doesn't correpond to the HV connectors according to Figure 6.20a. Nevertheless, the number of hits counted in the detector is much higher than in the CMS FEB case. Looking more carefully to Figure 6.21 presenting the hit time profile in both cases together with the time profile of the CMS RE2-2 detector tested with INFN preamplifiers, it is clear that the detector is noisier. Also, the reflections due to the impedance mismatch is clearly visible in Figure 6.21b.

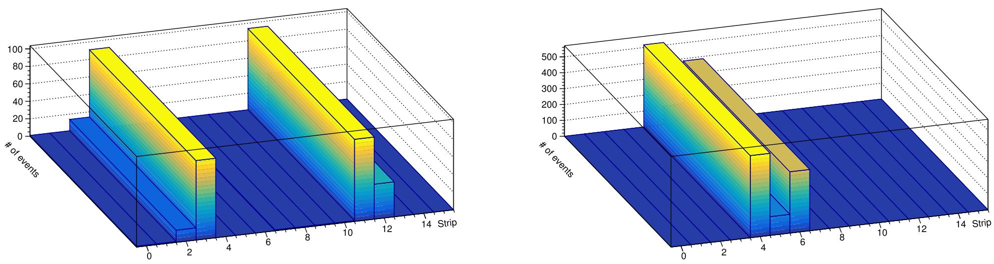

(a) *(b)*

Figure 6.20: Noise profile measured in the glass RPC built by Ghent tested with the standard CMS FEB (Figure 6.20a) and the INFN preamplifiers mounted on a CMS-like FEB (Figure 6.20b).

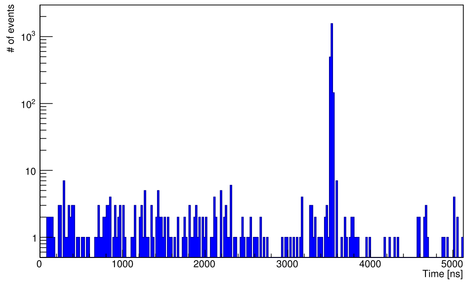

(a)

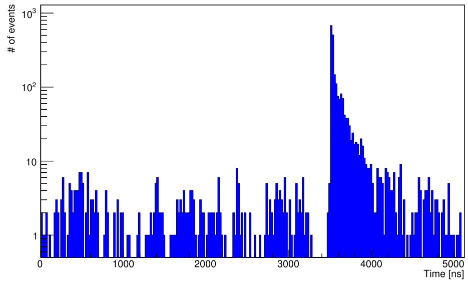

(b)

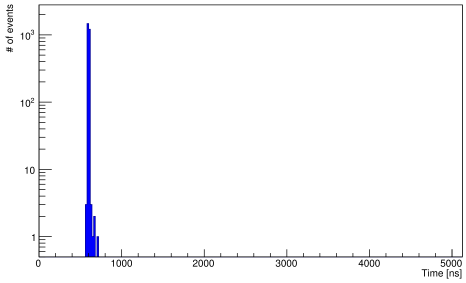

(c)

Figure 6.21: The arrival time of the hits recorded in the gRPC tested with the CMS FEB (Figure 6.21a) and with the INFN preamplifiers (Figure 6.21b), and recorded in the CMS RE2 RPC tested with the INFN preamplifiers (Figure 6.21c).

6.2.3 HARDROC 2 based RPC read-out

The HAdronic RPC Digital Read-Out Chip (HARDROC) ASIC, as its name suggests, has been developped for RPC applications and in particular for the read-out RPCs of the Semi-Digital HCAL (SDHCAL) that is being studied in the perspective of the International Linear Collider (ILC). The SDHCAL detectors are required to have a high granularity compared to the CMS RPCs and hence, they use $1\,\mathrm{cm}^2$ read-out pads instead of strips. This choice results in a huge number of channels. The ASIC is mounted directly on the read-out pannel for compactness as can be seen in Figure **??** and feature three thresholds to provide a semi-digital information.

The PETIROC that inspired the CMS RPCROC uses a similar technology than the one developed for the HARDROC and is manufactured by the same company. It is safe to conclude that the preliminary results obtained with the HARDROC electronics constitute a strong indication on the potential performance of a FEB developped specifically for CMS detectors. The leading institute in the development of the SDHCAL based on single-gap glass RPCs (gRPCs) is the Institut de Physique Nucléaire de Lyon (IPNL) which also played a great role in developing iRPCs for CMS.

A read-out pannel using the HARDROC 2 technology was lended by this institute and was tested onto a CMS RPC. Contrary to the tests with the INFN preamplifiers that were made using an RE2-2 CMS RPC built in 2007 for the second endcap disk of CMS, the choice was made to use an RE4-3 detector built during LS1 to equip the fourth endcap. Indeed, the pannel can't be sandwiched between two RPC gaps due to the embedded electronics and a single CMS RPC gap was used. At the time of this experiment, only RE4-3 gaps were available and the choice was made to change detector with respect to the previous series of tests conducted on the INFN preamplifiers. As for the INFN preamplifiers, the pannel has been tested on the gRPC built by UGent. The gRPC being smaller than the HARDROC read-out that was used for the experiment but thanks to the 2D read-out using pads, this was not a problem for the data acquisition.

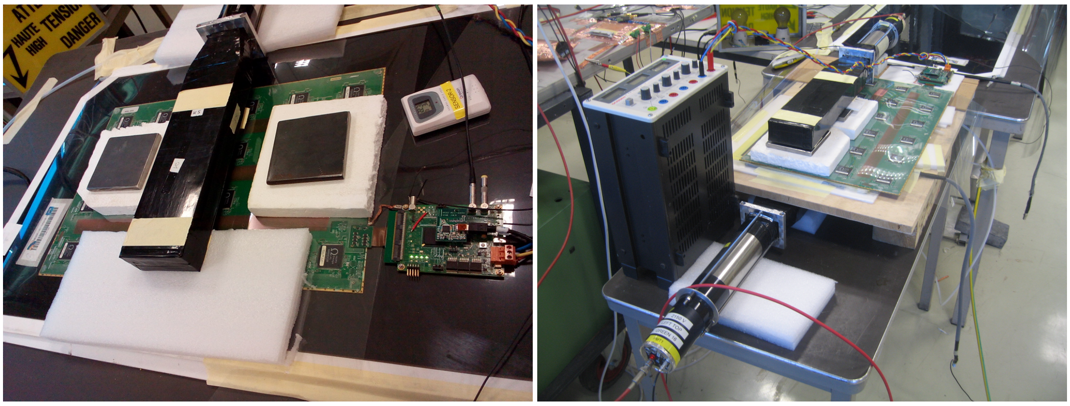

(a) *(b)*

Figure 6.22: Experimental setups used to test the HARDROC2 electronics with a CMS RE4-3 gap (Figure 6.22a) and a gRPC gap built in Ghent (Figure 6.22b).

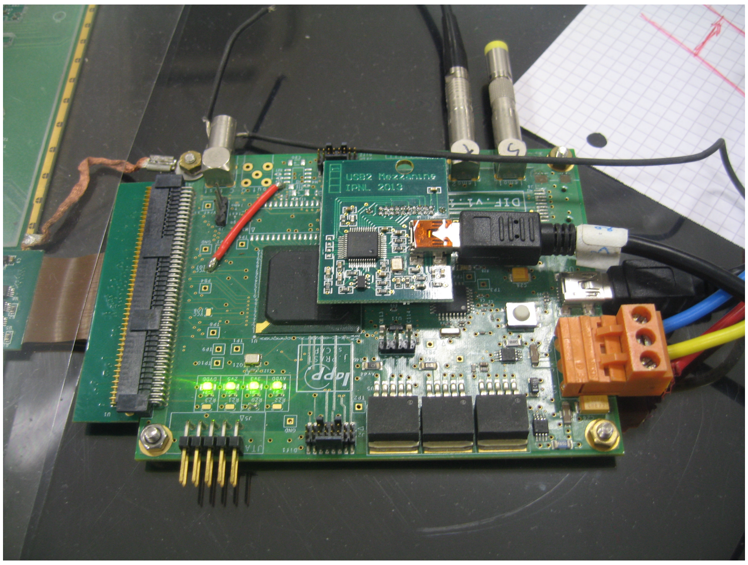

Figure 6.23: HARDROC2 control chip with its "Mezzanine" used to collect the data from the different HARDROC ASICs and communicate with the computer. On top of the picture, the trigger is brought by a coaxial cable. The connection with the computer is assured by both the USB cables.

Once again, the experiment was conducted in the CMS RPC assembly laboratory at CERN and the setups are shown in Figure 6.22. The read-out panel is placed directly on top of the gapsand pressed against the detector surface thanks to weights. The same PMTs are used to provide a trigger to the data acquisition. In the particular case of the HARDROC 2 electronics, the output signal does not correspond to the LVDS signals provided by the CMS FEB. Moreover, there would be more than 1500 channels to constently monitor and unfortunately, there would not be enough VME TDC modules to use with the DAQ software designed for the experiment involving the INFN preamplifiers. Nevertheless, a custom-made DAQ software was designed by the members of IPNL's team to read-out the electronics through the chip presented in Figure 6.23. The data is stored in the buffer of the ASIC continously and dumped into the computer when a trigger is signal is received.

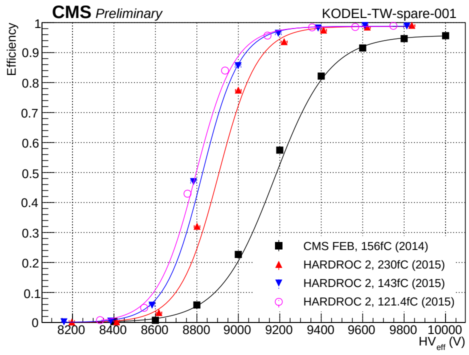

(a)

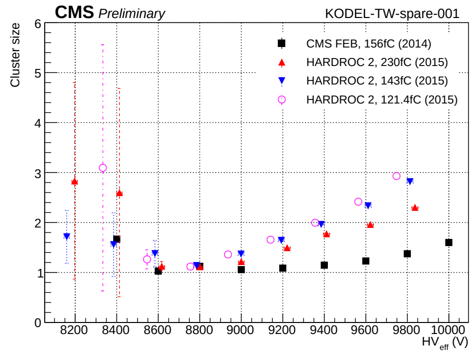

(b)

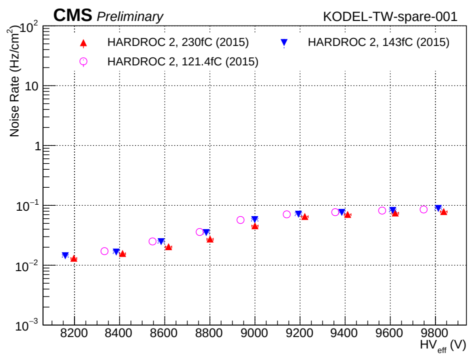

(c)

Figure 6.24: Efficiency (Figure 6.24a), cluster size (Figure 6.24b) and noise rate per unit area (Figure 6.24c) of the CMS RE4-3 detector tested in single gap mode with the standard CMS FEBs (black) and with the HARDROC 2 readout panel at different thresholds (red, blue and pink).

Data	ϵ_{max}	$\lambda\ (\cdot 10^{-2}\ \mathrm{V}^{-1})$	HV_{50} (V)	ϵ_{WP}	HV_{WP} (V)
CMS FEB, 156fC (2014)	(0.958 ± 0.000)	(0.75 ± 0.00)	(9174 ± 1)	(0.94 ± 0.00)	(9716 ± 2)
HARDROC 2, 230fC (2015)	(0.987 ± 0.002)	(1.06 ± 0.04)	(8905 ± 8)	(0.98 ± 0.01)	(9333 ± 17)
HARDROC 2, 143fC (2015)	(0.988 ± 0.001)	(1.10 ± 0.04)	(8826 ± 8)	(0.98 ± 0.01)	(9243 ± 17)
HARDROC 2, 121.4fC (2015)	(0.987 ± 0.001)	(1.07 ± 0.04)	(8795 ± 8)	(0.98 ± 0.01)	(9220 ± 17)

Table 6.4: Results of the sigmoid fit (Formula 4.24) performed on the data presented in Figure 6.24a. The working point and its corresponding efficiency are computed using Formulas 4.24 and 4.25.

The results of the tests conducted with the HARDROC 2 on a CMS gap are presented in Figure 6.24 and Table 6.4. These results can hardly be compared to what was measured with the INFN preamplifiers as the detector was not tested using the single-gap mode. The tested thresholds are high compared to the ones displayed by the INFN preamplifiers and are of the order of magnitude of the current CMS FEB. Nevertheless, the performance of the detector equipped with this read-out pannel is measured to be better. Indeed, a shift of 400 to $500\,\mathrm{V}$ is observed at thresholds ranging from 230 to $121.4\,\mathrm{fC}$. **[Here it could be nice to bring an explaination to this observation.]**

The cluster size is provided for information as a direct comparison of the cluster size measured with $1\,\mathrm{cm}^2$ pads and long copper strips with width of a few cm is not possible. The measured cluster size at working voltage with the CMS FEB is consistent with what would be expected of a single-gap RPC. Indeed, the usage of two gaps in an OR system allows for a stronger overall gain and hence, the cluster size is greater. A more precise estimation of the charge spread inside of the gap is obtained using pads instead of strips. At working voltage, an avalanche is detected within less than two pads on average. An extra information could be used to further improve the spatial resolution of the detector. Indeed, as stated in the introduction of the Section, the HARDROC 2 is a semi-digital electronics and features three threshold levels. Tuning these thresholds would lead to an approximation of the induced charge profile over the neighbouring pads. A gaussian fit over the digitized distribution would give an estimation of the position of the avalanche center.

Finally, the noise measured in the electronics is of the same order of what had been measured in Figure 6.12c. It is safe to assume that the noise level in the case of a single-gap RPC is expected to be of the same order of magnitude than its double-gap counterpart as the noise mainly is electromagnetic. Figure 6.25 provides a clearer understanding of the position of the trigger PMTs and of the noise measured with the HARDROC. The noise of the electronics itself is very small and the read-out pannel is sensitive enough to measure the noise in the RPC gap. Indeed, except for a few visible hot spots, the observed noise profile corresponds perfectly to the spacer positions inside of the gap volume. The PET buttons used to maintain the uniformity of the gas volume cause noise at their proximity as they modify the local electric field.

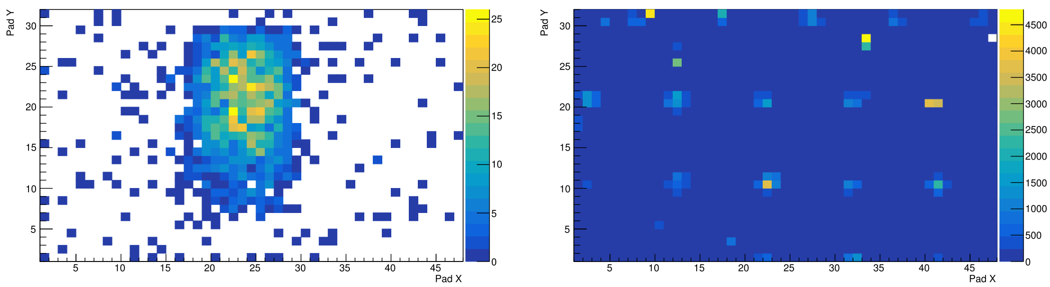

(a) *(b)*

Figure 6.25: Measured muon (Figure 6.25a) and noise (Figure 6.25a) profiles in the read-out pads of the HARDROC 2 over a CMS RE4-3 gap. The inner structure of the gap and the presence of the spacers in the volume is visible.

The results of the experiment with the gRPC are provided in Figure 6.26 and Table 6.5. Unfortunately the gRPC had not been tested in single gap mode with the CMS FEB. Thus, a direct comparison is not possible as the data were not collected in similar conditions. The detector could only be tested with a single HARDROC 2 threshold setting $(143\,\mathrm{fC})$. As for the double-gap, the efficiency of the single-gap reaches 95% at working voltage. The working voltage is consistent with the double-gap detector operated with the CMS FEB indicating that the HARDROC is more sensitive to lower charges. The difference in efficiency rising is consistent with the use of one gap versus two in the case of the CMS FEB.

As discussed in the case of the CMS RE4-3 gap, the direct comparison of the cluster sizes is not possible. In this sense, the proximity of both results only is fortuitous. The cluster size of approximately 1.6 measured with the HARDROC 2 at working voltage is of the same order than what had previously been measured for the CMS gap indicating that at equivalent performance, the gain and hence, the induced charge could be comparable.

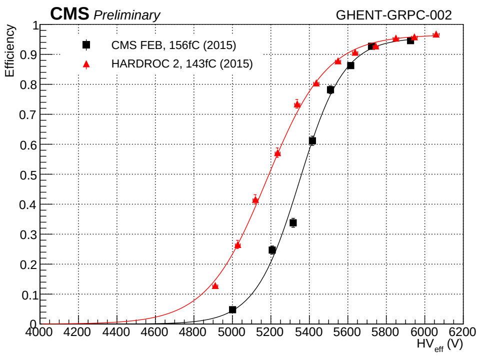

(a)

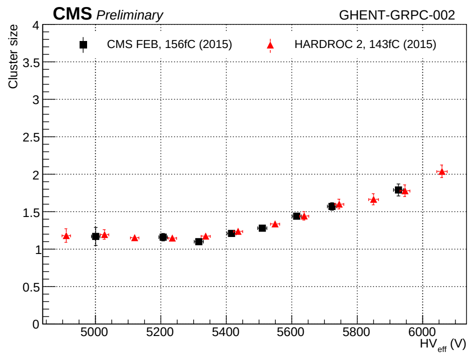

(b)

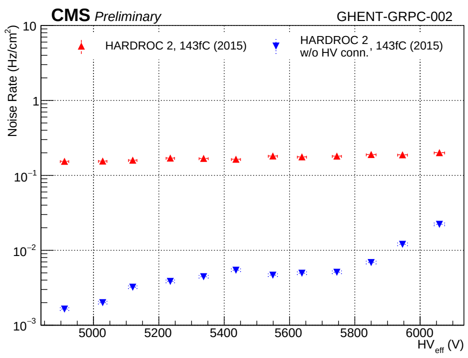

(c)

Figure 6.26: Efficiency (Figure 6.24a), cluster size (Figure 6.24b) and noise rate per unit area (Figure 6.24c) of the UGent gRPC tested in double-gap mode with the standard CMS FEBs (black) and in single-gap with the HARDROC 2 readout panel at a threshold of 143 fC *(red).*

Data	ϵ_{max}	λ $(\cdot 10^{-2}\ \mathrm{V}^{-1})$	HV_{50} (V)	ϵ_{WP}	HV_{WP} (V)
CMS FEB, 156fC (2015)	(0.956 ± 0.007)	(0.86 ± 0.04)	(5349 ± 8)	(0.94 ± 0.01)	(5839 ± 23)
HARDROC 2, 143fC (2015)	(0.966 ± 0.004)	(0.64 ± 0.02)	(5179 ± 7)	(0.95 ± 0.01)	(5790 ± 25)

Table 6.5: Results of the sigmoid fit (Formula 4.24) performed on the data presented in Figure 6.26a. The working point and its corresponding efficiency are computed using Formulas 4.24 and 4.25.

Finally, the noise measured in the electronics seemed higher than in the case of the CMS gap.

Looking closer to the noise profile provided in Figure 6.27, it can be seen that the noise measurement was affected by the HV connector. Indeed, the high noise measured in pads 41 and 42 along X and 22 to 25 along Y, corresponds exactly to the position of the HV connector on the cathode side. Contrary to the case of the CMS gap were the HV connector was far from the read-out area, the gRPC is smaller than the read-out and due to the poor grounding of the setup the electric field created by the HV connector could affect the read-out. Exclusing the corresponding pads gives a much more reliable noise measurement as can be seen in Figure 6.26c. Through the noise profile, a better understanding of the gRPC uniformity can be obtained. First of all, the row corresponding to Y=16 seem consistently noisier than the neighbouring pads an could correspond to the glueing line that lies along this pad row. The noise increase along this line is not very clear though and no corresponding behaviour can be observed along the other glueing line along column X=30. But the gas volume corresponding to the largest glass plate, spreading from columns 31 to 47 along X and rows 1 to 15 clearly shows a stronger noise in it's center. The detection area being small, only a few ceramic ball spacers were used to maintain the distance in between the electrodes. It not impossible that the ball spacer located in the center of this very volume popped out. Due to the absence of a spacer, the force applied by electric field onto the electrodes could have made the distance in between the electrodes smaller and artificially increased the observed electric field, also increasing the measured noise.

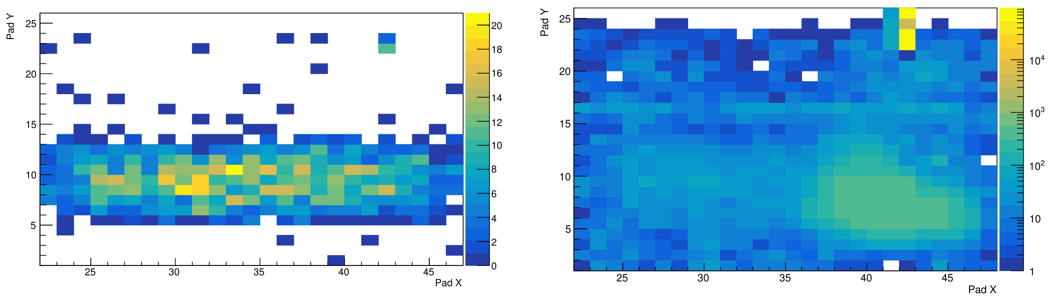

(a) *(b)*

Figure 6.27: Measured muon (Figure 6.27a) and noise (Figure 6.27a) profiles in the read-out pads of the HARDROC 2 over a gRPC gap built by Ghent.

6.3 Certification of the CMS RPCROC prototype

6.3.1 Preliminary tests with cosmic muons

6.3.2 Certification campaign at the new Gamma Irradiation Facility

6.4 Certification of the INFN FEB prototype

6.4.1 Preliminary tests with cosmic muons

6.4.2 Certification campaign at the new Gamma Irradiation Facility

7

Conclusions and outlooks

7.1 Conclusions

7.2 Outlooks

A

A data acquisition software for CAEN VME TDCs

Certifying detectors in the perspective of HL-LHC required to develop tools for the GIF++ experiment. Among them was the C++ Data Acquisition (DAQ) software that allows to make the communications in between a computer and TDC modules in order to retrieve the RPC data [281]. In this appendix, details about this software, as of how the software was written, how it functions and how it can be exported to another similar setup, will be given.

A.1 GIF++ DAQ file tree

GIF++ DAQ source code is fully available on github at `https://github.com/afagot/GIF_DAQ`. The software requires 3 non-optional dependencies:

- CAEN USB Driver, to mount the VME hardware,
- CAEN VME Library, to communicate with the VME hardware, and
- ROOT, to organize the collected data into a TTree.

The CAEN VME library will not be packaged by distributions and will need to be installed manually. To compile the GIF++ DAQ project via a terminal, from the DAQ folder use the command:

```
mkdir build
cd build
cmake ..
make install
```

The source code tree is provided below along with comments to give an overview of the files' content. The different objects created for this project (`v1718`, `v1190a`, `IniFile` & `DataReader`) will be described in details in the following sections.

```
GIF_DAQ
├── bin
│   └── daq ........................................ EXECUTABLE
├── build .............................................. BUILD FOLDER
│   └── ...
├── include ............................................ LIST OF C++ HEADER FILES
│   ├── DataReader.h ............................... DECLARATION OF OBJECT DATAREADER
│   ├── IniFile.h .................................. DECLARATION OF OBJECT INIFILE FOR INI PARSER
│   ├── MsgSvc.h ................................... DECLARATION OF DAQ LOG MESSAGES
│   ├── utils.h .................................... DECLARATION OF USEFUL VARIABLES AND COMM. FUNCTIONS
│   ├── v1190a.h ................................... DECLARATION OF OBJECT V1190A
│   └── v1718.h .................................... DECLARATION OF OBJECT V1718
├── obj ................................................ BINARY FILES CREATED BY COMPILER
│   └── ...
├── src ................................................ LIST OF C++ SOURCE FILES
│   ├── daq.cxx .................................... MAIN FILE
│   ├── DataReader.cxx ............................. DEFINITION OF DATAREADER'S METHODS
│   ├── IniFile.cxx ................................ DEFINITION OF INIFILE'S METHODS
│   ├── MsgSvc.cxx ................................. DEFINITION OF LOG MESSAGING FUNCTIONS
│   ├── utils.cxx .................................. DEFINITION OF USEFUL COMMUNICATION FUNCTIONS
│   ├── v1190a.cxx ................................. DECLARATION OF V1190A'S METHODS
│   └── v1718.cxx .................................. DECLARATION OF V1718'S METHODS
├── CMakeLists.txt ..................................... COMPILER INSTRUCTIONS
├── config.h.in ........................................ CODE VERSION
├── Doc-DAQ-v5.pdf ..................................... DOCUMENTATION (THIS APPENDIX)
└── README.md .......................................... REAMDE FILE FOR GITHUB
```

A.2 Usage of the DAQ

GIF++ DAQ, as used in GIF++, is not a standalone software. Indeed, the system being more complexe, the DAQ only is a sub-layer of the software architecture developped to control and monitor the RPCs that are placed into the bunker for performance study in an irradiated environment. The top layer of GIF++ is a Web Detector Control System (webDCS) application. The DAQ is only called by the webDCS when data needs to be acquired. The webDCS operates the DAQ through command line. To start the DAQ, the webDCS calls:

```
bin/daq /path/to/the/log/file/in/the/output/data/folder
```

where `/path/to/the/log/file/in/the/output/data/folder` is the only argument required. This log file is important for the webDCS as this file contains all the content of the communication of the webDCS and the different systems monitored by the webDCS. Its content is constantly displayed during data taking for the users to be able to follow the operations. The communication messages are normally sent to the webDCS log file via the functions declared in file `MsgSvc.h`, typically `MSG_INFO(string message)`.

A.3 Description of the readout setup

The CMS RPC setup at GIF++ counts 5 V1190A Time-to-Digital Converter (TDC) manufactured by CAEN [264]. V1190A are VME units accepting 128 independent Multi-Hit/Multi-Event TDC channels whose signals are treated by 4 100 ps high performance TDC chips developped by CERN / ECP-MIC Division. The communication between the computer and the TDCs to transfer data is done via a V1718 VME master module also manufactured by CAEN and operated from a USB port [265]. These VME modules are all hosted into a 6U VME 6021 powered crate manufactured by W-Ie-Ne-R than can accomodate up to 21 VME bus cards [282]. These 3 components of the DAQ setup are shown in Figure A.1.

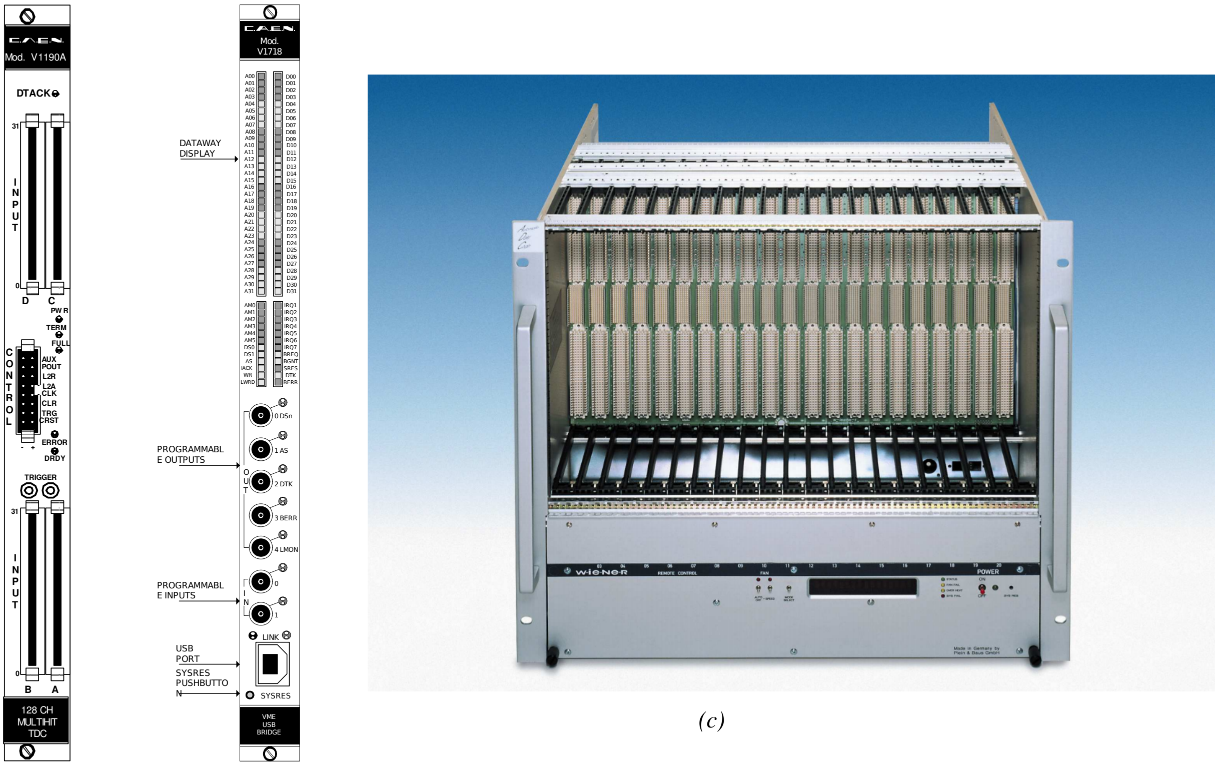

(a) *(b)* *(c)*

Figure A.1: (A.1a) View of the front panel of a V1190A TDC module [264]. (A.1b) View of the front panel of a V1718 Bridge module [265]. (A.1c) View of the front panel of a 6U 6021 VME crate [282].

A.4 Data read-out

To efficiently perform a data readout algorithm, C++ objects to handle the VME modules (TDCs and VME bridge) have been created along with objects to store data and read the configuration file that comes as an input of the DAQ software.

A.4.1 V1190A TDCs

The DAQ used at GIF takes profit of the *Trigger Matching Mode* offered by V1190A modules. This setting is enabled through the method `v1190a::SetTrigMatching (int ntdcs)` where `ntdcs` is the total number of TDCs in the setup this setting needs to be enabled for (Source Code A.1). A trigger matching is performed in between a trigger time tag, a trigger signal sent into the TRIGGER input of the TDC visible on Figure A.1a, and the channel time measurements, signals recorded from the detectors under test in our case. Control over this data acquisition mode, explained through Figure A.2, is offered via 4 programmable parameters:

- **match window:** the matching between a trigger and a hit is done within a programmable time window. This is set via the method
`void v1190a::SetTrigWindowWidth(Uint windowWidth,int ntdcs)`

- **window offset:** temporal distance between the trigger tag and the start of the trigger matching window. This is set via the method
`void v1190a::SetTrigWindowWidth(Uint windowWidth,int ntdcs)`

- **extra search margin:** an extended time window is used to ensure that all matching hits are found. This is set via the method
`void v1190a::SetTrigSearchMargin(Uint searchMargin,int ntdcs)`

- **reject margin:** older hits are automatically rejected to preven buffer overflows and to speed up the search time. This is set via the method
`void v1190a::SetTrigRejectionMargin(Uint rejectMargin,int ntdcs)`

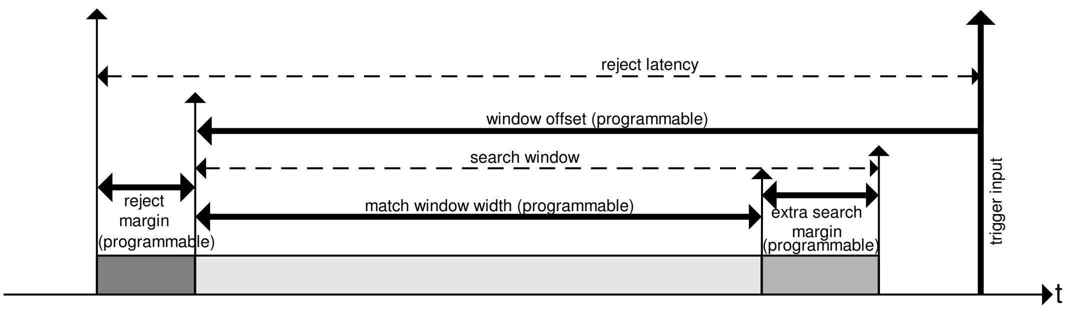

Figure A.2: Module V1190A Trigger Matching Mode timing diagram [264].

Each of these 4 parameters are given in number of clocks, 1 clock being 25 ns long. It is easy to understand at this level that there are 3 possible functionning settings:

- **1:** the match window is entirely contained after the trigger signal,
- **2:** the match window overlaps the trigger signal, or
- **3:** the match window is entirely contained before the trigger signal as displayed on Figure A.2.

In both the first and second cases, the sum of the window width and of the offset can be set to a maximum of 40 clocks, which corresponds to 1 µs. Evidently, the offset can be negative, allowing

for a longer match window, with the constraint of having the window ending at most 1 µs after the trigger signal. In the third case, the maximum negative offset allowed is of $2048\,\mathrm{clocks}$ (12 bit) corresponding to $51.2\,\mu\mathrm{s}$, the match window being strictly smaller than the offset. In the case of GIF++, the choice has been made to use this last setting by delaying the trigger signal. During the studies performed in GIF++, both the efficiency of the RPCs, probed using a muon beam, and the noise or gamma background rate are monitored. The extra search and reject margins are left unused.
To probe the efficiency of RPC detectors, the trigger time tag is provided by the coïncidence of scintillators when a bunch of muons passes through GIF++ area is used to trigger the data acquisition. For this measurement, it is useful to reduce the match window width only to contain the muon information. Indeed, the delay in between a trigger signal and the detection of the corresponding muon in the RPC being very contant (typically a few tens of ns due to jitter and cable length), the muon signals are very localised in time. Thus, due to a delay of approximalety $325\,\mathrm{ns}$ in between the muons and the trigger, the settings were chosen to have a window width of $24\,\mathrm{clocks}$ ($600\,\mathrm{ns}$) centered on the muon peak thanks to a negative offset of $29\,\mathrm{clocks}$ ($725\,\mathrm{ns}$).
On the otherhand, monitoring the rates don't require for the DAQ to look at a specific time window. It is important to integrate enough time to have a robust measurement of the rate as the number of hits per time unit. The triggerring signal is provided by the pulse generator integrated into the communication module V1718 at a frequency of $100\,\mathrm{Hz}$ to ensure that the data taking occurs in a random way, uncorrelated with beam physics, to probe only the irradiation spectrum on the detectors. The match window is set to $400\,\mathrm{clocks}$ ($10\,\mu\mathrm{s}$) and the negative offset to $401\,\mathrm{clocks}$ as it needs to exceed the value of the match window.

The v1190a object, defined in the DAQ software as in Source Code A.1, offers the possility to store all TDCs in the readout setup into a single object containing a list of hardware addresses (addresses to access the TDCs' buffer through the VME crate) and each constructor and method acts on the list of TDCs to set the different acquisition parameters as describe above. The type of trigger matching is chosen with `v1190a::SetTrigMatching()` and the time substraction, used to have a time measurement referring to the beggining of the time window, is set by `v1190a::SetTrigTimeSubstraction()`. Then, the wiwdow width and offset are respectively set thanks to `v1190a::SetTrigWindowWidth()` and `v1190a::SetTrigWindowOffset()`. The rejection and extra search margin, even if left unused and hence set to a default value of 0, can be set through `v1190a::SetTrigRejectionMargin()` and `v1190a::SetTrigSearchMargin()`. These methods are then called in `v1190a::SetTrigConfiguration()` that uses the information contained in the configuration file `IniFile *inifile` to set the different TDC parameters. A thorough explaination of the content of the configuration file is provided in Section A.5.2.

Among the other methods of class `v1190a` can be found a set of the detection mode (`v1190a::SetTDCDetectionMode()`), of the TDC time resolution (`v1190a::SetTDCResolution()`), of the dead time in between two consecutive signals recorded into a single channel (`v1190a::SetTDCDeadTime()`) or of the maximal number of signals that can be recorded per event (`v1190a::SetTDCEventSize()`). To help with setting these parameters, **`enum`** were used (`EdgeMode`, `Resolution`, `DeadTime` and `HitMax` are defined in `include/v1190a.h`).

```
class v1190a
{
 private :
    long              Handle;
    vector<Data32>    Address;
    CVDataWidth       DataWidth;
    CVAddressModifier AddressModifier;

 public:

    v1190a(long handle, IniFile *inifile, int ntdcs);
    ~v1190a();
    Data16 write_op_reg(Data32 address, int code, string error);
    Data16 read_op_reg(Data32 address, string error);
    void   Reset(int ntdcs);
    void   Clear(int ntdcs);
    void   TestWR(Data16 value,int ntdcs);
    void   CheckTDCStatus(int ntdcs);
    void   CheckCommunication(int ntdcs);
    void   SetTDCTestMode(Data16 mode,int ntdcs);
    void   SetTrigMatching(int ntdcs);
    void   SetTrigTimeSubstraction(Data16 mode,int ntdcs);
    void   SetTrigWindowWidth(Uint windowWidth,int ntdcs);
    void   SetTrigWindowOffset(Uint windowOffset,int ntdcs);
    void   SetTrigSearchMargin(Uint searchMargin,int ntdcs);
    void   SetTrigRejectionMargin(Uint rejectMargin,int ntdcs);
    void   GetTrigConfiguration(int ntdcs);
    void   SetTrigConfiguration(IniFile *inifile,int ntdcs);
    void   SetTDCDetectionMode(Data16 mode,int ntdcs);
    void   SetTDCResolution(Data16 lsb,int ntdcs);
    void   SetTDCDeadTime(Data16 time,int ntdcs);
    void   SetTDCHeadTrailer(Data16 mode,int ntdcs);
    void   SetTDCEventSize(Data16 size,int ntdcs);
    void   SwitchChannels(IniFile *inifile,int ntdcs);
    void   SetIRQ(Data32 level, Data32 count,int ntdcs);
    void   SetBlockTransferMode(Data16 mode,int ntdcs);
    void   Set(IniFile *inifile,int ntdcs);
    void   CheckStatus(CVErrorCodes status) const;
    int    ReadBlockD32(Uint tdc, const Data16 address,
               Data32 *data, const Uint words, bool ignore_berr);
    Uint   Read(RAWData *DataList,int ntdcs);
};
```

Source Code A.1: Description of C++ object `v1190a`.

The detection mode corresponds to the the type of edge detection the TDC will be using to record the data. The TDCs can record the time stamp of the leading edge alone, of the trailing edge alone, of both or they can operate in pair mode, meaning that the leading edge is recorded together with the time difference in between leading and trailing edges. This last mode is not very practical for the case of GIF++ measurements as the information is coded into a single words in the TDC's buffer, putting strong constraints on the time wondow and duration of the input signals. Indeed, when recording the edges individually (single edge or both edges), a 32-bit word, of which 18 are used to provide the time information alone, is stored into memory for each signal edge. With the pair mode, instead of having one 32-bit word per edge, only a single 32-bit word is written of which 12 are used for the leading edge time information and 6 for the width of the pulse, as described on p73 of reference [264]. This way, eventhough the pair mode is convenient to use as it automatically correlates a leading edge with the corresponding signal width in a single word, it is advised to be careful when using it and to be aware of the extra time constraints (for both leading time and signal width) that will come for chosing this setting. If it is necessary to work with large input signals, the mode recording both edges will be preferred to the pair mode and the association of a leading and trailing edges pair will then be performed offline by the user. Then, the time resolution is to be chosen in a range from 100 to 800 ps, the dead time in a range from 5 to 100 ns, and the maximal number of hits per event in a range from 0 to 128 with the possibility to chose to have no limits.

A.4.2 DataReader

Enabled thanks to `v1190a::SetBlockTransferMode()`, the data transfer is done via Block Transfer (BLT). Using BLT allows to tranfer a fixed number of events called a *block*. This is used together with an Almost Full Level (AFL) of the TDCs' output buffers, defined through `v1190a::SetIRQ()`. This AFL gives the maximum amount of 32735 words (16 bits, corresponding to the depth of a TDC output buffer) that can writen in a buffer before an Interrupt Request (IRQ) is generated and seen by the VME Bridge V1718, which sends a BUSY signal intended to stopping the data acquisition during the transfer of the content of each TDC buffers before resuming. For each trigger, 6 words or more are written into the TDC buffer:

- **a global header** providing information of the event number since the beginning of the data acquisition,
- **a TDC header** which is enabled thanks to `v1190a::SetTDCHeadTrailer()`,
- **the TDC data** (*if any*), 1 for each hit recorded during the event, providing the channel and the time stamp associated to the hit,
- **a TDC error** providing error flags,
- **a TDC trailer** which is enabled thanks to `v1190a::SetTDCHeadTrailer()`,
- **a global trigger time tag** that provides the absolute trigger time relatively to the last reset, and
- **a global trailer** providing the total word count in the event.

CMS RPC FEEs provide with 100 ns long LVDS output signals that are injected into the TDCs' input. Any avalanche signal that gives a signal above the FEEs threshold is thus recorded by the TDCs as a hit within the match window. Each hit is assigned to a specific TDC channel with a time stamp, with a precision of 100 ps. The reference time, $t_0 = 0$, is provided by the beginning of the match window. Thus for each trigger, coming from a scintillator coïncidence or the pulse generator, a list of hits is stored into the TDCs' buffers and will then be transfered into a ROOT Tree.
When the BLT is used, it is easy to understand that the maximum number of words that have been set as ALF will not be a finite number of events or, at least, the number of events that would be recorded into the TDC buffers will not be a multiple of the block size. In the last BLT cycle to tranfer data, the number of events to transfer will most propably be lower than the block size. In that case, the TDC can add fillers at the end of the block but this option requires to send more data to the computer and is thus a little slower. Another solution is to finish the transfer after the last event by sending a bus error that states that the BLT reached the last event in the pile. This method has been chosen in

GIF++.
Due to irradiation, an event in GIF++ can count up to 300 words per TDC. A limit of 4096 words (12 bits) has been set to generate IRQ which represent from 14 to almost 700 events depending on the average of hits collected per event. Then the block size has been set to 100 events with enabled bus errors. When an AFL is reached for one of the TDCs, the VME bridge stops the acquisition by sending a BUSY signal.

The data is then transfered one TDC at a time into a structure called `RAWData` (Source Code A.2). Note that the structure as presented here is used when a single edge detection is used as there is only one time stamp list associated to the hits. When using detection on both edges, a second time stamp list could be added and when using pair detection, a list with the signal width could be added instead.

```
struct RAWData{
    vector<int>              *EventList;
    vector<int>              *NHitsList;
    vector<int>              *QFlagList;
    vector<vector<int> >     *ChannelList;
    vector<vector<float> >   *TimeStampList;
};
```

Source Code A.2: Description of data holding C++ structure `RAWData`.

```
class DataReader
{
    private:
        bool      StopFlag;
        IniFile  *iniFile;
        Data32    MaxTriggers;
        v1718    *VME;
        int       nTDCs;
        v1190a   *TDCs;
        RAWData   TDCData;

    public:
        DataReader();
        virtual ~DataReader();
        void      SetIniFile(string inifilename);
        void      SetMaxTriggers();
        Data32    GetMaxTriggers();
        void      SetVME();
        void      SetTDC();
        int       GetQFlag(Uint it);
        void      Init(string inifilename);
        void      FlushBuffer();
        void      Update();
        string    GetFileName();
        void      WriteRunRegistry(string filename);
        void      Run();
};
```

Source Code A.3: Description of C++ object `DataReader`.

In order to organize the data transfer and the data storage, an object called `DataReader` was created (Source Code A.3). On one hand, it has `v1718` and `v1190a` objects as private members for communication purposes, such as VME modules settings via the configuration file `*iniFile` or data

read-out through `v1190a::Read()` and on the other hand, it contains the struture `RAWData` that allows to organise the data in vectors reproducing the tree structre of a ROOT file.
Each event is tranferred from `TDCData` and saved into branches of a ROOT `TTree` as 3 integers that represent the event ID (`EventCount`), the number of hits read from the TDCs (`nHits`), and the quality flag that provides information for any problem in the data transfer (`qflag`), and 2 lists of *nHits* elements containing the fired TDC channels (`TDCCh`) and their respective time stamps (`TDCTS`), as presented in Source Code A.4. The ROOT file file is named using information contained into the configuration file, presented in section A.5.2. The needed information is extracted using method `DataReader::GetFileName()` and allow to build the output filename format `ScanXXXXXX_HVX_DAQ.root` where `ScanXXXXXX` is a 6 digit number representing the scan number into GIF++ database and `HVX` the HV step within the scan that can be more than a single digit. An example of ROOT data file is provided with Figure A.3.

```
RAWData TDCData;
TFile *outputFile = new TFile(outputFileName.c_str(),"recreate");
TTree *RAWDataTree = new TTree("RAWData","RAWData");

int            EventCount = -9;
int            nHits = -8;
int            qflag = -7;
vector<int>    TDCCh;
vector<float> TDCTS;

RAWDataTree->Branch("EventNumber",&EventCount, "EventNumber/I");
RAWDataTree->Branch("number_of_hits",&nHits,"number_of_hits/I");
RAWDataTree->Branch("Quality_flag",&qflag,"Quality_flag/I");
RAWDataTree->Branch("TDC_channel",&TDCCh);
RAWDataTree->Branch("TDC_TimeStamp",&TDCTS);

//...
//Here read the TDC data using v1190a::Read() and place it into
//TDCData for as long as you didn't collect the requested amount
//of data.
//...

for(Uint i=0; i<TDCData.EventList->size(); i++){
    EventCount  = TDCData.EventList->at(i);
    nHits       = TDCData.NHitsList->at(i);
    qflag       = TDCData.QFlagList->at(i);
    TDCCh       = TDCData.ChannelList->at(i);
    TDCTS       = TDCData.TimeStampList->at(i);
    RAWDataTree->Fill();
}
```

Source Code A.4: Highlight of the data transfer and organisation within `DataReader::Run()` after the data has been collected into `TDCData`.

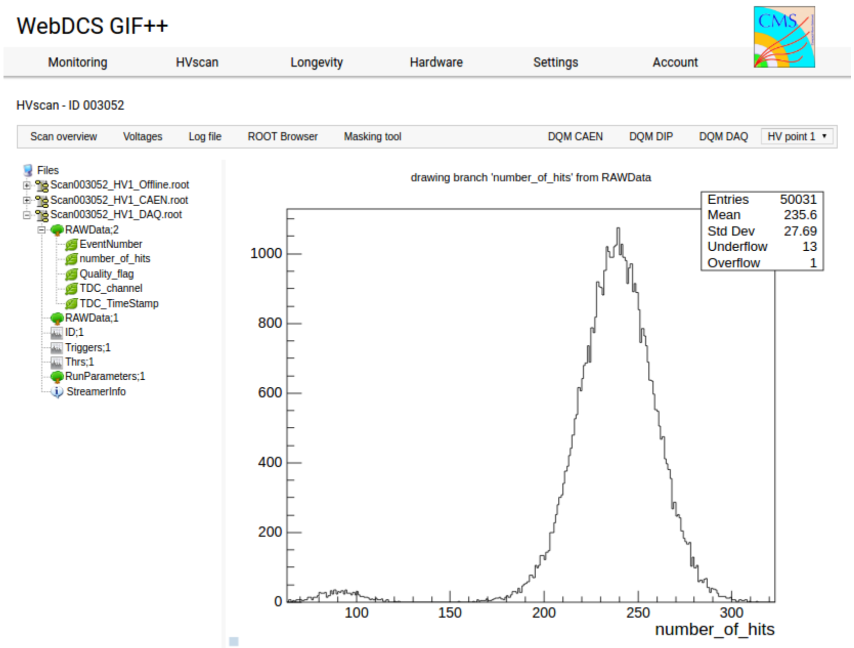

Figure A.3: Structure of the ROOT output file generated by the DAQ. The 5 branches (`EventNumber`, `number_of_hits`, `Quality_flag`, `TDC_channel` and `TDC_TimeStamp`) are visible on the left panel of the ROOT browser. On the right panel is visible the histogram corresponding to the variable `nHits`. In this specific example, there were approximately 50k events recorded to measure the gamma irradiation rate on the detectors. Each event is stored as a single entry in the `TTree`.

A.4.3 Data quality flag

Among the parameters that are recorded for each event, the quality flag is determined on the fly by checking the data recorded by every single TDC. An **enum** called `QualityFlag` was written to associate the key `GOOD` to the integer 1 and `CORRUPTED` to 0. From method `v1190a::Read()`, it can be understood that the content of each TDC buffer is readout one TDC at a time. Entries are created in the data list for the first TDC and then, when the second buffer is readout, events corresponding to entries that have already been created to store data for the previous TDC are added to the existing list element. On the contrary, when an event entry has not been yet created in the data list, a new entry is created.

It is possible that each TDC buffer contains a different number of events. In cases where the first element in the buffer list is an event for corresponds to a new entry, the difference in between the intry from the buffer and the last entry in the data list is recorded and checked. If it is greater than 1, what should never be the case, the quality flag is set to `CORRUPTED` for this TDC and an empty entry is created in the place of the missing ones. Missing entries are believe to be the result of a bad hold on the TDC buffers at the moment of the readout. Indeed, the software hold is effective only on 1 TDC at a time and no solution as been found yet to completely block the writting in the buffers when an IRQ is received.

At the end of each BLT cycle, the ID of the last entry stored for each TDC buffer is not recorded. When starting the next cycle, if the first entry in the pile corresponds to an event already existing in the list, the readout will start from this list element and will not be able to check the difference in between this entry's ID and the one of the last entry that was recorded for this TDC buffer in the previous cycle. In the case events were missing, the flag stays at its initial value of 0, which is similar to `CORRUPTED` and it is assumed that then this TDC will not contribute to `number_of_hits`, `TDC_channel` or `TDC_TimeStamp`. Finally, since there will be 1 `RAWData` entry per TDC for each event (meaning `nTDCs` entries, referring to `DataReader` private attribute), the individual flags of each TDC will be added together. The final format is an integer composed `nTDCs` digits where each digit is the flag of a specific TDC. This is constructed using powers of 10 like follows:

TDC 0: `QFlag` $= 10^0 \times$ `QualityFlag`

TDC 1: `QFlag` $= 10^1 \times$ `QualityFlag`

...

TDC N: `QFlag` $= 10^N \times$ `QualityFlag`

and the final flag to be with N digits:

`QFlag` = `n....3210`

each digit being 1 or 0. Bellow is given an example with a 4 TDCs setup.

If all TDCs were good : `QFlag` = `1111`,

but if TDC 2 was corrupted : `QFlag` = `1011`.

When data taking is over and the data contained in the dynamical `RAWData` structure is transfered to the ROOT file, all the 0s are changed into 2s by calling the method `DataReader::GetQFlag()`. This will help translating the flag without knowing the number of TDCs beforehand. Indeed, a flag `111` could be due to a 3 TDC setup with 3 good individual TDC flags or to a more than 3 TDC setup with TDCs those ID is greater than 2 being `CORRUPTED`, thus giving a 0.

The quality flag has been introduced quite late, in October 2017 only, to the list of GIF++ DAQ parameters to be recorded into the output ROOT file. Before this addition, the missing data, corrupting the quality for the offline analysis, was contributing to artificially fill data with lower multiplicity. Looking at `TBranch number_of_hits` provides an information about the data of the full GIF++ setup. When a TDC is not able to transfer data for a specific event, the effect is a reduction of the total number of hits recorded in the full setup, this is what can be seen from Figure A.4. After offline reconstruction detector by detector, the effect of missing events can be seen in the artificially filled bin at multiplicity 0 shown in Figure A.5. Nontheless, for data wih high irradiation levels, as it is he case for Figure A.5a, discarding the fake multiplicity 0 data can be done easily during the offline analysis. At lower radiation, the missing events contribution becomes more problematic as the multiplicity distribution overlaps the multiplicity 0 and that in the same time the proportion of missing events decreases. Attempts to fit the distribution with a Poisson or skew distribution function were not conclusive and this very problem has been at the origin of the quality flag that allows to give a non ambiguous information about each event quality.

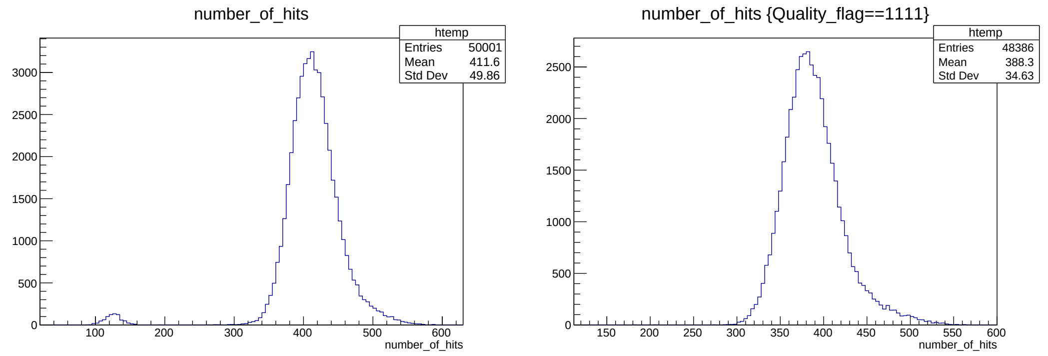

(a) *(b)*

Figure A.4: The effect of the quality flag is explained by presenting the content of `TBranch number_of_hits` of a data file without `Quality_flag` in Figure A.4a and the content of the same `TBranch` for data corresponding to a `Quality_flag` where all TDCs were labelled as `GOOD` in Figure A.4b taken with similar conditions. It can be noted that the number of entries in Figure A.4b is slightly lower than in Figure A.4a due to the excluded events.

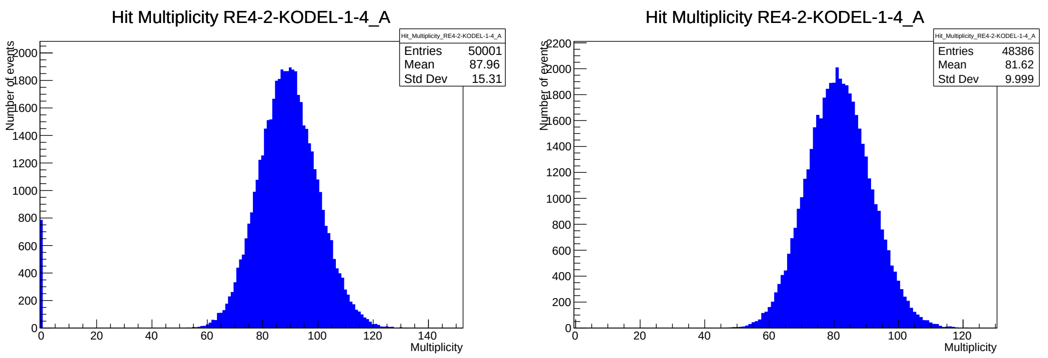

(a) *(b)*

Figure A.5: Using the same data as previously showed in Figure A.4, the effect of the quality flag is explained by presenting the reconstructed hit multiplicity of a data file without `Quality_flag` in Figure A.5a and the reconstructed content of the same RPC partition for data corresponding to a `Quality_flag` where all TDCs were labelled as `GOOD` in Figure A.5b taken with similar conditions. The artificial high content of bin 0 is completely suppressed.

A.5 Communications

To ensure data readout and dialog in between the machine and the TDCs or in between the webDCS and the DAQ, different communication solutions were used. First of all, it is important to have a module to allow the comminication in between the TDCs and the computer from which the DAQ operates. When this communication is effective, shifters using the webDCS to control data taking can thus send instructions to the DAQ.

A.5.1 V1718 USB Bridge

In the previous section, the data transfer as been discussed. The importance of the `v1718` object (Source Code A.5), used as private member of `DataReader`, was not explicited. VME master modules are used for communication purposes as they host the USB port that connects the powered crate buffer to the computer were the DAQ is installed. From the source code point of view, this object is used to control the communication status, by reading the returned error codes with `v1718::CheckStatus()`, or to check for IRQs coming from the TDCs through `v1718::CheckIRQ()`. To ensure that triggers are blocked at the hardware level, a NIM pulse is sent out of one the two first programmable outputs of the module (`v1718::SendBUSY()`) to the VETO of the coïndidence module where the trigger signals originate. As long as this signal is ON, no trigger can reach the TDCs anymore. Finally, used in the case of noise and background measurements in which the trigger needs not to be provided by the muon bean but by an uncorrelated source, a pulse generator is enabled with `v1718::RDMTriggerPulse()`. The ”random” pulse is sent through the third and fourth outputs of the module. Both the BUSY signal and the random pulse are shaped in the method `v1718::SetPulsers()` where the number of pulses to be generated, their width, as well as the period of the pulse generator is defined.

```
class v1718{
    private:
        int                 Handle;
        Data32              Data;           // Data
        CVIRQLevels         Level;          // Interrupt level
        CVAddressModifier AM;               // Addressing Mode
        CVDataWidth         DataSize;       // Data Format
        Data32              BaseAddress;    // Base Address

    public:
        v1718(IniFile *inifile);
        ~v1718();
        long                GetHandle(void) const;
        int                 SetData(Data16 data);
        Data16              GetData(void);
        int                 SetLevel(CVIRQLevels level);
        CVIRQLevels         GetLevel(void);
        int                 SetAM(CVAddressModifier am);
        CVAddressModifier GetAM(void);
        int                 SetDatasize(CVDataWidth datasize);
        CVDataWidth         GetDataSize(void);
        int                 SetBaseAddress(Data16 baseaddress);
        Data16              GetBaseAddress(void);
        void                CheckStatus(CVErrorCodes status) const;
        bool                CheckIRQ();
        void                SetPulsers(Uint RDM_Frequency);
        void                SendBUSY(PulserLevel level);
        void                RDMTriggerPulse(PulserLevel level);
};
```

Source Code A.5: Description of C++ object `v1718`.

A.5.2 Configuration file

The DAQ software takes as input a configuration file written using INI standard [283]. This file is partly filled with the information provided by the shifters when starting data acquisition using the webDCS, as shown by Figure A.6. This information is written in section `[General]` and will later be stored in the ROOT file that contains the DAQ data as can be seen from Figure A.3. Indeed, another `TTree` called `RunParameters` as well as the 2 histograms `ID`, containing the scan number, start and stop time stamps, and `Triggers`, containing the number of triggers requested by the shifter, are available in the data files. Moreover, `ScanID` and `HV` are then used to construct the file name thanks to the method `DataReader::GetFileName()`.

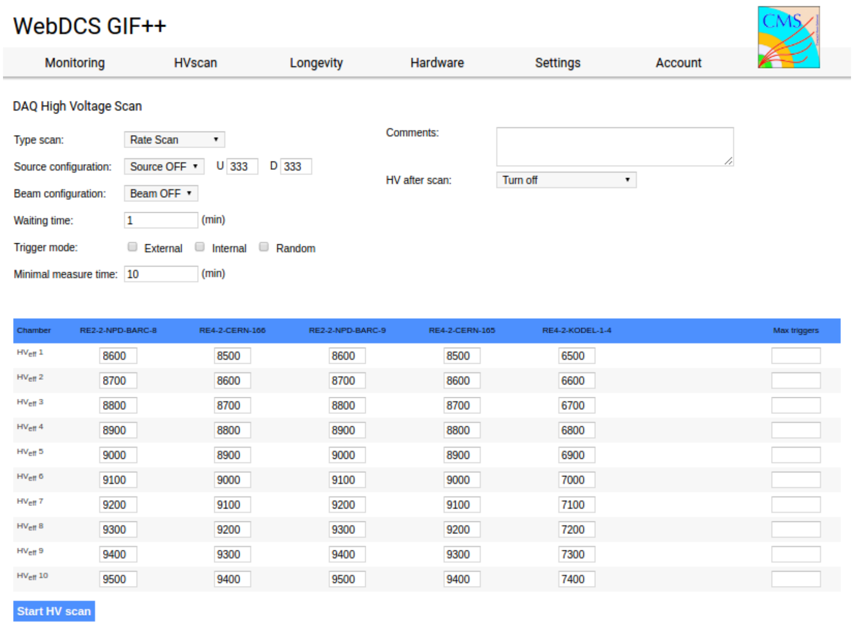

Figure A.6: WebDCS DAQ scan page. On this page, shifters need to choose the type of scan (Rate, Efficiency or Noise Reference scan), the gamma source configuration at the moment of data taking, the beam configuration, and the trigger mode. These information will be stored in the DAQ ROOT output. Are also given the minimal measurement time and waiting time after ramping up of the detectors is over before starting the data acquisition. Then, the list of HV points to scan and the number of triggers for each run of the scan are given in the table underneath.

The rest of the information is written beforehand in the configuration file template, as explicited in Source Code A.6, and contains the hardware addresses to the differents VME modules in the setup as well as settings for the TDCs. As the TDC settings available in the configuration file are not supposed to be modified, an improvement would be to remove them from the configuration file and to hardcode them inside of the DAQ code itself or to place them into a different INI file that would host only the TDC settings to lower the probability for a bad manipulation of the configuration file that can be modified from one of webDCS' menus.

```
[General]
Tdcs=4
ScanID=$scanid
HV=$HV
RunType=$runtype
MaxTriggers=$maxtriggers
Beam=$beam
[VMEInterface]
Type=V1718
BaseAddress=0xFF0000
Name=VmeInterface
int_trig_freq=100
[TDC0]
Type=V1190A
BaseAddress=0x00000000
Name=Tdc0
StatusA00-15=1
StatusA16-31=1
StatusB00-15=1
StatusB16-31=1
StatusC00-15=1
StatusC16-31=1
StatusD00-15=1
StatusD16-31=1
[TDC1]
Type=V1190A
BaseAddress=0x11110000
Name=Tdc1
StatusA00-15=1
StatusA16-31=1
StatusB00-15=1
StatusB16-31=1
StatusC00-15=1
StatusC16-31=1
StatusD00-15=1
StatusD16-31=1
[TDC2]
Type=V1190A
BaseAddress=0x22220000
Name=Tdc2
StatusA00-15=1
StatusA16-31=1
StatusB00-15=1
StatusB16-31=1
StatusC00-15=1
StatusC16-31=1
StatusD00-15=1
StatusD16-31=1
[TDC3]
Type=V1190A
BaseAddress=0x44440000
Name=Tdc3
StatusA00-15=1
StatusA16-31=1
StatusB00-15=1
StatusB16-31=1
StatusC00-15=1
StatusC16-31=1
StatusD00-15=1
StatusD16-31=1
[TDCSettings]
TriggerExtraSearchMargin=0
TriggerRejectMargin=0
TriggerTimeSubstraction=0b1
TdcDetectionMode=0b01
TdcResolution=0b10
TdcDeadTime=0b00
TdcHeadTrailer=0b1
TdcEventSize=0b1001
TdcTestMode=0b0
BLTMode=1
```

Source Code A.6: INI configuration file template for 4 TDCs. In section `[General]`, the number of TDCs is explicited and information about the ongoing run is given. Then, there are sections for each and every VME modules. There buffer addresses are given and for the TDCs, the list of channels to enable is given. Finally, in section `[TDCSettings]`, a part of the TDC settings are given.

```
typedef map< const string, string > IniFileData;

class IniFile{
    private:
        bool        CheckIfComment(string line);
        bool        CheckIfGroup(string line,string& group);
        bool        CheckIfToken(string line,string& key,string& value);
        string      FileName;
        IniFileData FileData;
        int         Error;

    public:
        IniFile();
        IniFile(string filename);
        virtual    ~IniFile();

        // Basic file operations
        void        SetFileName(string filename);
        int         Read();
        int         Write();
        IniFileData GetFileData();

        // Data readout methods
        Data32 addressType(string groupname,string keyname,Data32 defaultvalue);
        long intType(string groupname,string keyname,long defaultvalue);
        long long longType(string groupname,string keyname,long long
  ↪  defaultvalue);
        string stringType(string groupname,string keyname,string defaultvalue);
        float floatType(string groupname,string keyname,float defaultvalue);

        // Error methods
        string      GetErrorMsg();
};
```

Source Code A.7: Description of C++ object `IniFile` used as a parser for INI file format.

In order to retreive the information of the configuration file, the object `IniFile` has been developped to provide an INI parser, presented in Source Code A.7. It contains private methods returning a boolean to check the type of line written in the file, whether a comment, a group header or a key line (`IniFile::CheckIfComment()`, `IniFile::CheckIfGroup()` and `IniFile::CheckIfToken()`). The key may sometimes be referred to as *token* in the source code. Moreover, the private element `FileData` is a map of `const string` to `string` that allows to store the data contained inside the configuration file via the public method `IniFile::GetFileData()` following the formatting (see method `IniFile::Read()`):

```
string group, token, value;
// Get the field values for the 3 strings.
// Then concatenate group and token together as a single string
// with a dot separation.
token = group + "." + token;
FileData[token] = value;
```

More methods have been written to translate the different keys into the right variable format when used by the DAQ. For example, to get a `float` value out of the configuration file data, knowing the group and the key needed, the method `IniFile::floatType()` can be used. It takes 3 arguments being the group name and key name (both `string`), and a default `float` value used as exception in the case the expected combination of group and key cannot be found in the configuration file. This default value is then used and the DAQ continues on working after sending an alert in the log file for further debugging.

A.5.3 WebDCS/DAQ intercommunication

When shifters send instructions to the DAQ via the configuration file, it is the webDCS itself that gives the start command to the DAQ and then the 2 softwares use inter-process communication through file to synchronise themselves. This communication file is represented by the variable `const string __runstatuspath`.
On one side, the webDCS sends commands or status that are readout by the DAQ:

- `INIT`, status sent when launching a scan and read via function `CtrlRunStatus(...)`,
- `START`, command to start data taking and read via function `CheckSTART()`,
- `STOP`, command to stop data taking at the end of the scan and read via function `CheckSTOP()`, and
- `KILL`, command to kill data taking sent by user and read via function `CheckKILL()`. Note that the DAQ doesn't stop before the current ROOT file is safely written and saved.

and on the other, the DAQ sends status that are controled by the webDCS:

- `DAQ_RDY`, sent with `SendDAQReady()` to signify that the DAQ is ready to receive commands from the webDCS,
- `RUNNING`, sent with `SendDAQRunning()` to signify that the DAQ is taking data,
- `DAQ_ERR`, sent with `SendDAQError()` to signify that the DAQ didn't receive the expected command from the webDCS or that the launch command didn't have the right number of arguments,
- `RD_ERR`, sent when the DAQ wasn't able to read the communication file, and
- `WR_ERR`, sent when the DAQ wasn't able to write into the communication file.

A.5.4 Example of inter-process communication cycle

Under normal conditions, the webDCS and the DAQ processes exchange commands and status via the file hosted at the address `__runstatuspath`, as explained in subsection A.5.3. An example of cycle is given in Table A.1. In this example, the steps 3 to 5 are repeated as long as the webDCS tells the DAQ to take data. A data taking cycle is the equivalent as what is called a *Scan* in GIF++ jargon,

referring to a set a runs with several HV steps. Each repetition of steps 3 to 5 is then equivalent to a single *Run*.
At any moment during the data taking, for any reason, the shifter can decide that the data taking needs to be stopped before it reached the end of the scheduled cycle. Thus at any moment on the cycle, the content of the inter-process communication file will be changed to `KILL` and the DAQ will shut down right away. The DAQ checks for `KILL` signals every 5s after the TDCs configuration is over. So far, the function `CheckKILL()` has been used only inside of the data taking loop of method `DataReader::Run()` and thus, if the shifter decides to KILL the data taking during the TDC configuration phase or the HV ramping in between 2 HV steps, the DAQ will not be stopped smoothly and a *force kill* command will be sent to stop the DAQ process that is still awake on the computer. Improvements can be brought on this part of the software to make sure that the DAQ can safely shutdown at any moment.

step	actions of webDCS	status of DAQ	`__runstatuspath`
1	launch DAQ ramp voltages ramping over wait for currents stabilization	readout of IniFfile configuration of TDCs	`INIT`
2		configuration done send DAQ ready wait for `START` signal	`DAQ_RDY`
3	waiting time over send `START`		`START`
4	wait for run to end monitor DAQ run status	data taking ongoing check for `KILL` signal	`RUNNING`
5		run over send `DAQ_RDY` wait for next DCS signal	`DAQ_RDY`
6	ramp voltages ramping over wait for currents stabilization		`DAQ_RDY`
3	waiting time over send `START`		`START`
4	wait for run to end monitor DAQ run status	update IniFile information data taking ongoing check for `KILL` signal	`RUNNING`
5		run over send `DAQ_RDY` wait for next DCS signal	`DAQ_RDY`
7	send command `STOP`	DAQ shuts down	`STOP`

Table A.1: Inter-process communication cycles in between the webDCS and the DAQ through file string signals.

A.6 Software export

In section A.2 was discussed the fact that the DAQ as written in its last version is not a standalone software. It is possible to make it a standalone program that could be adapted to any VME setup using V1190A and V1718 modules by creating a GUI for the software or by printing the log messages that are normally printed in the webDCS through the log file, directly into the terminal. This method was used by the DAQ up to version 3.0 moment where the webDCS was completed. Also, it is possible to check branches of DAQ v2.X to have example of communication through a terminal. DAQ v2.X is nontheless limited in it's possibilities and requires a lot of offline manual interventions from the users. Indeed, there is no communication of the software with the detectors' power supply system that would allow for a user a predefine a list of voltages to operate the detectors at and loop over to take data without any further manual intervention. In v2.X, the data is taken for a single detector setting and at the end of each run, the softwares asks the user if he intends on taking more runs. If so, the software invites the user to set the operating voltages accordingly to what is necessary and to manual update the configuration file in consequence. This working mode can be a very first approach before an evolution and has been successfuly used by colleagues from different collaborations.

For a more robust operation, it is recommanded to develop a GUI or a web application to interface the DAQ. Moreover, to limit the amount of manual interventions, and thus the probability to make mistakes, it is also recommanded to add an extra feature into the DAQ by installing the HV Wrapper library provided by CAEN of which an example of use in a similar DAQ software developped by a master student of UGent, and called TinyDAQ, is provided on UGent's github. Then, this HV Wrapper will help you communicating with and give instructions to a CAEN HV powered crate and can be added into the DAQ at the same level where the communication with the user was made in DAQ v2.X. In case you are using another kind of power system for your detectors, it is stringly adviced to use HV modules or crates that can be remotely controled via a using C++ libraries.

B

Details on the offline analysis package

The data collected in GIF++ thanks to the DAQ described in Appendix A is difficult to interpret by a human user that doesn't have a clear idea of the raw data architecture of the ROOT data files. In order to render the data human readable, a C++ offline analysis tool was designed to provide users with detector by detector histograms that give a clear overview of the parameters monitored during the data acquisition [273]. In this appendix, details about this software in the context of GIF++, as of how the software was written and how it functions will be given.

B.1 GIF++ Offline Analysis file tree

GIF++ Offline Analysis source code is fully available on github at `https://github.com/afagot/GIF_OfflineAnalysis`. The software requires ROOT as non-optionnal dependency as it takes ROOT files in input and write an output ROOT file containing histograms. To compile the GIF++ Offline Analysis project is compiled with cmake. To compile, first a `build/` directory must be created to compile from there:

```
mkdir build
cd build
cmake ..
make
make install
```

To clean the directory and create a new build directory, the bash script `cleandir.sh` can be used:

```
./cleandir.sh
```

The source code tree is provided below along with comments to give an overview of the files' content. The different objects created for this project (`Infrastructure`, `Trolley`, `RPC`, `Mapping`, `RPCHit`, `RPCCluster` and `Inifile`) will be described in details in the following sections.

```
GIF_OfflineAnalysis
├── bin
│   └── offlineanalysis ........ executable
├── build ...................... cmake compilation directory
│   └── ...
├── include .................... list of C++ header files
│   ├── Cluster.h .............. declaration of object RPCCluster
│   ├── Current.h .............. declaration of GetCurrent analysis macro
│   ├── GIFTrolley.h ........... declaration of object Trolley
│   ├── Infrastructure.h ....... declaration of object Infrastructure
│   ├── IniFile.h .............. declaration of object IniFile for ini parser
│   ├── Mapping.h .............. declaration of object Mapping
│   ├── MsgSvc.h ............... declaration of offline log messages
│   ├── OfflineAnalysis.h ...... declaration of data analysis macro
│   ├── RPCDetector.h .......... declaration of object RPC
│   ├── RPCHit.h ............... declararion of object RPCHit
│   ├── types.h ................ definition of useful variable types
│   └── utils.h ................ declaration of useful functions
├── obj ........................ binary files created by compiler
│   └── ...
├── src ........................ list of C++ source files
│   ├── Cluster.cc ............. definition of object RPCCluster
│   ├── Current.cc ............. definition of GetCurrent analysis macro
│   ├── GIFTrolley.cc .......... definition of object Trolley
│   ├── Infrastructure.cc ...... definition of object Infrastructure
│   ├── IniFile.cc ............. definition of object IniFile for ini parser
│   ├── main.cc ................ main file
│   ├── Mapping.cc ............. definition of object Mapping
│   ├── MsgSvc.cc .............. definition of offline log messages
│   ├── OfflineAnalysis.cc ..... definition of data analysis macro
│   ├── RPCDetector.cc ......... definition of object RPC
│   ├── RPCHit.cc .............. definition of object RPCHit
│   └── utils.cc ............... definition of useful functions
├── cleandir.sh ................ bash script to clean build directory
├── CMakeLists.txt ............. set of instructions for cmake
├── config.h.in ................ definition of version number
└── README.md .................. REAMDE file for github
```

B.2 Usage of the Offline Analysis

In order to use the Offline Analysis tool, it is necessary to know the Scan number and the HV Step of the run that needs to be analysed. This information needs to be written in the following format:

```
Scan00XXXX_HVY
```

where `XXXX` is the scan ID and `Y` is the high voltage step (in case of a high voltage scan, data will be taken for several HV steps). This format corresponds to the base name of data files in the database of the GIF++ webDCS. Usually, the offline analysis tool is automatically called by the webDCS at the end of data taking or by a user from the webDCS panel if an update of the tool was brought. Nontheless, an expert can locally launch the analysis for tests on the GIF++ computer, or a user can get the code on is local machine from github and download data from the webDCS for is own analysis. To launch the code, the following command can be used from the `GIF_OfflineAnalysis` folder:

```
bin/offlineanalysis /path/to/Scan00XXXX_HVY
```

where, `/path/to/Scan00XXXX_HVY` refers to the local data files. Then, the offline tool will by itself take care of finding all available ROOT data files present in the folder, as listed bellow:

- `Scan00XXXX_HVY_DAQ.root` containing the TDC data as described in Appendix A.4.2 (events, hit and timestamp lists), and

- `Scan00XXXX_HVY_CAEN.root` containing the CAEN mainframe data recorded by the monitoring tool webDCS during data taking (HVs and currents of every HV channels). This file is created independently of the DAQ.

B.2.1 Output of the offline tool

B.2.1.1 ROOT file

The analysis gives in output ROOT datafiles that are saved into the data folder and called using the naming convention `Scan00XXXX_HVY_Offline.root`. Inside those, a list of `TH1` histograms can be found. Its size will vary as a function of the number of detectors in the setup as each set of histograms is produced detector by detector. For each partition of each chamber, can be found:

- `Time_Profile_Tt_Sc_p` shows the time profile of all recorded events (number of events per time bin),

- `Hit_Profile_Tt_Sc_p` shows the hit profile of all recorded events (number of events per channel),

- `Hit_Multiplicity_Tt_Sc_p` shows the hit multiplicity (number of hits per event) of all recorded events (number of occurences per multiplicity bin),

- `Time_vs_Strip_Profile_Tt_Sc_p` shows the 2D time vs strip profile of all recorded events (number of events per time bin per strip),

- `Strip_Mean_Noise_Tt_Sc_p` shows noise/gamma rate per unit area for each strip in a selected time range. After filters are applied on `Time_Profile_Tt_Sc_p`, the filtered version of `Hit_Profile_Tt_Sc_p` is normalised to the total integrated time and active detection area of a single channel,

- `Strip_Activity_Tt_Sc_p` shows noise/gamma activity for each strip (normalised version of previous histogram - strip activity = strip rate / average partition rate),

- `Strip_Homogeneity_Tt_Sc_p` shows the *homogeneity* of a given partition (homogeneity = exp(-strip rates standard deviation(strip rates in partition/average partition rate))),

- mask_Strip_Mean_Noise_Tt_Sc_p shows noise/gamma rate per unit area for each masked strip in a selected time range. Offline, the user can control the noise/gamma rate and decide to mask the strips that are judged to be noisy or dead. This is done via the *Masking Tool* provided by the webDCS,
- mask_Strip_Activity_Tt_Sc_p shows noise/gamma activity per unit area for each masked strip with repect to the average rate of active strips,
- NoiseCSize_H_Tt_Sc_p shows noise/gamma cluster size, a cluster being constructed out of adjacent strips giving a signal at the *same time* (hits within a time window of 25 ns),
- NoiseCMult_H_Tt_Sc_p shows noise/gamma cluster multiplicity (number of reconstructed clusters per event),
- Chip_Mean_Noise_Tt_Sc_p shows the same information than Strip_Mean_Noise_Tt_Scp using a different binning (1 chip corresponds to 8 strips),
- Chip_Activity_Tt_Sc_p shows the same information than Strip_Activity_Tt_Scp using chip binning,
- Chip_Homogeneity_Tt_Sc_p shows the homogeneity of a given partition using chip binning,
- Beam_Profile_Tt_Sc_p shows the estimated beam profile when taking efficiency scan. This is obtained by filtering Time_Profile_Tt_Sc_p to only consider the muon peak where the noise/gamma background has been subtracted. The resulting hit profile corresponds to the beam profile on the detector channels,
- Efficiency_Fake_Tt_Ss_p shows the efficiency given by fake hits by probing outside the peak in an uncorrelated window as wide as the peak window,
- Efficiency_Peak_Tt_Ss_p shows the efficiency given by hits contained in the peak window,
- PeakCSize_H_Tt_Sc_p shows the cluster size that was estimated using all the hits in the peak window,
- PeakCMult_H_Tt_Sc_p shows the cluster multiplicity that was estimated using all the hits in the peak window,
- L0_Efficiency_Tt_Sc_p shows the level 0 muon efficiency that was estimated **without** muon tracking after correction,
- MuonCSize_H_Tt_Sc_p shows the level 0 muon cluster size that was estimated **without** muon tracking after correction, and
- MuonCMult_H_Tt_Sc_p shows the level 0 muon cluster multiplicity that was estimated **without** muon tracking after correction.

In the histogram labels, t stands for the trolley number (1 or 3), c for the chamber slot label in trolley t and p for the partition label (A, B, C or D depending on the chamber layout) as explained in Chapter 5.3.

In the context of GIF++, an extra script called by the webDCS is called to extract the histograms from the ROOT files. The histograms are then stored in PNG and PDF formats into the corresponding folder (a single folder per HV step, so per ROOT file). An example of histogram organisation is given bellow for an hypothetical scan 001000 with at least 3 HV steps and whose chamber located in slot 1 of trolley 1 is called *Example_RPC1* and has at least 2 read-out partitions A and B. The goal is to then display the histograms graphs on the Data Quality Monitoring (DQM) page of the webDCS, as presented in Figure 5.27, in order for the users to control the quality of the data taking at the end of data taking.

```
Scan001000
├── Scan001000_HV1_DAQ.root
├── Scan001000_HV1_CAEN.root
├── Scan001000_HV1_Offline.root
├── HV1
│   ├── DAQ
│   │   ├── Beam_Profile_T1_S1_A.png
│   │   ├── Beam_Profile_T1_S1_A.pdf
│   │   ├── Beam_Profile_T1_S1_B.png
│   │   ├── Beam_Profile_T1_S1_B.pdf
│   │   └── ...
│   └── CAEN
│       ├── HVapp_Example_RPC1.pdf
│       ├── HVapp_Example_RPC1.png
│       └── ...
├── Scan001000_HV2_DAQ.root
├── Scan001000_HV2_CAEN.root
├── Scan001000_HV2_Offline.root
├── HV2
│   ├── DAQ
│   │   └── ...
│   └── CAEN
│       └── ...
├── Scan001000_HV3_DAQ.root
├── Scan001000_HV3_CAEN.root
├── Scan001000_HV3_Offline.root
├── HV3
│   └── ...
└── ...
```

B.2.1.2 CSV files

Moreover, up to 4 CSV files can be created depending on which ones of the 3 input files were in the data folder:

- `Offline-Corrupted.csv` , is used to keep track of the amount of data that was corrupted and removed from old data format files that don't contain any data quality flag.

- `Offline-Current.csv` , contains the summary of the currents and voltages applied on each RPC HV channel.

- `Offline-L0-EffCl.csv` , is used to write the efficiencies, cluster size and cluster multiplicity of efficiency runs. Note that `L0` refers here to *Level 0* and means that the results of effiency and clusterization are a first approximation calculated without performing any muon tracking in between the different detectors. This offline tool provides the user with a preliminar calculation of the efficiency and of the muon event parameters. Another analysis software especially dedicated to muon tracking is called on selected data to retrieve the results of efficiency and muon clusterization using a tracking algorithm to discriminate noise or gamma from muons as muons are the only particles that pass through the full setup, leaving hits than can be used to reconstruct their tracks.

- `Offline-Rate.csv` , is used to write the noise or gamma rates measured in the detector readout partitions.

Note that these 4 CSV files are created along with their *headers* (`Offline-[...]-Header.csv` containing the names of each data columns) and are automatically merged together when the offline analysis tool is called from the webDCS, contrary to the case where the tool is runned locally from the terminal as the merging bash script is then not called. Thus, the resulting files, used to make official plots, are:

- `Corrupted.csv` ,

- `Current.csv` ,

- `L0-EffCl.csv` .

- `Rate.csv` .

B.3 Analysis inputs and information handling

The usage of the Offline Analysis tool as well as its output have been presented in the previous section. It is now important to dig further and start looking at the source code and the inputs necessary for the tool to work. Indeed, other than the raw ROOT data files that are analysed, more information needs to be imported inside of the program to perform the analysis such as the description of the setup inside of GIF++ at the time of data taking (number of trolleys, of RPCs, dimensions of the detectors, etc...) or the mapping that links the TDC channels to the coresponding RPC channels in order to translate the TDC information into human readable data. Two files are used to transmit all this information:

- `Dimensions.ini`, that provides the necessary setup and RPC information, and

- `ChannelsMapping.csv`, that gives the link between the TDC and RPC channels as well as the *mask* for each channel (masked or not?).

B.3.1 Dimensions file and IniFile parser

GIF++ CMS RPC setup consists in detectors held into trolleys inside of the GIF++ bunker. Each of these detector may have a read-out segmented to cover different pseudo-rapidity range once intalled in CMS. The segmentation of the read-out is referred to as ”partitions”. This input file, present in every data folder, allows the analysis tool to know of the number of active trolleys, the number of active RPCs in those trolleys, and the details about each RPCs such as the number of RPC gaps, the number of pseudo-rapidity partitions, the number of strips per partion or the dimensions. To do so, there are 3 types of groups in the INI file architecture. Groups are sections of the INI file content starting with a title encapsulated in between sqaure brackets. A first general group, appearing only once at the head of the document, gives information about the number of active trolleys as well as their IDs, as presented in Source Code B.1. For each active trolley, a group similar to Source Code B.2 can be found containing information about the number of active detectors in the trolley and their IDs. Each trolley group as a `Tt` name format, where `t` is the trolley ID. Finally, for each detector stored in slots of an active trolley, there is a group providing information about their names and dimensions, as shown in Source Code B.3. Each slot group as a `TtSs` name format, where `s` is the slot ID of trolley `t` where the active RPC is hosted.

```ini
[General]
nTrolleys=2
TrolleysID=13
```

Source Code B.1: Example of `[General]` *group as might be found in* `Dimensions.ini`*. In GIF++, only 2 trolleys are available to hold RPCs and place them inside of the bunker for irradiation. The IDs of the trolleys are written in a signle string as ”13” and then read character by character by the program.*

```ini
[T1]
nSlots=4
SlotsID=1234
```

Source Code B.2: Example of trolley group as might be found in `Dimensions.ini`*. In this example, the file tells that there are 4 detectors placed in the holding slots of the trolley* `T1` *and that their IDs, written as a single string variable, are 1, 2, 3 and 4.*

```ini
[T1S1]
Name=RE2-2-NPD-BARC-8
Partitions=3
Gaps=3
Gap1=BOT
Gap2=TN
Gap3=TW
AreaGap1=11694.25
AreaGap2=6432
AreaGap3=4582.82
Strips=32
ActiveArea-A=157.8
ActiveArea-B=121.69
ActiveArea-C=93.03
```

Source Code B.3: Example of slot group as might be found in `Dimensions.ini`*. In this example, the file provides information about a detector named* `RE2-2-NPD-BARC-8`*, having 3 pseudo-rapidity readout partitions and stored in slot* `S1` *of trolley* `T1`*. This is a CMS RE2-2 type of detector. This information will then be used for example to compute the rate per unit area calculation.*

This information is read-out and stored in a C++ object called `IniFile`, that parses the information of the INI input file and stores it into a local buffer for later use. This INI parser is the exact same one that was previously developped for the GIF++ DAQ and described in Appendix A.5.2.

B.3.2 TDC to RPC link file and Mapping

The same way the INI dimension file information is stored using `map`, the channel mapping and mask information making the link in between TDC channels and RPC strips is stored and accessed through `map`. First of all, the mapping CSV file is organised into 3 columns separated by tabulations:

```
RPC_channel        TDC_channel        mask
```

using as formatting for each field:

```
TSCCC        TCCC        M
```

`TSCCC` is a 5-digit integer where `T` is the trolley ID, `S` the slot ID in which the RPC is held inside the trolley `T` and `CCC` is the RPC channel number, or *strip* number, that can take values up to 3-digits depending on the detector,

`TCCC` is a 4 digit integer where `T` is the TDC ID to which the RPC is connected, `CCC` is the TDC channel number linked to the RPC strip that can take values in between 0 and 127, and

`M` is a 1-digit integer indicating if the channel should be considered ($M = 1$) or discarded ($M = 0$) during analysis. Note that the absence of a third column is interpreted by the mapping file parser as $M = 1$ by default.

This mapping and masking information is readout and stored thanks to the object `Mapping`, presented in Source Code B.4. Similarly to `IniFile` objects, this class has private methods to provide with parser rules. The first one, `Mapping::CheckIfNewLine()` is used to find the newline character `'\n'` or return character `'\r'` (depending on which kind of operating system interacted with the file). Finding and identifying a newline or return character is used for the simple reason that the masking information has been introduced only during the year 2017 but the channel mapping files exist since 2015 and the very beginning of data taking at GIF++. This means that in the older data folders, before the upgrade, the channel mapping file only had 2 columns, the RPC channel and the TDC channel. For compatibility reasons, this method helps controling the character following the readout of the 2 first fields of a line. In case any end of line character is found, no mask information is present in the file and the default $M = 1$ is used. On the contrary, if the next character was a tabulation or a space, the mask information is present.

Once the 3 fields have been readout, the second private method `Mapping::CheckIfTDCCh()` is used to control that the TDC channel is an existing TDC channel by checking its format. Finally, the information is stored into 3 different maps (`Link`, `ReverseLink` and `Mask`) thanks to the public method `Mapping::Read()`. `Link` allows to get the RPC channel by knowing the TDC channel while `ReverseLink` does the opposite by returning the TDC channel by knowing the RPC channel. Finally, `Mask` returns the mask associated to a given RPC channel.

4708

```
typedef map<Uint,Uint> MappingData;

class Mapping {
    private:
        bool        CheckIfNewLine(char next);
        bool        CheckIfTDCCh(Uint channel);
        string      FileName;
        MappingData Link;
        MappingData ReverseLink;
        MappingData Mask;
        int         Error;
```

4709

```
    public:
        Mapping();
        Mapping(string baseName);
        ~Mapping();

        void SetFileName(const string filename);
        int Read();
        Uint GetLink(Uint tdcchannel);
        Uint GetReverse(Uint rpcchannel);
        Uint GetMask(Uint rpcchannel);
};
```

4710 *Source Code B.4: Description of C++ object `Mapping` used as a parser for the channel mapping and mask file.*

4711 ## B.4 Description of GIF++ setup within the Offline Analysis tool

4712 In the previous section, the tool input files have been discussed. The dimension file information is
4713 stored in a map hosted by the IniFile object. But this information is then used to create a series of
4714 new objects that helps defining the GIF++ infrastructure directly into the Offline Analysis. Indeed,
4715 from the `RPC`, to the more general `Infrastructure`, every element of the GIF++ infrastrucutre is
4716 recreated for each data analysis based on the information provided in input. All this information
4717 about the infrastructure will be used to assign each hit signal to a specific strip channel of a specific
4718 detector, and having a specific active area. This way, rate per unit area calculation is possible.

4719

4720 ### B.4.1 RPC objects

4721 `RPC` objects have been developped to represent physical active detectors in GIF++ at the moment
4722 of data taking. Thus, there are as many RPC objects created during the analysis than there were
4723 active RPCs tested during a run. Each `RPC` hosts the information present in the corresponding INI
4724 slot group, as showed in B.3, and organises it using a similar architecture. This can been seen from
4725 Source Code B.5.

4726 To make the object more compact, the lists of gap labels, of gap active areas and strip active
4727 areas are stored into `vector` dynamical containers. `RPC` objects are always contructed thanks to the
4728 dimension file information stored into the `IniFIle` and their ID, using the format `TtSs`. Using the
4729 RPC ID, the constructor calls the methods of `IniFile` to initialise the `RPC`. The other constructors
4730 are not used but exist in case of need. Finally, some getters have been written to access the different
4731 private parameters storing the detector information.

B.4.2 Trolley objects

`Trolley` objects have been developped to represent physical active trolleys in GIF++ at the moment of data taking. Thus, there are as many trolley objects created during the analysis than there were active trolleys hosting RPCs under test during a run. Each `Trolley` hosts the information present in the corresponding INI trolley group, as shown in B.2, and organises it using a similar architecture. In addition to the information hosted in the INI file, these objects have a dynamical container of `RPC` objects, representing the active detectors the active trolley was hosting at the time of data taking. This can been seen from Source Code B.6.

`Trolley` objects are always contructed thanks to the dimension file information stored into the `IniFIle` and their ID, using the format `Tt`. Using the Trolley ID, the constructor calls the methods of `IniFile` to initialise the `Trolley`. Retrieving the information of the RPC IDs via `SlotsID`, a new `RPC` is constructed and added to the container `RPCs` for each character in the ID `string`. The other constructors are not used but exist in case of need. Finally, some getters have been written to access the different private parameters storing the trolley and detectors information.

B.4.3 Infrastructure object

The `Infrastructure` object has been developped to represent the GIF++ bunker area dedicated to CMS RPC experiments. With this very specific object, all the information about the CMS RPC setup within GIF++ at the moment of data taking is stored. It hosts the information present in the corresponding INI general group, as shown in B.1, and organises it using a similar architecture. In addition to the information hosted in the INI file, this object have a dynamical container of `Trolley` objects representing the active tolleys in GIF++ area, themselves containing `RPC` objects. This can been seen from Source Code B.7.

The `Infrastructure` object is always contructed thanks to the dimension file information stored into the `IniFIle`. Retrieving the information of the trolley IDs via `TrolleysID`, a new `Trolley` is constructed and added to the container `Trolleys` for each character in the ID `string`. By extension, it is easy to understand that the process described in Section B.4.2 for the construction of RPCs takes place when a trolley is constructed. The other constructors are not used but exist in case of need. Finally, some getters have been written to access the different private parameters storing the infrastructure, trolleys and detectors information.

```
class RPC{
    private:
        string          name;        //RPC name as in webDCS database
        Uint            nGaps;       //Number of gaps in the RPC
        Uint            nPartitions; //Number of partitions in the RPC
        Uint            nStrips;     //Number of strips per partition
        vector<string>  gaps;        //List of gap labels (BOT, TOP, etc...)
        vector<float>   gapGeo;      //List of gap active areas
        vector<float>   stripGeo;    //List of strip active areas

    public:
        RPC();
        RPC(string ID, IniFile* geofile);
        RPC(const RPC& other);
        ~RPC();
        RPC& operator=(const RPC& other);

        string GetName();
        Uint   GetNGaps();
        Uint   GetNPartitions();
        Uint   GetNStrips();
        string GetGap(Uint g);
        float  GetGapGeo(Uint g);
        float  GetStripGeo(Uint p);
};
```

Source Code B.5: Description of C++ objects `RPC` *that describe each active detectors used during data taking.*

```
class Trolley{
    private:
        Uint         nSlots;  //Number of active RPCs in the considered trolley
        string       SlotsID; //Active RPC IDs written into a string
        vector<RPC*> RPCs;    //List of active RPCs

    public:
        Trolley();
        Trolley(string ID, IniFile* geofile);
        Trolley(const Trolley& other);
        ~Trolley();
        Trolley& operator=(const Trolley& other);

        Uint   GetNSlots();
        string GetSlotsID();
        Uint   GetSlotID(Uint s);
        RPC*   GetRPC(Uint r);
        void   DeleteRPC(Uint r);

        //Methods to get members of RPC objects stored in RPCs
        string GetName(Uint r);
        Uint   GetNGaps(Uint r);
        Uint   GetNPartitions(Uint r);
        Uint   GetNStrips(Uint r);
        string GetGap(Uint r, Uint g);
        float  GetGapGeo(Uint r, Uint g);
        float  GetStripGeo(Uint r, Uint p);
};
```

Source Code B.6: Description of C++ objects `Trolley` *that describe each active trolley used during data taking.*

```cpp
class Infrastructure {
    private:
        Uint             nTrolleys;  //Number of active Trolleys in the run
        string           TrolleysID; //Active trolley IDs written into a string
        vector<Trolley*> Trolleys;   //List of active Trolleys (struct)

    public:
        Infrastructure();
        Infrastructure(IniFile* geofile);
        Infrastructure(const Infrastructure& other);
        ~Infrastructure();
        Infrastructure& operator=(const Infrastructure& other);

        Uint   GetNTrolleys();
        string GetTrolleysID();
        Uint   GetTrolleyID(Uint t);

        Trolley* GetTrolley(Uint t);
        void     DeleteTrolley(Uint t);

        //Methods to get members of GIFTrolley objects stored in Trolleys
        Uint   GetNSlots(Uint t);
        string GetSlotsID(Uint t);
        Uint   GetSlotID(Uint t, Uint s);
        RPC*   GetRPC(Uint t, Uint r);

        //Methods to get members of RPC objects stored in RPCs
        string GetName(Uint t, Uint r);
        Uint   GetNGaps(Uint t, Uint r);
        Uint   GetNPartitions(Uint t, Uint r);
        Uint   GetNStrips(Uint t, Uint r);
        string GetGap(Uint t, Uint r, Uint g);
        float  GetGapGeo(Uint t, Uint r, Uint g);
        float  GetStripGeo(Uint t, Uint r, Uint p);
};
```

Source Code B.7: Description of C++ object `Infrastructure` *that contains the full information about CMS RPC experiment in GIF++.*

B.5 Handeling of data

As discussed in Appendix A.4.2, the raw data uses a `TTree` architecture where every entry is related to a trigger signal provided by a muon or a random pulse, whether the goal of the data taking was to measure the performance of the detector or the noise/gamma background respectively. Each of these entries, referred also as events, contain a more or less full list of hits in the TDC channels to which the detectors are connected. To this list of hits corresponds a list of time stamps, marking the arrival of the hits within the TDC channel.

The infrastructure of the CMS RPC experiment within GIF++ being defined, combining the raw data information with the information provided by both the mapping/mask file and the dimension file allows to build new physical objects that will help in computing efficiency or rates.

4780
B.5.1 RPC hits

4781 The raw data stored in the ROOT file as output of the GIF++ DAQ, is readout by the analysis tool
4782 using the structure `RAWData` presented in Source Code B.9 that differs from the structure presented
4783 in Appendix A.4.2 as it is not meant to hold all of the data contained in the ROOT file. In this sense,
4784 this structure is in the case of the offline analysis tool not a dynamical object and will only be storing
4785 a single event contained in a single entry of the `TTree`.

4786

4787
```
class RPCHit {
    private:
        Uint  Channel;    //RPC channel according to mapping (5 digits)
        Uint  Trolley;    //0, 1 or 3 (1st digit of the RPC channel)
        Uint  Station;    //Slot where is held the RPC in Trolley (2nd digit)
        Uint  Strip;      //RPC strip where the hit occured (last 3 digits)
        Uint  Partition;  //Readout partition along eta segmentation
        float TimeStamp;  //Time stamp of the arrival in TDC

    public:
        RPCHit();
        RPCHit(Uint channel, float time, Infrastructure* Infra);
        RPCHit(const RPCHit& other);
        ~RPCHit();
        RPCHit& operator=(const RPCHit& other);

        Uint  GetChannel();
        Uint  GetTrolley();
        Uint  GetStation();
        Uint  GetStrip();
        Uint  GetPartition();
        float GetTime();
};

typedef vector<RPCHit> HitList;
typedef struct GIFHitList {HitList rpc[NTROLLEYS][NSLOTS][NPARTITIONS];}
 ↪  GIFHitList;

bool SortHitbyStrip(RPCHit h1, RPCHit h2);
bool SortHitbyTime(RPCHit h1, RPCHit h2);
```

4788 *Source Code B.8: Description of C++ object* `RPCHit`*.*

4789
```
struct RAWData{
    int             iEvent;    //Event i
    int             TDCNHits;  //Number of hits in event i
    int             QFlag;     //Quality flag list (1 flag digit per TDC)
    vector<Uint>   *TDCCh;     //List of channels giving hits per event
    vector<float>  *TDCTS;     //List of the corresponding time stamps
};
```

4790 *Source Code B.9: Description of C++ structure* `RAWData`*.*

4791 Each member of the structure in then linked to the corresponding branch of the ROOT data tree,
4792 as shown in the example of Source Code B.10, and using the method `GetEntry(int i)` of the ROOT
4793 class `TTree` will update the state of the members of `RAWData`.
4794 The data is then analysed entry by entry and to each element of the TDC channel list, a `RPCHit` is
4795 constructed by linking each TDC channel to the corresponding RPC channel thanks to the `Mapping`

object. The information carried by the RPC channel format allows to easily retrieve the trolley and slot from which the hit was recorded (see section B.3.2). Using these 2 values, the readout partition can be found by knowing the strip channel and comparing it with the number of partitions and strips per partition stored into the `Infrastructure` object.

```
TTree*  dataTree = (TTree*)dataFile.Get("RAWData");
RAWData data;

dataTree->SetBranchAddress("EventNumber",    &data.iEvent);
dataTree->SetBranchAddress("number_of_hits", &data.TDCNHits);
dataTree->SetBranchAddress("Quality_flag",   &data.QFlag);
dataTree->SetBranchAddress("TDC_channel",    &data.TDCCh);
dataTree->SetBranchAddress("TDC_TimeStamp",  &data.TDCTS);
```

Source Code B.10: Example of link in between RAWData and TTree.

Thus `RPCHit` objects are then stored into 3D dynamical list called `GIFHitList` (Source Code B.8) where the 3 dimensions refer to the 3 layers of the readout in GIF++ : in the bunker there are *trolleys* (`T`) holding detectors in *slots* (`S`) and each detector readout is divided into 1 or more pseudo-rapidity *partitions* (`p`). Using these 3 information allows to assign an address to each readout partition and this address will point to a specific hit list.

B.5.2 Clusters of hits

All the hits contained in the ROOT file have been sorted into the different hit lists through the `GIFHitList`. At this point, it is possible to start looking for clusters. A cluster is a group of adjacent strips getting hits within a time window of 25 ns. These strips are then assumed to be part of the same physical avalanch signal generated by a muon passing through the chamber or by the interaction of a gamma stopping into the electrodes of the RPCs.

To keep the cluster information, `RPCCluster` objects have been defined as shown in Source Code B.11. Using the information of each individual `RPCHit` taken out of the hit list, it stores the cluster size (number of adjacent strips composing the cluster), the first and last hit, the center for spatial reconstruction and finally the start and stop time stamps as well as te time spread in between the first and last hit.

To investigate the hit list of a given detector partition, the function `Clusterization()` definied in `include/Cluster.h` needs the hits in the list to be time sorted. This is achieved by calling function `sort()` of library `<algorithm>` using the comparator `SortHitbyTime(RPCHit h1, RPCHit h2)` defined in `include/RPCHit.h` that returns `true` if the time stamp of hit `h1` is lower than that of `h2`. A first isolation of strips is made only based on time information. All the hits within the 25 ns window are taken separately from the rest. Then, this sub-list of hits is sorted this time by ascending strip number, using this time the comparator `SortHitbyStrip(RPCHit h1, RPCHit h2)`. Finally, the groups of adjacent strips are used to construct `RPCCluster` objects that are then stored in a temporary list of clusters that is at the end of the process used to know how many clusters were reconstructed and to fill their sizes into an histogram that will allows to know the mean size of muon or gamma clusters. This method to group hits together into clusters is limited as no systematic study of the average avalanche time development into TDC hits was performed and that there is no correlation of both spatial and time information to make the first selection of hits. Due to this, two clusters developping consecutively next to each other during a total time longer to 25 ns could be wrongly grouped as a cluster composed of the first developped cluster plus a part of the second cluster while the rest of the second cluster would be placed in a second truncated cluster. This kind of event is not likely but needs to be taken into account nontheless. A possible improvement would be to identify clusters in a 2D space whose dimensions are time and strip. In this 2D space, the cluster could be geometrically identified as isolated groups of adjacent strips recieving a hit at a similar time.

```
class RPCCluster{
    private:
        Uint  ClusterSize;  //Size of cluster #ID
        Uint  FirstStrip;   //First strip of cluster #ID
        Uint  LastStrip;    //Last strip of cluster #ID
        float Center;       //Center of cluster #ID ((first+last)/2)
        float StartStamp;   //Time stamp of the earliest hit of cluster #ID
        float StopStamp;    //Time stamp of the latest hit of cluster #ID
        float TimeSpread;   //Time difference between earliest and latest hits
                            //of cluster #ID
    public:
        RPCCluster();
        RPCCluster(HitList List, Uint cID, Uint cSize, Uint first, Uint firstID);
        RPCCluster(const RPCCluster& other);
        ~RPCCluster();
        RPCCluster& operator=(const RPCCluster& other);

        Uint GetID();
        Uint GetSize();
        Uint GetFirstStrip();
        Uint GetLastStrip();
        float GetCenter();
        float GetStart();
        float GetStop();
        float GetSpread();
};

typedef vector<RPCCluster> ClusterList;

//Other functions to build cluster lists out of hit lists
void BuildClusters(HitList &cluster, ClusterList &clusterList);
void Clusterization(HitList &hits, TH1 *hcSize, TH1 *hcMult);
```

Source Code B.11: Description of C++ object `Cluster`.

B.6 DAQ data Analysis

All the ingredients to analyse GIF++ data have been introduced. This section will focus on the different part of the analysis performed on the data, from determining the type of data the tool is dealing with to calculate the hit and cluster rate per unit area in each detector or reconstructing muon or gamma clusters.

B.6.1 Determination of the run type

In GIF++, both the performance of the detectors in detecting muons in an irradiated environment and the gamma or noise background can be independantly measured. These correspond to different run types and hence, to different TDC settings giving different data to look at.

In the case of performance measurements, the trigger for data taking is provided by the coincidence of several scintillators when muons from the beam passing through the area are detected. Data is collected in a 600 ns wide window centered around the arrival of muons in the RPCs. The expected time distribution of hits is shown in Figure B.1a. The muon peak is clearly visible in the center of the distribution and is to be extracted from the gamma background that composes the flat part of the distribution.

On the other hand, gamma background or noise measurements are focussed on the non muon related physics and the trigger needs to be independant from the muons to give a good measurement of the gamma/noise distribution as seen by the detectors. The trigger is then provided by a pulse generated by the DAQ at a frequency of 100 Hz whose pulse is not likely to be on time with a muon. In order to increase the integrated time without increasing proportionnaly the acquisition time, the width of the acquisition windows are increased to 10 µs. The time distribution of the hits is expected to be flat, as shown by Figure B.1b.

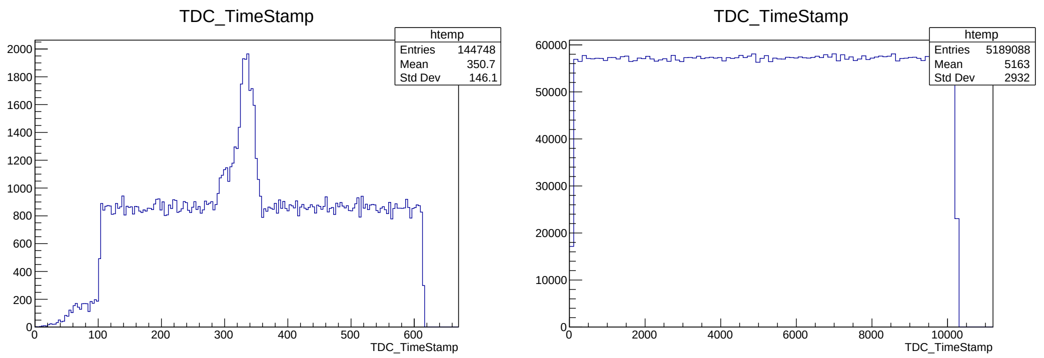

(a) *(b)*

Figure B.1: Example of expected hit time distributions in the cases of efficiency (Figure B.1a) and noise/gamma rate per unit area (Figure B.1b) measurements as extracted from the raw ROOT files. The unit along the x-axis corresponds to ns*. The fact that "the" muon peak is not well defined in Figure B.1a is due to the contribution of all the RPCs being tested at the same time that don't necessarily have the same signal arrival time. Each individual peak can have an offset with the ones of other detectors. The inconsistancy in the first* 100 ns *of both time distributions is an artefact of the TDCs and are systematically rejected during the analysis.*

The ROOT files include a `TTree` called `RunParameters` containing, among other things, the information related to the run type. The run type can then be accessed as described by Source Code B.12 and the function `IsEfficiencyRun()` is then used to determine if the run file is an efficiency run or, on the contrary, another type of run (noise or gamma measurement).

Finally, the data files will have a slightly different content whether it was collected before or after October 2017 and the upgrade of the DAQ software that brought a new information into the ROOT output. This is discussed in Appendix A.4.3 and implies that the analysis will differ a little depending on the data format. Indeed, as no information on the data quality is stored, in older data files, the corrections for missing events has to be done at the end of the analysis. The information about the type of data format is stored in the variable `bool isNewFormat` by checking the list of branches contained in the data tree via the methods `TTree::GetListOfBranches()` and `TCollection::Contains()`.

```
TTree* RunParameters = (TTree*)dataFile.Get("RunParameters");
TString* RunType = new TString();
RunParameters->SetBranchAddress("RunType",&RunType);
RunParameters->GetEntry(0);
```

Source Code B.12: Access to the run type contained in `TTree* RunParameters`.

B.6.2 Beam time window calculation for efficiency runs

Knowing the run type is important first of all to know the width of the acquisition window to be used for the rate calculation and finally to be able to seek for muons. Indeed, the peak that appears in the time distribution for each detectors is then fitted to extract the most probable time window in which the tool should look for muon hits. The data outside of this time window in then used to evaluate the noise or gamma background the detector was subbjected to during the data taking. Computing the position of the peak is done calling the function `SetBeamWindow()` defined in file `src/RPCHit.cc` that loops a first time on the data. The data is first sorted in a 3D array of 1D histograms (`GIFH1Array`, see `include/types.h`). Then the location of the highest bin is determined using `TH1::GetMaximumBin()` and is used to define a window in which a gaussian fit will be applied to compute the peak width. This window is a 80 ns defined by Formula B.1 around the central bin.

$$t_{center}(ns) = bin \times width_{bin}(ns) \tag{B.1a}$$

$$[t_{low}; t_{high}] = [t_{center} - 40; t_{center} + 40] \tag{B.1b}$$

Before the fit is performed, the average number of noise/gamma hits per bin is evaluated using the data outside of the fit window. Excluding the first 100 ns, the average number of hits per bin due to the noise or gamma is defined by Formula B.2 after extracting the amount of hits in the time windows $[100; t_{low}]$ and $[t_{high}; 600]$ thanks to the method `TH1::Integral()`. This average number of hits is then subtracted to every bin of the 1D histogram, in order to *clean* it from the noise or gamma contribution as much as possible to improve the fit quality. Bins where $\langle n_{hits}\rangle$ is greater than the actual bin content are set to 0.

$$\Delta t_{noise}(ns) = 600 \overbrace{-t_{high} + t_{low}}^{-80ns} - 100 = 420ns \tag{B.2a}$$

$$\langle n_{hits}\rangle = width_{bin}(ns) \times \frac{\sum_{t=100}^{t_{low}} + \sum_{t=t_{high}}^{600}}{\Delta t_{noise}(ns)} \tag{B.2b}$$

Finally, the fit parameters are extracted and saved for each detector in 3D arrays of `float` (`muonPeak`, see `include/types.h`), a first one for the mean arrival time of the muons, `PeakTime`, a second for the height or strength of the peak, `PeakHeight`, and a third one for the width of the peak, `PeakWidth`. The width is on purpose chosen to be wider than the peak and defined as 6σ of the gaussian fit, for a peak range being as given by Formula B.3.

$$[t^{peak}_{low}; t^{pean}_{high}] = [t^{peak}_{center} - 3\sigma; t^{peak}_{center} + 3\sigma] \tag{B.3}$$

For a finer analysis, it is advised to determine more precisely the width of the peak to exclude as much noise or background hits os possible. The same settings are applied to every partitions of the same detector. To determine which one of the detector's partitions is directly illuminated by the beam, the peak height of each partition is compared and the highest one is then used to define the peak settings.

It is not possible to identify the particles causing the hits, hence muons, background gamma particles or even noise could be responsible of hits within the time window. To be able to account for this effect, the peak width extracted from the fit on the peak will also be used to define a fake time window, uncorrelated to the muon peak and in which a fake efficiency, contribution from both background and noise, will be measured. This window corresponds to the time range described in Formula B.4.

$$[t_{low}^{fake}; t_{high}^{fake}] = [600 - 6\sigma; 600] \tag{B.4}$$

B.6.3 Data loop and histogram filling

3D arrays of histogram are created to store the data and display it on the DQM of GIF++ webDCS for the use of shifters. The dimensions correspond to the different layers held into the GIF++ infrastructure (trolleys `T` containing RPCs or *slots* `S` each being divided into read-out partitions `p`). These histograms, presented in section B.2.1.1, are filled while looping on the data. Before starting the analysis loop, it is necessary to control the entry quality for the new file formats featuring `QFlag`. If the `QFlag` value for this entry shows that 1 TDC or more have a `CORRUPTED` flag, then this event is discarded. The loss of statistics is low enough to be neglected. `QFlag` is controled using the function `IsCorruptedEvent()` defined in `src/utils.cc`. As explained in Appendix A.4.3, each digit of this integer represent a TDC flag that can be either 1 or 2. Each 2 is the sign of a `CORRUPTED` state. Then, the data is accessed entry by entry in the ROOT `TTree` using `RAWData` and each hit in the hit list is assigned to a detector channel and saved in the corresponding histograms. As described in Source Code B.13, in the first part of the analysis, in which the loop over the ROOT file's content is performed, the different steps are:

1- RPC channel assignment and control: a check is done on the RPC channel extracted thanks to the mapping via the method `Mapping::GetLink()`. If the channel is not initialised and is 0, or if the TDC channel is not contained in a range in between X000 and X127, X being the TDC ID, the hit is discarded. This means there was a problem in the mapping. Often a mapping problem leads to the failure of the offline tool.

2- Creation of a `RPCHit` object: to easily get the trolley, slot and partition in which the hit has been assigned, this object is particularly helpful.

3- General histograms are filled: the hit is filled into the time distribution, global hit distribution and time versus strip histograms, and if the arrival time is within the first 100 ns, it is discarded and nothing else happens and the loop proceeds with the next hit in the list, going back to step 1.

```
for(int h = 0; h < data.TDCCh->size(); h++){
    Uint tdcchannel = data.TDCCh->at(h);
    Uint rpcchannel = RPCChMap->GetLink(tdcchannel);
    float timestamp = data.TDCTS->at(h);
    //Get rid of the hits in channels not considered in the mapping
    if(rpcchannel != NOCHANNELLINK){
        RPCHit hit(rpcchannel, timestamp, GIFInfra);
        Uint T = hit.GetTrolley();
        Uint S = hit.GetStation()-1;
        Uint P = hit.GetPartition()-1;
        //Fill the time and hit profiles
        TimeProfile_H.rpc[T][S][P]->Fill(hit.GetTime());
        HitProfile_H.rpc[T][S][P]->Fill(hit.GetStrip());
        TimeVSChanProfile_H.rpc[T][S][P]->Fill(hit.GetStrip(),hit.GetTime());
        //Reject the 100 first ns due to inhomogeneity of data
        if(hit.GetTime() >= TIMEREJECT){
            Multiplicity.rpc[T][S][P]++;
            if(IsEfficiencyRun(RunType)){
                //Define peak time range for efficiency calculation
                float lowlimit_eff = PeakTime.rpc[T][S][P]
                                   - PeakWidth.rpc[T][S][P];
                float highlimit_eff = PeakTime.rpc[T][S][P]
                                    + PeakWidth.rpc[T][S][P];
                bool peakrange = (hit.GetTime() >= lowlimit_eff
                               && hit.GetTime() < highlimit_eff);
                //Fill hits inside of the defined peak and noise range
                if(peakrange){
                    BeamProfile_H.rpc[T][S][P]->Fill(hit.GetStrip());
                    PeakHitList.rpc[T][S][P].push_back(hit);
                } else {
                    StripNoiseProfile_H.rpc[T][S][P]->Fill(hit.GetStrip());
                    NoiseHitList.rpc[T][S][P].push_back(hit);
                }
                //Then define time range for fake efficiency
                float highlimit_fake = BMTDCWINDOW;
                float lowlimit_fake = highlimit_fake
                                   - (highlimit_eff-lowlimit_eff);
                bool fakerange = (hit.GetTime() >= lowlimit_fake
                               && hit.GetTime() < highlimit_fake);
                //Fill the hits inside of the fake window
                if(fakerange){
                    FakeHitList.rpc[T][S][P].push_back(hit);
                }
            } else {
                //Fill the hits inside of the defined noise range
                StripNoiseProfile_H.rpc[T][S][P]->Fill(hit.GetStrip());
                NoiseHitList.rpc[T][S][P].push_back(hit);
            }
        }
    }
}
```

Source Code B.13: For each entry of the raw ROOT data file, the code loops over the list of channels and corresponding time stamps contained in branches `TDC_channel` *and* `TDC_TimeStamp` *and constructs* `RPCHit` *objects that are filled in the peak, noise and fake hit lists and also fills the time, hit, beam and noise profiles.*

4- Multiplicity counter: the hit multiplicity counter of the corresponding detectors is incremented.

5-a-1 *Effiency runs* - Is the hit within the peak window? : if the hit is contained in the peak window previously defined by Formula B.3, it is filled into the beam hit profile histogram of the corresponding chamber, added into the list of peak hits and increments the counter of *in time* hits. The term *in time* here refers to the hits that are likely to be muons by arriving in the expected time window. If the hit is outside of the peak window, it is filled into the noise profile histogram of the corresponding detector, added into the list of noise/gamma hits and increments the counter of noise/gamma hits.

5-a-2 *Effiency runs* - Is the hit within the fake window? : if the hit is contained in the fake window previously defined by Formula B.4, it is added into the list of fake hits. Counting the fake hits outside the peak window allows to estimate the probability to detect in time background or noise.

5-b- *Noise/gamma rate runs* - Noise histograms are filled: the hit is filled into the noise profile histogram of the corresponding detector, added into the list of noise/gamma hits and increments the counter of noise/gamma hits.

```
for(Uint tr = 0; tr < GIFInfra->GetNTrolleys(); tr++){
    Uint T = GIFInfra->GetTrolleyID(tr);
    for(Uint sl = 0; sl < GIFInfra->GetNSlots(tr); sl++){
        Uint S = GIFInfra->GetSlotID(tr,sl) - 1;
        Uint  nStripsPart   = GIFInfra->GetNStrips(tr,sl);
        string rpcID = GIFInfra->GetName(tr,sl);
        for (Uint p = 0; p < GIFInfra->GetNPartitions(tr,sl); p++){
            //Clusterize noise/gamma data
            sort(NoiseHitList.rpc[T][S][p].begin(),
                 NoiseHitList.rpc[T][S][p].end(),SortHitbyTime);
            Clusterization(NoiseHitList.rpc[T][S][p],
                           NoiseCSize_H.rpc[T][S][p],NoiseCMult_H.rpc[T][S][p]);
            //Clusterize muon data and fill efficiency histograms based on
            //the content of peak and fake hit vectors if efficiency run
            if(IsEfficiencyRun(RunType)){
                //Peak data
                sort(PeakHitList.rpc[T][S][p].begin(),
                     PeakHitList.rpc[T][S][p].end(),SortHitbyTime);
                Clusterization(PeakHitList.rpc[T][S][p],
                           PeakCSize_H.rpc[T][S][p],PeakCMult_H.rpc[T][S][p]);
                if(PeakHitList.rpc[T][S][p].size() > 0)
                    EfficiencyPeak_H.rpc[T][S][p]->Fill(DETECTED);
                else EfficiencyPeak_H.rpc[T][S][p]->Fill(MISSED);

                //Fake data
                if(FakeHitList.rpc[T][S][p].size() > 0)
                    EfficiencyFake_H.rpc[T][S][p]->Fill(DETECTED);
                else EfficiencyFake_H.rpc[T][S][p]->Fill(MISSED);
            }
            //Save and reinitialise the hit multiplicity
            HitMultiplicity_H.rpc[T][S][p]->Fill(Multiplicity.rpc[T][S][p]);
            Multiplicity.rpc[T][S][p] = 0;
        }
    }
}
```

Source Code B.14: Loops to clusterize the hit lists and fill efficiency and multiplicity histograms.

After the loop on the hit list of the entry is over, the next step is too clusterize the 3D lists filled in the previous steps, as displayed in Source Code B.14. A 3D loop is then started over the active trolley, slot and RPC partitions to access these objects. Each `NoiseHitList` and `PeakHitList`, in case of efficiency run, are clusterized as decribed in section B.5.2. There corresponding cluster size and multiplicity histograms are filled at the end of the clustering process.

Then, the peak and fake effiency histograms are filled in case of efficiency run. The selection is simply made by checking whether the RPC detected signals in the peak window or/and fake window during this event. In the case a hit is recorded in either of both time windows, the histogram is filled with 1. On the contrary, the histogram is filled with 0. Finally, it is useful to remind that at this level, it is not possible yet to discriminate in between a muon hit and noise or gamma hit. the histograms `PeakCSize_H`, `PeakCMult_H` and `EfficiencyPeak_H` are then subjected to noise and background contamination. This contamination is estimated thanks to the fake efficiency histogram `EfficiencyFake_H` and corrected at the moment the results will be written into output CSV files and the histograms `MuonCSize_H`, `MuonCMult_H` and `Efficiency0_H` will be filled. The correction will be explained in Section B.6.4.3.

Finally, the loop ends on the filling of the general hit multiplicity histogram of each detector partitions.

B.6.4 Results calculation

As mentioned in section B.2.1, the analysis of DAQ data provides the user with 3 CSV files and a ROOT file associated to each and every ROOT data file. The fourth CSV file is provided by the extraction of the CEAN main frame data monitored during data tacking and will be discussed later. After looping on the data in the previous part of the analysis macro, the output files are created and a 3D loop on each RPC readout partitions is started to extract the histograms parameters and compute the final results.

B.6.4.1 Rate normalisation

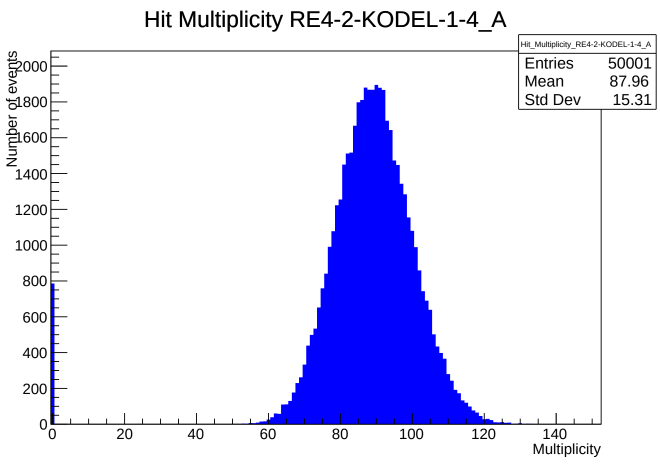

Figure B.2: The effect of the quality flag is explained by presenting the reconstructed hit multiplicity of a data file without `Quality_flag`. The artificial high content of bin 0 is the effect of corrupted data.

The hit rate normalization corresponds to translating a number of hits recorded during the full duration of data taking into a rate per unit area value. In order to achieve such result, it is first needed to know the total integrated time and the active area of the read-out partition on which the hits are counted. The total integrated is simply the noise window used for each event multiplied by the total number of events stored in the data file.

Nevertheless, to analyse old data format files, not containing any quality flag, it is needed to estimate the amount of corrupted data via a fit as the corrupted data will always fill events with a fake ”0 multiplicity”. Indeed, as no hits were stored in the DAQ ROOT files, these events artificially contribute to fill the bin corresponding to a null multiplicity, as shown in Figure B.2. In the case the mean of the hit multiplicity distribution is high, the contribution of the corrupted data can easily be evaluated for later correction by comparing the level of the bin at multiplicity 0 and of a skew fit curve that should indicate a value consistent with 0. A skew fit has been chosen over a Poisson fit as it was giving better results for lower mean multiplicity values. Nevertheless, for low irradiation cases, as explained in Appendix A.4.3, the hit multiplicity distribution mean is, on the contrary, rather small and the probability to record events without hits can't be considered small anymore, leading to a difficult and non-reliable estimation of the corruption.

```
if(!isNewFormat){
    TF1* GaussFit = new TF1("gaussfit","[0]*exp(-0.5*((x-[1])/[2])**2)",0,Xmax);
    GaussFit->SetParameter(0,100);
    GaussFit->SetParameter(1,10);
    GaussFit->SetParameter(2,1);
    HitMultiplicity_H.rpc[T][S][p]->Fit(GaussFit,"LIQR","",0.5,Xmax);

    TF1* SkewFit = new TF1("skewfit","[0]*exp(-0.5*((x-[1])/[2])**2) / (1 +
 ↪  exp(-[3]*(x-[4])))",0,Xmax);
    SkewFit->SetParameter(0,GaussFit->GetParameter(0));
    SkewFit->SetParameter(1,GaussFit->GetParameter(1));
    SkewFit->SetParameter(2,GaussFit->GetParameter(2));
    SkewFit->SetParameter(3,1);
    SkewFit->SetParameter(4,1);
    HitMultiplicity_H.rpc[T][S][p]->Fit(SkewFit,"LIQR","",0.5,Xmax);

    double fitValue = SkewFit->Eval(1,0,0,0);
    double dataValue = (double)HitMultiplicity_H.rpc[T][S][p]->GetBinContent(2);
    double difference = TMath::Abs(dataValue - fitValue);
    double fitTOdataVSentries_ratio = difference / (double)nEntries;
    bool isFitGOOD = fitTOdataVSentries_ratio < 0.01;
    double nSinglehit = (double)HitMultiplicity_H.rpc[T][S][p]->GetBinContent(1);
    double lowMultRatio = nSinglehit / (double)nEntries;
    bool isMultLOW = lowMultRatio > 0.4;
    if(isFitGOOD && !isMultLOW){
        nEmptyEvent = HitMultiplicity_H.rpc[T][S][p]->GetBinContent(1);
        nPhysics = (int)SkewFit->Eval(0,0,0,0);
        if(nPhysics < nEmptyEvent)
        nEmptyEvent = nEmptyEvent-nPhysics;
    }
}
double corrupt_ratio = 100.*(double)nEmptyEvent / (double)nEntries;
outputCorrCSV << corrupt_ratio << '\t';
float rate_norm = 0.;
float stripArea = GIFInfra->GetStripGeo(tr,sl,p);

if(IsEfficiencyRun(RunType)){
    float noiseWindow = BMTDCWINDOW - TIMEREJECT - 2*PeakWidth.rpc[T][S][p];
    rate_norm = (nEntries-nEmptyEvent)*noiseWindow*1e-9*stripArea;
} else
    rate_norm = (nEntries-nEmptyEvent)*RDMNOISEWDW*1e-9*stripArea;
```

Source Code B.15: Definition of the rate normalisation variable. It takes into account the number of non corrupted entries and the time window used for noise and background calculation, to estimate the total integrated time, and the strip active area to express the result as rate per unit area.

As can be seen in Source Code B.15, conditions have been applied to prevent bad fits and wrong corruption estimation in cases where :

- The difference in between the data for multiplicity 1 and the corresponding fit value should be lower than 1% of the total amount of data : $\frac{|n_{m=1}-sk(1)|}{N_{tot}} < 0.01$ where $n_{m=1}$ is the number of entries with multiplicity 1, $sk(1)$ the value of the skew fit, as defined by Formula 5.2, for multiplicity 1 and N_{tot} the total number of entries.

- The amount of data contained in the multiplicity 0 bin should not exceed 40% of the total data content: $\frac{n_{m=0}}{N_{tot}} \leq 0.4$ where $n_{m=0}$ is the number of entries with multiplicity 0. This number has been determined to be the maximum to be able to separate the excess of data due to corruption from the hit multiplicity distribution.

Those 2 conditions need to be fulfilled to estimate the corruption of old data format files. If the fit was successful, the level of corruption is written in `Offline-Corrupted.csv` and the number of corrupted entries, refered as the integer `nEmptyEvent`, is subtracted from the total number of entries when the rate normalisation factor is computed as explicited in Source Code B.15. Note that for new data format files, the number of corrupted entries being set to 0, the definition of `rate_norm` stays valid.

B.6.4.2 Rate and activity

```
int nNoise = StripNoiseProfile_H.rpc[T][S][p]->GetEntries();
float averageNhit = (nNoise>0) ? (float)(nNoise/nStripsPart) : 1.;

for(Uint st = 1; st <= nStripsPart; st++){
    float stripRate =
        StripNoiseProfile_H.rpc[T][S][p]->GetBinContent(st)/rate_norm;
    float stripAct =
        StripNoiseProfile_H.rpc[T][S][p]->GetBinContent(st)/averageNhit;

    StripNoiseProfile_H.rpc[T][S][p]->SetBinContent(st,stripRate);
    StripActivity_H.rpc[T][S][p]->SetBinContent(st,stripAct);
}
```

Source Code B.16: Description of the loop that allows to set the content of each strip rate and strip activity channel for each detector partition.

At this point, the strip rate histograms, `StripNoiseProfile_H.rpc[T][S][p]`, only contain an information about the total number of noise or background rate hits each channel received during the data taking. As described in Source Code B.16, a loop on the strip channels will be used to normalise the content of the rate distribution histogram for each detector partitions. The initial number of hits recorded for a given bin will be extracted and 2 values are computed.

- The strip hit rate, defined as the number of hits recorded in the bin normalised like described in the previous section, using the variable `rate_norm` and the corresponding bin in histogram `StripNoiseProfile_H.rpc[T][S][p]` is updated, and

- the strip activity, defined as the number of hits recorded in the bin normalised to the average number of hits per bin contained in the partition histogram, using the variable `averageNhit`. This value provides an information on the homogeneity of the detector response to the gamma background or of the detector noise. An activity of 1 corresponds to an average response. Above 1, the channel is more active than the average and bellow 1, the channel is less active. This value is filled in the histograms `StripActivity_H.rpc[T][S][p]`.

On each detector partitions, which are read-out by a single FEE, all the channels are not processed by the same chip. Each chip can give a different noise response and hence, histograms using a chip binning are used to investigate chip related noise behaviours. The average values of the strip rate or activity grouped into a given chip are extracted using the using the function `GetChipBin()` and stored in dedicated histograms as described in Source Codes B.17 and B.18 respectively.

```
float GetChipBin(TH1* H, Uint chip){
    Uint start = 1 + chip*NSTRIPSCHIP;
    int nActive = NSTRIPSCHIP;
    float mean = 0.;

    for(Uint b = start; b <= (chip+1)*NSTRIPSCHIP; b++){
        float value = H->GetBinContent(b);
        mean += value;
        if(value == 0.) nActive--;
    }

    if(nActive != 0) mean /= (float)nActive;
    else mean = 0.;

    return mean;
}
```

Source Code B.17: Function used to compute the content of a bin for an histogram using chip binning.

```
for(Uint ch = 0; ch < (nStripsPart/NSTRIPSCHIP); ch++){
    ChipMeanNoiseProf_H.rpc[T][S][p]->
        SetBinContent(ch+1,GetChipBin(StripNoiseProfile_H.rpc[T][S][p],ch));
    ChipActivity_H.rpc[T][S][p]->
        SetBinContent(ch+1,GetChipBin(StripActivity_H.rpc[T][S][p],ch));
}
```

Source Code B.18: Description of the loop that allows to set the content of each chip rate and chip activity bins for each detector partition knowing the information contained in the corresponding strip distribution histograms.

The activity variable is then used to evaluate the homogeneity of the detector response to background or of the detector noise. The homogeneity h_p of each detector partition can be evaluated using the formula $h_p = exp(-\sigma_p^R/\langle R\rangle_p)$, where $\langle R\rangle_p$ is the partition mean rate and σ_p^R is the rate standard deviation calculated over the partition channels. The more homogeneously the rates are distributed and the smaller will σ_p^R be, and the closer to 1 will h_p get. On the contrary, if the standard deviation of the channel's rates is large, h_p will rapidly get to 0. This value is saved into histograms as shown in Source Code B.19 and could in the future be used to monitor through time, once extracted, the evolution of every partition homogeneity. This could be of great help to understand the apparition of eventual hot spots due to ageing of the chambers subjected to high radiation levels. The monitored homogeneity information could then be combined with a monitoring of the activity of each individual channel in order to have a finer information. Monitoring tools have been suggested and need to be developped for this purpose.

```
float MeanPartSDev = GetTH1StdDev(StripNoiseProfile_H.rpc[T][S][p]);
float strip_homog = (MeanPartRate==0)
    ? 0.
    : exp(-MeanPartSDev/MeanPartRate);
StripHomogeneity_H.rpc[T][S][p]->Fill("exp -#left(#frac{#sigma_{Strip Rate}}{#mu_{Strip Rate}}#right)",strip_homog);
StripHomogeneity_H.rpc[T][S][p]->GetYaxis()->SetRangeUser(0.,1.);

float ChipStDevMean = GetTH1StdDev(ChipMeanNoiseProf_H.rpc[T][S][p]);
float chip_homog = (MeanPartRate==0)
    ? 0.
    : exp(-ChipStDevMean/MeanPartRate);
ChipHomogeneity_H.rpc[T][S][p]->Fill("exp -#left(#frac{#sigma_{Chip Rate}}{#mu_{Chip Rate}}#right)",chip_homog);
ChipHomogeneity_H.rpc[T][S][p]->GetYaxis()->SetRangeUser(0.,1.);
```

Source Code B.19: Storage of the homogeneity into dedicated histograms.

B.6.4.3 Correction of muon performance parameters

By previously filling the peak and fake efficiency histograms as well as the peak and noise cluster size and cluster multiplicity it is possible to compute the efficiency of muon detection, the muon cluster size, as well as the muon cluster multiplicity. This calculation is based on independant event probabilities. The independant events that can be measured in the data are, "μ: A muon was detected" and "γ: noise or background was detected". It is trivial to realize that the data in the peak window corresponds to the intersection of both events, "$\mu \cup \gamma$: a muon or noise or background was detected". This way, the efficiency measured in the peak window is actually the probability of the event $\mu \cup \gamma$ while the efficiency in the fake window is then the probability of the event γ alone. Assuming that μ and γ are indenpendant, the probability or their intersection can be written as in Formula B.5.

$$P(\mu \cup \gamma) = P(\mu) + P(\gamma) - P(\mu)P(\gamma) \tag{B.5}$$

Isolating the probability of the event μ alone, actually corresponding to the muon detection efficiency, can be then calculated with the quantities that are contained in the peak and fake histogram as in Formula B.6.

$$P(\mu) = \frac{P(\mu \cup \gamma) - P(\gamma)}{1 - P(\gamma)} \quad \Leftrightarrow \quad \epsilon_\mu = \frac{\epsilon_{peak} - \epsilon_{fake}}{1 - \epsilon_{fake}} \tag{B.6}$$

When it comes to the computation of the muon cluster size, a similar reasoning than for the muon detection efficiency computation can be used. Indeed, using Formula B.5, out of the total number of events where a muon or noise or background can be expressed as a sum of fractions of events μ, γ and $\mu \cap \gamma$, the later being the event corresponding to the detection of both events simultaneously, as showed in Formula B.7. The fractions can be expressed as a ratio of the probabilities already known, using this time the notation $P(\mu \cap \gamma)$ instead of $P(\mu)P(\gamma)$. This choice was made to make the code a little clearer.

$$1 = F_\mu + F_\gamma + F_{\mu\cap\gamma} = \frac{P(\mu) - P(\mu \cap \gamma)}{P(\mu \cup \gamma)} + \frac{P(\gamma) - P(\mu \cap \gamma)}{P(\mu \cup \gamma)} + \frac{P(\mu \cap \gamma)}{P(\mu \cup \gamma)} \tag{B.7}$$

```
if(IsEfficiencyRun(RunType)){
    //Evaluate the probabilities for each detection case with errors
    float P_peak = EfficiencyPeak_H.rpc[T][S][p]->GetMean();
    float P_fake = EfficiencyFake_H.rpc[T][S][p]->GetMean();
    float P_muon = (P_peak-P_fake)/(1-P_fake);
    float P_both = P_muon*P_fake;
    float P_peak_err = sqrt(P_peak*(1.-P_peak)/nEntries);
    float P_fake_err = sqrt(P_fake*(1.-P_fake)/nEntries);
    float P_muon_err = sqrt(P_muon*(1.-P_muon)/nEntries);
    float P_both_err = sqrt(P_both*(1.-P_both)/nEntries);
    Efficiency0_H.rpc[T][S][p]->Fill("muon efficiency",P_muon);
    Efficiency0_H.rpc[T][S][p]->Fill("muon efficiency error",P_muon_err);

    //For each case get the fractionof events it represents
    float F_both = P_both/P_peak;
    float F_muon = (P_muon-P_both)/P_peak;
    float F_fake = (P_fake-P_both)/P_peak;
    float F_both_err = F_both*(P_both_err/P_both+P_peak_err/P_peak);
    float F_muon_err = (P_muon_err+F_both_err+F_muon*P_peak_err)/P_peak;
    float F_fake_err = (P_fake_err+F_both_err+F_fake*P_peak_err)/P_peak;
    //Get the measured cluster sizes correcting using the fractions
    float CS_peak = PeakCSize_H.rpc[T][S][p]->GetMean();
    float CS_fake = NoiseCSize_H.rpc[T][S][p]->GetMean();
    float CS_peak_err = 2*PeakCSize_H.rpc[T][S][p]->GetStdDev()
                        /sqrt(PeakCSize_H.rpc[T][S][p]->GetEntries());
    float CS_fake_err = 2*NoiseCSize_H.rpc[T][S][p]->GetStdDev()
                        /sqrt(NoiseCSize_H.rpc[T][S][p]->GetEntries());
    float CS_muon = (CS_peak-CS_fake*(F_fake+F_both/2.))/(F_muon+F_both/2.);
    float CS_muon_err = (CS_peak_err
                         +(F_fake+F_both/2.)*CS_fake_err
                         +CS_muon*F_muon_err
                         +CS_fake*(F_fake_err+F_both_err/2.))
                        /(F_muon+F_both/2.);
    MuonCSize_H.rpc[T][S][p]->Fill("muon cluster size",CS_muon);
    MuonCSize_H.rpc[T][S][p]->Fill("muon cluster size error",CS_muon_err);

    //Finally get the muon cluster multiplicity as peak-fake
    float noiseWindow = BMTDCWINDOW - TIMEREJECT - 2*PeakWidth.rpc[T][S][p];
    float peakWindow = 2*PeakWidth.rpc[T][S][p];
    float CM_peak = PeakCMult_H.rpc[T][S][p]->GetMean();
    float CM_fake = NoiseCMult_H.rpc[T][S][p]->GetMean()*peakWindow/noiseWindow;
    float CM_muon = CM_peak-CM_fake;
    float CM_peak_err = 2*PeakCMult_H.rpc[T][S][p]->GetStdDev()
                        /sqrt(PeakCMult_H.rpc[T][S][p]->GetEntries());
    float CM_fake_err = 2*NoiseCMult_H.rpc[T][S][p]->GetStdDev()
                        /sqrt(NoiseCMult_H.rpc[T][S][p]->GetEntries())
                        * peakWindow/noiseWindow;
    float CM_muon_err = CM_peak_err + CM_fake_err;
    MuonCMult_H.rpc[T][S][p]->Fill("muon cluster multiplicity",CM_muon);
    MuonCMult_H.rpc[T][S][p]->Fill("muon cluster multiplicity
 ↪  error",CM_muon_err);

    //Write in the output CSV file
    outputEffCSV << P_muon << '\t' << P_muon_err << '\t'
                 << CS_muon << '\t' << CS_muon_err << '\t'
                 << CM_peak << '\t' << CM_peak_err << '\t';
}
```

Source Code B.20: Analysis algorithm to compute muon efficiency, cluster size and multiplicity knowing the peak and fake efficiency, cluster size and multiplicity.

Each ones of these events have an associated cluster size. The cluster size of the noise or background already is measured thanks to the clusterization of the noise hit list. In the same way, the peak cluster size corresponds to the cluster measured for the event $\mu \cup \gamma$. Nevertheless, the cluster of the event $\mu \cap \gamma$ is not known but it can be assumed that the probability of having more than 1 noise or background cluster contained in the peak window is very low if the peak wondow duration is compared to the background rate that rarely seen to go beyond $2000\,\mathrm{Hz/cm^2}$ **[to be confirmed]**. Hence, the cluster size that is likely to be measured in such kind of event where both a muon and a background or noise cluster was recorded is the average of the muon cluster size and the background cluster size. The cluster size $C_{\mu\cup\gamma}$ probed in the peak can then be written as in Formula B.8 and leads to the expression for the muon cluster size C_μ written in Formula B.9.

$$C_{\mu\cup\gamma} = C_\mu F_\mu + C_\gamma F_\gamma + \frac{C_\mu + C_\gamma}{2} \times F_{\mu\cap\gamma} \tag{B.8}$$

$$C_\mu = \frac{C_{\mu\cup\gamma} - C_\gamma \times (F_\gamma + F_{\mu\cap\gamma}/2)}{F_\mu + F_{\mu\cap\gamma}/2} \tag{B.9}$$

Finally, the computation of the muon cluster multiplicity comes quite naturally as the cluster multiplicity measured in the peak to which is subtracted the background cluster multiplpicity taken in a window of similar width. These calculations, as well as the error propagation that was not explicited here, can be seen going through Source Code B.20.

B.6.4.4 Strip masking tool

The offline tool is automatically called at the end of each data taking to analyse the data and offer the shifter DQM histograms to control the data quality. After the histograms have been published online in the DQM page, the shifter can decide to mask noisy or dead channels that will contribute to bias the final rate calculation by editing the mask column of `ChannelsMapping.csv` as can be seen in Figure B.3.

From the code point of view, the function `GetTH1Mean()` is used to retrieve the mean rate partition by partition after the rates have been calculated strip by strip and filled into the histograms `StripNoiseProfile_H.rpc[T][S][p]`, as described through Source Code B.21.

Once the mask for each rejected channel has been updated, the shifter can manually run the offline tool again to update the DQM plots, now including the masked strips, as well the rate results written in the output CSV file `Offline-Rate.csv`. If not done during the shifts, the strip masking procedure needs to be carefully done by the person in charge of data analysis on the scans that were selected to produce the final results.

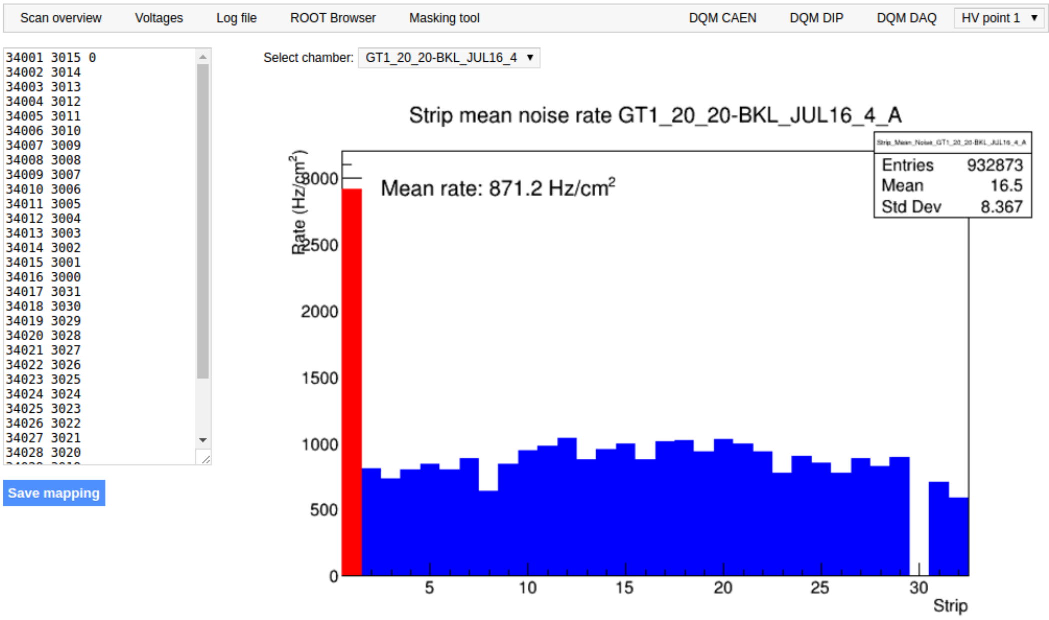

Figure B.3: Display of the maskting tool page on the webDCS. The window on the left allows the shifter to edit `ChannelsMapping.csv`. To mask a channel, it only is needed to set the 3rd field corresponding to the strip to mask to 0. It is not necessary for older mapping file formats to add a 1 for each strip that is not masked as the code is versatile and the default behaviour is to consider missing mask fields as active strips. The effect of the mask is directly visible for noisy channels as the corresponding bin turns red. The global effect of masking strips will be an update of the rate value showed on the histogram that will take into consideration the rejected channels.

```
float GetTH1Mean(TH1* H){
    int nBins = H->GetNbinsX();
    int nActive = nBins;
    float mean = 0.;

    for(int b = 1; b <= nBins; b++){
        float value = H->GetBinContent(b);
        mean += value;
        if(value == 0.) nActive--;
    }

    if(nActive != 0) mean /= (float)nActive;
    else mean = 0.;

    return mean;
}
```

Source Code B.21: The function `GetTH1Mean()` is used to return the mean along the y-axis of `TH1` histograms containing rate information. In order to take into account masked strips whose rate is set to 0, the function looks for masked channels and decrement the number of active channels for each null value found.

B.6.4.5 Output CSV files filling

```
for (Uint tr = 0; tr < GIFInfra->GetNTrolleys(); tr++){
    Uint T = GIFInfra->GetTrolleyID(tr);
    for (Uint sl = 0; sl < GIFInfra->GetNSlots(tr); sl++){
        Uint S = GIFInfra->GetSlotID(tr,sl) - 1;
        float MeanNoiseRate = 0.;
        float ClusterRate   = 0.;
        float ClusterSDev   = 0.;

        for (Uint p = 0; p < GIFInfra->GetNPartitions(tr,sl); p++){
            float MeanPartRate = GetTH1Mean(StripNoiseProfile_H.rpc[T][S][p]);
            float cSizePart = NoiseCSize_H.rpc[T][S][p]->GetMean();
            float cSizePartErr = (NoiseCSize_H.rpc[T][S][p]->GetEntries()==0)
                ? 0.
                : 2*NoiseCSize_H.rpc[T][S][p]->GetStdDev() /
                            sqrt(NoiseCSize_H.rpc[T][S][p]->GetEntries());
            float cMultPart = NoiseCMult_H.rpc[T][S][p]->GetMean();
            float cMultPartErr = (NoiseCMult_H.rpc[T][S][p]->GetEntries()==0)
                ? 0.
                : 2*NoiseCMult_H.rpc[T][S][p]->GetStdDev() /
                            sqrt(NoiseCMult_H.rpc[T][S][p]->GetEntries());
            float ClustPartRate = (cSizePart==0) ? 0.
                : MeanPartRate/cSizePart;
            float ClustPartRateErr = (cSizePart==0) ? 0.
                : ClustPartRate * cSizePartErr/cSizePart;

            outputRateCSV << MeanPartRate << '\t'
                << cSizePart << '\t' << cSizePartErr << '\t'
                << cMultPart << '\t' << cMultPartErr << '\t'
                << ClustPartRate << '\t' << ClustPartRateErr << '\t';

            RPCarea       += stripArea * nStripsPart;
            MeanNoiseRate += MeanPartRate * stripArea * nStripsPart;
            ClusterRate   += ClustPartRate * stripArea * nStripsPart;
            ClusterSDev   += (cSizePart==0)
                ? 0.
                : ClusterRate*cSizePartErr/cSizePart;
        }
        MeanNoiseRate /= RPCarea;
        ClusterRate   /= RPCarea;
        ClusterSDev   /= RPCarea;
        outputRateCSV << MeanNoiseRate << '\t' << ClusterRate << '\t'
                      << ClusterSDev << '\t';
    }
}
```

Source Code B.22: Description of rate result calculation and writing into the CSV output `Offline-Rate.csv`*. Are saved into the file for each detector, the mean partition rate, cluster size and cluster mutiplicity, along with their errors, for each partition and as well as a detector average.*

All the histograms have been filled. Parameters will then be extracted from them to compute the final results that will later be used to produce plots. Once the results have been computed, the very last step of the offline macro is to write these values into the corresponding CSV outputs. Aside of the file `Offline-Corrupted.csv`, 2 CSV files are being written by the macro `OfflineAnalysis()`, `Offline-Rates.csv` and `Offline-L0-EffCl.csv` that respectively contain information about noise or gamma rates, cluster size and multiplicity, and about level 0 reconstruction of the detector efficiency, muon cluster size and multiplicity. Details on the computation and file writing are respectively given in Sources Codes B.22 and B.20.

Noise/gamma background variables are computed and written in the output file for each detector partitions. A detector average of the hit and cluster rate is also provided, as shown through Sources Code B.22. The variables that are written for each partition are:

- The mean partition hit rate per unit area, `MeanPartRate`, that is extracted from the histogram `StripNoiseProfile_H` as the mean value along the y-axis, as described in section B.6.4.4. No error is recorded for the hit rate as this is considered a single measurement. No statistical error can be associated to it and the systematics are unknown.

- The mean cluster size, `cSizePart`, is extracted from the histogram `NoiseCSize_H` and it's statistical error, `cSizePartErr`, is taken to be 2σ of the total distribution.

- The mean cluster multiplicity per trigger, `cMultPart`, is extracted from the histogram `NoiseCMult_H` and it's statistical error, `cMultPartErr`, is taken to be 2σ of the total distribution. It is important to point to the fact that this variable gives an information that is dependent on the buffer window width used for each trigger for the calculation.

- The mean cluster rate per unit area, `ClustPartRate`, is defined as the mean hit rate normalised to the mean cluster size and it's statistical error, `ClustPartRateErr`, is then obtained using the relative statistical error on the mean cluster size.

Muon performance variables are computed as discussed in the Section B.6.4.3 and written in the output file for each detector partitions as shown through Sources Code B.20. It is reminded that this offline tool doesn't include any tracking algorithm to identify muons from the beam and only relies on the hits arriving in the time window corresponding to the beam time and is corrected thanks to the estimation of the contribution of the background and noise to the efficiency of the detector. Assuming that the detection of background and muons were independent events, a probabilistic approach was then used to correct efficiency, muon cluster size and muon cluster multiplicity. The variables that are written for each partition are:

- The muon efficiency, referred to as the probability to detect a muon in the peak window `P_muon`, also filled in histogram `Efficiency0_H`. The statistical error related to the efficiency, `P_muon_err`, is computed using a binomial distribution, as the efficiency measures the probability of "success" and "failure" to detect muons.

- The mean muon cluster size, `CS_muon`, and its related statistical error, `CS_muon_err`, also filled in the histogram `MuonCSize_H`.

- The mean muon cluster multiplicity, `CM_muon`, and its related statistical error, `CM_muon_err`, also filled in the histogram `MuonCMult_H`.

In addition to these 2 CSV files, the histograms are saved in ROOT file `Scan00XXXX_HVY_Offline.root` as explained in section B.2.1.1.

B.7 Current information extraction

Detectors under test at GIF++ are connected both to a CAEN HV power supply and to a CAEN ADC that reads the currents inside of the RPC gaps bypassing the supply cable. During data taking, the webDCS records into a ROOT file called `Scan00XXXX_HVY_CAEN.root` histograms with the monitored parameters of both CAEN devices. Are recorded for each RPC channels (in most cases, a channel corresponds to an RPC gap):

- the effective voltage, HV_{eff}, set by the webDCS using the PT correction on the CAEN power supply,
- the applied voltage, HV_{app}, monitored by the CAEN power supply, and the statistical error related to the variations of this value through time to follow the variation of the environmental parameters defined as the RMS of the histogram divided by the square root of the number of recorded points,
- the monitored current, I_{mon}, monitored by the CAEN power supply, and the statistical error related to the variations of this value through time to follow the variation of the environmental parameters defined as the RMS of the histogram divided by the square root of the number of recorded points,
- the corresponding current density, J_{mon}, defined as the monitored current per unit area, $J_{mon} = I_{mon}/A$, where A is the active area of the corresponding gap,
- the ADC current, I_{ADC}, recorded through the CAEN ADC module that monitors the dark current in the gap itself. First of all, the resolution of such a module is better than that of CAEN power supplies and moreover, the current is not read-out through the HV supply line but directly at the chamber level giving the real current inside of the detector. The statistical error is defined as the RMS of the histogram distribution divided by the square root of the number of recorded points.

Once extracted through a loop over the element of GIF++ infrastructure via the C++ macro `GetCurrent()`, these parameters, organised in 9 columns per detector HV supply line, are written in the output CSV file `Offline-Current.csv`. The macro can be found in the file `Current.cc`.

References

[1] K. Ruedenberg and W.H.E. Schwarz. "Three Millennia of Atoms and Molecules". In: *Pioneers of Quantum Chemistry*. Ed. by E. Thomas Strom and Angela K. Wilson. Vol. 1122. ACS Symposium Series, 2013, pp. 1–45.

[2] A. Lavoisier. *Traité élémentaire de chimie*. Éditions la Bibliothèque Digitale, 2014 (first published 1789).

[3] J. Dalton. *A New System of Chemical Philosophy*. William Dawson and Sons, 1808.

[4] J. von Fraunhofer. "Bestimmung des Brechungs- und des Farben-Zerstreuungs - Vermögens verschiedener Glasarten, in Bezug auf die Vervollkommnung achromatischer Fernröhre". In: *Denkschriften der Königlichen Akademie der Wissenschaften zu München*. Die Akademie, 1817, pp. 193–226.

[5] J.J. Thomson. "XL. Cathode Rays". In: *The London, Edinburgh, and Dublin Philosophical Magazine and Journal of Science* 44:269 (1897), pp. 293–316.

[6] J.B. Perrin. "Nouvelles propriétés des rayons cathodiques". In: *Comptes Rendus Hebdomadaires des Séances de L'Académie des Sciences*. Vol. 121. Académie des Sciences, 1895, pp. 1130–1134.

[7] H. Becquerel. "Déviation du rayonnement du radium dans un champ électrique". In: *Comptes Rendus Hebdomadaires des Séances de L'Académie des Sciences*. Vol. 130. Académie des Sciences, 1900, p. 809.

[8] J.J. Thomson. "XXIV. On the structure of the atom: an investigation of the stability and periods of oscillation of a number of corpuscles arranged at equal intervals around the circumference of a circle; with application of the results to the theory of atomic structure". In: *The London, Edinburgh, and Dublin Philosophical Magazine and Journal of Science* 7:39 (1904), pp. 237–265.

[9] E. Rutherford and T. Royds. "XXIV. Spectrum of the radium emanation". In: *The London, Edinburgh, and Dublin Philosophical Magazine and Journal of Science* 16:92 (1904), pp. 313–317.

[10] H. Geiger. "On the scattering of the α-particles by matter". In: *Proceedings of the Royal Society A* 81 (1908), pp. 174–177.

[11] H. Geiger and E. Marsden. "On a diffuse reflection of the α-particles". In: *Proceedings of the Royal Society A* 82 (1909), pp. 495–500.

[12] H. Geiger. "The scattering of α-particles by matter". In: *Proceedings of the Royal Society A* 83 (1910), pp. 492–504.

[13] H. Geiger and E. Marsden. "LXI. The laws of deflexion of a particles through large angles". In: *The London, Edinburgh, and Dublin Philosophical Magazine and Journal of Science* 25:148 (1913), pp. 604–623.

[14] E. Rutherford. “LXXIX. The Scattering of α and β Particles by Matter and the Structure of the Atom”. In: *The London, Edinburgh, and Dublin Philosophical Magazine and Journal of Science* 21:125 (1911), pp. 669–688.

[15] E. Rutherford. “LIV. Collision of α particles with light atoms. IV. An anomalous effect in nitrogen”. In: *The London, Edinburgh, and Dublin Philosophical Magazine and Journal of Science* 37:222 (1919), pp. 581–587.

[16] O. Masson. “XXIV. The constitution of atoms”. In: *The London, Edinburgh, and Dublin Philosophical Magazine and Journal of Science* 41:242 (1921), pp. 281–285.

[17] W. Prout. “On the Relation between the Specific Gravities of Bodies in their Gaseous State and the Weights of their Atoms.” In: *Annals of Philosophy* 6 (1815), pp. 321–330.

[18] W. Prout. “Correction of a Mistake in the Essay on the Relation between the Specific Gravities of Bodies in their Gaseous State and the Weights of their Atoms”. In: *Annals of Philosophy* 7 (1816), pp. 111–113.

[19] E. Rutherford. “Bakerian Lecture: Nuclear constitution of atoms”. In: *Proceedings of the Royal Society A* 97 (1920), pp. 374–400.

[20] W. Bothe and H. Becker. “Künstliche Erregung von Kern-γ-Strahlen”. In: *Zeitschrift für Physik* 66 (1930), pp. 289–306.

[21] H. Becker and W. Bothe. “Die in Bor und Beryllium erregten γ-Strahlen”. In: *Zeitschrift für Physik* 76 (1932), pp. 421–438.

[22] I. Curie and F. Joliot. “Émission de protons de grande vitesse par les substances hydrogenées sous l’influence de rayons γ très pénétrants”. In: *Comptes Rendus Hebdomadaires des Séances de L’Académie des Sciences*. Vol. 194. Académie des Sciences, 1932, pp. 273–275.

[23] J. Chadwick. “Possible Existence of a Neutron”. In: *Nature* 129 (1932), p. 312.

[24] J. Chadwick. “Bakerian lecture. The neutron”. In: *Proceedings of the Royal Society A* 142 (1933), pp. 1–25.

[25] Max Plank. “Ueber das Gesetz der Energieverteilung im Normalspectrum”. In: *Annalen Der Physik* 309 (1901), pp. 553–563.

[26] A. Einstein. “Über einen die Erzeugung und Verwandlung des Lichtes betreffenden heuristischen Gesichtspunkt”. In: *Annalen Der Physik* 322 (1905), pp. 132–148.

[27] N. Bohr. “I. On the constitution of atoms and molecules”. In: *The London, Edinburgh, and Dublin Philosophical Magazine and Journal of Science* 26:151 (1913), pp. 1–25.

[28] H.G.J. Moseley. “XCIII. The high-frequency spectra of the elements”. In: *The London, Edinburgh, and Dublin Philosophical Magazine and Journal of Science* 26:156 (1913), pp. 1024–1034.

[29] A. Sommerfeld. “Zur Quantentheorie der Spektrallinien”. In: *Annalen Der Physik* 356 (1916), pp. 1–94.

[30] P. Zeeman. “XXXII. On the influence of magnetism on the nature of the light emitted by a substance”. In: *The London, Edinburgh, and Dublin Philosophical Magazine and Journal of Science* 43:262 (1897), pp. 226–239.

[31] P. Zeeman. “VII. Doublets and triplets in the spectrum produced by external magnetic forces”. In: *The London, Edinburgh, and Dublin Philosophical Magazine and Journal of Science* 44:266 (1897), pp. 55–60.

[32] P. Zeeman. “VII. Doublets and triplets in the spectrum produced by external magnetic forces.—(II.)” In: *The London, Edinburgh, and Dublin Philosophical Magazine and Journal of Science* 44:268 (1897), pp. 255–259.

[33] P. Zeeman. “XXI. Measurements concerning radiation-phenomena in the magnetic field.—(I.)” In: *The London, Edinburgh, and Dublin Philosophical Magazine and Journal of Science* 45:273 (1898), pp. 197–201.

[34] W. Gerlach and O. Stern. “Der experimentelle Nachweis der Richtungsquantelung im Magnetfeld”. In: *Zeitschrift für Physik* 9 (1922), pp. 349–352.

[35] W. Pauli. “Über den Einflußder Geschwindigkeitsabhängigkeit der Elektronenmasse auf den Zeemaneffekt”. In: *Zeitschrift für Physik* 31 (1925), 373–385.

[36] W. Pauli. “Über den Zusammenhang des Abschlusses der Elektronengruppen im Atom mit der Komplexstruktur der Spektren”. In: *Zeitschrift für Physik* 31 (1925), 765–783.

[37] G.E. Uhlenbeck and S. Goudsmit. “Spinning Electrons and the Structure of Spectra”. In: *Nature* 117 (1926), pp. 264–265.

[38] W. Pauli. “Zur Quantenmechanik des magnetischen Elektrons”. In: *Zeitschrift für Physik* 43 (1927), 601–623.

[39] L. De Broglie. “Recherches sur la théorie des Quanta”. PhD thesis. University of Paris, 1924.

[40] E. Schrödinger. “An Undulatory Theory of the Mechanics of Atoms and Molecules”. In: *Phys. Rev.* 28 (1927), pp. 1049–1070.

[41] P. Dirac. “The quantum theory of the emission and absorption of radiation”. In: *Proceedings of the Royal Society A* 114 (1928), pp. 243–265.

[42] P. Dirac. “The quantum theory of the electron”. In: *Proceedings of the Royal Society A* 117 (1928), pp. 610–624.

[43] J. R. Oppenheimer. “On the Theory of Electrons and Protons”. In: *Phys. Rev.* 35 (1930), pp. 562–563.

[44] P. Dirac. “Quantised singularities in the electromagnetic field”. In: *Proceedings of the Royal Society A* 133 (1931), pp. 60–72.

[45] J. R. Oppenheimer. “Note on the Theory of the Interaction of Field and Matter”. In: *Phys. Rev.* 35 (1930), pp. 461–477.

[46] H.A. Bethe. “The Electromagnetic Shift of Energy Levels”. In: *Phys. Rev.* 72 (1947), pp. 339–341.

[47] H.F.J. Dyson. “The Radiation Theories of Tomonaga, Schwinger, and Feynman”. In: *Phys. Rev.* 75 (1949), pp. 486–502.

[48] H. Yukawa. “On the Interaction of Elementary Particles. I”. In: *Proc. Phys. Math. Soc. Jap.* 17 (1935), pp. 48–57.

[49] C.D. Anderson and S.H. Neddermeyer. “Cloud Chamber Observations of Cosmic Rays at 4300 Meters Elevation and Near Sea-Level”. In: *Phys. Rev.* 50 (1936), pp. 263–271.

[50] S.H. Neddermeyer and C.D. Anderson. “Note on the Nature of Cosmic-Ray Particles”. In: *Phys. Rev.* 51 (1937), pp. 884–886.

[51] J.C. Street and E.C. Stevenson. “New Evidence for the Existence of a Particle of Mass Intermediate Between the Proton and Electron”. In: *Phys. Rev.* 52 (1937), pp. 1003–1004.

[52] C.M.G. Lattes et al. “Processes involving charged mesons”. In: *Nature* 159 (1947), pp. 694–697.

[53] C.M.G. Lattes et al. “Observations on the Tracks of Slow Mesons in Photographic Emulsions (Part 1)”. In: *Nature* 160 (1947), pp. 453–456.

[54] C.M.G. Lattes et al. “Observations on the Tracks of Slow Mesons in Photographic Emulsions (Part 2)”. In: *Nature* 160 (1947), 486–492.

[55] R. Blorklund et al. “High Energy Photons from Proton-Nucleon Collisions”. In: *Phys. Rev.* 77 (1950), pp. 213–218.

[56] G.D. Rochester and C.C. Butler. “Evidence for the Existence of New Unstable Elementary Particles”. In: *Nature* 160 (1947), 855–857.

[57] A. Pais. “Some Remarks on the V-Particles”. In: *Phys. Rev.* 86 (1952), pp. 663–672.

[58] M. Gell-Mann. “Symmetries of Baryons and Mesons”. In: *Phys. Rev.* 125 (1962), pp. 1067–1084.

[59] K. Nishijima and T. Nakano. “Charge Independence for V-particles”. In: *Progress of Theoretical Physics* 10 (1953), 581–582.

[60] K. Nishijima. “Charge Independence Theory of V-Particles”. In: *Progress of Theoretical Physics* 13 (1955), pp. 285–304.

[61] M. Gell-Mann. “The interpretation of the new particles as displaced charge multiplets”. In: *Il Nuovo Cimento* 4 (1956), 848–866.

[62] W. Heisenberg. “Über den Bau der Atomkerne. I”. In: *Zeitschrift für Physik* 77 (1932), 1–11.

[63] V.E. Barnes et al. “Observation of a Hyperon with Strangeness Minus Three”. In: *Phys. Rev. Lett.* 12 (1964), pp. 204–206.

[64] M. Gell-Mann. “A schematic model of baryons and mesons”. In: *Physics Letters* 8 (1964), pp. 214–215.

[65] G. Zweig. *An $SU(3)$ Model for Strong Interaction Symmetry and its Breaking*. Tech. rep. CERN-TH-401. CERN, 1964.

[66] G. Zweig. *An $SU(3)$ Model for Strong Interaction Symmetry and its Breaking (II)*. Tech. rep. CERN-TH-412. CERN, 1964.

[67] E.D. Bloom et al. “High-Energy Inelastic $e-p$ Scattering at 6° and 10°”. In: *Phys. Rev. Lett.* 23 (1969), pp. 930–934.

[68] M. Breidenbach et al. “Observed Behavior of Highly Inelastic Electron-Proton Scattering”. In: *Phys. Rev. Lett.* 23 (1969), pp. 935–939.

[69] B.J. Bjørken and S.L. Glashow. “Elementary particles and SU(4)”. In: *Physics Letters* 11 (1964), pp. 255–257.

[70] S. Glashow et al. “Weak Interactions with Lepton-Hadron Symmetry”. In: *Phys. Rev. D* 2 (1970), pp. 1285–1292.

[71] J.H. Christenson et al. “Evidence for the 2π Decay of the K_2^0 Meson”. In: *Phys. Rev. Lett.* 13 (1964), pp. 138–140.

[72] M. Kobayashi and T. Maskawa. “CP-Violation in the Renormalizable Theory of Weak Interaction”. In: *Progress of Theoretical Physics* 49 (1973), pp. 652–657.

[73] H. Harari. “A new quark model for hadrons”. In: *Physics Letters B* 57 (1975), pp. 265–269.

[74] B. Richter et al. “Discovery of a Narrow Resonance in e^+e^- Annihilation”. In: *Phys. Rev. Lett.* 33 (1974), pp. 1406–1408.

[75] S. Ting et al. “Experimental Observation of a Heavy Particle J”. In: *Phys. Rev. Lett.* 33 (1974), pp. 1404–1405.

[76] S.W. Herb et al. "Observation of a Dimuon Resonance at $9.5\,\mathrm{GeV}$ in $400\,\mathrm{GeV}$ Proton-Nucleus Collisions". In: *Phys. Rev. Lett.* 39 (1977), pp. 252–255.

[77] S. Abashi et al. "Search for High Mass Top Quark Production in $\bar{p}p$ Collisions at $\sqrt{s} = 1.8\,\mathrm{TeV}$". In: *Phys. Rev. Lett.* 74 (1995), pp. 2422–2426.

[78] F. Abe et al. "Observation of Top Quark Production in $\bar{p}p$ Collisions with the Collider Detector at Fermilab". In: *Phys. Rev. Lett.* 74 (1995), pp. 2626–2631.

[79] F. Tkachov. "A contribution to the history of quarks: Boris Struminsky's 1965 JINR publication". In: (2009).

[80] O.W. Greenberg. "Spin and Unitary-Spin Independence in a Paraquark Model of Baryons and Mesons". In: *Phys. Rev. Lett.* 13 (1964), pp. 598–602.

[81] M.Y. Han and Y. Nambu. "Three-Triplet Model with Double $SU(3)$ Symmetry". In: *Phys. Rev.* 139 (1965), B1006–B1010.

[82] R.P. Feynman. "The behavior of hadron collisions at extreme energies". In: *Conf. Proc.* C690905 (1969), pp. 237–258.

[83] J.D. Bjorken and E.A. Paschos. "Inelastic Electron-Proton and γ-Proton Scattering and the Structure of the Nucleon". In: *Phys. Rev.* 185 (1969), pp. 1975–1982.

[84] H. Fritzsch et al. "Advantages of the color octet gluon picture". In: *Physics Letters B* 47 (1973), pp. 365–368.

[85] D.J. Gross and F. Wilczek. "Ultraviolet Behavior of Non-Abelian Gauge Theories". In: *Phys. Rev. Lett.* 30 (1973), pp. 1343–1346.

[86] H.D. Politzer. "Reliable Perturbative Results for Strong Interactions?" In: *Phys. Rev. Lett.* 30 (1973), pp. 1346–1349.

[87] S. Bethke. "α_s 2002". In: *Nuclear Physics B* 121 (2003), pp. 74–81.

[88] E. Fermi. "Versuch einer Theorie der β-Strahlen. I". In: *Zeitschrift für Physik* 88 (1934), pp. 161–177.

[89] W. Pauli. "Dear radioactive ladies and gentlemen". In: *Phys. Today* 31N9 (1978), p. 27.

[90] C.L. Cowan Jr. et al. "Detection of the Free Neutrino: a Confirmation". In: *Science* 20 (1956), pp. 103–104.

[91] E.J. Konopinski and H.M. Mahmoud. "The Universal Fermi Interaction". In: *Phys. Rev.* 92 (1953), pp. 1045–1049.

[92] L.M. Lederman et al. "Observation of High-Energy Neutrino Reactions and the Existence of Two Kinds of Neutrinos". In: *Phys. Rev. Lett.* 9 (1962), pp. 36–44.

[93] T.D. Lee and C.N. Yang. "Question of Parity Conservation in Weak Interactions". In: *Phys. Rev.* 104 (1956), pp. 254–258.

[94] G. Gamow and E. Teller. "Selection Rules for the β-Disintegration". In: *Phys. Rev.* 49 (1936), pp. 895–899.

[95] C.S. Wu et al. "Experimental Test of Parity Conservation in Beta Decay". In: *Phys. Rev.* 105 (1957), pp. 1413–1415.

[96] S. Weinberg. "A Model of Leptons". In: *Phys. Rev. Lett.* 19 (1967), pp. 1264–1266.

[97] Y. Nambu and G. Jona-Lasinio. "Dynamical Model of Elementary Particles Based on an Analogy with Superconductivity. I". In: *Phys. Rev.* 122 (1961), pp. 345–358.

[98] Y. Nambu and G. Jona-Lasinio. "Dynamical Model of Elementary Particles Based on an Analogy with Superconductivity. II". In: *Phys. Rev.* 124 (1961), pp. 246–254.

[99] J. Bardeen et al. “Microscopic Theory of Superconductivity”. In: *Phys. Rev.* 106 (1957), pp. 162–164.

[100] Y. Nambu. “Quasi-Particles and Gauge Invariance in the Theory of Superconductivity”. In: *Phys. Rev.* 117 (1960), pp. 648–663.

[101] J. Goldstone. “Quasi-Particles and Gauge Invariance in the Theory of Superconductivity”. In: *Il Nuovo Cimento* 19 (1961), pp. 154–164.

[102] P.W. Anderson. “Plasmons, Gauge Invariance, and Mass”. In: *Phys. Rev.* 130 (1963), pp. 439–442.

[103] J. Schwinger. “Gauge Invariance and Mass”. In: *Phys. Rev.* 125 (1962), pp. 397–398.

[104] F. Englert and R. Brout. “Broken Symmetry and the Mass of Gauge Vector Mesons”. In: *Phys. Rev. Lett.* 13 (1964), pp. 321–323.

[105] P.W. Higgs. “Broken Symmetries and the Masses of Gauge Bosons”. In: *Phys. Rev. Lett.* 13 (1964), pp. 508–509.

[106] G.S. Guralnik et al. “Global Conservation Laws and Massless Particles”. In: *Phys. Rev. Lett.* 13 (1964), pp. 585–587.

[107] Wikipedia. *Standard Model*. 2018. URL: `https://en.wikipedia.org/wiki/Standard_Model`.

[108] UA1 Collaboration. “Experimental observation of isolated large transverse energy electrons with associated missing energy at $s = 540\,\mathrm{GeV}$”. In: *Physics Letters B* 122 (1983), pp. 103–116.

[109] UA2 Collaboration. “Observation of single isolated electrons of high transverse momentum in events with missing transverse energy at the CERN pp collider”. In: *Physics Letters B* 122 (1983), pp. 476–485.

[110] UA1 Collaboration. “Experimental observation of lepton pairs of invariant mass around $95\,\mathrm{GeV/c^2}$ at the CERN SPS collider”. In: *Physics Letters B* 126 (1983), pp. 398–410.

[111] UA2 Collaboration. “Evidence for $Z_0 \to e^+e^-$ at the CERN pp collider”. In: *Physics Letters B* 129 (1983), pp. 130–140.

[112] ATLAS Collaboration. “Observation of a new particle in the search for the Standard Model Higgs boson with the ATLAS detector at the LHC”. In: *Physics Letters B* 716 (2012), pp. 1–29.

[113] CMS Collaboration. “Observation of a new boson at a mass of 125 GeV with the CMS experiment at the LHC”. In: *Physics Letters B* 716 (2012), pp. 30–61.

[114] ATLAS Collaboration and CMS Collaboration. “Combined Measurement of the Higgs Boson Mass in *pp* Collisions at $\sqrt{s} = 7$ and $8\,\mathrm{TeV}$ with the ATLAS and CMS Experiments”. In: *Physical Review Letters* 114 (2015). 191803.

[115] M. Tanabashi et al. (Particle Data Group). “Review of Particle Physics”. In: *Phys. Rev. D* 98 (2018), p. 030001.

[116] A.A. Arkhipov. “Proton proton total cross-sections from the window of cosmic ray experiments”. In: *Elastic and diffractive scattering. Proceedings, 9th Blois Workshop, Pruhonice, Czech Republic*. 2001, pp. 293–304.

[117] H. Pointcaré. “The Milky Way and the Theory of Gases”. In: *Popular Astronomy* 14 (1906), pp. 475–488.

[118] J.C. Kapteyn. “First Attempt at a Theory of the Arrangement and Motion of the Sidereal System”. In: *Astrophysical Journal* 55 (1922), p. 302.

[119] F. Zwicky. "Republication of: The redshift of extragalactic nebulae (First published in 1933)". In: *General Relativity and Gravitation* 41 (2009), pp. 207–224.

[120] F. Zwicky. "On the Masses of Nebulae and of Clusters of Nebulae". In: *Astrophysical Journal* 86 (1937), p. 217.

[121] H.W. Babcock. "The rotation of the Andromeda Nebula". In: *Lick Observatory bulletin* 498 (1939), pp. 41–51.

[122] V.C. Rubin and W.K. Ford Jr. "Rotation of the Andromeda Nebula from a Spectroscopic Survey of Emission Regions". In: *Astrophysical Journal* 159 (1970), p. 379.

[123] D.H. Rogstad and G.S. Shostak. "Gross Properties of Five Scd Galaxies as Determined from 21-CENTIMETER Observations". In: *Astrophysical Journal* 176 (1972), p. 315.

[124] Planck Collaboration. "Planck 2015 results. XIII. Cosmological parameters". In: *A&A* 594.A13 (2016).

[125] N. Jarosik et al. "Seven-year Wilkinson Microwave Anisotropy Probe (WMAP*) observations: Sky maps, Systematic errors, and Basic Results". In: *ApJS* 192.14 (2011).

[126] E. Verlinde. "Emergent Gravity and the Dark Universe". In: *SciPost Phys.* 2 (2017), p. 016.

[127] A. Maeder. "An alternative to the ΛCDM model: the case of scale invariance". In: *ApJ* 834.194 (2017).

[128] E. Corbelli and P. Salucci. "The extended rotation curve and the dark matter halo of M33". In: *Monthly Notices of the Royal Astronomical Society* 311 (2000), pp. 441–447.

[129] S. Dimopoulos and H. Georgi. "Softly broken supersymmetry and SU(5)". In: *Nuclear Physics B* 193 (1981), pp. 150–162.

[130] F. Tanedo. *The Hierarchy Problem: why the Higgs has a snowball's chance in hell.* 2012. URL: `https://www.quantumdiaries.org/2012/07/01/the-hierarchy-problem-why-the-higgs-has-a-snowballs-chance-in-hell/`.

[131] G. Jungman et al. "Supersymmetric dark matter". In: *Physics Reports* 267 (1996), pp. 10–14.

[132] A.H. Chamseddine et al. "Locally Supersymmetric Grand Unification". In: *Phys. Rev. Lett.* 49 (1982), pp. 970–974.

[133] A. Askew et al. "Searching for dark matter at hadron colliders". In: *International Journal of Modern Physics A* 29 (2014), p. 1430041.

[134] N. Arkani–Hamed et al. "The hierarchy problem and new dimensions at a millimeter". In: *Physics Letters B* 429 (1998), pp. 263–272.

[135] N. Arkani–Hamed et al. "Phenomenology, astrophysics, and cosmology of theories with submillimeter dimensions and TeV scale quantum gravity". In: *Phys. Rev. D* 59 (1999), p. 086004.

[136] T. Kaluza. "Zum Unitätsproblem der Physik". In: *Sitzungsber. Preuss. Akad. Wiss. Berlin (Math. Phys.)* 1921 (1921), pp. 966–972.

[137] O. Klein. "The Atomicity of Electricity as a Quantum Theory Law". In: *Nature* 118 (1926), p. 516.

[138] L. Randall and R. Sundrum. "Large Mass Hierarchy from a Small Extra Dimension". In: *Phys. Rev. Lett.* 83 (1999), pp. 3370–3373.

[139] L. Randall and R. Sundrum. "An Alternative to Compactification". In: *Phys. Rev. Lett.* 83 (1999), pp. 4690–4693.

[140] M. Strassler and K. Zurek. "Echoes of a hidden valley at hadron colliders". In: *Phys. Let. B* 651 (2007), pp. 374–379.

[141] A. Sakharov. "Violation of CP i variance, C asymmetry, and baryon asymmetry of the universe". In: *JETP Letters* 5 (1967), pp. 24–27.

[142] M.E. Shaposhnikov and G. Farrar. "Baryon asymmetry of the Universe in the minimal standard model". In: *Phys. Rev. Lett.* 70 (1993), pp. 2833–2836.

[143] V.A. Kuzmin et al. "On anomalous electroweak baryon-number non-conservation in the early universe". In: *Physics Letters B* 155 (1985), pp. 36–42.

[144] L. Canetti et al. "Matter and antimatter in the universe". In: *New J. Phys.* 14.095012 (2012).

[145] CMS Collaboration. "Search for black holes and sphalerons in high-multiplicity final states in proton-proton collisions at $\sqrt{s} = 13$ TeV". In: *Journal of High Energy Physics* 11 (2018).

[146] B. Shuve and Y. Cui. "Probing baryogenesis with displaced vertices at the LHC". In: *Journal of High Energy Physics* 2 (2015).

[147] The ACME Collaboration. "Order of Magnitude Smaller Limit on the Electric Dipole Moment of the Electron". In: *Science* 343 (2014), pp. 269–272.

[148] N. Neri et al. "On the search for the electric dipole moment of strange and charm baryons at LHC". In: *The European Physical Journal C* 77 (2017), p. 181.

[149] J. Stevens and M. Sher. "Detecting a heavy neutrino electric dipole moment at the LHC". In: *Physics Letters B* 777 (2018), pp. 246–249.

[150] R. Davis Jr. et al. "Search for Neutrinos from the Sun". In: *Physical Review Letters* 20 (1968), pp. 1205–1209.

[151] B. Pontecorvo. "Neutrino Experiments and the Problem of Conservation of Leptonic Charge". In: *Sov. Phys. JETP* 26 (1968), pp. 984–988.

[152] SNO Collaboration. "Direct Evidence for Neutrino Flavor Transformation from Neutral-Current Interactions in the Sudbury Neutrino Observatory". In: *Physical Review Letters* 89.011301 (2002).

[153] Z. Maki et al. "Remarks on the Unified Model of Elementary Particles". In: *Progress of Theoretical Physics* 28 (1962), pp. 870–880.

[154] P. Minkowski. "$\mu \longrightarrow e\gamma$ at a rate of one out of 10^9 muon decays?" In: *Physics Letters B* 67 (1977), pp. 421–428.

[155] R.N. Mohapatra and G. Senjanović. "Neutrino Mass and Spontaneous Parity Nonconservation". In: *Phys. Rev. Lett.* 44 (1980), pp. 912–915.

[156] CERN. Geneva. LHC Experiments Committee. *CMS Physics Technical Design Report Volume II: Physics Performance*. Tech. rep. CERN-LHCC-2006-021 ; CMS-TDR-8-2. CMS Collaboration, 2006.

[157] P.W.F. Valle. "Neutrino physics overview". In: *J. Phys.: Conf. Ser.* 53 (2006), pp. 473–505.

[158] T. Massam et al. "Experimental observation of antideuteron production". In: *Il Nuovo Cimento A* 63 (1965), pp. 10–14.

[159] ALEPH Collaboration. "Determination of the number of light neutrino species". In: *Physics Letters B* 231 (1989), pp. 519–529.

[160] CERN, ed. (1985).

[161] CERN, ed. (1986).

[162] CERN, ed. (1994).

[163] CERN, ed. (1998).

[164] CERN, ed. (1999).

[165] CERN. Geneva. LHC Experiments Committee. *Letter of Intent for A Large Ion Collider Experiment [ALICE]*. Tech. rep. CERN-LHCC-93-016. ALICE Collaboration, 1993.

[166] CERN. Geneva. LHC Experiments Committee. *ATLAS : technical proposal for a general-purpose pp experiment at the Large Hadron Collider at CERN*. Tech. rep. CERN-LHCC-94-43. ATLAS Collaboration, 1994.

[167] CERN. Geneva. LHC Experiments Committee. *CMS : letter of intent by the CMS Collaboration for a general purpose detector at LHC*. Tech. rep. CERN-LHCC-92-003. CMS Collaboration, 1992.

[168] CERN. Geneva. LHC Experiments Committee. *LHCb : letter of intent*. Tech. rep. CERN-LHCC-95-5. LHCb Collaboration, 1995.

[169] L. Evans and P. Bryant. "LHC Machine". In: *JINST* 3 (2008). S08001.

[170] LHCb Collaboration. "Observation of $J/\psi p$ Resonances Consistent with Pentaquark States in $\Lambda_b^0 \to J/\psi K^- p$ Decays". In: *Physical Review Letters* 115 (2015). 072001.

[171] LHCb Collaboration. "Observation of $J/\psi\phi$ Structures Consistent with Exotic States from Amplitude Analysis of $B^+ \to J/\psi\phi K^+$ Decays". In: *Physical Review Letters* 118 (2017). 022003.

[172] ALICE Collaboration. *First results from proton-lead collisions*. URL: `http://aliceinfo.cern.ch/Public/en/Chapter1/results-pPb.html`.

[173] ATLAS Collaboration. "Observation of a New χ_b State in Radiative Transitions to $\Upsilon(1S)$ and $\Upsilon(2S)$ at ATLAS". In: *Physical Review Letters* 108 (2012). 152001.

[174] LHCb Collaboration. "First Evidence for the Decay $B_s^0 \to \mu^+\mu^-$". In: *Physical Review Letters* 110 (2013). 021801.

[175] CERN. Geneva. *High-Luminosity Large Hadron Collider (HL-LHC) Technical Design Report V. 0.1* . Tech. rep. CERN-2017-007-M. 2017.

[176] CERN. Geneva. LHC Experiments Committee. *CMS, the Compact Muon Solenoid : technical proposal*. Tech. rep. CERN-2015-005. 2015.

[177] CERN. Geneva. LHC Experiments Committee. *The Phase-2 Upgrade of the CMS Muon Detectors*. Tech. rep. CERN-LHCC-2017-012, CMS-TDR-016. CMS Collaboration, 2017.

[178] M. Drees and X. Tata. "Signals for heavy exotics at hadron colliders and supercolliders". In: *Physics Letters B* 252 (1990), pp. 695–702.

[179] D.A. Milstead et al. "Stable massive particles at colliders". In: *Physics Reports* 438 (2007), pp. 1–63.

[180] Z. Ligeti et al. "Supermodels for early LHC". In: *Physics Letters B* 690 (2010), pp. 280–288.

[181] CMS Collaboration. "Search for long-lived charged particles in proton-proton collisions at $\sqrt{(s)} = 13\,\mathrm{TeV}$". In: *Phys. Rev. D* 94 (2016), p. 112004.

[182] V. Khachatryan et al. "Search for long-lived charged particles in proton-proton collisions at $\sqrt{s} = 13\,\mathrm{TeV}$". In: *Phys. Rev. D* 94 (2017). 112004.

[183] A. Kusenko and M. Shaposhnikov. "Supersymmetric Q-balls as dark matter". In: *Physics Letters B* 418 (1998), pp. 46–54.

[184] B. Koch et al. "Black holes at LHC?" In: *J. Phys. G: Nucl. Part. Phys.* 34 (2007). S535.

[185] J. Schwinger. “Magnetic Charge and Quantum Field Theory”. In: *Phys. Rev.* 144 (1966). 1087.

[186] M Yu Khlopov et al. “Dark matter with invisible light from heavy double charged leptons of almost-commutative geometry?” In: *Class. Quantum Grav.* 23 (2006). 7305.

[187] PoS, ed. *Search for Heavy Stable Charged Particles in CMS*. Vol. 084-EPS-HEP2009. 2009, p. 438.

[188] L.E. Medina Medrano et al. “Studies on Luminous Region, Pile-up and Performance for HL-LHC Scenarios”. In: *Proc. of International Particle Accelerator Conference (IPAC’17), Copenhagen, Denmark, 14-19 May, 2017*. JACoW, 2017, pp. 1908–1911.

[189] CMS Collaboration. *CMS Luminosity - Public Results*. Version 158. 2019. URL: https://twiki.cern.ch/twiki/bin/view/CMSPublic/LumiPublicResults.

[190] CERN. Geneva. LHC Experiments Committee. *Technical Proposal for the Phase-II Upgrade of the CMS Detector*. Tech. rep. CERN-LHCC-2015-010, CMS-TDR-15-02. CMS Collaboration, 2015.

[191] CERN. Geneva. LHC Experiments Committee. *The Phase-2 Upgrade of the CMS Level-1 Trigger - Interim Report to the LHCC*. Tech. rep. CERN-LHCC-2017-013, CMS-TDR-017. CMS Collaboration, 2017.

[192] CERN. Geneva. LHC Experiments Committee. *The CMS muon project : Technical Design Report*. Tech. rep. CERN-LHCC-97-032. CMS Collaboration, 1997.

[193] CERN. Geneva. LHC Experiments Committee. *High-Luminosity Large Hadron Collider (HL-LHC) Preliminary Design Report*. Tech. rep. CERN-LHCC-94-38. CMS Collaboration, 1994.

[194] F. Sauli. “GEM: A new concept for electron amplification in gas detectors”. In: *Nucl. Instr. Meth. Phys. Res.* 386 (1997), pp. 531–534.

[195] CERN. Geneva. LHC Experiments Committee. *CMS Technical Design Report for the Muon Endcap GEM Upgrade*. Tech. rep. CERN-LHCC-2015-012, CMS-TDR-013. CMS Collaboration, 2015.

[196] A. Gelmi. *CMS iRPC at HL-LHC: background study*. 2018. URL: https://indico.cern.ch/event/732794/contributions/3021836/attachments/1657792/2654574/iRPC_bkg_study_Upgrade29_05_18.pdf.

[197] A. Gelmi and E. Voevodina. “Background rate study for the CMS improved-RPC at HL-LHC using GEANT4”. In: *Nucl. Instr. Meth. Phys. Res. A* (2018).

[198] IEEE, ed. *Petiroc, a new front-end ASIC for time of flight application*. Vol. 2013 IEEE Nuclear Science Symposium and Medical Imaging Conference (2013 NSS/MIC). 2014.

[199] JINST, ed. *Petiroc and Citiroc: front-end ASICs for SiPM read-out and ToF applications*. Vol. Topical Workshop on Electronics for Particle Physics 2013 (TWEPP-13). 2014.

[200] P.Bortignon. “Design and performance of the upgrade of the CMS L1 muon trigger”. In: *Nucl. Instr. Meth. Phys. Res.* 824 (2016), pp. 256–257.

[201] The European Parliament and the Council of the European Union. “Regulation (EU) No 517/2014 of 16 April 2014 on fluorinated greenhouse gases and repealing Regulation (EC) No 842/2006”. In: *Official Journal of the European Union* 150 (2014), pp. 195–230.

[202] D. Piccolo. *Preliminary results of Resis1ve Plate Chambers operated with eco-riendly gas mixtures for applica1on in the CMS experiment*. 2016. URL: https://indico.ugent.be/event/0/session/18/contribution/28/material/slides/0.pdf.

[203] R. Santonico and R. Cardarelli. "Development of resistive plate counters". In: *Nucl. Instr. Meth. Phys. Res.* 187 (1981), pp. 377–380.

[204] Yu.N. Pestov and G.V. Fedotovich. *A picosecond time-of-flight spectrometer fot eh VEPP-2M based on local-discharge spark counter*. Tech. rep. SLAC-TRANS-0184. SLAC, 1978.

[205] W.W. Ash, ed. *Spark Counter With A Localized Discharge*. Vol. SLAC-R-250. 1982, pp. 127–131.

[206] I. Crotty et al. "The non-spark mode and high rate operation of resistive parallel plate chambers". In: *NIMA* 337 (1993), pp. 370–381.

[207] I. Crotty et al. "Further studies of avalanche mode operation of resistive parallel plate chambers". In: *NIMA* 346 (1994), pp. 107–113.

[208] R. Cardarelli et al. "Avalanche and streamer mode operation of resistive plate chambers". In: *NIMA* 382 (1996), pp. 470–474.

[209] R. Cardarelli et al. "Performance of a resistive plate chamber operating with pure CF_3Br". In: *NIMA* 333 (1993), pp. 399–403.

[210] M. Abbrescia et al. "Performance of a Resistive Plate Chamber operated in avalanche mode under ^{137}Cs irradiation". In: *NIMA* 392 (1997), pp. 155–160.

[211] M. Abbrescia et al. "Properties of C2H2F4-based gas mixture for avalanche mode operation of resistive plate chambers". In: *NIMA* 398 (1997), pp. 173–179.

[212] P. Camarri et al. "Streamer suppression with SF6 in RPCs operated in avalanche mode". In: *NIMA* 414 (1998), pp. 317–324.

[213] E. Cerron Zeballos et al. "Effect of adding SF6 to the gas mixture in a multigap resistive plate chamber". In: *NIMA* 419 (1998), pp. 475–478.

[214] E. Cerron Zeballos et al. "A new type of resistive plate chamber: The multigap RPC". In: *NIMA* 374 (1996), pp. 132–135.

[215] M.C.S. Williams. "The development of the multigap resistive plate chamber". In: *Nucl. Phys. B* 61 (1998), pp. 250–257.

[216] H. Czyrkowski et al. "New developments on resistive plate chambers for high rate operation". In: *NIMA* 419 (1998), pp. 490–496.

[217] CERN. Geneva. LHC Experiments Committee. *ATLAS muon spectrometer: Technical design report*. Tech. rep. CERN-LHCC-97-22. ATLAS Collaboration, 1997.

[218] CERN. Geneva. LHC Experiments Committee. *ALICE Time-Of-Flight system (TOF) : Technical Design Report*. Tech. rep. CERN-LHCC-2000-012. ALICE Collaboration, 2000.

[219] The CALICE collaboration. "First results of the CALICE SDHCAL technological prototype". In: *JINST* 11 (2016).

[220] PoS, ed. *Density Imaging of Volcanoes with Atmospheric Muons using GRPCs*. International Europhysics Conference on High Energy Physics - HEP 2011. 2011.

[221] C. Lippmann. "Detector Physics of Resistive Plate Chambers". PhD thesis. Johann Wolfgang Goethe-Universität, 2003.

[222] W. Riegler. "Induced signals in resistive plate chambers". In: *NIMA* 491 (2002), pp. 258–271.

[223] M. Abbrescia et al. "Effect of the linseed oil surface treatment on the performance of resistive plate chambers". In: *NIMA* 394 (1997), pp. 13–20.

[224] G.Battistoni et al. "Sensitivity of streamer mode to single ionization electrons". In: *NIMA* 235 (1985), pp. 91–97.

[225] M.Abbrescia et al. "Cosmic ray tests of double-gap resistive plate chambers for the CMS experiment". In: *NIMA* 550 (2005), pp. 116–126.

[226] JINST, ed. *Performance of the Resistive Plate Chambers in the CMS experiment*. The 9^{th} International Conference on Positioin Sensitive Detectors. 2012.

[227] PoS, ed. *The CMS RPC detector performance during Run-II data taking*. The European Physical Society Conference on High Energy Physics (EPS-HEP2017). 2018.

[228] Honeywell International Inc. *Solstice(R) ze Refrigerant (HFO-1234ze): The Environmental Alternative to Traditional Refrigerants*. Tech. rep. FPR-003/2015-01. 2015.

[229] E. Cerron Zeballos et al. "A comparison of the wide gap and narrow gap resistive plate chamber". In: *NIMA* 373 (1996), pp. 35–42.

[230] ALICE Collaboration. "A study of the multigap RPC at the gamma irradiation facility at CERN". In: *NIMA* 490 (2002), pp. 58–70.

[231] B. Bonner et al. "A multigap resistive plate chamber prototype for time-of-flight for the STAR experiment at RHIC". In: *NIMA* 478 (2002), pp. 176–179.

[232] S. Yang et al. "Test of high time resolution MRPC with different readout modes for the BESIII upgrade". In: *NIMA* 763 (2014), pp. 190–196.

[233] A. Akindinovg et al. "RPC with low-resistive phosphate glass electrodes as a candidate for the CBM TOF". In: *NIMA* 572 (2007), pp. 676–681.

[234] JINST, ed. *Development of the MRPC for the TOF system of the MultiPurpose Detector*. RPC2016: XII Workshop on Resistive Plate Chambers and Related Detectors. 2016.

[235] M.C.S. Williams. "Particle identification using time of flight". In: *Journal of Physics G* 39 (2012).

[236] A. Alici et al. "Aging and rate effects of the Multigap RPC studied at the Gamma Irradiation Facility at CERN". In: *NIMA* 579 (2007), pp. 979–988.

[237] M. Abbrescia et al. "The simulation of resistive plate chambers in avalanche mode: charge spectra and efficiency". In: *NIMA* 431 (1999), pp. 413–427.

[238] JINST, ed. *Description and simulation of physics of Resistive Plate Chambers*. RPC2016: XII Workshop on Resistive Plate Chambers and Related Detectors. 2016.

[239] V. Français. "Description and simulation of the physics of Resistive Plate Chambers". PhD thesis. LPC - Laboratoire de Physique Corpusculaire - Clermont-Ferrand, 2017.

[240] H. Bethe. "Zur Theorie des Durchgangs schneller Korpuskularstrahlen durch Materie". In: *Annalen der Physik* 397 (1930), pp. 325–400.

[241] International Commission on Radiation Units and Measurements. *Stopping Powers for Electrons and Positions*. Tech. rep. Report 37. 1984.

[242] International Commission on Radiation Units and Measurements. *Stopping Power and Ranges for Protons and Alpha Particles*. Tech. rep. Report 49. 1994.

[243] H. Bichsel. "A method to improve tracking and particle identification in TPCs and silicon detectors". In: *NIMA* 562 (2006), pp. 154–197.

[244] W. W. M. Allison and J. H. Cobb. "Relativistic charged particle identification by energy loss". In: *Annual Review of Nuclear and Particle Science* 30 (1980), 253–298.

[245] International Commission on Radiation Units and Measurements. *Average energy to produce an ion pair*. Tech. rep. Report 31. 1994.

[246] I.B. Smirnov. “Modeling of ionization produced by fast charged particles in gases”. In: *NIMA* 554 (2005), pp. 474–493.

[247] J. Phys.: Conf. Ser., ed. *https://doi.org/10.1088/1742-6596/587/1/012035Results of the CALICE SDHCAL technological prototype*. 16th International Conference on Calorimetry in High Energy Physics (CALOR 2014). 2015.

[248] W. Riegler et al. “Detector physics and simulation of resistive plate chambers”. In: *NIMA* 500 (2003), pp. 144–162.

[249] I.B. Smirnov. *HEED++ simulation program*. 2010. URL: `http://ismirnov.web.cern.ch/ismirnov/heed`.

[250] S.F. Biagi. “Monte Carlo simulation of electron drift and diffusion in counting gases under the influence of electric and magnetic fields”. In: *NIMA* 421 (1999), pp. 234–240.

[251] W. H. Furry. “On Fluctuation Phenomena in the Passage of High Energy Electrons through Lead”. In: *Phys. Rev.* 52 (1937), pp. 569–581.

[252] H. Genz. “Single electron detection in proportional gas counters”. In: *Nucl. Instr. and Meth.* 112 (1973), pp. 83–90.

[253] M. Abbrescia et al. “Resistive plate chambers performances at cosmic rays fluxes”. In: *NIMA* 359 (1995), pp. 603–609.

[254] M. Abbrescia et al. “Resistive plate chambers performances at low pressure”. In: *NIMA* 394 (1997), pp. 341–348.

[255] M. Abbrescia. “Operation, performance and upgrade of the CMS Resistive Plate Chamber system at LHC”. In: *NIMA* 732 (2013), pp. 195–198.

[256] F. Thyssen. “Commissioning, Operation and Performance of the CMS Resistive Plate Chamber System”. PhD thesis. Universiteit Gent, 2014.

[257] M. Bianco. “ATLAS RPC certification and commissioning with cosmic rays”. PhD thesis. Università del Salento, 2007.

[258] M. Bianco. “ATLAS RPC certification with cosmic rays”. In: *NIMA* 602 (2009), pp. 700–704.

[259] M. Abbrescia et al. “Study of long-term performance of CMS RPC under irradiation at the CERN GIF”. In: *NIMA* 533 (2004), pp. 102–106.

[260] H.C. Kim et al. “Quantitative aging study with intense irradiation tests for the CMS forward RPCs”. In: *NIMA* 602 (2009), pp. 771–774.

[261] S. Agosteo et al. “A facility for the test of large-area muon chambers at high rates”. In: *NIMA* 452 (2000), pp. 94–104.

[262] PoS, ed. *CERN GIF ++ : A new irradiation facility to test large-area particle detectors for the high-luminosity LHC program*. Vol. TIPP2014. 2014, pp. 102–109.

[263] D. Pfeiffer et al. “The radiation field in the Gamma Irradiation Facility GIF++ at CERN”. In: *NIMA* 866 (2017), pp. 91–103.

[264] CAEN. *Mod. V1190-VX1190 A/B, 128/64 Ch Multihit TDC*. 14th ed. 2016.

[265] CAEN. *Mod. V1718 VME USB Bridge*. 9th ed. 2009.

[266] A. Fagot. *GIF Cosmic Muon Monte Carlo Simulation*. 2017. URL: `https://github.com/afagot/Cosmics-Simulation`.

[267] G. Pugliese et al. “Long-term performance of double gap resistive plate chambers under gamma irradiation”. In: *NIMA* 477 (2002), pp. 293–298.

[268] G. Pugliese et al. “Aging study for resistive plate chambers of the CMS muon trigger detector”. In: *NIMA* 515 (2003), pp. 342–347.

[269] M. Capeans et al. on behalf of the GIF and GIF++ User Communities. “A GIF++ Gamma Irradiation Facility at the SPS H4 Beam Line”. CERN-SPSC-2009-029 / SPSC-P-339. 2009.

[270] R. Guida et al. “Results about HF production and bakelite analysis for the CMS Resistive Plate Chambers”. In: *NIMA* 594 (2008), pp. 140–147.

[271] F. Bellini et al. “Study of HF production in BaBar Resistive Plate Chambers”. In: *NIMA* 594 (2008), pp. 33–38.

[272] J. Eysermans. *WebDCS GIF++*. CERN. 2016. URL: https://www.webdcs.cern.ch.

[273] A. Fagot and S. Carrillo. *GIF++ Offline Analysis v6*. 2017. URL: https://github.com/afagot/GIF_OfflineAnalysis.

[274] H. Reithler. *Filters for GIF++*. RWTH Aachen University, CMS-CERN. 2013. URL: https://edms.cern.ch/document/1324028/1.

[275] R. Cardarelli et al. “RPC performance vs. front-end electronics”. In: *NIMA* 661 (2012), S198–S200.

[276] C. Combaret et al. “Fast timing measurement for CMS RPC Phase-II upgrade”. In: *JINST* 13 (2018), p. C09001.

[277] L. Pizzimento et al. “Development of a new Front End electronics in Silicon and Silicon-Germanium technology for the Resistive Plate Chamber detector for high rate experiments”. XIV RPC 2018 - Workshop on resistive plate chambers and related detectors. 2018.

[278] E. Alunno Camelia et al. “Optimization of RPCs read-out panel with electromagnetic simulation”. XIV RPC 2018 - Workshop on resistive plate chambers and related detectors. 2018.

[279] R. Cardarelli et al. “Performance of RPCs and diamond detectors using a new very fast low noise preamplifier”. In: *JINST* 8 (2013), P01003.

[280] J. de Urquijo et al. “Electron swarm coefficients in 1,1,1,2 tetrafluoroethane (R134a) and its mixtures with Ar”. In: *The European Physical Journal D* 51 (2009), pp. 241–246.

[281] A. Fagot. *GIF++ Data Acquisition Software for CMS RPC*. 2016. URL: https://github.com/afagot/GIF_DAQ.

[282] W-Ie-Ne-R. *VME 6021-23 VXI*. 5th ed. 2016.

[283] Wikipedia. *INI file*. 2017. URL: https://en.wikipedia.org/wiki/INI_file.